CYRIC

ANNUAL REPORT

2009

(January 2009 - December 2009)

CYCLOTRON AND RADIOISOTOPE CENTER
TOHOKU UNIVERSITY
http://www.cyric.tohoku.ac.jp/

PREFACE

In this thirtieth issue of the CYRIC Annual Report, we summarize the activities in research and development, and in training of radioisotope safe-treatment at the Cyclotron and Radioisotope Center (CYRIC) during the calendar year 2009.

Research at CYRIC was carried out in the fields of nuclear physics, nuclear chemistry, material sciences, nuclear medicine using PET (oncology, brain study, pharmacology), radiopharmaceutical chemistry, health physics, nuclear instrumentation, nuclear medical engineering (diagnosis and therapy technology), nuclear engineering and elemental analysis using PIXE.

Developments and improvements on nuclear instruments and techniques have progressed; one of the 2009 highlights is the development of a disposable chip for electrochemical concentration of aqueous [^{18}F]fluoride, which demonstrates a successful application to microfluidic radiosynthesis of several PET probes.

Both the K=110 MeV AVF cyclotron and K=12 MeV AVF cyclotron were steady operated in this year. The standalone commissioning of new 10 GHz ECR ion source has started. A new project for producing a spin polarization of unstable nuclei has been launched aiming at the study of nuclear moments. The NMR signal of dynamically polarized protons was observed in a crystal of p-terphenyl doped with pentacene. The beam line to produce the high intensity radioactive element of ^{210}Fr was constructed at 51 course in the TR5 to search for the electric dipole moment of the electron. The newly developed thermal ionizer was installed and operated successfully in this course to achieve the Fr^+ yield of 10^6 ions/s.

Experimental studies of proton therapy combined with the novel vascular disrupting agent AVE8062 have been performed in a murine tumor model using the proton therapy system for small animals at CYRIC. An enhanced tumor-growth delay has been observed in the combined treatment compared to those in monotherapies. In order to assess therapeutic effects of the combined treatment, [^{18}F]FDG-PET has been carried out using the high-resolution semiconductor small animal PET (Fine-PET). The high-resolution [^{18}F]FDG-PET measurements have successfully revealed distributions of

FDG uptake and their changes which are expected to be associated with vascular shutdown in the tumor and antitumor effects induced by the combined treatment.

[^{18}F]FDG (19 preparations), [^{18}F]FRP-170 (4), [^{18}F]FACT (7), [^{11}C]methionine (0), [^{11}C]doxepin (18), [^{11}C]raclopride (5), [^{11}C]donepezil (11), [^{11}C]BF-227 (18) and [^{15}O]water (12) for clinical PET studies were routinely prepared for PET clinical studies in this year. Each number of their preparations was reduced nearly by half because the HM-12 cyclotron had worked only until the end of July and stopped for renewal of the facility building. Our research activities in new PET probe developments and evaluations, also considerably affected by this temporary but long-term shutdown, was focused on successive development of 2-deoxy-2-[^{18}F]fluoro-D-mannose as a promising tumor imaging agent and a disposable chip for electrochemical concentration of aqueous [^{18}F]fluoride. The latter demonstrated successful application to microfluidic radiosynthesis of several PET probes and was presented at an international congress for the first time.

In 2009, Molecular Imaging Educational Program of Tohoku University was further expanded with support from the Japanese Ministry of Education, Culture, Sports, Science and Technology. Important findings using [^{11}C]BF-227 were obtained, demonstrating the superiority of [^{11}C]BF-227 PET to MRI volumetry and [^{18}F]FDG PET in diagnosis of Alzheimer's disease (AD) and mild cognitive impairment (MCI). Using the [^{11}C]BF-227, CYRIC contributed to a multicenter study project "Alzheimer's Disease Neuroimaging Initiative-Japan (J-ADNI)". New applications of conventional tracers such as [^{11}C]doxepin and [^{11}C]doxepin lead to several important publications regarding pathophysiology of anorexia nervosa and AD and clinical pharmacology. PET studies using [^{18}F]FDG and [^{15}O]H_2O were also active and resulted in new papers in orthopedic surgery and pharmacogenomics.

The research program on PIXE analysis has been carried out by using electrostatic accelerator (4.5 MV Dynamitron) at the Fast Neutron Laboratory, Graduate School of Engineering, Tohoku University, under the scientific tip up between CYRIC and FNL. Research studies using submilli-PIXE camera, microbeam analysis system, and Micron-CT have been routinely carried out. A total of 902 hours of beam-time was served to this program without serious problems. A computer-aided beam transport control system was newly developed to achieve easy tuning and operation for both novices and experienced users.

The beginners training for safe handling of radiation and radioisotopes was carried out as usual. In 2009, a total of 1028 staffs and students of Tohoku University took three

courses: 1) Radioisotopes and radiation generators (503 trainees), 2) X-ray machines and electron microscope (437), and 3) Synchrotron Radiation (88). The number of trainees in this year was almost the same as that of the previous year (1031). The English classes for each course were practiced for 86 foreign students and scientists.

Selective separation of Cs-137 and Sr-90, which are major heat-generating nuclides, from the high-level liquid waste (HLLW) generated from reprocessing of spent nuclear fuel by using macroporous silica-based supramolecular recognition absorbents (Calix[4]arene-R14/SiO_2-P, DtBuCH18C6/SiO_2-P) has been studied. Chromatographic separation of Cs and Sr from a simulated HLLW by the column containing with Calix[4]arene-R14/SiO_2-P and DtBuCH18C6/SiO_2-P adsorbents were carried out. Cs and Sr were separated selectively from other fission products.

Thallium bromide (TlBr) has been investigated as a semiconductor material for fabrication of gamma-ray detectors exhibiting extremely high detection efficiency. Planar detectors, strip detectors and double-sided strip detectors were fabricated from TlBr crystals grown by the traveling molten zone method using zone-purified material. The detector performance including the leakage current, energy resolutions and timing performance were evaluated in order to assess the capability of the detectors for the PET applications. The TlBr detectors exhibited excellent spectroscopic performance at room temperature.

In addition to our above activities, we announce three items of news encouraging our center. First, the main building of our center was renewed which consists of accelerator rooms, target rooms, research rooms, meeting rooms, staff rooms, office rooms etc. Second, the program of "Breaking new ground in the research of atomic energy application" started under the support of the Ministry of Education, Sports, Culture, Science and Technology and in collaboration with Hachinohe Institute of Technology and Aomori prefecture. In this program, the research study on useful applications of high level radioactive waste and training nuclear engineers is performed. To achieve this program, two research divisions were established in our center, which are the division of nuclear fuel chemistry and the division of advanced radiation application and a prefectural research center is planning to be built in Rokkasho village of Aomori prefecture. Third, the new scientific project on the search for the electron electric dipole moment to study the matter-antimatter asymmetry in the universe has been started with the support by Grant-in-Aid for Scientific Research on Innovative Areas ``Extreme quantum world opened up by atoms" from the Ministry of Education, Culture, Sports, Science, and Technology.

The construction of the high intensity laser cooled radioactive atom factory will be completed at the 51 course within 3 years, and the new phenomena beyond the standard model of the elementary particle physics will be investigated with this new facility.

We are most grateful to Tohoku University and to the Ministry of Education, Sports, Culture, Science and Technology for continuous support.

January 2010

Keizo ISHII
Director
Cyclotron and Radioisotope Center, Tohoku University

EDITORS:

Keizo	*ISHII*
Ren	*IWATA*
Hiromichi	*YAMAZAKI*
Yasuhiro	*SAKEMI*
Etusyu	*Kuraoka*
Tsutomu	*SHINOZUKA*
Manabu	*TASHIRO*

WORD PROCESSED BY

Yu-ko YAMASHITA

CONTENTS

I. NUCLEAR PHYSICS

II. NUCLEAR INSTRUMENTATION

III. NUCLEAR ENGINEERING

IV. NUCLEAR MEDICAL ENGINEERING

V. PIXE AND ENVIRONMENTAL ANALYSIS

I. NUCLEAR PHYSICS

I. 1. Thermal-neutron Capture Cross-section by ^{151}Eu Leading to the 9.27-hours Isomer

Orihara H.[1,2], Satoh Y.[1], and Umeda K.[1]

[1]*Center for General Education, Tohoku Institute of Technology*
[2]*Division of Instrumentation CYRIC, Tohoku University*

In the course to accumulate the data estimating activation of concrete in the nuclear power plant due to thermal neutron capture by ^{151}Eu, the capture cross-section for ^{151}Eu Leading to the 9.27-hours isomer is discussed. Europium oxide powder in natural abundance and enriched samples are irradiated by thermal neutrons from the 12-MeV AVF cyclotron together with Sc, Co and Au samples. The latter have been used to determine the neutron flux used, by their known neutron capture rates. The law of "clearance level" was enacted in 2007 as one of the law to regulate radiation safety of nuclear plants. The law excludes wastes from the regulation when their radiation level is smaller than the "clearance level". The radiation level of concrete that composes a big part of the building structure of the nuclear installation is examined by measurements and calculations, and the results are compared with "clearance level". For the effective and safety enforcement of the law, accumulation of the database of thermal-neutron capture-rate is essential as well as development of accurate and steady measurement-systems for low-level radiations.

For evaluation of radiation level of concrete by calculation, important radioactive nuclides are ^{152}Eu and ^{154}Eu, the half-life for which are, respectively, 13.542 and 8.593 y, formed by thermal neutron capture by ^{151}Eu and ^{153}Eu with larger capture cross-sections over several thousand barns[1]. We have reported[2] high-Resolution measurements of gamma-rays from thermal-neutron capture by ^{151}Eu and ^{153}Eu. Europium oxide powder in natural abundance were bombarded by thermal neutrons. We concluded that by peak analysis, for the prominent peaks leading to the 121 keV state, thermal-neutron capture cross-section ratio has been determined to be $\sigma(^{154}\mathrm{Eu})/\sigma(^{152}\mathrm{Eu})$= 55,923/721567=0.075. Further analyses of activated data for other nuclide ^{45}Sc and ^{59}Co could yield more precise neutron flux, by which we were able to deduce the absolute Cross-sections $\sigma(^{154}\mathrm{Eu})$ and

$\sigma(^{152}Eu)$, separately.

In this report, we discuss thermal neutron capture cross-section of ^{151}Eu leading to the 9.27-hr isomer in ^{152}Eu. Decay scheme of the he 9.27-hr isomer is illustrated in Fig. 1. There are seven gamma-ray decays[3,4] in which four decays are prominent, and three decays may be week. Note that the lowest transition between $2^+ \rightarrow 0^+$ states is singlet since transition in ^{154}Gd the $2^+ \rightarrow 0^+$ transition is not observed in the short-lived transition .

Thermal-neutron activation has been carried out by those from an AVF cyclotron used for RI-production for PET works at Cyclotron and Radioisotope Center, Tohoku University. Several samples, as listed in Table 1, have been simultaneously irradiated in order to estimate the neutron flux, since thermal neutron capture rates are much well known for these nuclides than those for $^{151,153}Eu(n,\gamma)$. The neutron flux thus obtained by Au-experiments is estimated to be in the order of 10^4 (n/s.cm^2).

Gamma rays from activated samples have been analyzes with high-resolution HPGe detector in low-background surroundings with the iron shield-box made of RI-free steel sheet, used in battleship "MUTSU" over 60-years ago. Figure 2 shows the simple electric diagram for the gamma ray analyzing system.

A sample of gamma ray spectrum, taken from europium sample at the time of one hour after two-hours bombardment, is illustrated in Fig. 3. The seven transition pointed out in Fig. 1 are observed as the results of peak identification. Figure 4 shows time dependence of decay of the 9.27-hr isomeric state obtained by counting 121.78-, 344.3-, 841.6-, 9643.4-keV gamma rays. The decay curve of seven decays is consistent with the life of ^{152m}Eu as shown in Fig. 4 by fitting.

In the general theory of RI-decay, the number of radioactive nucleus at the time t is:

$$N(t) = N_0 e^{-\lambda t} = N_0 e^{-\frac{0.693}{t_{1/2}}t}, \frac{dN(t)}{dt}[Bq] = -N_0\left(\frac{0.693}{t_{1/2}}\right)e^{-\frac{0.693}{t_{1/2}}t} \quad (1)$$

where $t_{1/2}$ is the half life of the radioisotope. After bombardment of thermal neutron, the initial number of radioisotope is:

$$N_0 = I(number\ of\ terget\ atom) \times n[(number\ of\ neutron)/cm^2] \times S^{AA}[barn\ 10^{-24}\ cm^2] \quad (2)$$

where S^{AA} is capture cross section for nucleus-AA measured by barn (10^{-24} cm^2), and N_0 is obtained with the unit of $n \cdot S^{AA}$. For example, N_0 of $^{151}Eu_2O_3$ is:

$$N_0 = \frac{1.03 \times 0.48}{352} \times 2 \times 6.0 \times 10^{23} \times 10^{-24} n S^{Eu} \quad (3)$$

On the other hand, N_0 is related to the activity: $Act.(Bq)$ as following:

$$\left.\begin{array}{l} {}^{46}Sc \;\; 83.79d \;\; (1/1.0444\times10^{7})N_0 \\ {}^{60}Co \;\; 5.271y \;\; (1/2.3988\times10^{8})N_0 \\ {}^{152}Eu \;\; 13.542y \;\; (1/6.1625\times10^{8})N_0 \\ {}^{152m}Eu \;\; 9.274h \;\; (1/4.8176\times10^{4})N_0 \\ {}^{154}Eu \;\; 8.593y \;\; (1/3.9104\times10^{8})N_0 \\ {}^{198}Au \;\; 2.696d \;\; (1/3.3612\times10^{5})N_0 \end{array}\right\} = Act.(Bq) = \sum[counts/\sec]\times\frac{1}{\varepsilon(E_\gamma)} \qquad (4)$$

where ε denotes energy dependent detector efficiency, and summation should be taken over transitions concerning the amount of N_0. Measurement of gamma-ray counts gives us the corresponding ^{152m}Eu-activity in Bq. Then, by inserting N_0 in eq. (3) into eq. (4), we obtain $n\cdot S^{^{152m}Eu} = 7.187\times10^{10}$, where summation in eq.(4) is taken over 841.6-(13.1counts/sec, ε = 0.0671) and 963.4-keV(10.8 counts/sec, ε = 0.0609) gamma transitions. On the other hand, by counting gamma ray for ^{197}Au target, which have been bombarded in the same experimental condition, we obtain $n \cdot S^{Au} = 1.016\times10^{10}$. Note that the amount of neutron number is common for these two cases. Thus, by using S^{Au} =200 (barn) we obtain $S^{^{152m}Eu}$=1.41$\times10^3$ (barn).

We have observed gamma-ray from the decay of 9.27-hr isomer in ^{152}Eu. Observation of activity by this transition gives prompt information about radiation level by neutron capture by Europium. Together with data for activation of ^{197}Au, we have concluded that the thermal neutron capture cross-section leading to the 9.27-hr isomer is 1.41$\times10^3$ barn. This method to deduce thermal neutron capture cross-section may be applied to obtain capture cross-section e.g. to the 13.542-y ground state in ^{152}Eu.

References

1) JENDLE-3.2, Japan Atomic Energy Research Institute, Nuclear Data Center.
2) Orihara H., Satoh Y., and Umeda K., CYRIC annual Report 2007, P1.
3) Table of Isotopes, Firestone R.B. EIGHTH Edition 1998.
4) Selen L., Friedlander H. N. and Turkel S. H. Phys. Rev. 77 (1947) 888.

Table 1. Irradiated samples in the present experiment.

Element	Nuclide	Half-life	Amount
Sc	^{46}Sc	83.79d	1.0g
Co	^{60}Co	5.271y	1.0g
Au	^{198}Au	2.696d	0.21g
Eu	^{152}Eu	13.542y	1.0g
	^{154}Eu	8.593y	

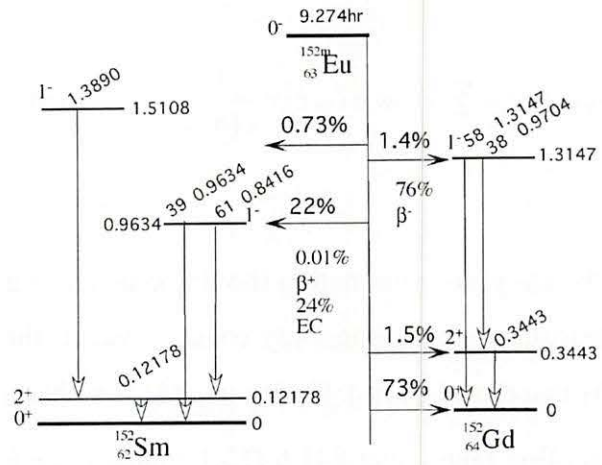

Figure 1. Decay scheme of the 9.27-hr isomer in ^{152}Eu.

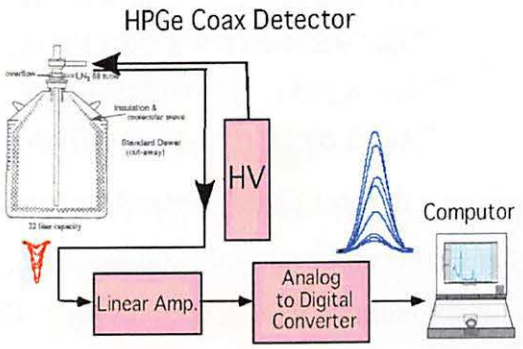

Figure 2. Electric diagram for the gamma ray measurement.

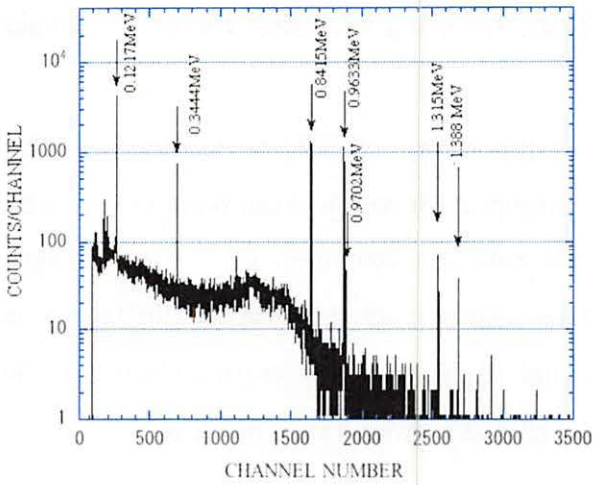

Figure 3. Gamma-ray spectrum for decay of the 9.27-hr isomer in ^{152}Eu. Seven gamma ray peaks indicated in Fig. 1 are seen.

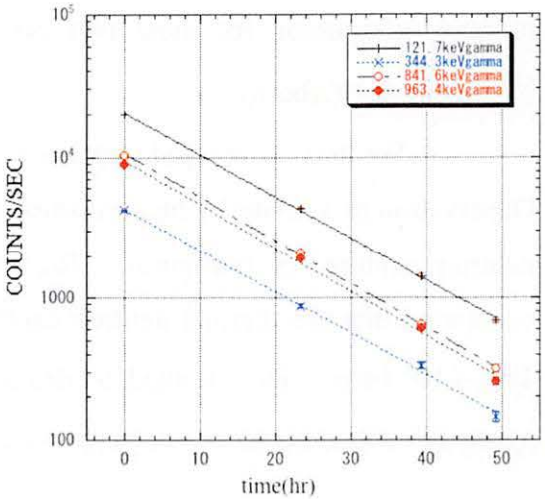

Figure 4. Decay curves of the 9.27-hr isomer measured with the 121.7-, 344.3-, 841.6-, and 963.4-keV gamma decays.

I. 2. Measurement of Decay α Particles from the 15.1 MeV 0^+ State in ^{16}O via the $^{12}C(^{16}O,^{16}O^*[\alpha + X])^{12}C$ Reaction

Itoh M., Takahashi T., Hayamizu T., Oikawa A., Sakemi Y., and Yoshida H.

Cyclotron and Radioisotope Center, Tohoku University

The excited state of 15.1 MeV 0^+ in ^{16}O is considered to be the 4-α condensed state[1]. The concept of the α condensed state was proposed by Tohsaki et al[2]. They explained the 7.65 MeV, 0_2^+ state of ^{12}C as the 3-α condensed state in which all constituent α clusters condensed into the lowest S-orbit, and loosely bound. As for the 4-α condensed state, it is not established. In this study, we measured decay α particles from the 15.1 MeV 0^+ state in ^{16}O via the $^{12}C(^{16}O,^{16}O^*[\alpha+X])^{12}C$ reaction in order to investigate the 4-α condensed state. Since the wave function of 4-α condensed state has a large overlap amplitude of the $\alpha + ^{12}C(0_2^+)$ channel, the branching ratio of this decay channel is considered to be large in comparison with the cascade statistical model.

The experiment was performed at the CYRIC 41 course beam line by using the large scattering chamber. The 160 MeV $^{16}O^{5+}$ beam accelerated in the K=110 MeV AVF cyclotron was transported into the large scattering chamber in the experimental room TR-4 and bombarded the self-supporting carbon target. The experimental setup was almost same as the test experiment reported previously[3] and details were reported in Ref.[4]. Here, we present the brief outline of the experiment and procedures specified to this experiment. The beam current was typically 10 pnA. The target was the natural carbon foil of the 51.5 μg/cm^2 thick and rotated by 45° against the beam axis in order to keep the energy loss of the recoil carbon below 400 keV. The recoil ^{12}C was catch in SSDs placed at 61° (SSD0), 48.5° (SSD1). SSD2 placed at 73.5° was used for the beam position monitor. The kinetic energy of recoil ^{12}C from elastic scattering of $^{16}O+^{12}C$ changes drastically when the recoil angle changes. If the beam position shifts by 1 mm, the recoil energy changes about 600 keV. In this experiment, we used the position sensitive detector (PSD) of the 50 mm×50 mm size and 994 μm thick, which is a double sided silicon strip type and has 16 strips in

each side, for the detector of decay particles. We measured decay particles in three angles of the PSD, 9°, 17.5°, 26° to cover decay-α particles from the $^{16}O^{*}\rightarrow\alpha+^{12}C(g.s.)$ channel. We installed two BGO detectors in order to estimate the contribution of the $^{12}C(^{16}O,^{16}O^{*}[\alpha+X])^{12}C(2^{+})$ reaction. However, it was so small that it was neglected in this analysis. The detectors setup in the large scattering chamber is shown in Fig. 1.

The particle identifications for both SSD and PSD were done by the TOF method. The $^{12}C(^{16}O,^{16}O^{*})$ reaction was reconstructed by kinematical condition of the angle and kinetic energy of the recoil ^{12}C. The missing mass energy of the reaction was calculated as follows,

$$Mx = M(^{16}O) + Ex(^{16}O) - Ec.m.(\alpha) - Ec.m.(^{12}C)$$

where $M(^{16}O)$ is the mass of the ^{16}O nucleus, $Ex(^{16}O)$ is the excitation energy of $^{16}O^{*}$, which was fixed at 15.1 MeV. The energy of the decay particle in the center of mass system, Ec.m.(α or ^{12}C), which was not detected in the PSD, was calculated kinematically by using that of the detected particle. Obtained missing mass spectra were shown in Fig. 2. The peak around Mx = 0 MeV was corresponding to the $\alpha+^{12}C(g.s.)$ channel, on the other hand, that around Mx = 4.5 MeV was corresponding to the $\alpha+^{12}C(2^{+})$ channel. The branching ratio was obtained by multiplying this spectrum by the detection efficiency of the PSD. The detection efficiencies were estimated by a simple simulation program. The branching ratio between the $\alpha + ^{12}C(g.s.)$ and the $\alpha + ^{12}C(2^{+})$ channels was obtained to be about 7:3 from the missing mass spectrum of the decay ^{12}C at 9° of the PSD by assuming that all decay ^{12}C came from the 15.1 MeV 0^{+} state in ^{16}O. It was consistent with the predicted number of Ref. 1). However, that obtained from decay α was inconsistent with the result of the decay ^{12}C due to the complicated loci of the decay α. Figure 3 shows the 2-dimensional histograms on θ_{decay} vs E_{decay}. θ_{decay} is the angle between the scattered $^{16}O^{*}$ and the decay particle. E_{decay} means the kinetic energy of the decay particle. Upper figures (a), (b) of Fig. 3 show experimental results. Lower figures (c), (d) show results of the simple simulation. As shown in figures (b) and (d), loci below 5° were complicated. To understand these loci, more precise analysis is needed.

References

1) Funaki Y., et al., Phys. Rev. Lett. **101** (2008) 082502.; Funaki Y., et al., Phys. Rev. **C80 F**(2001) 064326.
2) Tohsaki A., et al., Phys. Rev. Lett. **87** (2001) 192501.

3) Itoh M. *et al*, CYRIC Annual Report (2006) 1.
4) Itoh M. *et al*, Proceedings of International conference Niigata2010, to be published.

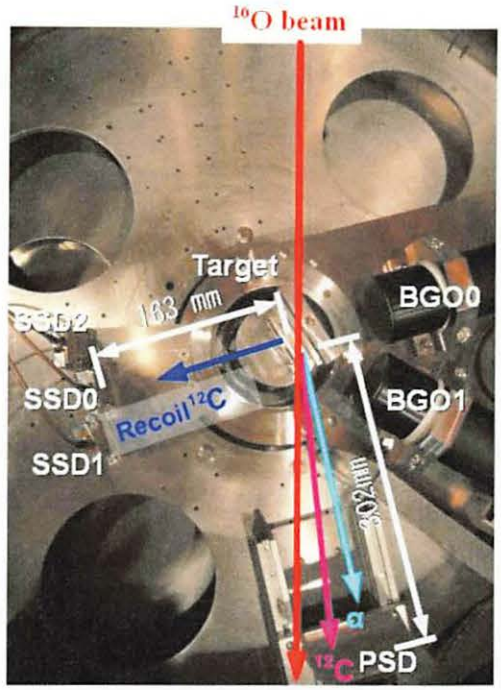

Figure 1. Detectors set-up in the large scattering chamber.

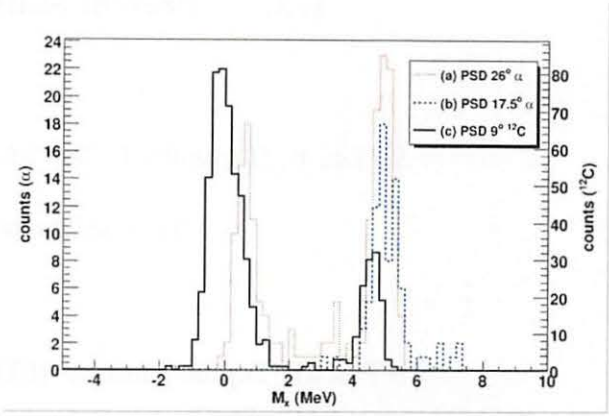

Figure 2. Missing mass spectra obtained from decay-particles. (a): Missing mass spectrum obtained from decay-α measured in the PSD at 26°. (b): That obtained from decay-α measured at 17°. (c): That obtained from decay-^{12}C measured at 9°.

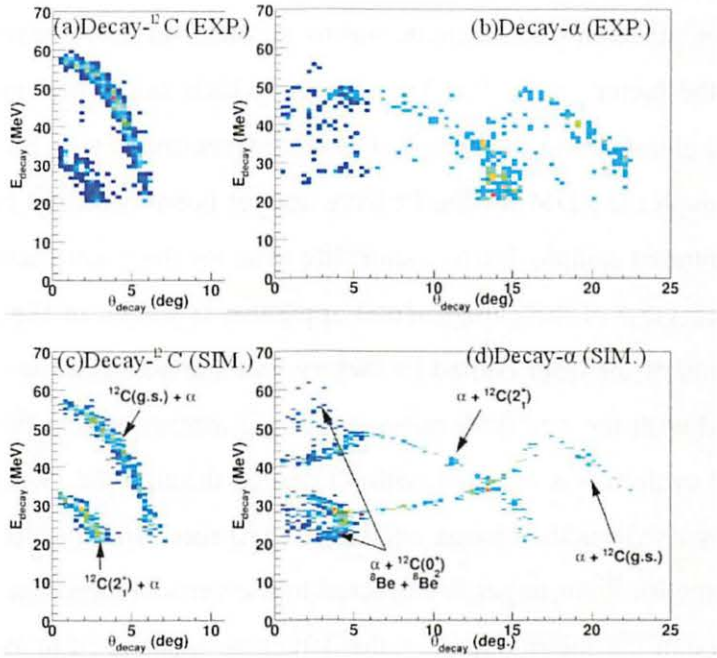

Figure 3. The 2-dimensional histograms on θ_{decay} vs E_{decay}. (a) and (b) are experimental results obtained from the decay ^{12}C (a) and the decay α (b). (c) and (b) are results of the simple simulation program for the decay ^{12}C (c) and decay α (d). In the simulation, the branching ratio of each decay channel was assumed to be same.

I. 3. Present Status of the Search for Fr EDM

Sakemi Y., Hayamizu T., Itoh M., Oikawa A., Takahashi T., and Yoshida H.

Cyclotron and Radioisotope Center, Tohoku University

An Electric Dipole Moment (EDM) of the elementary particle is a good prove to study the fundamental symmetry and observe the phenomena beyond the Standard Model (SM). A finite value of the EDM means the evidence of the time reversal violation, and it suggests the CP violation (matter-antimatter asymmetry) based on the CPT invariance. The SM predicts quite small EDM such as less than 10^{-37} e · cm for the electron. A non-zero EDM is considered as a background free signal of CP violation beyond the SM. However the EDM is considered to be quite small, and many ideas to detect the tiny signal from EDM are considered. We decided to search for the EDM on the radioactive atoms with large atomic number, since in paramagnetic atoms an electron EDM results in an atomic EDM enhanced by the factor ~ $Z^3\alpha^2$ [1]. The element which has largest enhancement factor is a heaviest alkali element and the radioactive atom francium (Fr). So we will search for the Fr EDM, although the EDM for the Fr have not yet been measured because it is difficult to make a concentrated sample due to a short life time for the experiment.

The overview of the experimental apparatus is shown in Fig. 1. The development and construction of the laser cooled Fr factory was started since the summer in 2009. The Fr is produced with the newly developed thermal ionizer, where the primary beam of ^{18}O from the AVF cyclotron is injected with 45 degree through the swinger magnet, which has been originally used for the charge exchange (p,n) reaction, and the produced Fr from the fusion reaction with ^{197}Au target is extracted to the vertical direction. Based on the results of the prototype of the thermal ionizer, this structure is designed to avoid for the ^{197}Au target material to be lost due to the melting and flowing down of the target head. The extracted Fr ion beam is bended 90 degree with the electrostatic prism and transported with about 10 m to the neutralizer and the MOT located at the TOF room. This beam transport system is

effective to reduce the background such as the neutrons and gamma rays produced from the fusion reaction together with the Fr, which damage a certain kind of the detectors. Also the structure of the beam line is designed to achieve the high vacuum 10^{-9} Torr in the end of the beam line with the differential pumping. The Fr is produced at the 51 course of the TR5, and produced Fr is transported from the TR5 to TOF room, and finally the Fr atoms are accumulated and its EDM is measured at TOF room. The goal of this project is to establish the experimental technique to produce and collect the Fr atoms, transport to the trapping chamber with high transmission efficiency, and to get more than10^7 Fr atoms/s which is the highest production rate in the world.

At present, the new thermal ionizer is developed and the offline test is in progress. The Fr is produced with a heavy-ion fusion reaction between an oxygen beam and a gold target ($^{18}O+^{197}Au \rightarrow {}^{210}Fr$ +5n etc.) with the primary beam energy (E_{18O}~100 MeV) just above the coulomb barrier. The target consists of a lump of gold melted and flattened onto the end of a tungsten rod. The target is surrounded by the oven, which is heated by coil heater made by tungsten wire, and the target itself is heated by the radiant heat from the oven up to 1500 degree in the design. The target rod is also cooled by the cooled air from the bottom, and we can control the temperature of the target and oven with/without the primary beam. The embedded Fr from fusion reaction diffuses rapidly to the surface and evaporates. The francium desorbs from the target surface as atoms and ions according to the Langmuir-Saha equation:

$$\frac{n_+}{n_0} = \frac{\omega_+}{\omega_0} \exp\left(\frac{E_{WF} - E_{IP}}{k_T}\right),$$

where n_+/n_0 is the ratio of ions to atoms desorbed, w_+/w_0 is the ratio of the statistical weights and equals 1/2 for alkali atoms, E_{WF} is the work function of the surface, and E_{IP} is the ionization potential of the desorbed atom. Since for gold E_{WF} is 5.1 eV and 4.08 eV for E_{IP}, we have $E_{WF}>E_{IP}$, and consequently the target emits primarily Fr ions. While Fr isotopes can be produces in other fusion reaction, we choose to use gold as a target since it is a noble metal, naturally monoisotopic, and provides an ionizing surface for alkali atoms. Many other radioisotopes are produced in the fusion reaction, but the ionization potential of those RIs are large compared with the work function of the target material gold, so only the Fr is emitted from the surface. The produced Fr ions are extracted from the electrode which is located to the upper direction, and the focusing electrodes are configured after the

extraction electrodes. We can achieve the small emittance Fr ion beam thanks to the curvature and shape of the electrode designed in detail by TOSCA simulation code. The structure of the surface ionizer is shown in Fig. 2. We also make a port to inject the Rb atomic beam to the target surface for the offline calibration and optimization of the operation parameters with Rb beam whose chemical properties are similar to the Fr atom. The offline test by the Rb beam was done to check the operation of the new thermal ionizer and the beam profile of the Rb ion beam was successfully observed as shown in Fig. 3.

We are providing the TR5 and TOF with the developed experimental apparatus, performing the repair of the floor, and constructing the clean room. The construction of the thermal ionizer, the beam transport system, and the neutralizer will be completed in 2010, and the Fr production and beam transport test will be done in the autumn in 2010. The MOT and laser cooling will be also completed in 2010 and tested with Rb. All the equipments will be shaken down until the summer of 2011.

Reference

1) Sandars P.G.H., Phys. Lett. **14** (1965) 194.

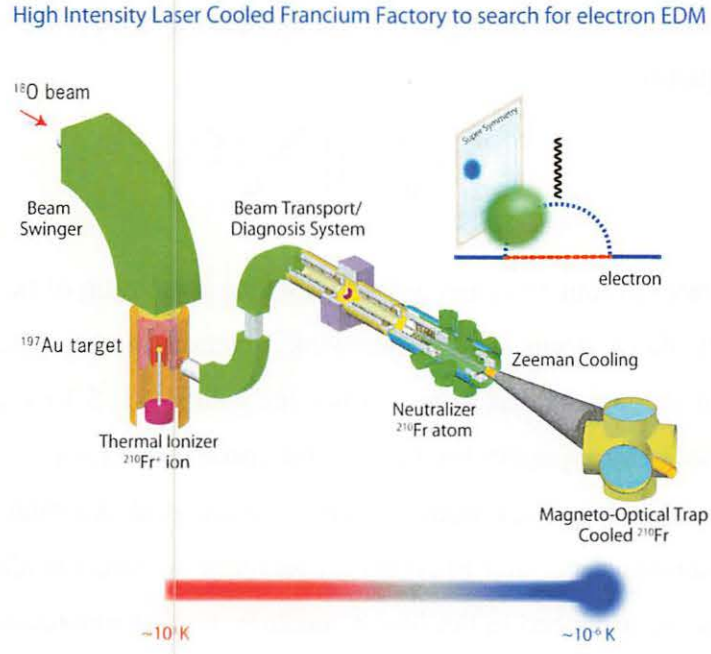

Figure 1. The overview of the laser cooled Fr factory at CYRIC. The Fr is produced by the fusion reaction and extracted from the thermal ionizer. The transported Fr is accumulated in the MOT in the final stage.

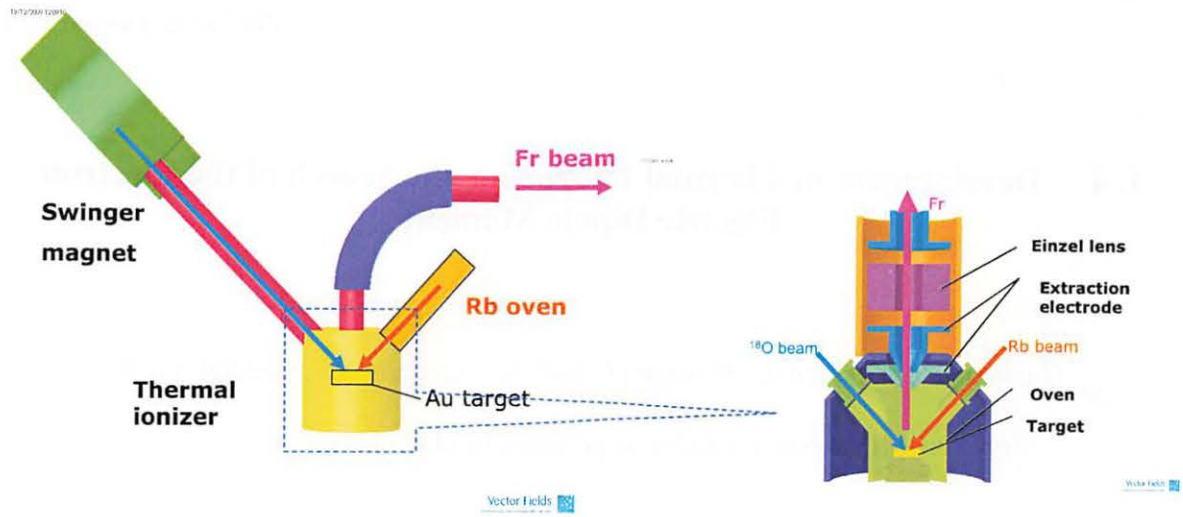

Figure 2. The structure of the newly developed thermal ionizer.

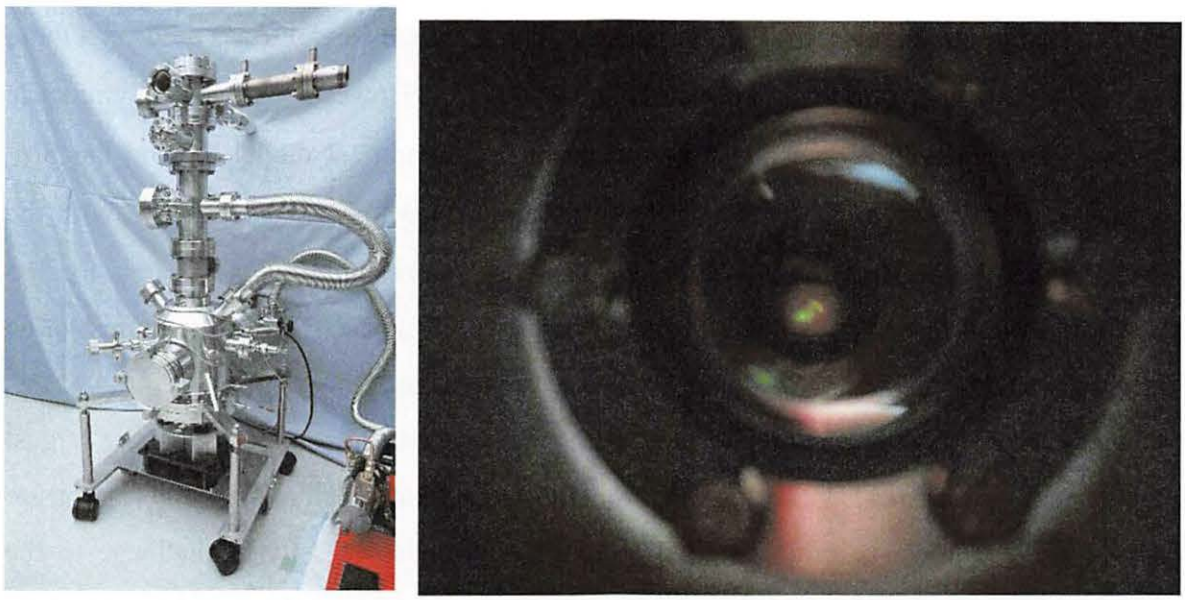

Figure 3. The left picture shows the developed thermal ionizer, and right picture shows the Rb beam profile which was observed from the thermal ionizer for the first time.

I. 4. Development of Thermal Ionizer for the Search of the Electron Electric Dipole Moment

Hayamizu T., Oikawa A., Yoshida H., Itoh M., Takahashi T., and Sakemi Y.

Cyclotron and Radioisotope center, Tohoku University

An existence of non-zero Electric Dipole Moment (EDM) on an elementary particle means the direct observation of the Time-reversal symmetry (T) violation and also suggests the CP violation assuming the CPT invariance. The Standard Model (SM) predicts a quite small EDM value ($d_e < 10^{-37}$ e・cm) nearly equal to zero. However, the Super Symmetric Model (SUSY), which is one of the candidate of the theoretical model beyond the SM, predicts a large value ($d_e = 10^{-27} \sim 10^{-29}$ e・cm) enough to which we can observe with the modern experimental technique. The EDM is very important prove to search for the phenomena beyond the SM. In paramagnetic atoms, an electron EDM results in an atomic EDM enhanced by the factor $K \sim Z^3\alpha^2$ [1]. For accurate measurement of the electron EDM, we will use the Francium (Z=87) which is the heaviest alkali atom and has the largest enhancement factor K=1150 from the accurate theoretical calculation with relativistic coupled cluster model or other detailed atomic theory. So we set our challenge to the measurement accuracy of $d_e \sim 10^{-28}$ e・cm using Fr atom to overcome the world record of the electron EDM at present with $d_e \sim 10^{-27}$ e・cm determined by the Tl atom[2]. Unfortunately, the Fr is radioactive atom with the half-life 3 minutes, but we will get over this problem to develop a high intensity Fr source using the quantum optical techniques.

Now we are constructing the high intensity laser cooled Fr factory to be completed in 2011. The unique points of the factory are to realize the high intensity Fr production using the accelerator and to apply the laser cooling and trapping technique to measure the EDM by the beam transport system consisting from the electrostatic prism, electrostatic lenses and the beam profile monitor with SSD and faraday cup and ZnS viewer. In the end of the beam line, the Fr is neutralized in this experimental apparatus and the neutral Fr atom is produced. The Fr atom is cooled to almost ~μK and trapped in the Magneto-Optical Trap

to produce cooled atoms vapor for the final stage to measure the EDM. In this report, we describe the present status of the development of the prototype of the thermal ionizer, which is important to design the next generation thermal ionizer.

The thermal Ionizer[1] was developed to produces the high intensity and small emittance Fr ion beam source. We used the fusion reaction of $^{18}O + ^{197}Au \rightarrow ^{210}Fr + 5n$ with a primary beam $^{18}O^{5+}$ 100 MeV supplied from the AVF cyclotron. The Fr was produced in the gold target (φ10 mm×t50 μm), and diffused and appeared on the surface of the target by keeping it just before the melting point of the target ~1300K. Finally, the Fr ion was emitted from the target surface with the surface ionization and the ratio of the emitted Fr ions and neutral atoms depended on the work function of the target and the ionization potential of the Fr with the Saha-Langmuier equation. The gold target was surrounded by the high temperature oven to collect all the Fr ions in the limited space[2]. The ion stuck on the oven wall was ionized again because the oven wall kept to the high temperature (~1300K) again. The size and shape of the extraction electrode hole (φ1~mm as an oven hole and φ4mm as a ground electrode) was optimized and designed to achieve the small emittance beam. We performed a tracking simulation of the Fr ions with the realistic electric field, and estimated the beam emittance with 15π mm mrad. We had already gotten the maximum yield as 4×10^4 atoms/sec with the experiment at RCNP, Osaka University in previous year, also found the trouble of the low extraction efficiency up to 0.3% because of an interruption of ionized at oven surface by the low oven temperature and dirty condition. Another problem was difficulty to perform the stable operation for a long time because of the gold target melting down and flowing out. In this time, we improved to concentrate the first points of the problems. We changed the oven heater to more powerful one, took gold gilding (~1 μm) with the ionizer parts, and widen extraction hole out to 1.5 μm.

We performed the experiments at the beam course 34 in the target room 3 to measure the extraction efficiency of the produced Fr. The typical primary beam size was about 10 mm, and the beam energy is 100 MeV as mentioned before. The Fr produced in the thermal ionizer extracted and injected a solid state detector (SSD) in the end of the beam line[3]. We had wanted to obtain the maximum yield, however, we got low intensity Fr ion to order of 10 for low temperature condition (~800K) due to the unstable heating condition, and also we could use the low primary beam (~0.15 eμA). The extraction efficiency of the Francium in experiment was 0.0023%. We interpreted this low efficiency due to the

quality of the oven surface, which main reason was target temperature, and other reason was affection of changing work function from the change of the chemical property and loss of Fr attached to the oven. As a result, we found out some improvement points to modify the heating system to more powerful one like a metallic coil heater, and the material of the oven and target rod should be changed to the chemically stable material to keep the work function and higher temperature. Also, we will get high intensity primary beam since new 10 GHz ECR ion source will be upgraded in 2010. After the experiments, we started to develop new thermal ionizer to feedback these experimental data into the design work. We have aimed to get the yield 10^6 atoms/sec and the efficiency 10%, and be able to operate and extract the Fr for stable long time.

References

1) Sanders P. G. H., Phys. Lett. **14** (1965) 194.
2) Regan et al, Phys. Rev. Lett. **88** (2002) 071805.

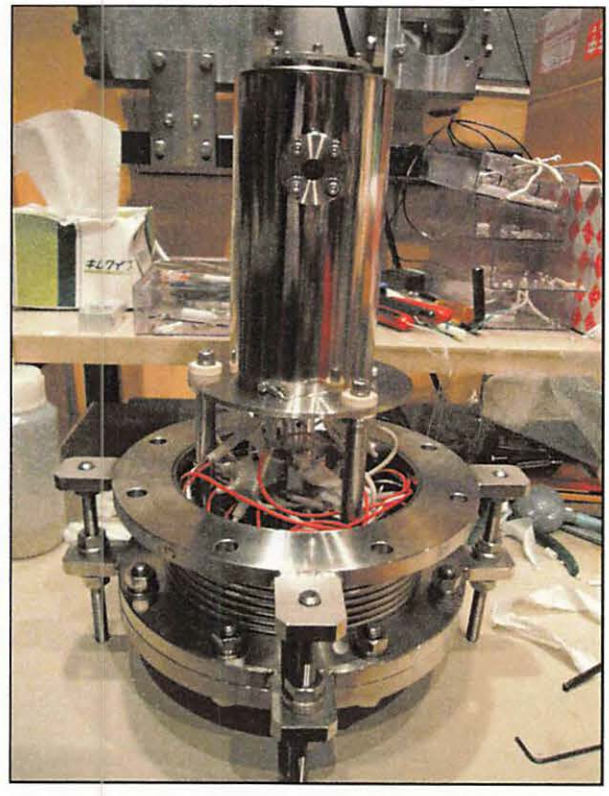

Figure 1. The thermal ionizer.

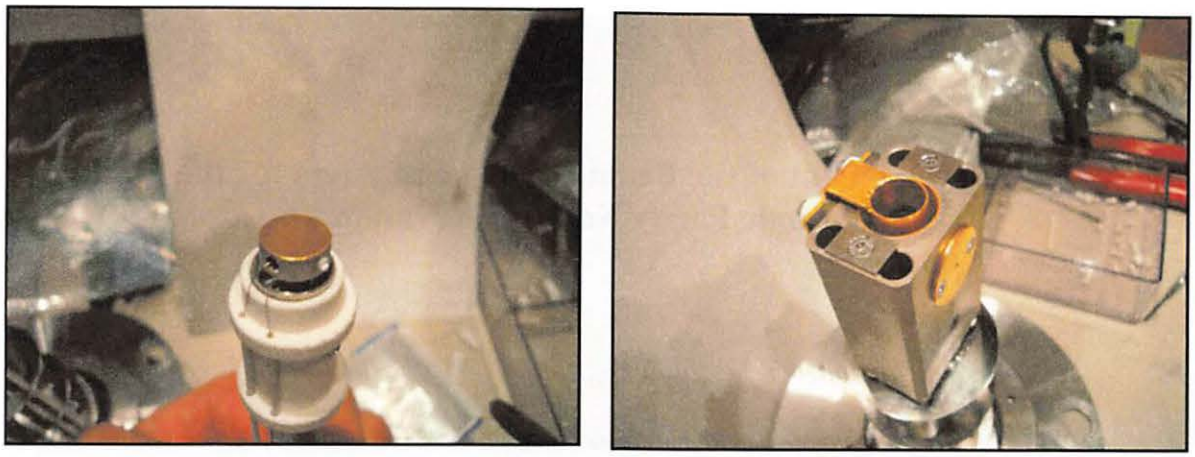

Figure 2. The left figure shows φ10mm gold target for Fr production. The right figure shows the oven with gilding parts which were the upper site hole for injected primary beam, and the side hole of the oven for extracted Fr ion beam.

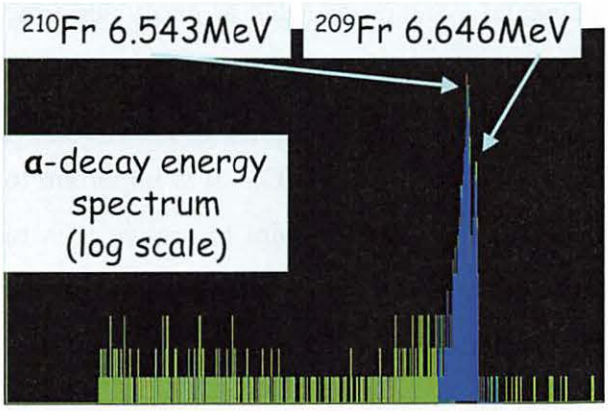

Figure 3. The Fr spectrum detected by SSD.

I. 5. Development of the Beam Transport System for the Study on Atomic Parity Non Conservation

Oikawa A., Hayamizu T., Yoshida H., Itoh M., Takahashi T., and Sakemi Y.

Cyclotron and Radioisotpoe Center, Tohoku University

Francium is one of the best candidates for measurements of atomic Parity Non Conservation (PNC) and in the search for permanent Electric Dipole Moment (EDM). These precise measurements to study the fundamental symmetries, such as parity and time reversal can be achieved by the accurate atomic spectroscopy with the experimental technique of the laser cooling and magneto-optical trap (MOT)[1]. At present, we are constructing the high intensity laser cooled francium factory at CYRIC. It is important to get the high accumulation yield of Fr in the MOT, and the key point to realize it is to transport the Fr beam with high transmission efficiency. The present status of the development of the Fr beam transport system is reported here.

Our goal is to study the atomic PNC with the search for an anapole moment to understand the propagation mechanism of weak interaction between the nucleons in the nucleus, PNC ingredient's amplitude in nuclear force experimentally, and neutral current of neutral weak boson Z^0. The reason of studying the atomic PNC using Fr atom is that the PNC effect is enhanced in proportion to atomic number Z^3 as well as studying electron EDM with Fr atom[2]. The Fr atom needs to be accumulated in the MOT to reduce the error due to the ununiformity of the external field, which is the dominant component of the systematic errors, by confining the atoms in the small region. However at the MOT, we have to realize the high vacuum with ~10^{-9} (Torr) to obtain a long life time of accumulated atoms, and the MOT should be placed at the radiation free area since the detector to measure the number of the Fr atoms will be damaged due to the neutrons and gammas. At the nuclear reaction point, the neutrons and gammas with the energy of a few MeV are produced together with Fr, so we need to transport the Fr far from the reaction point. Therefore we designed the Fr beam transport system with the total length ~10m at the 51

course from the TR5 to TOF. This beam transport system also has the function to realize the high vacuum with the differential pumping. It consists of Electrostatic Quadrupole Triplet (Triplet-Q), Electrostatic Prism (Prism) and Beam Diagnosis System (Diagnosis System).

Triplet-Q (Q1, Q2, Q3) has some unique features. The Triplet-Q is segmented into two regions, which means the inner region where the beam is transported with the high vacuum, and the outer region where the electrodes and cables are installed. These two regions are separated by the quartz pipe with the baking heater. The electrostatic lenses consist of three sets of electrodes with F(focus)D(defocus)F or DFD function. At the both ends of the Triplet-Q, we set the earth plates, and the heater on the surface of the quartz pipe is also used as the earth plates. We realize the definite effective field boundary with earth plates. The structure of the Triplet-Q is shown in Fig. 1. The devel those opment of the Prism is now in progress. It consists of main electrodes, steering electrodes, earth plates and movable silicon detector (SSD). The two holes are prepared in the outer main electrode, which are used for the alignment of the beam line and the measurement of the Fr ions and the temperature of the Thermal Ionizer. Steering electrodes adjust the tracks of the Fr ion beam. The earth plates suppress the turbulence of the electric fields. The model of these features is shown in Fig. 2. The Diagnosis System is designed to enable us to select some kinds of detectors. First, SSD detects Fr alpha decay energy spectrum. Second, Faraday Cup counts Rb ion's beam current. Third, ZnS Viewer shows us the Rb ion's beam profile. The model of these detectors is shown in Fig. 3.

In July 2009, we have performed the experiment to measure transmission efficiency with prototype Triplet-Q (Q0) whose siz e is half of the Q1~3 and without quartz pipe. Experimental setup is shown in Fig. 4. At first, 100 MeV $^{18}O^{5+}$ beam accelerated by AVF cyclotron (Beam Intensity:120~170 nA) was injected into ^{197}Au target in Thermal Ionizer and ^{210}Fr was produced by fusion reaction ($^{18}O + {}^{197}Au \rightarrow {}^{210}Fr + 5n$). Produced Fr atoms were ionized into Fr ion when Fr atom reached to the surface of Au target. Then Fr ions were extracted by extraction electrodes with a small beam emittance (~40 π mm mrad). This beam was transported into the SSD by Q0. So we measured alpha decay spectrum from ^{210}Fr that adhered on the surface of the SSD. These experimental results are shown in Fig. 5 and Fig. 6. As a result of this experiment, Q0 worked as well as we anticipated, and Fr yields on the SSD were ~70 atoms/sec. The analysis of the beam transport efficiency is in progress. Until 2011, high intensity laser cooled francium factory will be built at CYRIC. To trap a lot of Fr atom at MOT, we designed and are developing the Fr beam

transport system with high transmission efficiency (80~100%).

1) Stancari G., et al., Eur. Phys. J. Special Topics **150** (2007) 389.
2) Bouchiat M.A., Bouchiat C., Phys. **60** (1997) 1351.

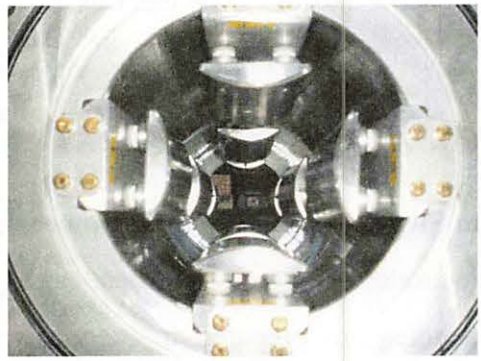

Figure 1. Sectional view of Triplet-Q.

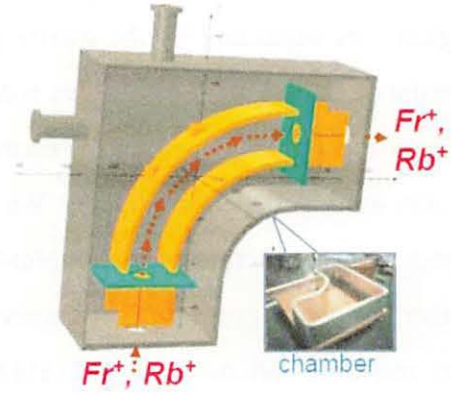

Figure 2. Model of Electrostatic Prism.

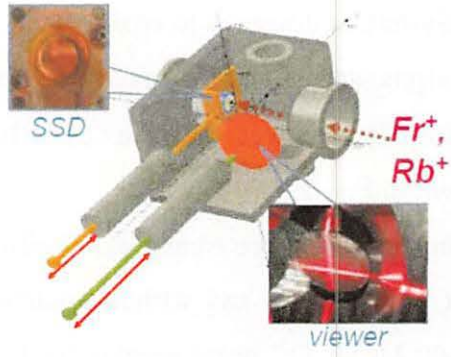

Figure 3. Model of Beam Diagnosis System.

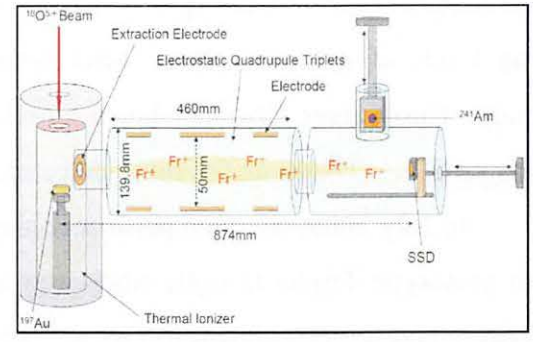

Figure 4. Experimental Setup.

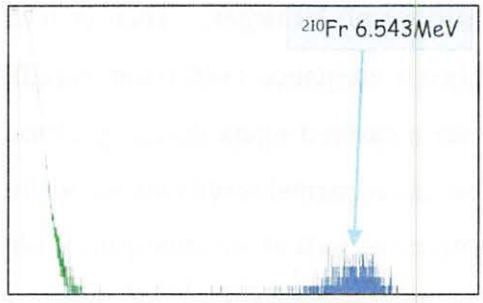

Figure 5. Fr alpha decay energy spectrum.

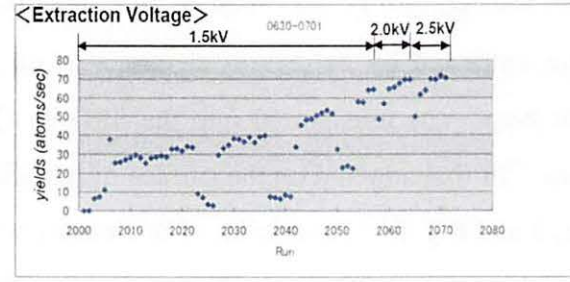

Figure 6. Fr ion's yields on the SSD.

II. NUCLEAR INSTRUMENTATION

II. 1. Improvement in Cross-Polarization System for Radioisotope Polarization

Izumi S.[1], Wakui T.[2], Shimada K.[2], and Shinozuka T.[2]

[1]Department of Physics, Tohoku University
[2]Cyclotron and Radioisotope Center, Tohoku University

We have proposed a new technique to polarize unstable nuclei by a cross polarization method[1]. The aim of this study is to find a possibility to produce a polarization of unstable nuclei better than 10%. The highly polarized unstable nuclei would be useful in the study of nuclear structure as well as material science.

As the first step, we constructed a proton polarizing system[1] which contains a permanent-magnet with variable field strength. The magnet can continuously change the field strength and polarity by rotating cylindrical permanent-magnet rods. The maximum field strength was 326 mT. The field uniformity, however, was a few percent over a volume of 10 mm diameter and was insufficient to observe an NMR signal of polarized protons. We have thus performed a calculation of magnetic field to attain field uniformity better than 10^{-3} over the volume. The magnetic field was calculated by changing a dimension of a shim using the Poisson/Superfish code. Based on the results of calculations, we have modified the magnet with the shim of 128×90×15 mm^3.

By using the modified magnet, we have performed an experiment to polarize protons by means of a cross polarization[2,3]. The magnetic field was 58 mT, and the temperature was 305 K. To confirm an enhancement of proton polarization by the cross polarization, we are using a pulsed NMR technique with a quadrature detection. Figure 1 shows a measured NMR signal of polarized protons. In the figure, we also plot a NMR signal observed before polarizing protons as a background. We have clearly succeeded in polarizing protons.

We have also measured polarizations in a buildup and a relaxation processes to evaluate a polarization rate. The proton polarization, P_p, in the buildup process can be written as

$$P_p = P_e \frac{A}{A+\Gamma}\{1 - \exp[-(A+\Gamma)t]\}, \quad (1)$$

while that in the relaxation process can be written as

$$P_p = P_p(0)\exp(-\Gamma' t), \quad (2)$$

where P_e is an electron population difference in the photo-excited triplet state[4,5], A is the polarization rate of protons, G is a relaxation rate of protons, and G' is a measured relaxation rate of protons. Figure 2 shows a result of the proton polarization as a function of time in the buildup process. By fitting the data with Eq. (1), the buildup time, $1/(A+G)$, was derived as 3.6(9) min. Figure 3 shows a decrease in proton polarization as a function of time. The measurement was performed after stopping the polarization buildup process. From the measurement, the relaxation rate, $1/G$', was obtained as 4.0(4) min by fitting the data using Eq. (2). The relaxation rate in the buildup process is now assumed to be almost same as the measured relaxation rate, i.e., $G = G$'. We then obtain A as 0.03(7).

The evaluated value of polarization rate is very small to attain proton polarization of better than 10%. This small value is mainly caused by a reflection of laser light at a surface of the crystal. To avoid the reflection, we will irradiate the laser light onto a cleavage plane of the crystal. We are also planning to optimize the power and duty rate of the laser to increase the polarization rate.

References

1) Tateoka M., Wakui T., Hoshino S., Ishida T., Shimada K., Miyashita Y., Sato N., Nagano T., Ouchi H., Shinozuka T., CYRIC Annual Report 2007 (2008) 9.
2) Henstra A., Lin T. S., Schmidt J., Wenckebech W. Th., Chem. Phys. Lett. **165** (1990) 6.
3) Henstra A., Dirksen P., Wenckebech W. Th., Phys. Lett. A **134** (1988) 134.
4) Kim S. S., Weissman S.I., Rev. Chem. Intermed. **3** (1979) 107.
5) Sloop D.J., Yu H.L., Lin T.S., Weissman S. I., J.Chem.Phys. **75** (1981) 3746.

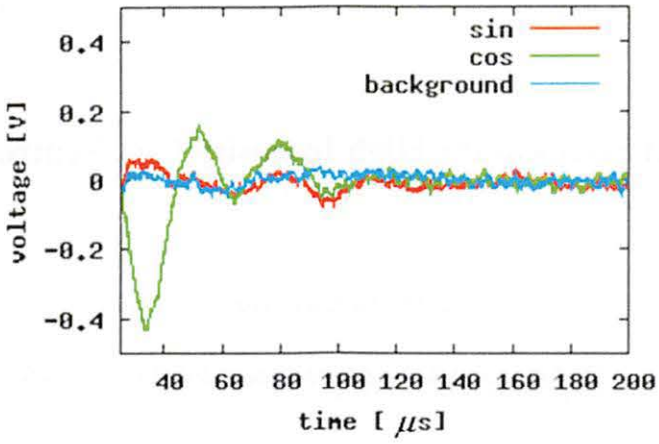

Figure 1. NMR signals of polarized protons in a p-terphenyl crystal. The red line is an NMR signal on the x axis of the rotating frame and the green one is that on the y axis of the rotating frame. The blue line is an NMR signal observed before polarizing protons

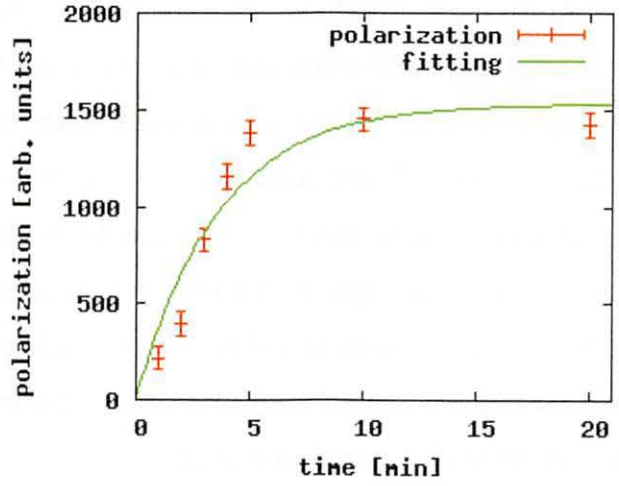

Figure 2. Proton polarization as a function of time in the buildup process. The red points are amplitude of NMR signals. The green line is the fitting line using Eq. (1).

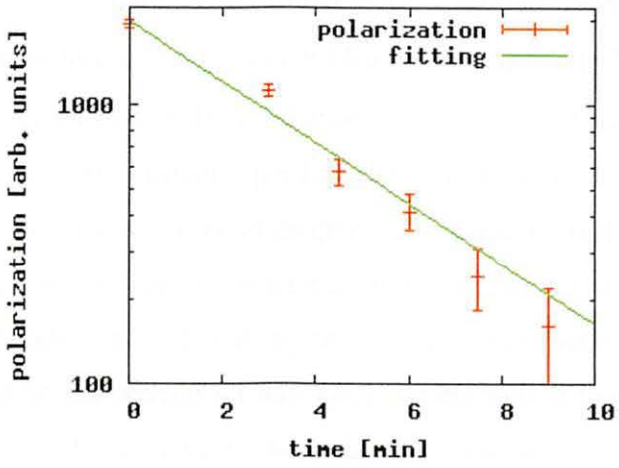

Figure 3. Decrease in proton polarization as a function of time. The red points are amplitude of NMR signals. The green line is the fitting line using Eq. (2).

II. 2. Present Status of the High Intensity Fast Neutron Beam Facility

Yoshida H., Itoh M., and Sakemi Y.

Cyclotron and Radioisotope Center, Tohoku University

The improvements of the beam line to test the radiation damage of the integrated circuits of the CPU, FPGA (Field Programmable Gate Array), and different kinds of memories such as the S-RAM and D-RAM etc, were continued. The two beam lines are ready for the radiation damage test of the semiconductors; one is the beam line (32 course) to supply the high intensity neutron beam, and another is the beam line (33 course located at the TR3) to supply the ion beam. These beam lines were used by many semiconductor developing companies, typically once or twice a month, so we need to improve the beam quality and intensity, the experimental support structures for the users to be able to install the target materials such as the semiconductors, CPU boards, and servers easily to realize the smooth experimental preparation and efficient irradiation experiments. In this report, we will describe the present status of the neutron beam line.

The quasi-monoenergetic neutron beam is produced with the charge exchange reaction such as (p,n) reaction using the thick ^{7}Li target. We have already obtained the high intensity neutron beam with the energy over than 11 MeV up to 66 MeV. The maximum neutron flux with 1×10^{6} n/(cm^{2} · s · μA) was achieved at the primary proton energy of 70 MeV. The obtained typical neutron spectrum is shown in Fig. 1. The Li target with the thickness of 8 mm is used in the standard experiment. We can use the thicker target to increase the beam flux, although the neutron beam energy resolution becomes worse. In this year, we tried to get the quasi-monoenergetic neutron beam with lowest energy such as 11 MeV. The obtained neutron beam energy distribution is shown in Fig. 2. We can see the two peaks, where higher energy peak can be interpreted as the real neutron from the ^{7}Li(p,n)^{7}Be reaction, but another peak can not be understood still. We need to understand this beam energy distribution to get the low energy quasi-monoenergetic neutron beam from 930 AVF cyclotron, or another option is to use the FNL.

This beam line is originally designed to supply the high intensity neutron beam, but this course is also utilized to supply the high intensity proton beam to study the radiation damage of the silicon detector, since this beam course was configured with a straight line from the exit of the AVF cyclotron, and the ion optics for the primary beam transport is simple and it is expected that there is almost no beam loss along the beam line. However we need to be careful for the radiation in the experimental room when we extract the primary proton beam from the vacuum chamber to the external area. Then, we also prepared the new movable beam dump system consisting of the concrete blocks and irons to stop and collect the extracted proton beam efficiently by setting the dump near the beam extraction window. By this new beam dump system, we can minimize for the air to be exposed to the radiation in the nuclear reaction area. Also we set the ozone monitor to protect the human health when the people prepare the experiment during and after the proton irradiation experiment.

The data acquisition system (DAQ) was also upgraded. The measurement of the neutron flux is important for the accurate determination of the memory soft error. The error rate becomes decreased gradually, as the production process and package structure of the integrated circuits and the semiconductor material itself are modified to protect the radiation damage. This means that the low dead time DAQ system is required, since it is necessary to know the accurate error rate with limited beam time. So we have upgraded the DAQ system as shown in Fig. 3 to measure the high neutron flux with the neutron counter consisting of the liquid scintillaters, NE213. The new system is based on the standard CAMAC readout system, and the DAQ software is prepared by modifying the "nagiDAQ" system developed by K. Shouji at Kyoto Univ. To check the neutron flux, we compared it with new DAQ system and also the existing system which have been used so far. It became clear that there is no difference on the measured flux between new and existing DAQ system, so we will move to the new system gradually. Also the slow control system is upgraded to realize the user friendly interface to control the vacuum pumps, beam line slits, and other devices with LabVIEW.

The new DAQ and control system are used with the stable operation during the long irradiation experiment at present. In the next step, we need to get the smaller sized neutron beam to confine the irradiation area more precisely, and the further user friendly interface to start/stop the beam and control the devices need to be prepared.

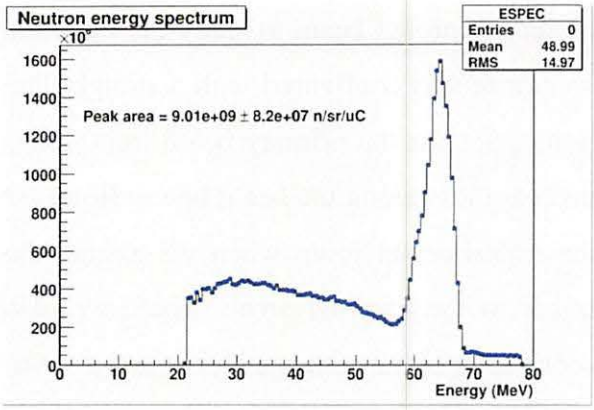

Figure 1. The typical neutron energy spectrum with the proton beam energy at 70 MeV. The obtained energy resolution with FWHM is about 6 MeV measured by Time of Flight (TOF) method.

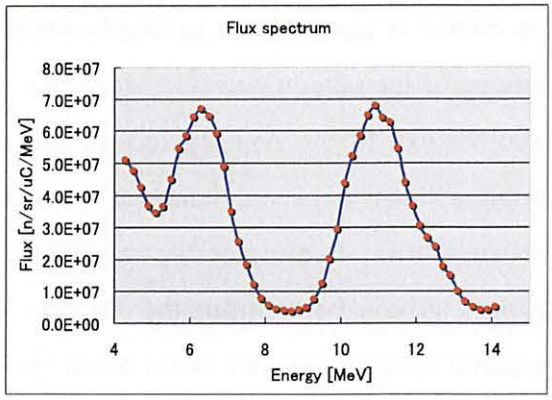

Figure 2. The energy distribution of the neutron beam with 11 MeV.

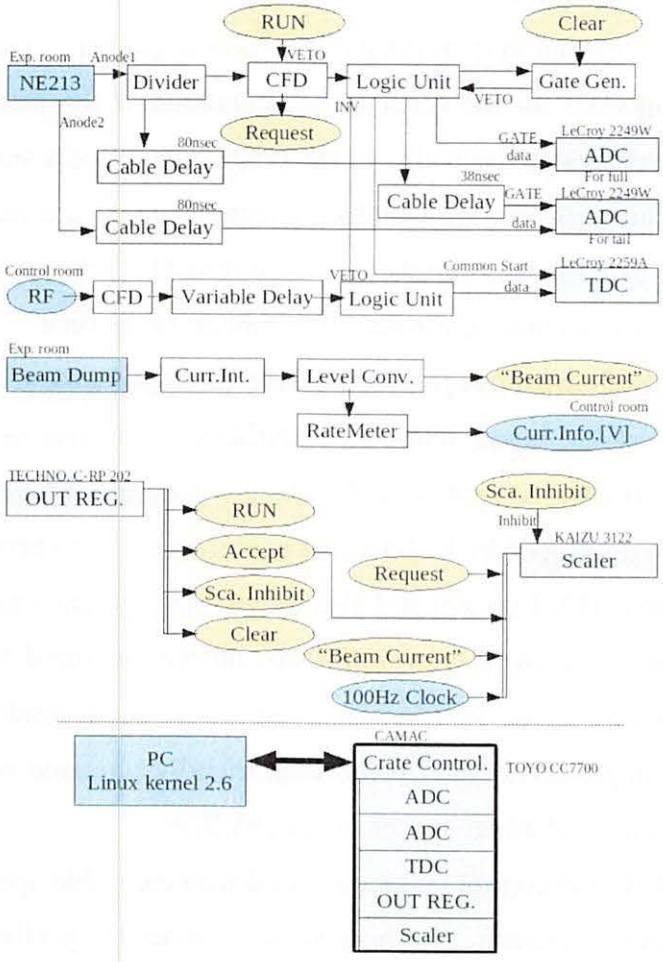

Figure 3. The configuration of the new DAQ system.

II. 3. Proton Irradiation Effects for GaN Schottky Diode

Narita S.[1], Ichinose D.[1], Nishibori Y.[1], Hitora T.[2], Yamaguchi E.[2,3], Sakemi Y.[4], Itoh M.[4], and Yoshida H.[4]

[1]*Department of Electrical Engineering and Computer Science, Iwate University*
[2]*ALGAN K.K.*
[3]*Doshisha University*
[4]*Cycrotron and Radioisotope Center, Tohoku University*

III-N semiconductors have attracted much interest with their excellent electrical and optical properties. Among them, gallium nitride (GaN) has been applied optoelectronic and high power devices with the characteristics of thermal, mechanical and chemical stability[1,2]. In addition, the GaN based devices are expected to have high radiation hardness due to its lower generation rate of charge carriers and higher atomic displacement energy. Thus, the GaN based devices are considered to be really useful in harsh radiation environments. The radiation hardness of the III-N materials has been investigated experimentally from the various points of view[3-7]. We have examined the resistance for the radiation damage with the GaN Schottky diode, irradiating high energy electron and proton beams. We found that no serious degradation in the diode characteristics was observed even after irradiating 10^{14}~10^{15} protons/cm^2 [8-10]. In this study, we have irradiated the GaN Schottky diodes with proton beam to verify the radiation tolerance suggested in our previous experiments. Then, we tried to understand the proton irradiation effects more precisely by mean of the measurement of some electrical properties. Moreover, we examined the relaxation process of the characteristics over a long time period after the irradiation.

The epitaxial GaN layer was grown on n-type SiC substrate through the medium of buffer layer. The cross-sectional and top views of GaN Schottky barrier diode used in this study are shown in Fig. 1. The thickness of the undoped GaN (u-GaN) layer was 1800 nm. The diode chip was mounted on the thin (t=0.6 or 1.2 mm) FR-4 universal board as shown in Fig. 2. We prepared several samples and each sample was irradiated with protons with different fluence. After the irradiation, the samples were kept in the room temperature and

the characteristics were measured with certain time intervals.

The energy of the proton beam was 70 MeV in this experiment. The beam current was set to be ~100 nA. In prior to the irradiation to the sample, an aluminum foil was exposed to the beam, then, the radioactivity of meshed area on the foil was measured by a imaging plate to obtain the beam profile. Assuming that the beam condition was stable over the experiment periods, the profile measurement was employed just once in. The beam intensity profile obtained by this method is shown in Fig. 3. The target diode was placed at the center of the beam. The proton fluences on the diode were determined considering the beam current and the profile. The irradiated proton fluences for each sample are summarized in Table 1.

Figure 4 shows the current-voltage (I-V) characteristics before and after irradiation for the samples 1 and 2. The high energy proton irradiation causes the atomic displacement in the crystal and the intrinsic defects affect the electric property of the devices such as increase of noise, change in electric conductivity, lowering the break down voltage and so on. We did not see obvious increase in the reverse dark currents or change in the breakdown voltage for the fluence up to 10^{14} protons/cm^2. Figure 5 shows the I-V characteristics for the sample 3-5 irradiated with the order of ~10^{15} protons/cm^2. Although the individual sample has a variety in the I-V characteristics even before irradiation, the dark currents increased by a factor of 10^3-10^4. The proton irradiation can induce the trap states in the material which affect the electric conductivity. As the result, the dark currents can increase. In terms of the time variation of the characteristics, the dark currents seem to get smaller with lapse of time. This recovery may be associated with the defect annihilation process at low temperature. Unstable behaviors in the reverse currents were observed for the samples 4 and 5, and they almost disappeared 181 days after irradiation. These phenomena might indicate the forming and vanishing of the localized level at the metal-semiconductor interface.

Figure 6 shows the capacitance-voltage (C-V) characteristics for the samples 3 and 4. The capacitance decrease was observed significantly after irradiation and the change is likely to be larger with higher fluence. Formation of the trapping level was supposed to cause the change of the capacitance. Additionally, the fluctuations of the capacitance as a function of supplied biases were recognized at 50 days after irradiation, and such behavior disappeared at 82 days after irradiation. This fluctuation might be concerned with the unstable behavior in the I-V plots. The effective density of the impurity carrier N_d can be

derived by the C-V characteristic by the following formula;

$$N_d = \frac{-2}{q\varepsilon_s\varepsilon_0 A^2 \left(\frac{d(1/C^2)}{dV} \right)}$$

where, q is electron charge magnitude, ε_s is relative dielectric constant of GaN, ε_0 is dielectric constant in the vacuum and A is the area size of the electrode. The calculated densities are shown in Table 2. Note that we could not determine the density from the data after 50 days of irradiation because the fluctuation of the C-V curve was significantly large. We have found that the density before irradiation was larger than that after irradiation, and it seemed to decrease with increase of the time after irradiation. The density is related to the number of defects induced by the radiation, in principle. Now it is assumed that considerable defects were generated by the proton irradiation and the electrically active carries in the original sample were disappeared. Then, the remaining defects were vanished with annealing effect at room temperature so that the capacitance decreased gradually. This assumption can be clarified by quantitative measurement of the trapping level and the relaxation process, which is an important issue in the future study.

References

1) Ruterana P., Albrecht M., Neugebauer J., "Nitride Semiconductors" (WILEY-VCH, 2003).
2) Adachi S., "Properties of Group-IV, III-V and II-VI semiconductors" (John Wiley and Sons, Ltd, 2005).
3) Grant J., et al., Nuclear Instruments and Methods A **576** (2007) 60.
4) Sonia G., et al., Solid-State Elec. **52** (2008) 1011.
5) Jha S., et al., Microelectronic Eng. **86** (2009) 37.
6) Ohyama H., et al., Materials Science and Engineering B **173** (2010) 57.
7) Chang P.H., et al., J. Alloys and Compounds **504S** (2010) S429.
8) Narita S., et al., Research Report of LNS **40** (2007) 31.
9) Narita S., et al., CYRIC Annual Report (2008) 14.
10) Narita S., et al., CYRIC Annual Report (2009) 56.

Table 1. Proton fluences for each sample.

	Fluence (protons/cm^2)
Sample 1	8.5×10^{12}
Sample 2	5.1×10^{13}
Sample 3	1.2×10^{15}
Sample 4	3.1×10^{15}
Sample 5	6.1×10^{15}

Table 2. Effective density of impurity calculated by $1/C^2$-V plots.

	Fluence (protons/cm^2)
Sample 1	8.5 x 10^{12}
Sample 2	5.1 x 10^{13}
Sample 3	1.2 x 10^{15}
Sample 4	3.1 x 10^{15}
Sample 5	6.1 x 10^{15}

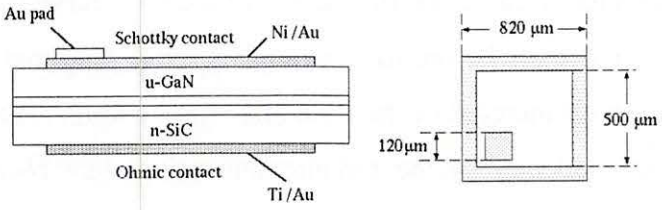

Figure 1. GaN Schottky diode.

Figure 2. The diode chip mounted on FR-4 universal board.

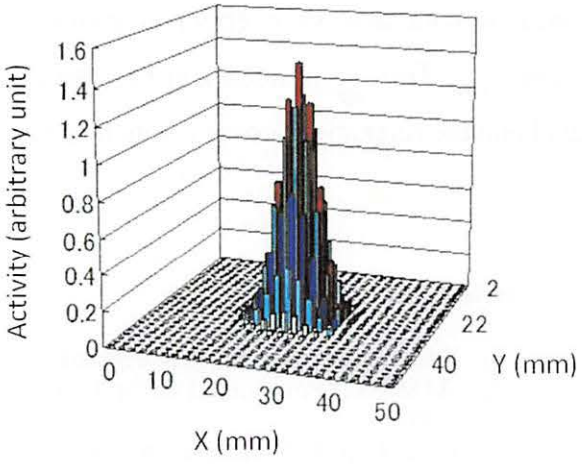

Figure 3. The beam profile measured by a imaging plate exposed with activated aluminum foil.

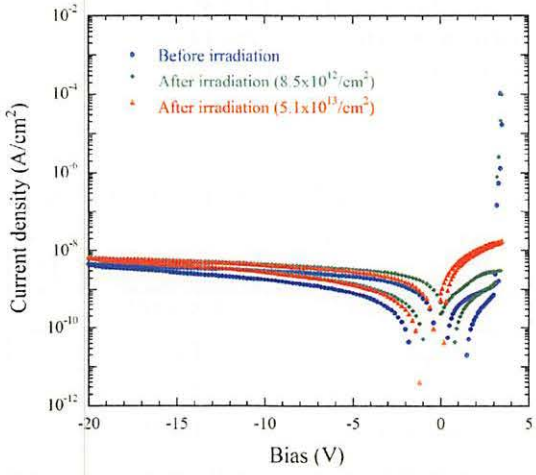

Figure 4. I-V characteristics before and after irradiation with fluences of 8.5×10^{12} (sample 1) and 5.1×10^{13} (sample 2) protons/cm^2.

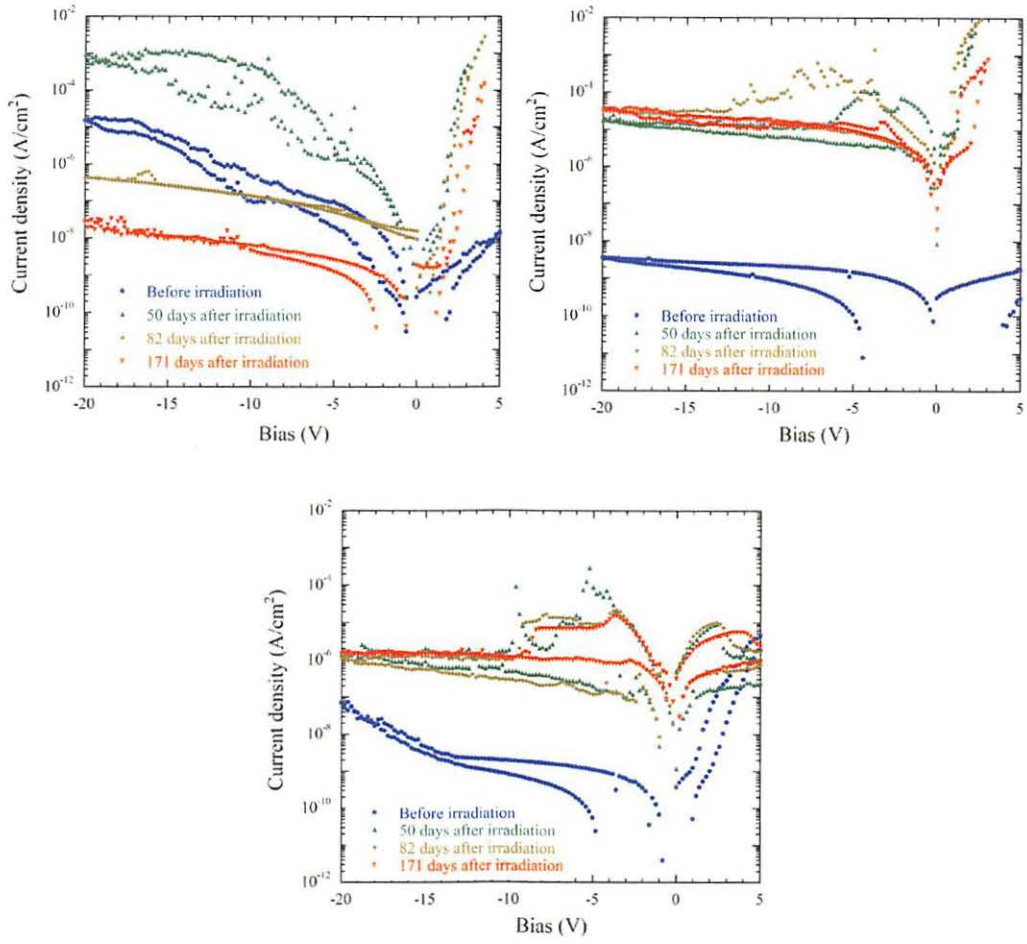

Fiure 5. I-V Characteristics before and after irradiation with fluences of 1.2×10^{15} (top-left), 3.1×10^{15} (top-right) and 6.1×10^{15} (bottom) protons/cm^2.

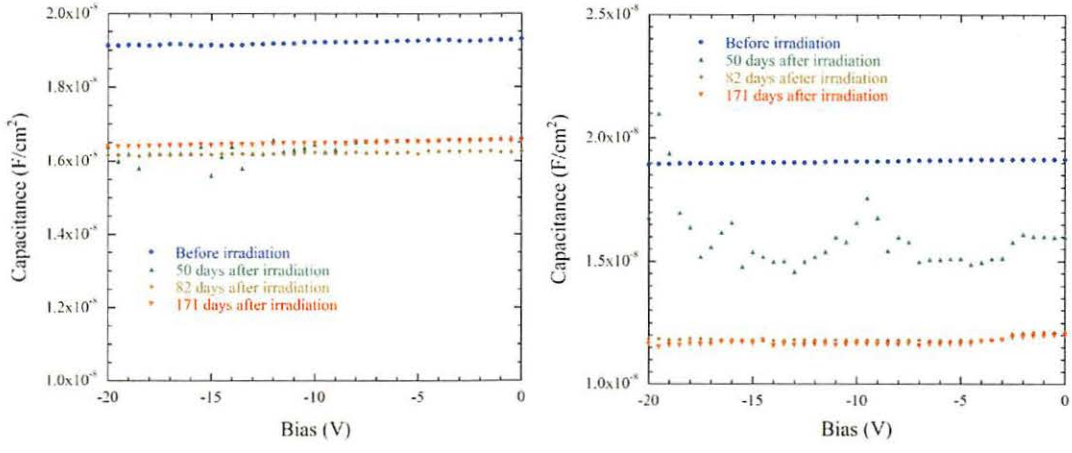

Figure 6. C-V Characteristics of sample 3 (left) and sample 4 (right) before and after irradiation.

III. NUCLEAR ENGINEERING

III. 1. High Temperature Helium Embrittlement of 316FR Steel

Hasegawa A., Nogami S., and Imaseki K.

Department of Quantum Science and Energy Engineering, Tohoku University,

Introduction

Helium is produced in the structural materials of nuclear plants by the nuclear transmutation following the neutron irradiation. Since the solubility of helium in all the metals is extremely low, helium tends to be trapped at defects such as vacancies and dislocations and at the grain boundaries[1]. Additionally, depending on the helium concentration, temperature history and stress loading condition, helium can accumulate at the grain boundary and possibly accelerate the nucleation and growth of voids and form the helium bubble[2]. One possible mechanism of the helium accumulation at grain boundary is considered to be the diffusion of helium atoms from the matrix to the grain boundary at high temperature[1,3]. As a result, a bubble denuded zone occurs near the grain boundary[4,5]. Another one is considered to be dragging of helium atoms by dislocation[6,7]. Because of the accumulation of the helium at grain boundary due to these mechanisms, the reduction of bonding strength of the grain boundary and the grain boundary embrittlement (helium embrittlement) would occur[8]. From the viewpoint of material design and lifetime prediction of components, the helium embrittlement is a common and important issue for the structural materials of nuclear plants.

Authors have reported the helium effects on the tensile property of 316FR austenitic stainless steel, which is one of the candidate structural materials of the fast breeder reactor in Japan[9], by the tensile test at 650 and 750°C after the helium implantation below 100°C up to 30 appm and the post-implantation annealing at 650 and 750°C for 100 hr in previous study[10]. The fracture mode of the helium-implanted specimen tested at 650°C was mainly transgranular and partially intergranular. While, the fracture mode of the helium-implanted specimen tested at 750°C was fully intergranular. The objective of this study is to investigate the effect of helium concentration and annealing time on the tensile

property of 316FR steel at 750°C and related phenomena such as the microstructural change and helium desorption behavior to clarify the helium embrittlement mechanism in the 316FR steel at high temperature.

Experimental Procedure

The chemical composition of the 316FR in this study is shown in Table 1. This material was annealed at 1050°C for 30 min and then water-quenched. The average grain size was about 90 μm, which corresponded to the ASTM grain size number 4[11]. Miniature tensile specimen was fabricated by the electric discharge machining, in which tensile direction was parallel to the rolling direction of the material. The length, width and thickness of its gauge section of the specimen were 5 mm, 1.2 mm and 300±20 μm, respectively.

Helium implantation was carried out using 50 MeV alpha particle (helium nucleus) beam of the cyclotron accelerator of Tohoku University. Energy degrader was used to obtain a uniform helium distribution along the specimen thickness. Figure 1 shows the distribution of helium concentration and displacement damage in the 316FR steel calculated by the SRIM 2006 code, when the helium concentration at the uniformly implanted region was 1 appm. Since the depth of the uniformly implanted region was about 380 μm, which exceeded the specimen thickness, helium ion was implanted to all the region of the specimen. The concentration of implanted helium was 5, 30 and 100 appm. The average ratio of helium concentration to displacement damage was about 5300 appm/dpa. The implantation temperature was below 100°C, which was monitored during the implantation test using a thermo couple directly attached to the specimen surface.

After the helium implantation, some specimens were annealed at 750°C for 10 and 100 hr in vacuum. Microstructural observation for the helium-implanted specimens with and without the post-implantation annealing was conducted using a transmission electron microscope (TEM, JEOL-2010).

Tensile tests were carried out at 750°C in vacuum using an electromotive testing machine with a 5 kN load cell fabricated by INTESCO, Japan. The strain rate was about 3×10^{-4} s^{-1}. The number of the helium atoms released from the helium-implanted tensile specimen during the tensile test was measured using a quadrupole mass spectrometer installed to the tensile testing machine. Calibration of this measurement was performed using a standard helium leak unit attached to the same system. After the tensile test,

fracture surface of the ruptured specimens was observed using a scanning electron microscope (SEM, HITACHI Miniscope TM1000).

Result and Discussion

Tensile properties change

Figure 2 (a) shows the tensile strength of the helium-implanted and annealed specimens. The tensile strength of the unimplanted specimen showed almost no change due to the annealing up to 100 hr. Almost no change of the tensile strength was observed after the helium implantation and the post-implantation annealing at 750°C regardless of the helium concentration and the annealing time.

Figure 2 (b) shows the yield stress (0.2% proof stress) of the helium-implanted and annealed specimens. Though no change of the yield stress due to the helium implantation up to 5 appm was observed without the post-implantation annealing, its increment occurred after the annealing at 750°C for 10 and 100 hr. After the helium implantation up to 30 appm, the increment of the yield stress occurred regardless of the annealing time. The yield stress of the helium-implanted specimen up to 100 appm with the annealing for 100 hr was the same as the one up to 30 appm with the annealing for 100 hr.

Figure 2 (c) shows the total elongation of the helium-implanted and annealed specimens. Significant reduction of the total elongation was observed after the helium implantation. Approximately 53% reduction of the total elongation occurred after the helium implantation up to 5 appm, and the further reduction occurred due to the post-implantation annealing. Moreover, approximately 82% reduction of the total elongation occurred after the helium implantation up to 30 appm. The total elongation of the specimen helium-implanted up to 30 appm was about 10%, which was independent of the annealing time. The total elongation of the helium-implanted specimen up to 100 appm with the annealing for 100 hr was the same as the one up to 30 appm with the annealing for 100 hr.

Helium embrittlement behavior

The fracture surfaces of the helium-implanted and annealed specimens observed using SEM are shown in Fig. 3. The fully transgranular fracture was observed in the unimplanted specimens regardless of the annealing time. On the other hand, the helium-implanted specimens showed fully intergranular fracture regardless of the helium

concentration and the annealing time. Threshold helium concentration for the helium embrittlement in the 316FR steel was considered to be below 5 appm because the intergranular fracture occurred due to the helium implantation up to 5–100 appm without the annealing.

The microstructures in the matrix and at the grain boundary of the helium-implanted and annealed specimens before tensile test are shown in Fig. 4. The helium concentration was 30 appm. No microstructural changes were observed at the grain boundary and the matrix of the as-implanted specimen without the annealing, which showed fully intergranular fracture by the tensile test. It is known that the helium bubble formation and growth is enhanced due to the tensile loading[2]. The grain boundary cracking due to helium bubble could occur during the re-welding process in the neutron-irradiated stainless steel containing transmutant helium by the thermal heating and the transitional tensile stress loading during the welding, when the helium concentration and the heat input by the welding exceeded the particular values[12-16]. Thus, one possible mechanism for the helium embrittlement in the as-implanted 316FR steel without the annealing could be the helium bubble formation at the grain boundary due to the simultaneous heat input and tensile loading during the tensile test at 750°C. As another mechanism, it was considered that the helium embrittlement could occur without the helium bubble formation at the grain boundary. The accumulation of helium atoms and their clusters at the grain boundary, which were undetectable by the TEM, might induce the helium embrittlement of the 316FR steel.

The helium bubble with diameter of a few nanometers was sparsely observed in the matrix of the specimen annealed for 10 and 100 hr and at the grain boundary of the specimen annealed for 100 hr. Therefore, the accumulation of helium atoms and bubbles, and the formation of the helium bubbles would be slightly induced by the post-implantation annealing above 10 hr. The relatively small change of the microstructure due to the post-implantation annealing would be attributed to the obstruction of migration of the helium atoms and their bubbles by small precipitates in the matrix, which might trap them during the implantation and the annealing[17-19].

Figure 5 shows the stress-strain curves and helium release rate during tensile test in the helium-implanted and annealed specimens. The gradual release of the helium started after the yielding and the sharp peak of the helium release was detected in the final fracture phase excluding the helium-implanted specimen up to 5 appm without the

post-implantation annealing. The total number of the released helium per the unit area of the fracture surface is summarized in Fig. 6. Generally, the total number of the released helium was strongly dependent on the implanted helium concentration, rather than the annealing time. The total number of the released helium slightly increased due to the post-implantation annealing at 750°C for 100 hours in the helium-implanted specimen up to 5 appm. While, the effect of the post-implantation annealing at 750°C for 100 hr on it could be small in the helium-implanted specimen up to 30 appm. Therefore, as mentioned above, relatively small enhancement of the accumulation of helium atoms and bubbles, and the formation of the helium bubbles at the grain boundary occurred by the post-implantation annealing below 100 hr.

Conclusion

The helium embrittlement behavior of 316FR austenitic stainless steel at high temperature was investigated by the tensile test at 750°C in vacuum using miniature tensile specimens, which were helium-implanted below 100°C up to 5, 30 and 100 appm using cyclotron accelerator, and were post-implantation annealed at 750°C for 10 and 100 hr in vacuum. The results of this work are summarized as follows:

(1) The fully transgranular fracture was observed in the unimplanted specimens regardless of the annealing time. On the other hand, the helium-implanted specimens showed fully intergranular fracture regardless of the helium concentration and the annealing time.
(2) No microstructural changes in the as-implanted specimen up to 30 appm and formation of the small number of the helium bubbles due to the post-implantation annealing were observed by the TEM. The helium bubble with diameter of a few nanometers was sparsely observed in the matrix of the specimen annealed for 10 and 100 hr and at the grain boundary of the specimen annealed for 100 hr.
(3) The gradual release of the helium during the tensile test started after the yielding and the sharp peak of the helium release was detected in the final fracture phase. The total number of the released helium was strongly dependent on the implanted helium concentration, rather than the annealing time.

Acknowledgements

The authors are grateful to all the staffs of Cyclotron and Radioisotope Center of

Tohoku University for their operation of the Cyclotron accelerator, and to Mr. M. Satou and Mr. F. Moriyama for their help with the experiments using radioactive materials at RI laboratory of Tohoku University. This study was partly supported by Grant-in-Aid for JSPS Fellows 21-4403 from Japan Society for the Promotion of Science.

References

1) Trinkaus H., Radiation Effects **101** (1986) 91.
2) Braski D.N., Schroeder H., Ullmaier H., J. Nucl. Mater. **83** (1979) 265.
3) Trinkaus H., Singh B.N., J. Nucl. Mater. **323** (2003) 229.
4) Foreman A.J.E., Singh B.N., J. Nucl. Mater. **133–134** (1985) 451.
5) Singh B.N., Leffers T., Green W.V., Victoria M., J. Nucl. Mater. **125** (1984) 287.
6) Shinno H., Shiraishi H., Watanabe R., Kamitsubo H., Kohno I., Shikata T., J. Nucl. Mater. **97** (1981) 291.
7) Barnes R.S., J. Nucl. Mater. **11** (1964) 135.
8) Trinkaus H., Ullmaier H., J. Nucl. Mater. **212–215** (1994) 303.
9) Nakazawa T., Kimura H., Kimura K., Kaguchi H., J. Mater. Proc. Tech. **143–144** (2003) 905.
10) Imasaki K., Hasegawa A., Nogami S., Satou M., "Helium effects on the tensile property of 316FR stainless steel at 650 and 750oC," J. Nucl. Mater. to be published.
11) ASTM E112-85, Standard Methods for Determining the Average Grain Size, Annual Book of ASTM (1986) 227.
12) Asano K., Nishimura S., Saito Y., Sakamoto H., Yamada Y., Kato T., Hashimoto T., J. Nucl. Mater. **264** (1999) 1.
13) Morishima Y., Koshiishi M., Kashiwakura K., Hashimoto T., Kawano S., J. Nucl. Mater. **329–333** (2004) 663.
14) Wang C.A., Grossbeck M.L., Aglan H., Chin B.A., J. Nucl. Mater. **239** (1996) 85.
15) Lin H.T., Grossbeck M.L., Chin B.A., Metal. Trans. **A21** (1990) 2585.
16) Kanne W.R., Jr., Welding J. **67** (1988) 33.
17) Miyaji Y., Abe K., Aoto K., Kaneda K., Proc. the 33rd Symposium on Strength of Materials at High Temperatures, Yokohama, Japan, Dec. **7–8** (1995) 134.
18) Miyaji N., Abe Y., Asayama T., Aoto K., Ukai S., J. Soc. Mat. Sci. Japan **46–5** (1997) 500.
19) Miyaji N., Abe Y., Ukai S., Onose S., J. Nucl. Mater. **271–272** (1999) 173.

Table 1. The chemical composition of 316FR austenitic stainless steel.

Fe	C	Si	Mn	P	S	Cu	Ni	Cr	Mo	V	N
Bal.	0.01	0.59	0.84	0.026	0.003	0.26	11.19	16.87	2.23	0.08	0.08

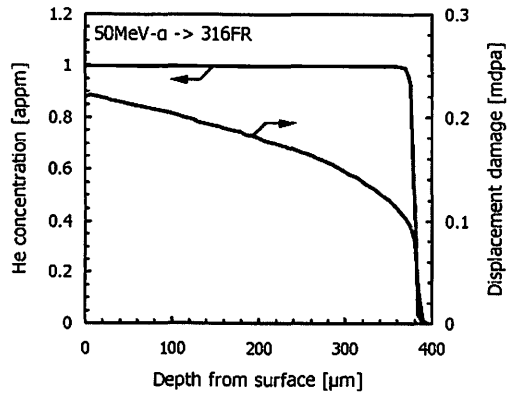

Figure 1. Calculated distribution of helium concentration and displacement damage in the 316FR steel implanted by 50 MeV alpha particle with energy degrader.

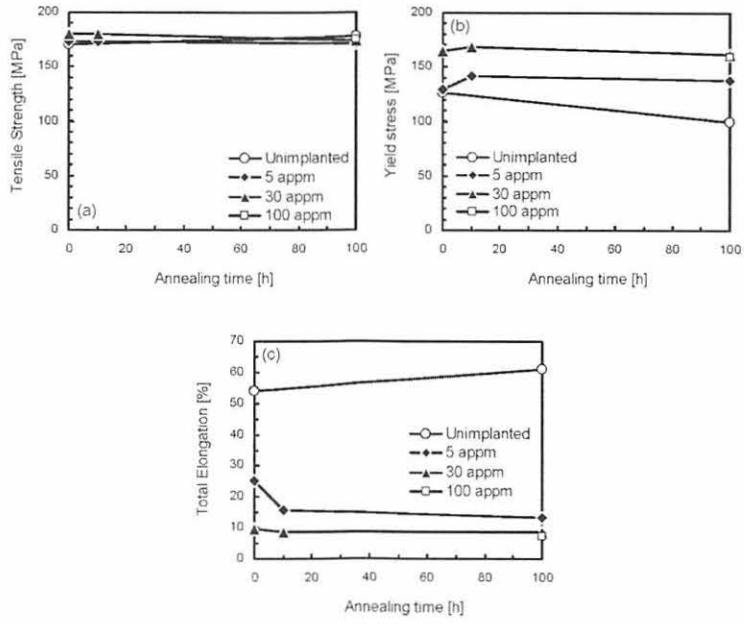

Figure 2. (a) Tensile strength, (b) yield stress and (c) total elongation of helium-implanted and annealed 316FR steel in tensile test at 750°C.

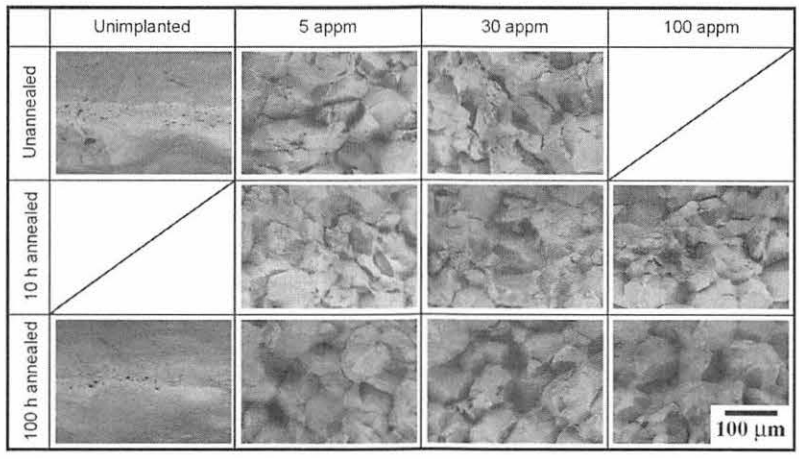

Figure 3. Fracture surfaces of helium-implanted and annealed 316FR steel after tensile test at 750°C.

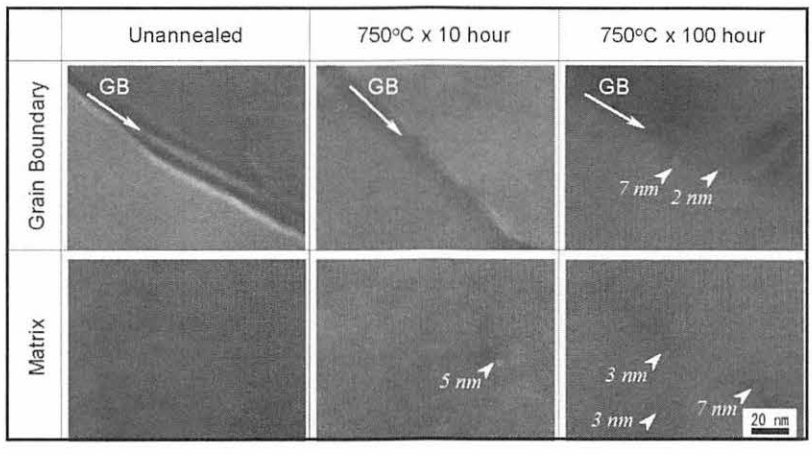

Figure 4. Microstructures of helium-implanted and annealed 316FR steel before tensile test (Helium concentration: 30 appm).

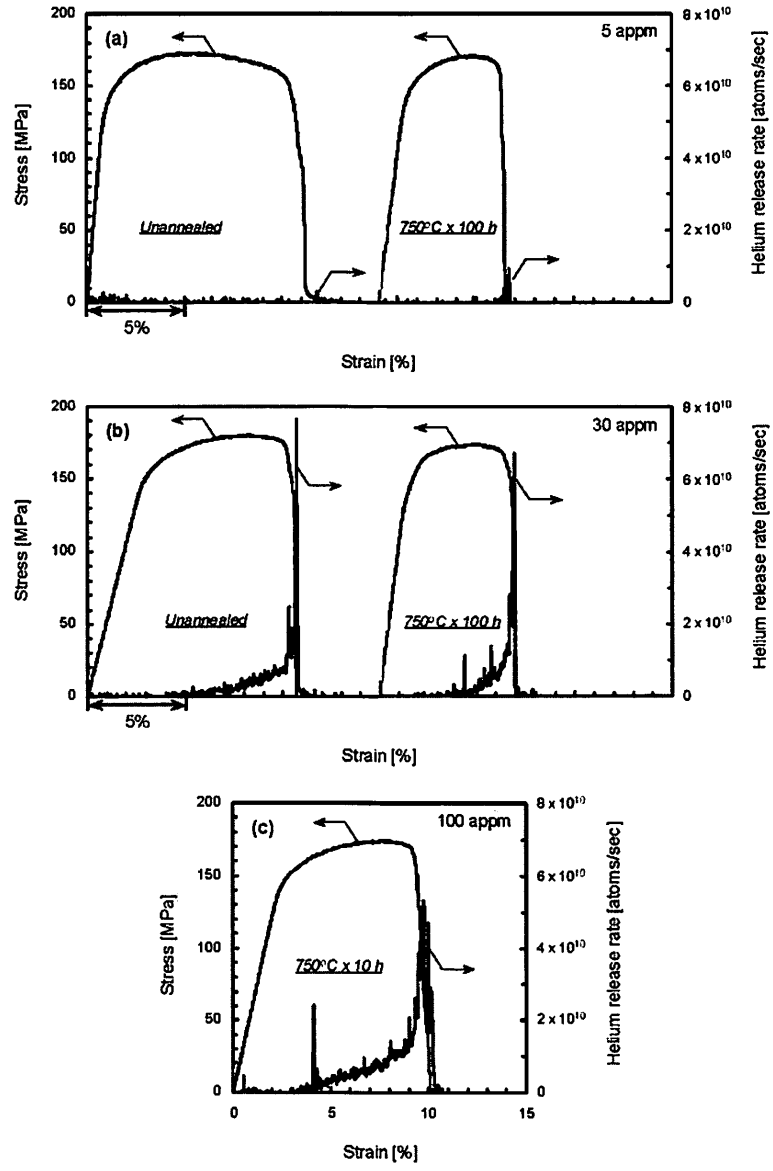

Figure 5. Stress-strain curves of tensile test at 750°C and helium release rate during tensile test in helium-implanted and annealed 316FR steel ((a): 5 appm, (b): 30 appm, (c): 100 appm).

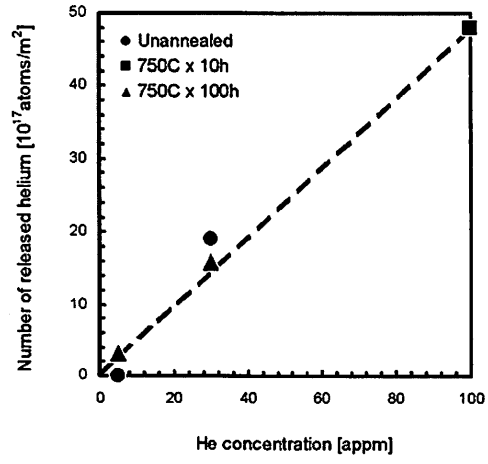

Figure 6. Number of released helium atoms per cross-section of fracture surface after tensile test at 750°C in helium-implanted and annealed 316FR steel.

III. 2. Proton Irradiation to Commercial Back-Thinned TDI-CCD for ASNARO Project

Akiyama M.[1], Miura M.[1], Noguchi K.[2], Sakashita T.[2], Mitsuishi S.[2], and Ishiwa T.[2]

[1]Institute for Unmanned Space Experiment Free Flyer (USEF)
[2]NEC TOSHIBA Space Systems, Ltd.

Introduction

It is the time when quick space utilization is expected worldwide now. Under the background, USEF initiated ASNARO Project to realize small size and high performance earth observation satellite whose cost and manufacturing time will be drastically less than the current conventional satellite development methodologies. The expected performance of the mission is better than 0.5 m of GSD from 504 km altitude which is the same level as the high performance spacecraft in the world. The total mass of the spacecraft is 450 kg. The development of the spacecraft will be completed by the end of JFY2010, and expected to be launched in the year of 2012.

In order to use commercial parts for space , it is necessary to confirm the tolerance of radioation to meet with in orbit to use . We have completed the proton irradiated test for commercial Back-Thinned TDI-CCD which will be used for ASNARO spacecraft at Cyclotron and Radioisotope Center, Tohoku University.

Explanations of ASNARO spacecraft performance and USEF are shown at the end.

General

The major radiation damage for space use CCD and Optocouplers is generally displacement damage by proton (non-ionizing effect), rather than total ionizing dose (ionizing effect). Therefore, we irradiated proton to commercial Back-Thinned TDI-CCD (Time Delay integration-CCD: which is made in Japan, and manufactured by the same process as ASNARO project's CCD) in order to evaluate the shift and degradation of dark output level and signal output level after irradiation and annealing(after irradiation).

Ater the evaluation, we confirmed that same process's CCD is possible to use for ASNARO Project in the proton space environment.

Evaluation Sample and Test Method & Condition

Evaluation sample

The evaluation sample is commercial Back-Thinned TDI-CCD which is made in Japan.

Test Facility

We used 3rd target room of Cyclotron and Radioisotope Center, Tohoku University.

Test Method

The test configuration is shown in Fig. 1. The drive board is shown in Fig. 2, which drives CCD and measures function, electrical & electro-optical characteristics of CCD before & after irradiation or annealing(after irradiation) . We shielded the devices placed around CCD on the drive board from irradiated proton by the shield block, which is lead plate and aluminum block(50 mm thickness). The shield block is shown in Fig. 3. For the functional check of the CCD during proton irradiation, we monitored CCD's output pictures (dark output level). CCD S/N 6 was biased during proton irradiation, the others were not biased.

Test Condition

(1) Irradiated proton condition

The test conditions and sample assignment are shown in Table 1. The applied maximum irradiated proton fluence (3E+10 p/cm^2: Step-4 @70 MeV) is equivalent to two times of ASNARO project's proton space environment (Integral Fluence at 10 MeV). During ASNARO project's application, CCD is used with no bias condition for most of the time, so we selected "not-applied bias" as primary condition .

(2) Annealing (after irradiation) condition

In order to evaluate the drift and degradation of electrical & electro-optical characteristics of CCD by annealing (after irradiation), we performed annealing (room temp, non-bias) during 60 days, and measured electrical & electro-optical characteristics at

suitable phase of intermediate periods.

(3) Measured function, electrical & electro-optical characteristics

We measured dark output level and signal output level (including function, used light source colors were blue, red, green and white) at each irradiated step of Table 1 and suitable intermediate phase of anneal periods, using light sources.

Test Results and Consideration

Test Results

The trend of dark output level and signal output level by irradiation and annealing are shown in Figs. 4~6. Those trends are increased in almost proportion to fluence at irradiation phase. At annealing phase, those trends are not indicated complete saturation in 60 days annealing, and a little increases are observed.

Consideration

The test results were approximately within a supposition , except the dependence on proton energy. In our supposition, shift & degradation of electrical & electro-optical characteristics were larger by 30 MeV-proton than 70 MeV-proton, because NIEL (Non-Ionizing Energy Loss)was larger at 30 MeV-proton than 70 MeV-proton, therefore displacement damage was larger by 30MeV-proton than 70 MeV-proton. However test results showed smaller shift & degradation by 30 MeV-proton than 70 MeV-proton. If it is possible, we will evaluate the dependence on proton energy again by more samples.

Explanations of ASNARO Spacecraft Performance and USEF

ASNARO Spacecraft Performance

ASNARO spacecraft performance and characteristics is shown in Table 2, and on-orbit configuration is shown in Fig 8.

USEF

USEF (Institute for Unmanned Space Experiment Free Flyer) was established on May 16, 1986 by 13 major aerospace companies under the supervision of former MITI (now METI: Ministry of Economy, Trade and Industry) to promote industrialization , commercialization and utilization of the space, and has been developing and operated

spacecraft system with missions those are related to the articles of the USEF.

Acknowledgments

ASNARO Project has been implemented by USEF and NEC under the entrustment of the NEDO (New Energy and Industrial Technology Development Organization), and under the direction of the METI (Ministry of Economy, Trade and Industry). The project is supervised by the engineering committee consisted of expert members from various organizations such as ISAS, universities and government institutions. The appreciation for the fruitful support from all members mentioned above are expressed here as the acknowledgement.

Table 1. Proton Irradiated Condition.

S/No. (CCD)	Bias (During Irradiation)	Proton Energy	Accumulated Fluence (p/cm2)	
S/No.1	Not Applied	70MeV	Step-1	1E+9
			Step-2	3E+9
			Step-3	1E+10
			Step-4	3E+10
S/No.2	Not Applied	70MeV	Step-1	1E+9
			Step-2	3E+9
			Step-3	1E+10
			Step-4	3E+10
S/No.6	Applied	70MeV	Step-1	1E+9
			Step-2	3E+9
			Step-3	1E+10
			Step-4	3E+10
S/No.5	Not Applied	30MeV	Step-1	Not Performed
			Step-2	
			Step-3	1E+10
			Step-4	3E+10

Flux rage: 1E+7~ 5E+7 p/cm2・sec

Table 2. ASNARO spacecraft performance and characteristics.

Mission - Optical Sensor - Data Transmission	 Pan/Multi GSD < 0.5m/2m (Pan/Multi. from504km) Swath: 10km X Band 16QAM, App. 800Mbps
Launch Orbit	JFY2012 (Expected) ISAS/JAXA New Solid (Assumed) (Compatible with H-IIA, Dnepr, etc.) Sun Synchronous Polar Orbit(504km) Inclination:97.4 deg LST. of Descending Node: AM 11:00
Ground Tracking Network	S Band: TBD X Band Data: new station
Design Life Expected Operation	3 Years 3 Years
Spacecraft Mass Size	Bus 250kg Mission 150 kg Propellant 50kg <Total> App. 450 kg App. 2.5m X 3.5m X 3.2m (On orbit)
Electrical Power	SAP Power: App. 1300 W (EOL) (For Mission: 400 W)

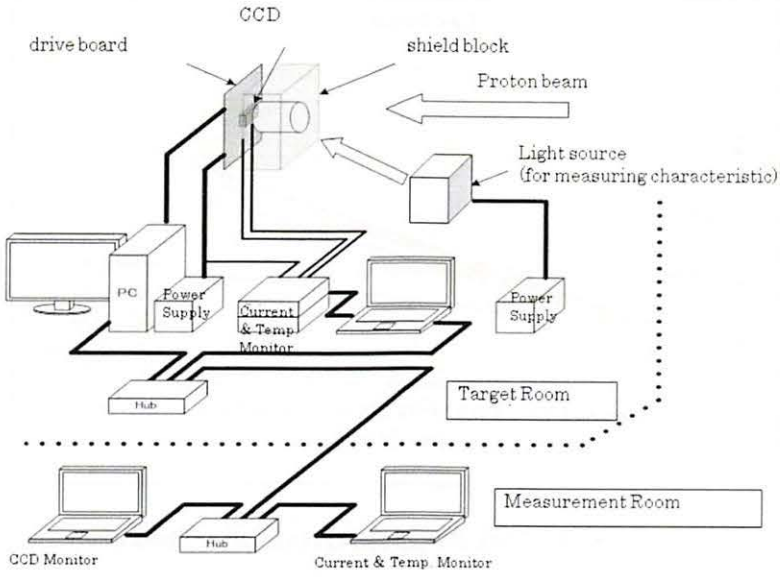

Figure 1. Test configuration.

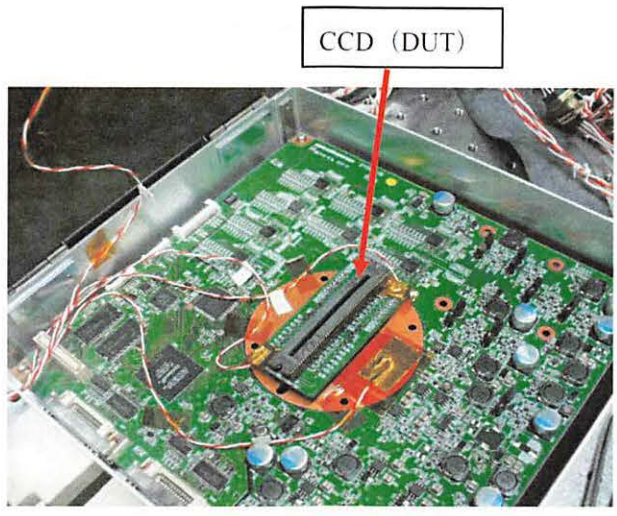

Figure 2. Drive Board

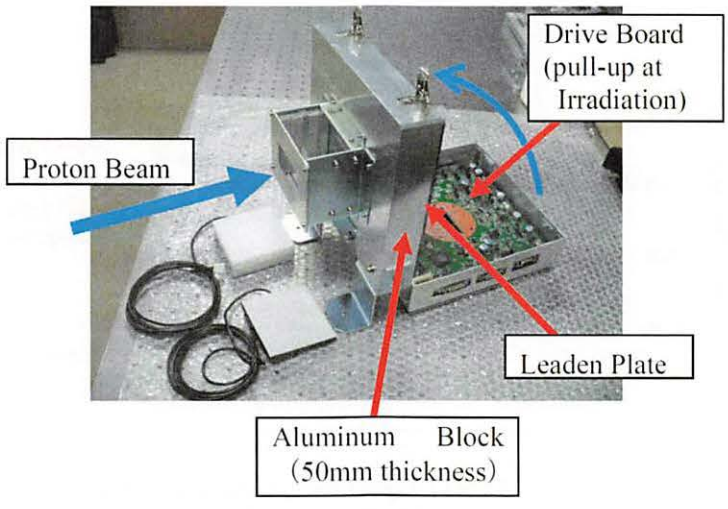

Figure 3. Shield Block

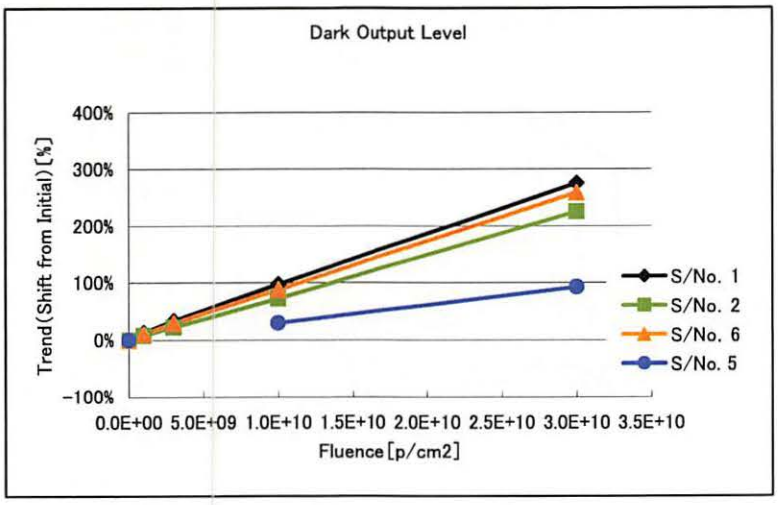

Figure 4. Dark Output Level (Irradiation Phase).

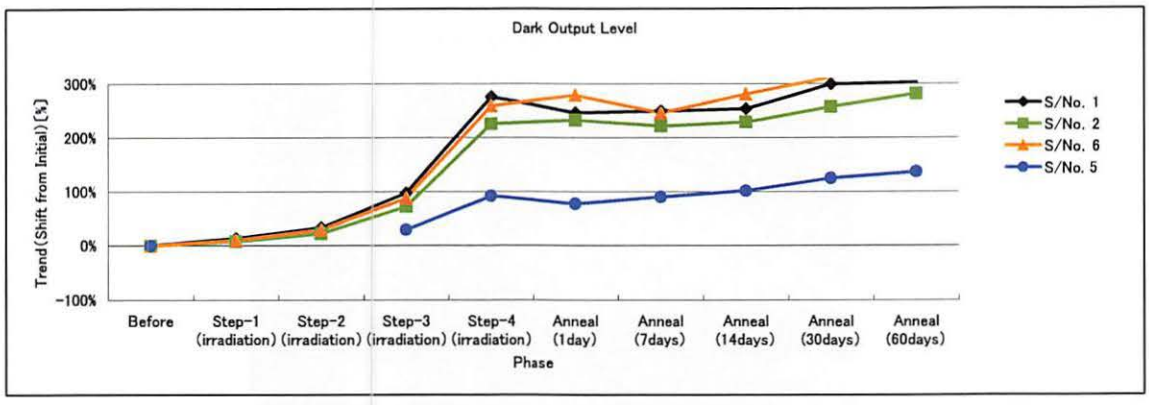

Figure 5. Dark Output Level (Irradiation ~ Annealing Phase).

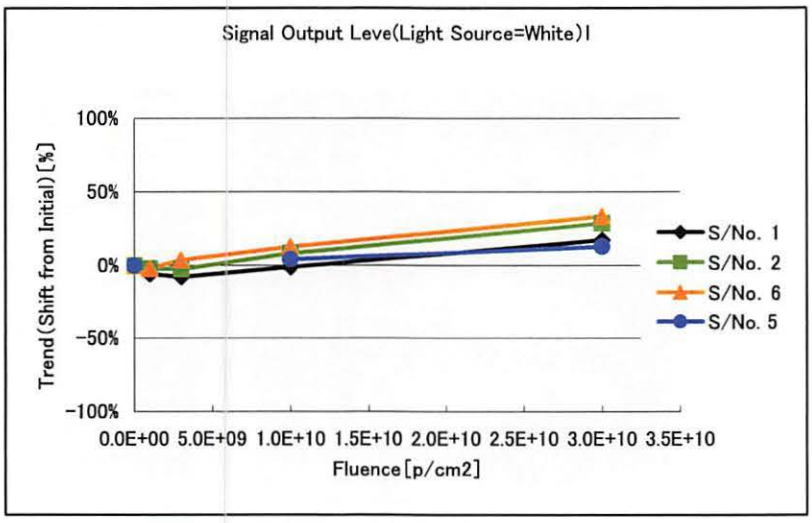

Figure 6. Signal Output Level (Irradiation Phase).

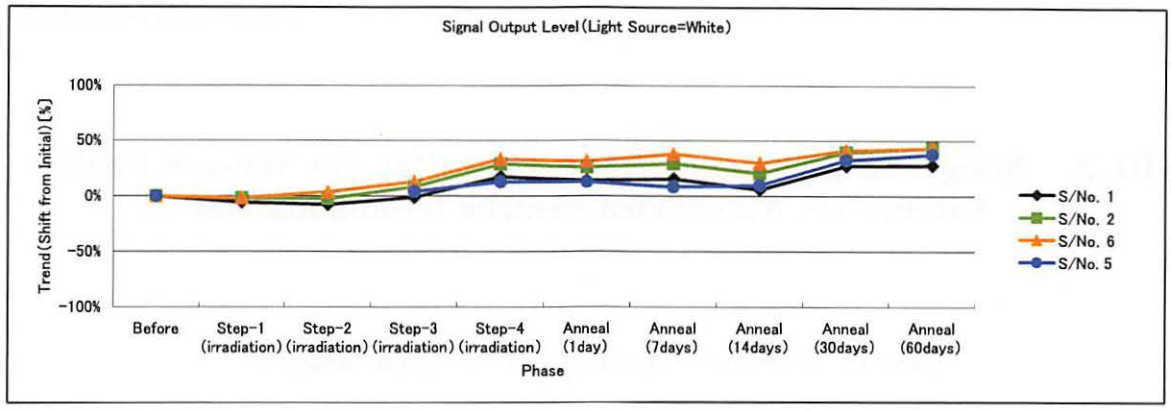

Figure 7. Signal Output Level (Irradiation ~ Annealing Phase).

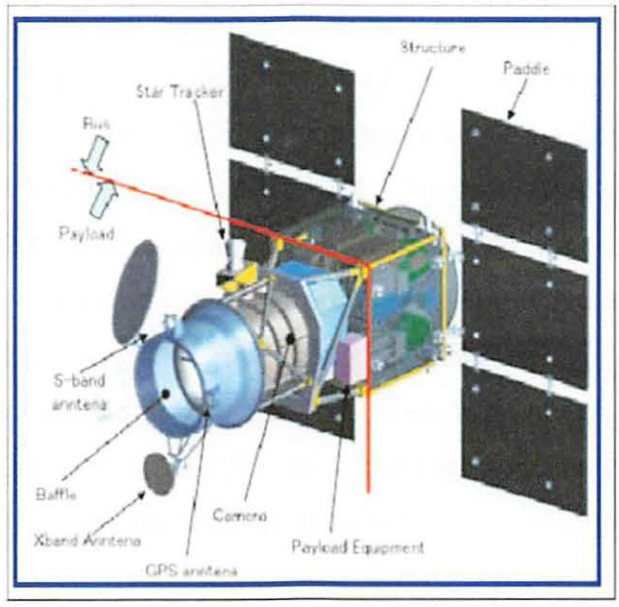

Figure 8. On-orbit configuration.

III. 3. Mitigation Techniques of Soft-Error Rates in Network Routers Validated in Accelerated Neutron Irradiation Test

Toba T.[1], Shimbo K.[1], Nishii K.[2], Ibe E.[1], and Yahagi Y.[1]

[1]Production Engineering Research Laboratory, Hitachi, Ltd.
[2]Telecommunication & Network System Division, Hitachi, Ltd.

Scaling down of semiconductor devices to sub-100 nm technology encounters a wide variety of technical challenges like V_{th} variation[1)] and short-channel effect and so on. Terrestrial neutron-induced single event upset (SEU) is one of such key issues that can result in major setbacks in scaling[2)]. MCU (Multi-Cell Upset) in memory devices are currently regarded as one of the most crucial issues, since they can result in MBU (Multi-Bit Upset, defined as MCU in occurring within the same word), a major cause of system downtimes in network components or microprocessors. These problems eventually become system-level issues. For this reason, the methods of irradiation experiments at the system level are significant. While full chip irradiation tests have been performed with microprocessors, servers, and routers, this report describes the first partial board irradiation test involving routers.

CYRIC (No.3 TR32 line), a quasi-monoenergetic neutron facility, is used for irradiation tests with a neutron peak energy of 65 MeV. Figure 1 shows the neutron energy spectrum. High energy protons are used to bombard a thin Li target, generating neutrons from the Li nuclei with energy nearly equal to that of the protons. Neutron beams are collimated by a concrete collimator into a 10 cm×10 cm square cross section.

In the quasi-monoenergetic neutron test, the SEU cross section σ_{seu} (E_n) is generally measured as a function of neutron energy. The measured data are approximated by the Weibull fit function σ_{seu} (E_n):

$$\sigma_{seu}(E_n) = \sigma_{\infty}\left[1 - \exp\left\{-\left(\frac{E_n - E_{th}}{W}\right)^S\right\}\right] \quad (2)$$

where,

σ_∞ : saturation value of SEU cross section (cm^2);

E_n: neutron energy at the flux maximum (MeV);

E_{th}: threshold energy (MeV); W: width factor (MeV); S: shape factor (-).

Figure 2 shows a typical example of this type of excitation curve. The curve starts from E_{th} and increases gradually to saturation value σ_∞.

The SER at any location on Earth can be obtained by integrating the Weibull fit function and differential flux over the energy range from E_{th}:

$$SER = 10^9 \times \int_{E_{th}}^{\infty} \sigma_{seu}(E_n) \frac{\partial \phi(E_n)}{\partial E_n} dE_n \quad (3)$$

where,

SER: soft error rate (FIT); $\phi(E_n)$: neutron flux ($n/cm^2/h$).

Neutron beams with other energy peaks are not utilized due to limit of machine time. The parameters in Eq. (2) are estimated from our test results carried out for SRAMs.

Figure 3 illustrates the test equipment layout. The BUT (Board Under Test) is set up perpendicular to the neutron beam, centered 125 cm above the floor surface and 40 cm from the aperture of the neutron collimator. The position on the table at which the BUT is set up is altered depending on the part to be irradiated. An FPGA chip, a CPU chip, and a memory chip (SRAMs and SRAMs partially replaced by DRAMs) are chosen as partial irradiation components on the board, since they are regarded as the most vulnerable to neutron-induced soft-errors, recognized by system reboot. Figure 4 shows two types (Set A and Set B) of memory architectures. In the memory chip, all 48 MB of memory cells are SRAMs for Set A; in Set B, 12.5 MB of memory cells for timer information that does not require high-speed operation are replaced by DRAMs. The remaining 25.5 MB of SRAM memory cells are unchanged, since they are used to handle session information and the need for high-speed operation. Overall performance between Set A and Set B is nearly equivalent. The actual sizes of the SRAMs in the test application are 14.5 MB and 2.7 MB, respectively, for Set A and Set B. The contribution of DRAMs to overall failures is believed to be negligible compared to that of the SRAMs and is disregarded[3].

The system reboot procedure is repeated about 10 times to obtain the average cross section for each chip. Figure 5 illustrates the process of data acquisition. The neutron flux is roughly stable, as shown at the bottom. The neutron flux is roughly stable, as

shown at the bottom. The neutron beam is shut off when rebooting takes place—for example, due to parity errors in SRAMs—and fluence Φ_1 in the *i*-th irradiation period is estimated from the total proton charge directed toward the Li target in the *i*-th period. If root cause analysis determines rebooting to be attributable to other components—for example, FPGA bus errors (as shown in Fig. 5) not caused by direct irradiation, the data is eliminated from the data analysis for the chip in question.

Since each irradiation cycle corresponds to a single failure, σ^i_{seu} for the *i*-th cycle is given by

$$\sigma^i_{seu} = \frac{1}{\Phi_i} . \tag{4}$$

Or,

$$\sigma_{seu} = \frac{1}{n}\sum^{n}\sigma^i_{seu} \tag{5}$$

where,

n: total number of cycles for the chip in question.

Table 1 summarizes test results for the estimated SER at Tokyo sea level for total, SRAM, CPU, and FPGA in Set A and Set B, respectively. The table also gives the incidence of system reboots measured at Tokyo sea level for about one year for Sets A and B in the table. The architectural mitigation method is effective and can reduce SERs in the BUT by a factor of about 8 to 9. As Figure 6 also shows, this reduction ratio is consistent for field and accelerator tests. The most vulnerable of the three components types is SRAM (accounting for approximately 95% of all reboot events), based on partial board irradiation tests. While CPU vulnerability appears to be low, care is required, since vulnerability depends on the CPU and the number of FPGAs actually operating. In the present BUT, the number and operating ratio of FPGAs are relatively small. The total time of irradiation during the accelerated test is a mere 18 hours, showing the efficacy of a partial irradiation test compared to a one-year field test. The results indicate the architectural mitigation method can reduce SERs in both field and accelerator tests by a factor of about 10. The absolute values, however, are not consistent with each other: SERs in the field are higher than in the accelerator test by a factor of 6 to 7.

Three factors potentially giving rising to this discrepancy are evaluated below.

(i) SER estimation errors from the accelerator test due to potential oversimplification in

the Weibull fit methodology. Given the maximum error in the estimated SER of approximately 15%, this mechanism would not appear to explain the discrepancy.

(ii) The application applied to the accelerator test is a simple write-once-read-many operation. The timing of the start of the irradiation may be premature relative to the timing whereby the critical data (leading to rebooting) in SRAMs is stabilized. Additionally, the number of SRAMs with critical data may be less than expected.

(iii) The contributions of low energy neutrons (1-10 MeV) to SER are unexpectedly enhanced as device scaling proceeds from 90 nm to 22 nm[2]. This would call for a revision of the Weibull fit. Experimental data for low energy protons and theoretical work supporting this prediction are accumulating rapidly[4].

We introduced here a novel chip-level to board-level SER evaluation method for network routers using 65 MeV quasi-monoenergetic neutron beams and demonstrated an architectural mitigation technique against terrestrial neutron SERs. Based on the replacement of SRAMs by DRAMs in a chip for which speed is not the first priority, in light of operating ratios, the method resulted in an approximately 10-fold reduction in board-level SERs. This reduction ratio is consistent with field data for commercial operation over a period of approximately one year. However, the absolute SER level estimated from the accelerated test is 6 to 7 times lower than the field data. This suggests that a study of the effects of low energy is in order as the first step in future investigations.

We proposed herein a generic strategy for low-cost and low power consumption mitigation of chip and board-level SERs, based on stepwise upper bound reductions. The partial irradiation method is a key technique within this strategy.

References

1) Sugii N., Tsuchiya R., Ishigaki T., Morita Y., Yoshimoto H., Torii K., Kimura S., IEDM, San Francisco, Dec. 15-17, (2008) 249.
2) Ibe E., Taniguchi H., Yahagi Y., Shimbo K., Toba T., IEEE Trans. Electron Device, in press (2010)
3) Borucki. L., Schindlbeck. G., Slayman. C., IRPS 2008, Phoenix, Arizona, April 27-May 1, Phoenix Convention Center No.5A.4 (2008).
4) Heidel D.F., Marshall P.W., Pellish J.A., Rodbell K.P., LaBe K.A., Schwank J.R., Rauch S.E., Hakey M.C., Berg M.D., Castaneda C.M., Dodd P.E., Friendlich M.R., Phan A.D., Seidleck C.M., Shaneyfelt M.R., Xapsos M.A., Trans. Nucl. Sci. **56** (2009) 3499.

Table 1. Test results of SER normalized at Tokyo sea level for set A and B in accelerated and field tests [© IEEE].

Set	SRAM Density Used	SER Estimated at Tokyo Sea Level (A.U.)				
		Field Test	Accelerated Test			
		Board	board	chip	SER	Ratio
A	14.5MB	46.8	7.6	SRAM	7.22	95%
				CPU	0.38	5%
				FPGA	-	-
B	2.7MB	5.2	1.0	SRAM	0.96	96%
				CPU	0.03	3%
				FPGA	0.01	1%

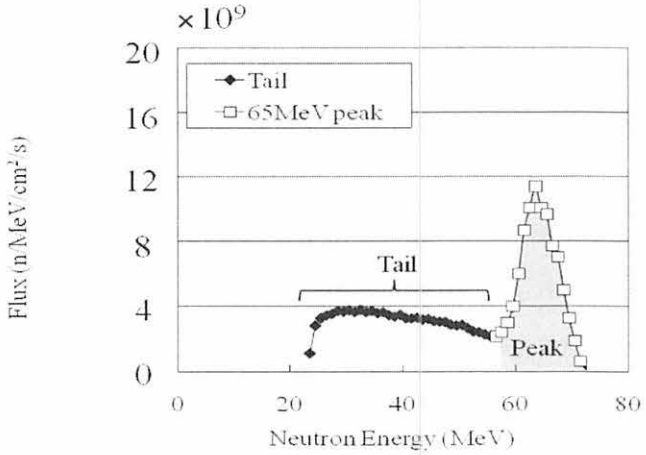

Figure 1. Neutron spectrum used for the partial irradiation test in CYRIC. Peak flux is obtained at about 65 MeV. [© IEEE].

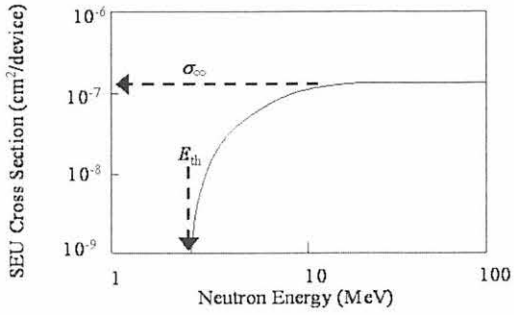

Figure 2. Typical conventional Weibull Fit curve [© IEEE].

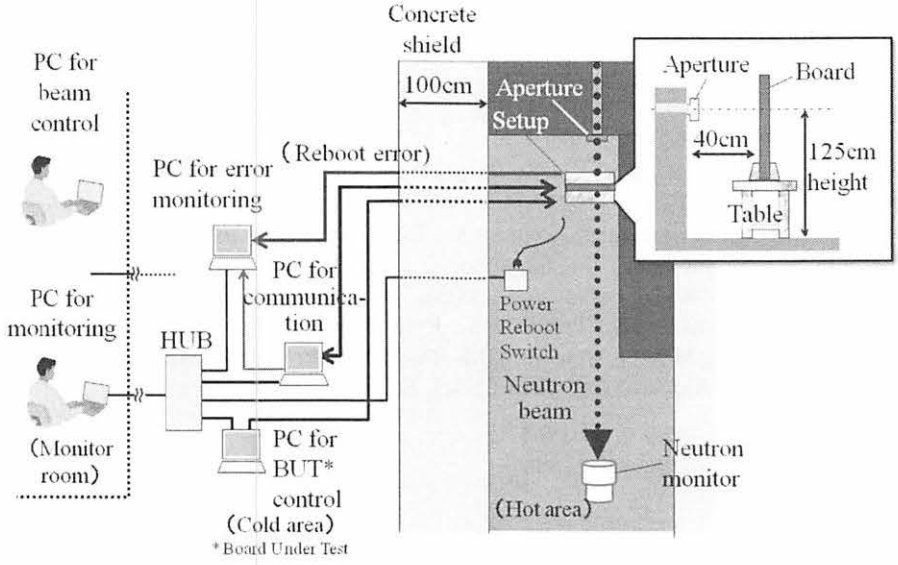

Figure 3. Board setup and conceptual layout of experimental components [© IEEE].

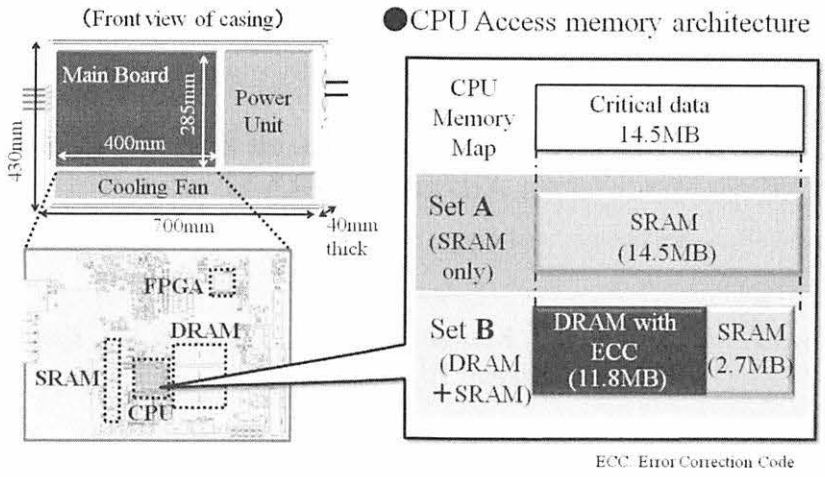

Figure 4. Board casing and CPU access memory map for set A and set B [© IEEE].

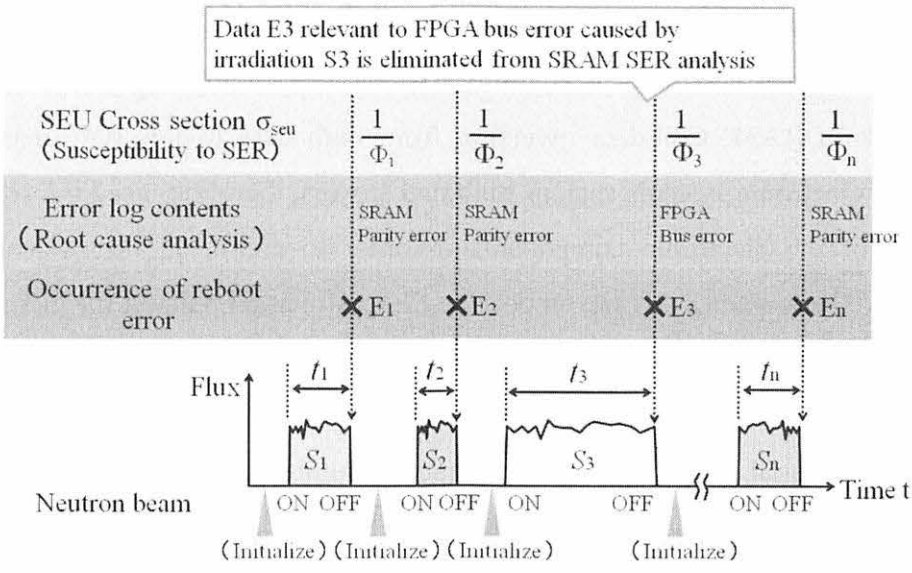

Figure 5. Image of data acquisition and handling [©

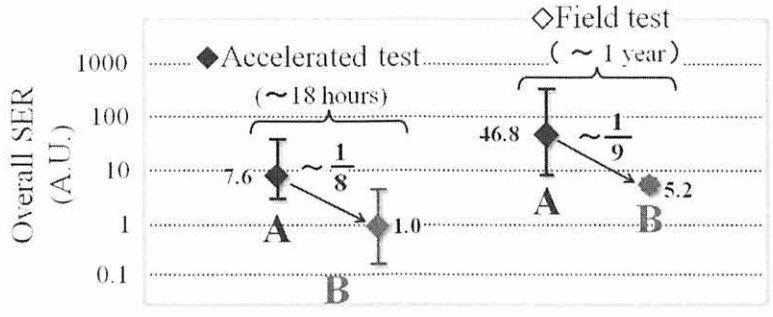

Figure 6. Comparison of estimated SER in accelerator test and measured SER in field for Set A and B [© IEEE].

III. 4. Study of Neutron-Induced Soft Error Rate on Advanced DRAM

Hayakawa T.[1], Matsumoto T.[1], Yahagi Y.[2], Saito A.[1], Hidaka M.[1], Ibe E.[2], Itoh M.[3], Sakemi Y.[3], and Baba M.[3]

[1]*Elpida Memory, Inc.*
[2]*Production Engineering Research Laboratory, Hitachi, Ltd.*
[3]*Cyclotron and Radioisotope Center, Tohoku University*

Terrestrial neutron-induced soft-error or single event upset (SEU) in semiconductor devices is one of the most crucial reliability-issues in the cutting-edge memory devices[1-3]. In the case of DRAM, Cell-data inversion from high-state to low-state mainly occurs. Designers of electronic systems such as high-end servers, therefore, need the soft-error rate (SER) data of the electronic components in order to architecht the system reliability securely. We have intensively developed the SER estimation method for memory devices mainly using monoenergetic and quasi-monoenergetic neutron beams generated by accelerators, which is well reflected also in JEDEC Standard/JESD89A [4] published in Dec. 2006. The essential concept of the method is summarized as follows: the inherent excitation function of a device $\sigma(E)$ is described as the Weibull-type function[1-4],

$$\sigma(E) = \sigma_{\infty}\left[1 - \exp\left\{-\left(\frac{E - E_{th}}{W}\right)^{S}\right\}\right], \quad (1)$$

where σ_{∞} is the saturated value of the SEU cross section, E_{th}, the threshold neutron energy for SEU, W, the scale factor, and S, the shape factor of the Weibull function, respectively. The SER of the device is estimated in the unit of FIT (failure in time; a number of errors in 10^9 hr) by the formula

$$\mathrm{SER\,[FIT]} = 3.6 \times 10^{12} \int_{E_{th}}^{\infty} \sigma(E) \frac{\partial \phi_v(E)}{\partial E} dE, \quad (2)$$

where $\phi_v(E)$ means the flux of terrestrial neutrons at a specific place on the ground, for example, at sea level (0 m) in New York City.

Neutron irradiation experiments concerning DRAMs with stacked capacitors from

250-nm to 110-nm process were performed using monoenergetic and quasi-monoenergetic neutron beams of peak energy from 5 to 174 MeV at FNL (Fast Neutron Lab.) and CYRIC of Tohoku Univ. in Japan, and at TSL (The Svedberg Lab.) of Uppsala Univ. in Sweden[5,6]. Neutron energy dependence of SEU cross sections of each device is acquired by using monoenergetic and quasi-monoenergetic neutron beams[7]. Neutron irradiation experiments of DRAM beyond 100 nm process were performed using quasi-monoenergitic neutron beams of peak energy 70 MeV at CYRIC of Tohoku University. Typical neutron spectra, which were used in this experiment, are shown in Fig. 1. The experiments were performed using a special evaluation tool. The setup of evaluation tool in 32 neutron course is shown in Fig. 2. The estimated SER of each device from monoenergetic and quasi-monoenergetic neutron irradiation tests is shown in Fig. 3. According to Fig. 3, the SER of the DRAMs was effectively suppressed as its down-sizing from 220 nm to 150 nm. This is estimated the effect of the shrinking of junction-volumes and the securing of constant storage capacitance. However, the SER beyond 150 nm process was found constant. This is estimated the offset of the scaling effect and the gradual decreasing of storage capacitance by the lower voltage to capacitor. The securing of storage capacitance may be becoming difficult on advanced DRAM because of the reduction of the Cell area and the lower voltage to capacitor. The soft-error estimation of DRAM should be continued. A high intensity neutron source with a neutron flux around 1.5×10^6 n/cm^2/s is needed for estimating the soft-error on advanced DRAM.

References

1) Nakamura T., Ibe R., Baba M., Yahagi Y., Kameyama H., "Terrestrial Neutron-Induced Soft Errors in Advanced Memory Devices," World Scientific, 2008.
2) Yahagi Y., Ibe R., Saito Y., Eto A., Sato M., Kameyama H., Hidaka M., Terunuma K., Nunomiya T., Nakamura T., Renberg P.U., Prokofiev A., Final Report of IEEE 2002 International Integrated Reliability Workshop, 143, 2002.
3) Ibe E., Yahagi Y., Kataoka F., Saito Y., Eto A., Sato M., Kameyama H., Hidaka M., IEEE 1st International Conference on Information Technology & Applications, Paper No.273-21, 2002.
4) JEDEC Standard/JESD89A, 2006.
5) Johansson K., Dyreklev P., Granbom B., Olsson N., Blomgren J., Renberg P.U., IEEE Trans. Nucl. Sci. **45** (1998) 2519.
6) Prokofiev A.V., Pomp S., Blomgren J., Bystrom O., Ekstrom C., Reistad D., Tippawan U., Wessman D., Ziemann V., Osterlund M., Workshop of Radiation Effects on Components and Systems, Data Workshop Paper PW-14, 2005.
7) Yahagi Y., Saito A., Matsumoto T., Hayakawa T., Ibe E., Itoh M., Yoshida P.H., Sakemi Y., Baba M., CYRIC Annual report 2009, 53.

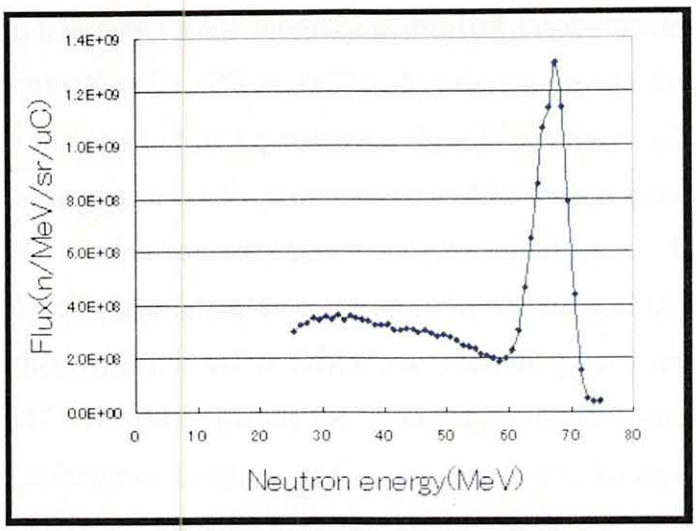

Figure 1. Typical energy spectra of quasi-monoenergetic neutron sources.

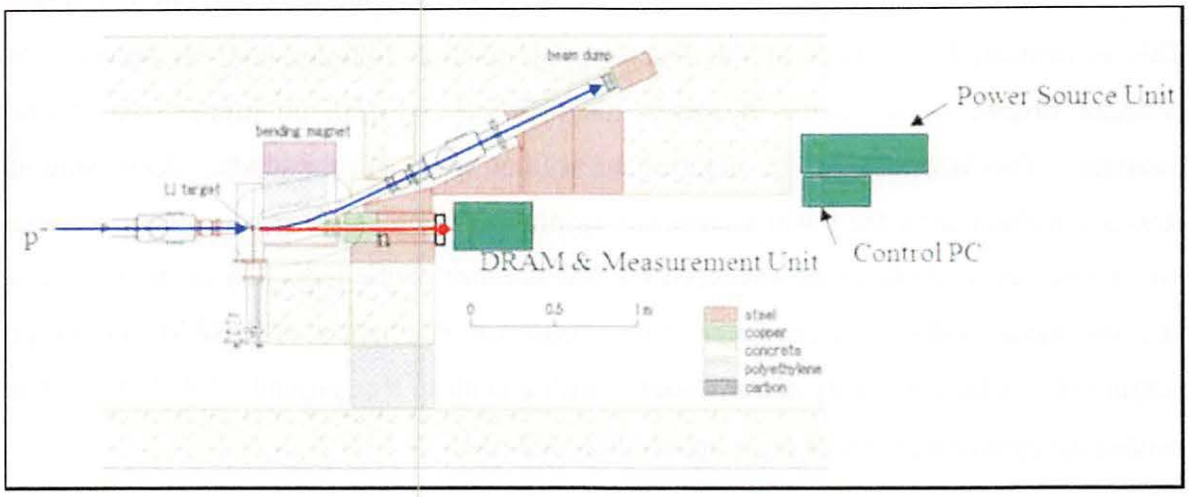

Figure 2. The setup of evaluation tool in 32 neutron course.

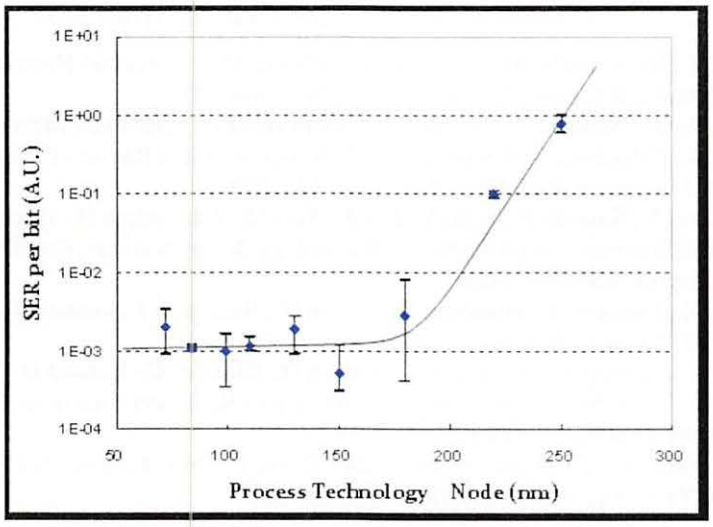

Figure 3. The SER-trend of DRAM with stacked capacitor from 250 to 70 nm process technology node. The solid line is an eye-guide for the trend. *The data form 110nm to 220nm quoted from references 7.

III. 5. Improvement of Energy Resolutions for Planar TlBr Detectors Using the Digital Pulse Processing Method

Tada T.[1], Tanaka T.[2], Kim S.-Y.[1], Wu Y.[1], Hitomi K.[1], Yamazaki H.[1], and Ishii K.[3]

[1]*Cyclotoron and Radioisotope Center, Tohoku University*
[2]*Graduate School of Electronics, Tohoku Institute of Technology*
[3]*Graduate School of Engineering, Tohoku University*

Introduction

Thallium bromide (TlBr) is a new promising semiconductor material for X- and gamma-ray detectors. It has the wide band gap (2.68 eV), the high density (7.56 g/cm^3) and the high atomic numbers (Tl: 81, Br: 35). Also, its low melting point (460°C) makes it easy to grow the crystal.

Improvement of the energy resolution is one of the main issues for researches on semiconductor detectors such as CdTe, CZT, HgI_2, and TlBr. Various methods including pulse shape discrimination, depth sensing technique, and co-planar grid structure have been applied to these detectors in the past decades[1-6]. In this paper, the digital pulse processing method is proposed to improve the energy resolution for planar TlBr detectors. The method is based on the fact that the energy resolution of TlBr detectors is limited by the drift properties of charge carriers[7,8]. The mobilities for holes are very small and it results in the long carrier transit times in the detectors. Although a long time constant (~10 ms) is required for the pulse shaping in order to obtain sufficient energy resolutions from TlBr detectors, the low-frequency noise and the pulse pile-up problems are severe for such case. The proposed digital pulse processing is effective to minimize the problems and is a simple method without complex electronics used by other previous techniques.

In this study, the digital pulse processing method was applied to the output pulses of planar TlBr detectors in order to improve the energy resolutions. The low-frequency noise was suppressed by using an optimum short shaping time and the effect of pulse height deficit due to incomplete charge collection was minimized by the depth correction.

TlBr detectors and experimental setup

The TlBr detectors were fabricated from a crystal grown by the traveling molten zone (TMZ) method. The starting material for the crystal growth was commercially available TlBr powder with nominal purity of 99.999%. The material was zone-purified with a horizontal zone furnace. After the purification, single zone pass was performed to improve crystallinity. In order to fabricate planar TlBr detectors, the grown crystals were cut into wafers with a diamond wire saw. The two surfaces of the wafers were polished mechanically. The resultant wafers had the dimensions of 5×5×0.5 mm^3. Circular electrodes with a diameter of 3 mm were deposited on the polished surfaces by vacuum deposition of thallium through a shadow mask. Then, aluminum was deposited onto the thallium electrodes and thin palladium electrodes were attached to the electrodes by using a carbon paste. The detector was encapsulated in an aluminum box with a BNC connector for connection to a charge-sensitive preamplifier (Clear Pulse 580K). The preamplifier output pulse was directly digitized by means of a digital oscilloscope (Tektronix DPO3032) with a sampling rate of 100 MS/s and 8 bit resolution. The pulses were transferred to a personal computer for analysis. The analysis was performed using a program written in Labview programming environment. All measurements in this study were performed at room temperature and the detectors were operated at 150 V.

Digital pulse processing and results

The height of output pulse obtained from a TlBr detector depends on the depth of interaction (DOI) of incident gamma-rays because holes are trapped within the detector due to its low mobility-lifetime product. In order to correct the pulse height deficit causing degradation of energy resolutions, the depth information (DOI parameter) was extracted from a ratio between pulse heights for fast-shaped and slow-shaped signals. The shaping time of 1 ms was used as the fast shaping to select the pulse height originating from an electron component. The sum of electron and hole components was obtained by using 2 and 10 ms time constants (slow shaping). A digital version CR-$(RC)^4$ filter was constructed and was used for the shaping. The calculated ratios were grouped into 100 bins and the energy spectrum of signals associated with each bin was obtained to correct the depth effect.

Figure 1(a) shows ^{137}Cs spectrum obtained by using the time constant of 10 ms for the pulse shaping. The shaping time was determined to give the best energy resolution

without the depth correction. The energy resolution of 5.8% at 662 keV was obtained. The relationship between the pulse height and the estimated depth of interaction is shown in Fig. 1(b). The photo-peak position in the spectrum seems to be almost independent on the depth of interaction. The result indicates that the depth effect is enough small at the shaping time. However, the energy resolution is apparently restricted by a large low-frequency noise. The noise can be reduced by using a short shaping time. The energy spectrum at the shaping time of 2 ms is shown in Figs. 2(a) and 2(b). In this spectrum, although the low-frequency noise is appreciably suppressed, the depth effect is considerably large compared to that of 10 ms shaping (Fig. 1) and is the dominant factor causing degradation of the energy resolution. The depth effect was minimized by the depth correction. In order to minimize the depth effect, the photo-peak channel associated with each depth of the spectrum was aligned to form an overall energy spectrum with an improved energy resolution. The results are shown in Figs. 3(a) and 3(b). The energy resolution of 4.2% at 662 keV was obtained. The spectra with distorted energy resolution can be rejected based on the depth information to construct the energy spectrum with a better resolution. The best energy resolution of 3.1% was recorded at the DOI parameter between 95 and 99 (Fig. 4).

Conclusion

A digital pulse processing was applied to the output pulses from planar TlBr detectors. The spectra were considerably suffered from a low frequency noise when an only conventional CR-$(RC)^4$ filter with a long time constant was applied to the pulses. In order to suppress the low frequency noise, a short shaping time constant was applied to the output pulses. The depth effect due to the use of the short shaping time was corrected based on the depth information. The energy resolution of the spectrum was appreciably improved by the method.

Since the output pulses contain various information on the detector property, the digital pulse processing can be used not only to improve the energy resolution but also to investigate the other detector properties such as timing performance and carrier mobilities.

References

1) Redus R., Squillante M. R., Lund J., Nucl. Instr. and Meth. **A380** (1996) 312.
2) Jordanov V. T., Panatazis J. A., Huber A., Nucl. Instr. and Meth. **A380** (1996) 353.
3) Richter M., Siffer P., Nucl. Instr. and Meth. **A322** (1992) 529.
4) Luke P. N., Appl. Phys. Lett. **65** (1994) 2884.

5) He Z., Vigil R. D., Nucl. Instr. and Meth. **A492** (2002) 387.
6) Hitomi K., et al., Nucl. Instr. and Meth. **A607** (2009) 112.
7) McGregor D.S., Hermon H., Nucl. Instr. and Meth. **A395** (1997) 101.
8) Owens A., Peacock A., Nucl. Instr. and Meth. **A531** (2004) 18.

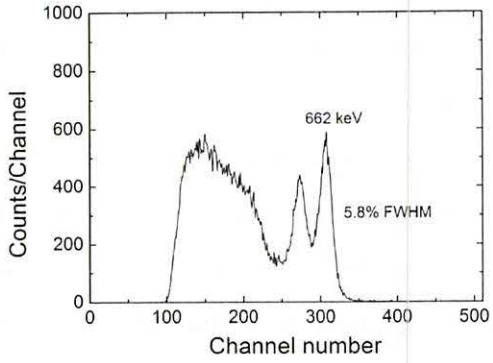

Figure 1(a). ^{137}Cs spectrum obtained from a TlBr detector 0.5 mm thick. Shaping time was 10 ms.

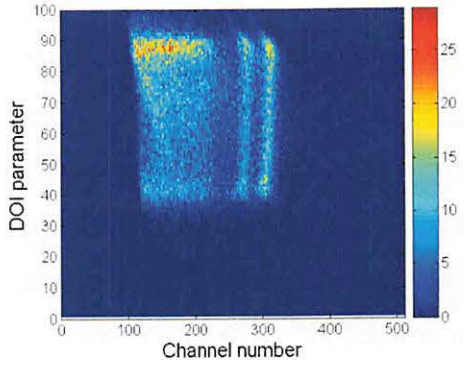

Figure 1(b). Relationship between the pulse height and the estimated interaction depth.

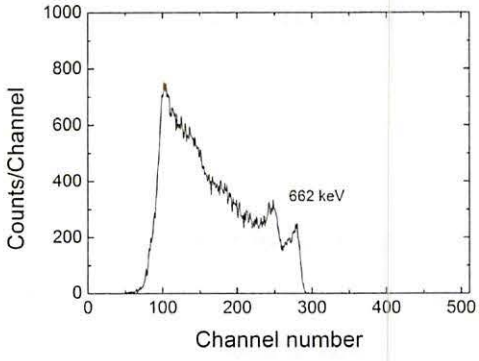

Figure 2(a). ^{137}Cs spectrum obtained from a TlBr detector 0.5 mm thick. Shaping time was 2 ms.

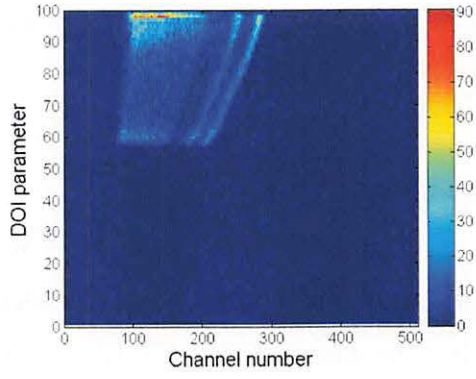

Figure 2(b). Relationship between the pulse height and the estimated interaction depth.

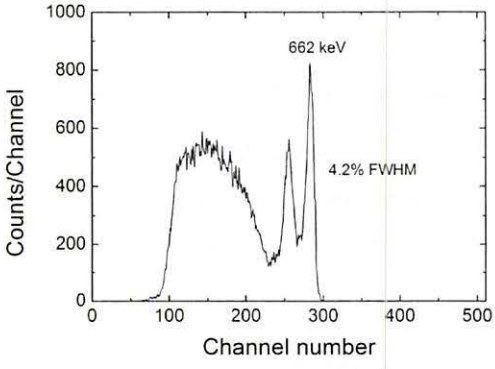

Figure 3(a). ^{137}Cs spectrum obtained with correcting the depth effect. Shaping time was 2 ms.

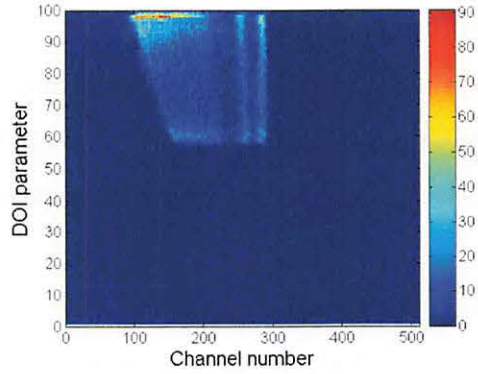

Figure 3(b). Relationship between the pulse height and the estimated interaction depth.

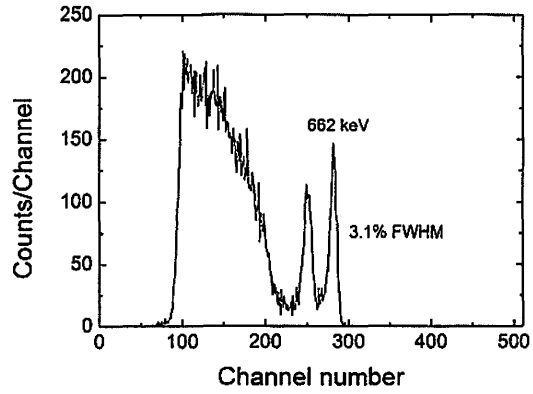

Figure 4. ^{137}Cs spectrum for the depth parameter between 95 and 99. Shaping time was 2 ms.

IV. NUCLEAR MEDICAL ENGINEERING

IV. 1. High-Resolution [^{18}F]FDG-PET Measurement of a Murine Fibrosarcoma Treated With Proton Therapy Combined With the Vascular Disrupting Agent AVE8062

Terakawa A.[1,2], Ishii K.[1,2], Matsuyama S.[1], Kikuchi Y.[1], Akiyama H.[1], Koyata K.[1], Ito Y.[1], Tagawa A.[1], Yasunaga S.[1], Kawamura T.[1], Takahashi Y.[1], Yamazaki H.[3], Tashiro M.[3], Funaki Y.[3], Furumoto S.[3,4], Itoh N.[5], Wada S.[5], and Orihara H.[6]

[1]*Department of Quantum Science and Energy Engineering, Tohoku University*
[2]*Graduate School of Biomedical Engineering, Tohoku University*
[3]*Cyclotron and Radioisotope Center, Tohoku University*
[4]*Tohoku University Graduate School of Medicine*
[5]*School of Veterinary Medicine and Animal Sciences, Kitasato University*
[6]*Department of Intelligent Electronics, Tohoku Institute of Technology*

Recently, therapeutic strategies targeting tumor vasculature have received a great ×attention in cancer treatment. Although vascular disrupting agents (VDAs) cause a rapid vascular shutdown in solid tumors leading to extensive tumor necrosis as a result of oxygen and nutrient deprivation. However, tumor cells in the tumor periphery survive VDA treatment alone. It is suggested that the tumor cells in the tumor edge are expected to be nutritionally supported in part by normal vessels in the surrounding healthy tissue[1]. In order to kill these surviving cells, VDA treatments are needed to be combined with conventional treatment such as radiotherapy or chemotherapy.

In the previous CYRIC annual report[2], we demonstrated that tumor growth delay was significantly enhanced in NFSa fibrosarcoma tumors by the combined treatment of proton irradiation and the vascular disrupting agent AVE8062 in comparison to proton therapy alone or AVE8062 treatment alone, as shown in Fig. 1. It is expected that the proton irradiation may induce therapeutic effects on tumor cells at the tumor periphery which survive AVE8062 treatment alone. In this work, we performed a high-resolution PET study using a semiconductor animal PET scanner (Fine-PET)[3] and ^{18}F-labeled fluorodeoxyglucose (FDG) to evaluate therapeutic effects caused by the combined treatment.

NFSa fibrosarcoma cells (5×10^6/50μL) were transplanted into both hind legs of

C3H/HeSlc male mice aged around 12 weeks old. When each tumor diameter reached about 8 mm, the tumors of the right hind leg were locally irradiated (15 or 30 Gy) using a clinical proton beam provided from a horizontal proton irradiation system[4] so that the tumor volume was covered by the maximum depth dose distribution, the so-called spread-out Bragg peak (SOBP). The size of SOBP was 20 mm in this work. The tumor of the left hind leg was not irradiated. AVE8062 was administered intraperitonealy to a part of the mice receiving 15 Gy at a dose of 40 mg/kg 2 hours after irradiation. As a result, we classified the tumors of the right and left hind legs into proton therapy (15 or 30 Gy), AVE8062 treatment (40 mg/kg), combined treatment (15 Gy + 40 mg/kg) and control groups. Therapeutic effects caused by each treatment in this work were evaluated 1 day and 4 days after each single treatment on the basis of glucose uptake inside the tumor. FDG (37 MBq) was administered to the mice from the tail vein. The FDG-PET scan was performed using the Fine-PET scanner from 60 to 120 min after the FDG administration.

Figure 2 shows results of the FDG-PET measurements. A significant difference was observed in the distribution of FDG uptake between the tumors treated with and without AVE8062. For control and 15-Gy proton therapy groups, FDG uptake was significantly high in the whole tumor region on both day 1 and day 4. On the other hand, FDG concentrated only in the tumor periphery on day 1 in the AVE8062 treatment alone and the combined treatment due to the shutdown of tumor vasculature. In addition, FDG accumulation in the tumor edge of the combined treatment decreased on day 4 in comparison to that of AVE8062 treatment alone. On the basis of these findings, it is expected that AVE8062 may give rise to necrosis in the central region of the tumor and that proton irradiation may cause therapeutic effects leading to reduction in FDG uptake on cells in the tumor periphery.

This work was supported by Grants-in-Aid for Scientific Research (B) Nos. 17300169 (A. Terakawa) and 20300174 (A. Terakawa), and by Exploratory Research No. 19650128 (A. Terakawa) of the Ministry of Education, Culture, Science, Sports and Technology.

References

1) Dietmar W. Siemann et al., Cancer, **100** (2004) 2491.
2) Terakawa A. et al., CYRIC Annual Report 2008 p61.
3) Ishii K., et al., Nucl. Instr. and Meth. **A 576** (2007) 435.
4) TERAKAWA Atsuki et al., Proceedings of the 16th Pacific Basin Nuclear Conference (16PBNC), Oct. 13-18, 2008, Aomori, Japan, PapaerID P16P1378, p1-p6.

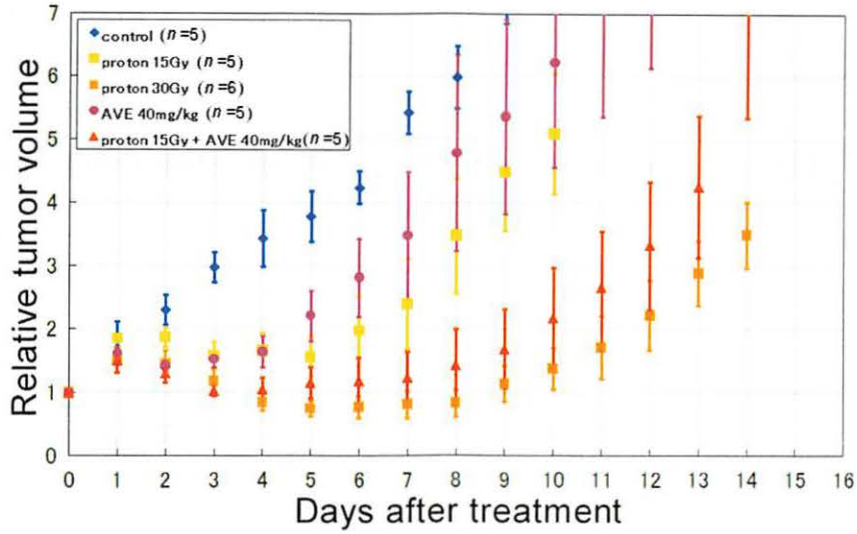

Figure 1. Time course of changes in relative tumor volume caused by each single treatment on day 0. Data are shown with the mean ± standard error. The number of the tumors in each group is indicated with *n*.

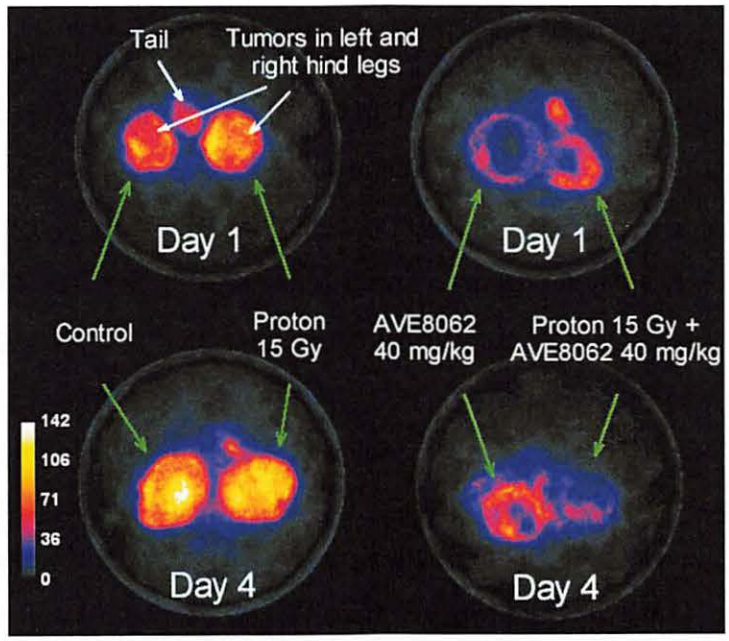

Figure 2. High-resolution [^{18}F]FDG-PET images of NFSa tumors 1 or 4 days after each single treatment.

IV. 2. Tritium Measurement Using a Photo-Stimulable Phosphor BaFBr(I):Eu^{2+} Plate

Ohuchi H.[1] and Hatano Y.[2]

[1]*Graduate School of Pharmaceutical Sciences, Tohoku University*
[2]*Hydrogen Isotope Research Center, University of Toyama*

Introduction

Tritium measurement is indispensable for the fuel-processing systems of deuterium-tritium (DT)-fusion facilities. Tritium emits beta particles with a maximum energy of 18.6 keV and an average of 5.7 keV. These have a range of about several micrometers in graphite and hence the technique is sensitive to tritium up to a depth of a few microns. This means that the tritium IP technique based on detecting the beta particles is unsuitable for use in regions deeper than the escape depth of beta-rays from tritium. We have developed a new approach to detecting tritium using the bremsstrahlung induced by tritium beta-rays with the IP. The measurement principle of this approach to tritium detection is to observe bremsstrahlung X-rays generated by the interaction between the beta particles from tritium and matter, on the basis that X-rays penetrate materials much more easily than the weak beta-rays from tritium. In this study, the characteristics of the IP for measuring tritium by detecting bremsstrahlung X-rays it produces have been examined, in particular a fading effect and the energy dependence of photostimulated luminescence (PSL) sensitivities. The fading effect after irradiation with bremsstrahlung X-rays from tritium was compared with that obtained after irradiation with the beta particles emitted from tritium.

Materials and Methods

A BAS-MS type-IP was used to detect bremsstrahlung X-rays from tritium and a BAS-TR-type IP (FUJIFILM Co., Ltd.) to detect beta particles. The differences in structures of these two are listed in Table 1. To read out the IP, an image reader fabricated by FUJIFILM Co., Ltd. was used. We used four small borosilicate glass tubes with a wall

thickness of 0.088 mm, length of 6.36 mm, and diameter of 0.60 mm, filled with pure tritium gas of 12.5, 25, 50, and 100 MBq, respectively (manufactured by mb-microtec ag) as the tritium sources that generate bremsstrahlung X-rays. Ten strips of microscale-labelled polymer layers (manufactured by GE Healthcare) were used as the beta-ray radiation source. Each strip contained approximately 2.96 kBq of tritium. The temperature dependence of the fading effect of the latent image was measured for time periods from 0.05 to 380 h after 1 h irradiation with beta rays or bremsstrahlung X-rays from tritium, at temperatures of 0, 30, and 50°C. The IPs were kept in an aluminum IP cassette inside an incubator during irradiation and for the time prior to reading the latent image. The detection limit was obtained by irradiating the IP with a borosilicate glass tube filled with 12.5 MBq of gaseous tritium for an irradiation time from 1 to 24 h. The IP was placed inside a 10-cm-thick lead outer shield during irradiation to reduce the effect of natural radiation. The energy response of the BAS-MS-type IP was measured by using 8.0, 10.0, 13.5, 16.0, and 18.6 keV monoenergetic X-ray beam sources. The experiments using the X-ray beam sources were performed on a beam line at the Photon Factory (PF) of the High Energy Accelerator Research Organization (KEK). The PSL sensitivities of the IPs covered with aluminum filters of three different thicknesses, 0.1, 0.3, and 0.5 mm, were measured in order to investigate the variation of the energy response with filters present.

Results and discussion

Figure 1 compares the experimental results for the measured PSL values after irradiation with the tritium source generating bremsstrahlung X-rays using the BAS-MS and the beta-ray source using the BAS-TR in the range 0 to 50°C. In Fig. 1, the BAS-MS-type IP shows a good fading characteristic, exhibiting only a small difference in the fading effect between 0°C and 30°C. In all the fading curves, however, the fading effect becomes stronger as the temperature increases. We found the relevant relation between the ambient temperature and PSL intensity[1] and established a method to develop a functional equation to correct for the fading effect[2]. By fitting the experimental results to the Arrhenius' equation, we developed a functional equation that includes two variables: elapsed time (t) and temperature (K). The fading equation after irradiation by bremsstrahlung X-rays using the BAS-MS is written as

$$(PSL)_{t,k} / (PSL)_{0,k} =$$
$$0.348 \cdot \exp\{-2.08\times10^{12} \cdot t \cdot \exp(-8.92\times10^{3}/K)\}$$

$$+0.087 \cdot \exp\{-9.89\times10^{10} \cdot t \cdot \exp(-8.69\times10^{3}/K)\}$$
$$+0.374 \cdot \exp\{-4.37\times10^{10} \cdot t \cdot \exp(-9.31\times10^{3}/K)\}$$
$$+0.150 \cdot \exp\{-2.41\times10^{10} \cdot t \cdot \exp(-9.54\times10^{3}/K)\}$$
$$+0.041 \cdot \exp\{-2.07\times10^{9} \cdot t \cdot \exp(-9.53\times10^{3}/K)\} \quad (2)$$

By using Eq. (2), we are able to correct the PSL values obtained at different elapsed times and/or at different temperatures and compare them.

When the target is borosilicate glass, an energy yield fraction Yi for the maximum energy of monoenergetic electrons converted to bremsstrahlung is calculated to be approximately 10^{-4} [3]. This rather low yield fraction can be compensated to some degree by irradiating the IP with the source for much longer, utilizing the good fading characteristic of the BAS-MS-type IP. Relationships among the PSL density of the background (BG) (left y-axis), the detection limit of tritium (right y-axis), and the irradiation time (h) are shown in Fig. 2. The detection limit was estimated from the equation obtained from the relationship between tritium radioactivity (Bq) and PSL intensity after irradiation with the glass tube filled with tritium gas of 12.5, 25, 50, and 100 MBq (not shown here) and three standard deviations from the mean PSL density of the background for each irradiation time. For 1 h of irradiation, the detection limit was estimated to be 970 kBq/cm^2. Longer irradiation periods increase the PSL intensity attributed to the background as well. To reduce this background effect, the IP was kept inside a lead outer shield during irradiation. The detection limit obtained was improved to approximately 90 kBq/cm^2 for a 24 h irradiation.

PSL responses are affected by the variation of the energy spectrum depending on the thickness of the target (or absorbing material) and the energy dependence of the PSL sensitivities. The measured IP sensitivity (PSL per arbitrary unit) with and without aluminum filters of different thicknesses is plotted against the X-ray energy (keV) in Fig. 3. The result shows that the IP's sensitivity depends greatly on the X-ray energy. By combining the sensitivity data measured using aluminum filters 0.1, 0.3 and 0.5-mm thick, and without a filter, a constant PSL sensitivity of an IP per arbitrary unit independent of the X-ray energy can be obtained. By taking the weighted sum, Res_{sum} shown in Eq. (3) below, a response having a flat energy dependence can be obtained, as shown in Fig. 4:

$$Res_{sum} = 8.00 \cdot Res_{no\ filter} - 8.76 \cdot Res_{Al0.1mm} - 2.00 \cdot Res_{Al0.3mm} + 2.45 \cdot Res_{Al0.5mm} \quad (3)$$

where $Res_{no\ filter}$, $Res_{Al0.1mm}$, $Res_{Al0.3mm}$, and $Res_{Al0.5mm}$ are the IP sensitivities measured without a filter, and with aluminum filters 0.1, 0.3, and 0.5-mm-thick, respectively. The IP sensitivity obtained was constant to within ±14% deviation for X- rays with energies from 8.0 to 18.6 keV except at 13.5 keV, where Ressum shows ±25% deviation.

Figure 4 shows the results of measured PSL densities when different thicknesses of nickel (Ni) foil in the range 5 to 25 μm were sandwiched between the glass tube containing 12.5 MBq of tritium and the IP, simulating migration of tritium into deeper regions of the nickel. PSL densities were measured with and without aluminum filters of different thicknesses in the range 0.1 to 0.5 mm. The relative PSL density was obtained by normalizing each PSL density to that without a nickel foil or aluminum filters (left y-axis). By combining the sensitivities measured using aluminum filters 0.1, 0.3 and 0.5 -mm thick, and those without filters, PSL densities were corrected by using Eq. (3). The corrected PSL values are shown in Fig. 4 (right y-axis). Error bars show 25% deviation for each corrected PSL value. Using Eq. (3), we can correct the energy dependence of the PSL sensitivities as shown in Fig. 4. In combination with the energy spectrum information (depth profiles), the amount of tritium in deeper regions can be quantified by this technique. These comprehensive results indicate that the tritium IP technique based on detecting bremsstrahlung X-rays can be a new method for the non-destructive monitoring of tritium migration into deeper layers.

References

1) Ohuchi H., Yamadera A., Nakamura T., Nucl. Instr. and Meth. **A450** (2000) 343.
2) Ohuchi H., Yamadera A., Rad. Meas. **35** (2002) 135.
3) Martin, J.E.: Physics for Radiation Protection, 2nd ed., Litges & Dopf Buchbinderei GmbH, Heppenheim (2006) 371.

Table 1. Structures of the two types of imaging plates.

IP	BAS-MS	BAS-TR
Thickness of protective layer (μm)	9	0
Thickness of phosphor layer (μm)	115	50
Phosphor	$BaF(Br_{0.85}+I_{0.15})$	BaFBrI[1]
Thickness of base (μm)	190	250
Thickness of ferrite layer (μm)	160	160

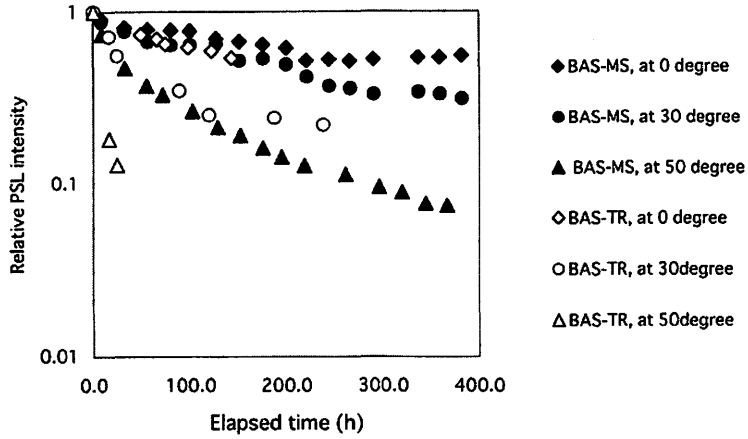

Figure 1. Comparison of the experimental results for the measured PSL values after irradiation with the tritium source generating bremsstrahlung X-rays using the BAS-MS and the beta-ray source using the BAS-TR.

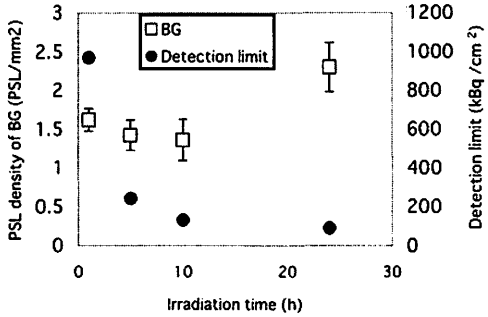

Figure 2. Relationships between PSL density of background (left y-axis), detection limit of tritium (right y-axis), and irradiation time (h).

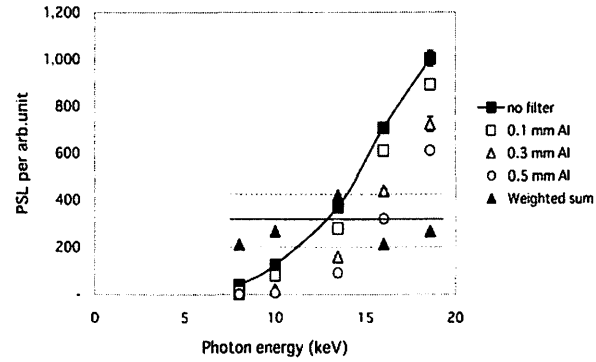

Figure 3. PSL sensitivities measured with and without aluminum filters of different thicknesses. The ▲ symbols show the weighted sum of PSL sensitivities measured with and without the different filters. The IP sensitivity was constant to within ±14% deviation for X- rays with energies from 8.0 to 18.6 keV except at 13.5 keV, where Ressum shows ±25% deviation.

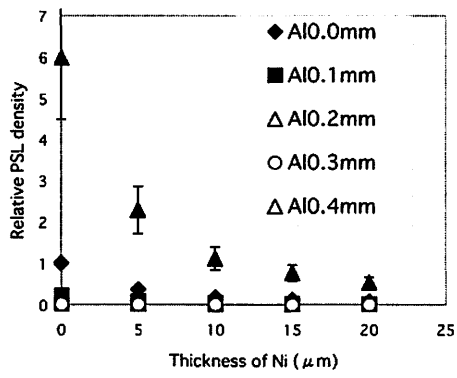

Figure 4. Measured PSL densities and corrected PSL responses from Eq. (3) when different thicknesses of Ni foil in the range 5 to 25 μm were sandwiched between the glass tube containing 12.5 MBq of tritium and the IP. Error bars show 25% deviation for each corrected PSL value.

IV. 3. Deeply Trapped Electrons in Imaging Plates and Their Utilization for Extending the Dynamic Range

Ohuchi H.[1] and Kondo Y.[2]

[1]Graduate School of Pharmaceutical Sciences, Tohoku University
[2]Ishinomaki Senshu University

Introduction

Despite of many excellent characteristics of imaging plates (IPs), unexpected effects have become known, i.e., the phenomena of unerasable and reappering latent images. In our previous study[1)], we obtained the following results: (1) unerasable latent images almost disappeared when the IP was held at a temperature of 120°C for 28 days; (2) ultraviolet light of wavelength around 290 nm promoted the reappearance of photostimulated luminescence (PSL) signals; and (3) the amount of PSL signal reappearance increased in proportion to the irradiation dose. These results indicate that electrons are trapped in deep centers, they can be excited optically by 290 nm ultraviolet light and transferred towards the longer wavelength of around 633 nm, producing F centers and they cause latent images to reappear. The number of deeply trapped electrons will increase in proportion to the irradiation dose. In this study, the absorption spectra of deep centers in an over-irradiated IP were studied in the ultraviolet region. By utilizing deeply trapped electrons, we have attempted to extend the dynamic range of an IP readout under a higher irradiation dose.

Materials and methods

Square pieces were cut from the PSL sheet (type BAS-MS2025: FUJIFILM Co., Ltd.) as samples. The BAS-MS samples were uniformly exposed to 150-kV X-ray beams from an MBR-1520R unit (Hitachi Medico Co.). A fluorescent eraser (IP Erase 3:FUJIFILM Co., Ltd.) was used to erase the IP samples with visible light.

Diffracted ultraviolet light from a deep ultraviolet lamp (UXM500SX: USHIO INC.) was used as a light source for excitation of electrons in deep centers. Figure 1 shows a schematic illustration of the diffracted ultraviolet light irradiation system. In order

to obtain an ultraviolet spectral distribution curve, a Si pin photodiode (S1226-18BQ: Hamamatsu Photonics K.K.) was used. The curve was calibrated in wavelength by atomic lines emitted from a mercury (Hg) lamp. The spectral distribution curve obtained over the range from 200 nm to 500 nm is exhibited in Fig. 2. IP samples were irradiated with an X-ray dose of 30 Gy and fully erased with visible light. These were used as the IP samples with unerasable latent images. The IP sample was irradiated with diffracted ultraviolet light for 10 min. Then, it was scanned by an IP reader FLA3000 (FUJIFILM Co., Ltd.) with a He-Ne laser and profiles were readout with 0.1-mm steps to obtain spectrum. These procedures are developed for this study and called measurements of luminescence inducing spectra in the following text. A luminescence inducing spectrum can be obtained by correcting each measured spectrum with the spectral distribution curve shown in Fig. 2. A luminescence inducing spectrum of non-irradiated IP samples was obtained in the same manner.

For obtaining dose-response curves, two types of readout system were used; one was the imaging plate reader, FLA3000 and the other a PSL detection system. When an IP sample irradiated with X-ray doses higher than 100 μGy was read out with the FLA3000, the technique of using color cellophane[2)] was used to avoid saturation of the output currents of a photomultiplier tube (PMT), installed in the IP reader. Using two color cellophanes, red and blue, the upper limit of the measurable dose of the IP reader, is extended to 1 Gy and further extended to 100 Gy by the combinations of three colors, red-red-blue[2)]. The homemade PSL detection system consists of a semi-conductor laser, LDU33-635-4.5 (635 nm, SIGMA KOKI CO., LTD.) and a photon counting detector, H7467 (Hamamatsu Photonics K.K.) and a schematic illustration of the PSL detection system is given in Fig. 3. This system was used to read out deeply trapped electrons by continuously stimulating an IP sample showing unerasable latent images with 635-nm light to the level at which the PSLs can no longer be detected. After irradiation with X-ray doses ranging from 8.07 mGy to 80.7 Gy, IP samples were measured using the FLA3000 with the cellophane technique and fully erased with visible light, then measured again with the FLA3000. They were then read out by the PSL detection system.

Results and discussion

Luminescence inducing spectra from 200 nm to 500 nm of the IP sample irradiated with a 30 Gy dose and one not irradiated are shown in Fig. 4. In the irradiated IP sample,

a dominant peak is observed at around 320 nm, followed by two small peaks at around 345 nm and 380 nm. However, no intense peak is seen in the non-irradiated sample. This result indicates that several deep centers were created in the irradiated IP sample in the ultraviolet region.

The level scheme of the PSL material has been reported by Iwabuchi et al[3]. However, deep centers are not shown there. In Fig. 5, they are illustrated in the level scheme, presuming that they act as competitive trap centers to the F centers in the PSL material. A model of the excitation of deeply trapped electrons and PSL processes is exhibited in Fig. 5. Deeply trapped electrons are excited optically with a 320-nm ultraviolet light to the conduction band and produced F centers. Electrons trapped by F centers, are then stimulated by a He-Ne laser light of 633 nm and emit PSL of 390 nm.

The dose response curves measured by the FLA3000 using sheets of red-blue and red-red-blue cellophane are shown in Fig. 6. A dotted line demonstrates a linear relationship from 8.07 mGy up to 0.8 Gy. The dose response curves begin to decline above 0.8 Gy, indicating that the F centers become saturated. The dose response curve in the IP samples measured by the FLA3000 after fully erasing with visible light is shown in Fig. 7. The dotted line demonstrates a linear relationship from 8.07 mGy up to 2.4 Gy, after that the curve shows another linear relationship up to 80.7 Gy with a considerably smaller slope. The result of total photon counts read out by the PSL detection system from the IP samples are shown in a log-log expression as a function of the irradiated dose (Gy) in Fig. 8, giving a further two orders of magnitude extended the dynamic range up to 80.7 Gy. The dose response curve shows a linear log-log relationship up to 40 Gy and increases steeply up to 80.7 Gy. The differences between Fig. 7 and Fig. 8, which were obtained from the same IPs by the FLA3000 and the PSL detection system, respectively, are explained by the difference in the two readout systems. The FLA3000 readout system scans a large area of an IP at high speed so that it has insufficient time to read out deeply trapped electrons. In contrast, the PSL detection system can read out them efficiently by continuously stimulating an over-irradiated IP sample with 635-nm light.

Comprehensive results show the possibility of utilizing deeply trapped electrons for extending the dynamic range by stimulating over-irradiated IP samples with 635-nm light. In order to read out deeply trapped electrons more effectively, a method to stimulate them by a light with the proper wavelength, appropriate to the absorption peaks, is necessary.

References

1) Ohuchi H., KondoY., Nucl. Instr. and Meth. **A596** (2008) 390.
2) Ohuchi H., Yamadera A., J.Nucl.Sci.Tech. **Suppl.4** (2004) 140.
3) Iwabuchi Y., Mori N., Takahashi K., Matsuda T., Shionoya S., Jpn. J. Appl. Phys. **33** (1994) 178.

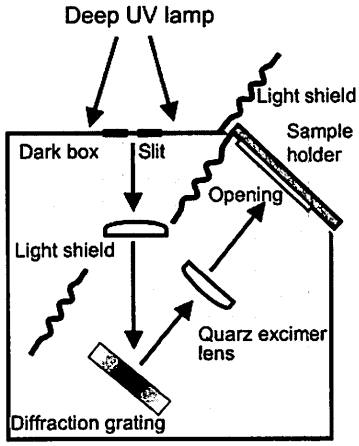

Figure 1. Schematic illustration of the diffracted ultraviolet light irradiation system.

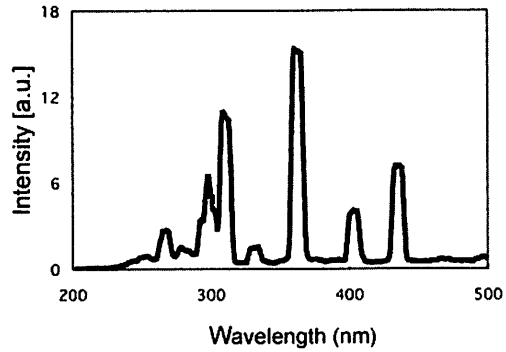

Figure 2. Spectral distribution curve over the range from 200 nm to 500 nm emitted from the diffracted ultraviolet light irradiation system.

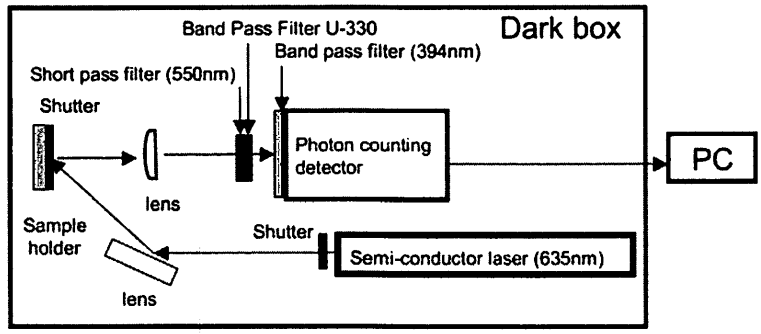

Figure 3. Schematic illustration of the PSL detection system.

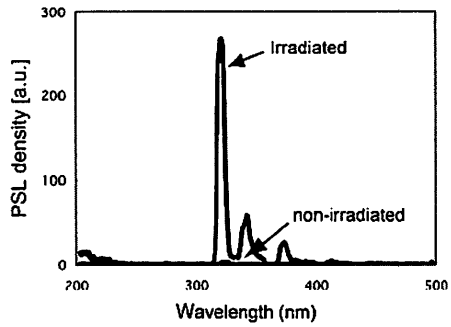

Figure 4. Luminescence inducing spectra from 200 nm to 500 nm of the IP sample irradiated with a 30 Gy dose and one not irradiated.

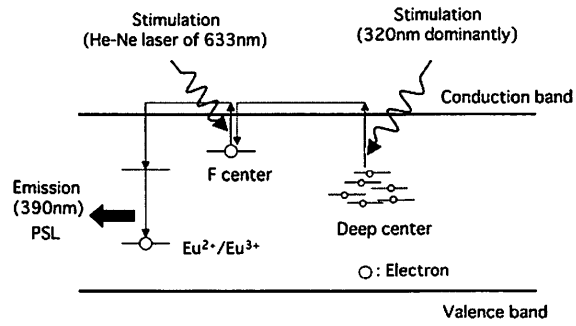

Figure 5. Deep centers are illustrated in the level scheme of the PSL material. A model of the excitation of deeply trapped electrons and PSL processes is also exhibited.

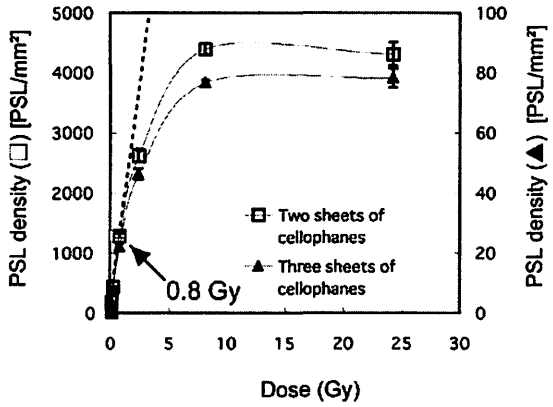

Figure 6. Dose response curves measured by the FLA3000 using sheets of red-blue and red-red-blue cellophane.

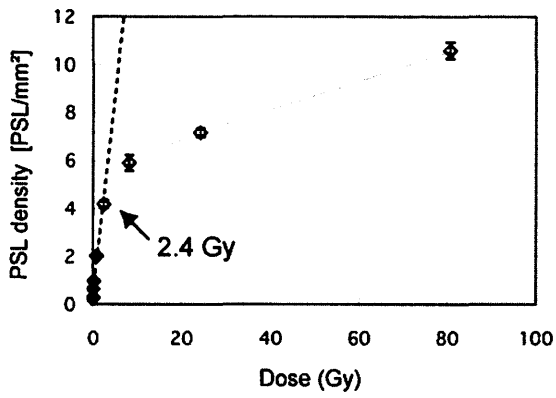

Figure 7. Dose response curve in the IP samples measured by the FLA3000 after fully erasing with visible light.

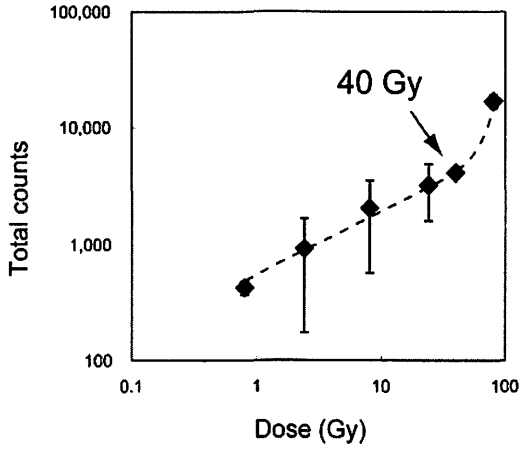

Figure 8. Total photon counts read out by the PSL detection system from the IP samples in a log-log expression as a function of the irradiated dose (Gy). It shows a further two orders of magnitude extended the dynamic range up to 80.7 Gy.

V. PIXE AND ENVIRONMENTAL ANALYSIS

V. 1. Progress of The Tohoku Microbeam System

Matsuyama S.[1], Ishii K.[1], Yamazaki H.[1], Kikuchi Y.[1], Inomata K.[1], Watanabe Y.[1], Ishizaki A.[1], Oyama R.[1], Kawamura Y.[1], Yamaguchi T.[1], Momose G.[1], Nagakura M.[1], Takahashi M.[1], and Kamiya T.[2]

[1]*Department of Quantum Science and Energy Engineering, Tohoku University*
[2]*Takasaki Advanced Radiation Research Institute, Japan Atomic Energy Agency*

Introduction

High-energy ion microbeams are powerful analytical tools that combine various ion beam analysis techniques such as PIXE, RBS, STIM, and SEM[1-3]. They are also attractive as a direct lithographic technique. We have developed a microbeam analysis system for biological applications with sub-micrometer resolution. The primary purpose was to develop a 3D μ-CT, in which a microbeam is used as a monoenergetic point X-ray source. The second was to develop a microbeam analysis system for biological samples. The microbeam line was installed in July 2002; the system produced a beam spot size of 2×2 μm^2 with a beam current of 10 pA. Both the beam size and beam current were insufficient for ion beam analyses. Optimization and modification of the system were performed and the analysis system was re-developed. After optimization and modification of the system, the beam performance was remarkably improved and a multimodal analysis system was developed. This paper presents a description of recent progress of the microbeam system.

Microbeam System

The microbeam system was designed to achieve sub-micrometer beam sizes and was developed in collaboration with Tokin Machinery Corp[4]. The system is connected to the 4.5 MV Dynamitron accelerator at Tohoku University. A high-resolution energy analysis system is installed upstream of the microbeam line to confine the energy variation so as to achieve sub-micrometer beam sizes. The microbeam line comprises a quadrupole doublet and three slit systems: micro-slit (MS), divergence-defining slit (DS), and baffle slit (BS). These components are mounted on a heavy rigid support with vibration isolation. We set

the working distance and the objective distance at 26 cm and 6 m, respectively. The demagnification factors are 9.2 and 35.4 for horizontal and vertical directions, respectively. The focused microbeam is scanned across a target two-dimensionally using an electrostatic beam scanner. The scanner is located downstream of the quadrupole doublet and the maximum scanning area is larger than 1×1 mm^2 for 3 MeV proton beams.

Analysis System Improvements

The target chamber is a rectangular box and is applicable to either in-vacuum or in-air analysis without changing the main body. For multimodal analysis, two X-ray detectors and three charged particle detectors can be mounted simultaneously[6-8]. For 3D μ-CT, an X-ray CCD camera (C8800X; Hamamatsu photonics), a rotating sample stage and a target to produce X-rays are also mounted on this chamber[9-11]. In the present study, further improvements were introduced to the target chamber, as shown in Fig. 1. Two X-ray detectors are attached to both sides of the chamber and are not shown.

For in-vacuum analysis, hydrogen is analyzed using off-axis STIM. In a previous study, a Si-PIN photodiode was used for both off-axis STIM and Direct STIM measurements. Superior energy resolution of the Si-PIN photodiode is efficient for direct STIM measurement[8]. However, the small size of the detector occasionally restricted detection efficiency in hydrogen analyses. For that reason, an ion-implanted Si detector with a larger sensitive area of 50 mm^2 was installed. Detection efficiency of the system is now three times higher than that of the previous system. The scattering angle is 28 degrees, which is sufficient to separate proton peaks that are scattered from hydrogen and from other elements, even in the thickness of 50 μm of organic films.

For the in-air system, on/off axis STIM for simultaneous density mapping with PIXE and RBS is newly available. It will be useful for damage monitoring in biological cell analysis and for correction of X-ray self-absorption in samples. A thin scattering foil (C or Al) is placed ~20 mm downstream of the sample. Scattered protons are detected by a Si-PIN photodiode which is set at 28 degrees with respect to the beam axis. The detector is well collimated to reduce energy broadening by kinematics.

A compact secondary electron detector is newly installed for secondary electron imaging (see Fig. 1). In the previous system, secondary electrons were detected by a plastic scintillator with a photomultiplier. The detector was not compact, and was therefore not able to cooperate with other detector systems. A compact ceramic channel electron

multiplier (CEM, MD-502; Amptek Inc.) is very compact (1.9 cm diameter×3.8 cm long) and is not obstructive to other detector systems.

Microbeam system performance

After the installation, performance of the system was tested by a micro-PIXE analysis for a Cu mesh (1000 lines/inch). The lower limit of the beam spot size was 2 μm, which is much larger than the design value[4]. The main reason for the limitation is parasitic field contamination from microbeam line components. Especially, the tungsten carbide slit chips cause strong field contamination. X-ray maps from Cu mesh (1000 lines/inch) measured with the baffle slit open and with the baffle slit closed are shown in Fig. 2. Although the mesh image was clearly apparent when the baffle slit was opened, the beam was defocused and was shifted when the baffle slit was closed. This is an effect of parasitic field existing at the baffle slit. The baffle slit has no an electric driving mechanism which might cause electric or magnetic fields. Two of the slit chips used in the baffle slit were magnetized strongly and attracted paper clips. The field contamination was therefore ascribed to the tungsten carbide slit chips. This magnetism is caused by cobalt element that is used as a binder in the slit chip. Although the tungsten carbide itself is not magnetized, cobalt shows strong magnetism and is magnetized easily[13]. The slit chip contains about 10% cobalt. The magnetization arises from manufacturing processes and should be eliminated. Finally, the slit chips of the divergence-defining slit and the baffle slit, whose parasitic field strongly affects microbeam formation, were replaced by the other chips whose elemental concentration of cobalt is less than 10% that of previous chips. After replacement of the chips, defocusing and beam shifting do not occur in any slit position.

Effects of parasitic field contamination was measured using the grid-shadow method[5]. In the grid shadow method, the beam is focused on the image plane, where a fine mesh grid is placed, by a single quadrupole lens and casts shadow pattern on a scintillator downstream. The shadow pattern is influenced strongly by lens aberrations and parasitic field contaminations of the microbeam system. In the present study, a Au mesh (2000 lines/inch) was placed on the image plane and a shadow pattern was obtained on a ZnS(Ag) scintillator located 53 mm downstream of the grid. The sensitivity of the grid shadow method is also increased by reducing the angle between the divergence axis of quadrupole and the grid bar. Smaller angles produce fewer grid bar shadows and higher sensitivity, especially for higher order field contamination. In this study, we set the angle as 1.75

degrees. Figure 3 shows theoretical grid shadow patterns with 0–0.2% sextupole field contamination superimposed onto the quadrupole field calculated by the beam optics computer codes, PRAM and OXTRACE[3], with identical beam conditions. The theoretical shadow pattern shows that the minimum detectable limit corresponds to approximately 0.05% for sextupole field contamination. Figure 4 shows the measured grid shadow patterns for the two quadrupole lenses with a 3 MeV proton beam. The beam is screened by the beam scanner in the divergence plane. Therefore, the number of grid bars is fewer than the theoretical pattern. Although measured shadow patterns in the horizontal focus show slight deformation resulting from sextupole field contamination, shadow patterns in the vertical focus are not deformed. Both lenses show a similar trend. In comparison with the calculated results, sextupole field contamination in the horizontal focusing is estimated as less than 0.1%. Contamination of the skew sextupole field is less than 0.1%. Therefore, it is difficult to observe deformation in the measured pattern, which implies that sextupole field contamination in the horizontal plane (skew sextupole field contamination in the vertical plane) remains. This contamination source might be the lens itself or another part of the microbeam line. One possibility is that the cancellation of excitation current of the quadrupole is not perfect. This lens was designed so that the excitation current from pole to pole is canceled by the return current. However, no cancellation is made in the upper part of the lens where terminals exist. Because the coils consist of only 22 turns, such effects might cause the problem. To reduce the effect of the contamination field, the 1st quadrupole uses horizontal focusing and the 2nd lens uses vertical focusing (divergence-convergence); the scanner is located downstream.

Then, the beam spot size was measured by scanning the beam across mesh samples (Ni and Au mesh, 2000 lines/inch) and measuring X-rays. Horizontal and vertical line profiles were fitted by symmetric double Gaussian convolution and beam spot sizes were obtained. The line profiles were well reproduced using the symmetric double Gaussian convolution, which implies that the beam profile can be assumed to be of Gaussian shape. Figure 5 shows horizontal and vertical beam spot sizes versus object sizes. These measurements were carried out in the same beam divergence of 0.2 mrad which corresponded to our normal divergence in the high-current regime for ion beam analyses. Beam spot sizes diminished concomitant with the object slit sizes and were better than those that were predicted from the calculation. A spot size of 0.4×0.4 μm^2 was obtained at an object size of 30×10 μm^2 with a beam current of several tens of pA. Beam size estimations

using the deconvolution method are strongly dependent on the mesh quality and are sometimes overestimated in the range less than 1 μm because we assume the mesh edges to be very sharp. The cross sections of mesh grid bars are trapezoidal or round to some degree. Therefore, the beam spot size will be better than 0.4×0.4 μm^2. Figure 6 shows secondary electron images of Ni mesh (1000 lines/inch) measured using an electron microscope and the microbeam system with object size of 25×10 μm^2 and beam divergence of 0.2 mrad. The secondary electron image measured using the microbeam system clearly represents the steps of the bars and round shape of the corner, which corresponds to the image obtained using the electron microscope. This fact shows that resolution of better than 0.4 μm is obtained and is consistent with that obtained using deconvolution method. These measurements were carried out with the divergence of 0.2 mrad for the high-current regime. The result of the grid shadow implies that a better beam spot size will be obtained in a low-current regime where the object size and beam divergence are one-tenth lower.

Even in the same beam condition mentioned above, the beam spot size of 1 μm is a lower limit in the actual experimental setup where X-ray detectors, RBS detector, and other detectors are set in a chamber. The grid-shadow method revealed the source of this problem. The grid-shadow patterns in this situation are shown in Fig. 7. Strong sextupole or higher order field contamination are observed. By removing the annular Si surface barrier detector (TC-019-150-100; Ortec) positioned 40 mm upstream of the sample position, field contamination was eliminated. The grid-shadow pattern in Fig. 7 was measured without applying bias voltage to the annular detector. The holder of the annular detector is made of plastic, which adds no field. Therefore, the parasitic field was ascribed to the magnetic field of the annular Si surface barrier detector itself. In fact, the annular detector imparted a field strength of ~10 μT, as measured using a magnetometer. Elements that show strong magnetism are used in the detector body. The RBS detector was replaced by another annular ion-implanted Si detector (ANPD 300-19-100RM; Canberra). The detector gave a weaker magnetic field, which was also measured using a magnetometer. Following change, the field contamination of the system was reduced to a normal level and performance of the microbeam system was improved greatly, even in the actual analysis. Components that must be set near the beam path should have their magnetism eliminated; the grid shadow method is very effective to clarify the source of parasitic field.

Conclusion

A microbeam system was constructed at the Tohoku University Dynamitron laboratory and optimization of the system was undertaken. Minimum beam spot size of the microbeam was limited at 2×2 μm^2 by parasitic field contamination. This parasitic field contamination was ascribed to the tungsten carbide slit chips and the annular Si surface barrier detector in the case of RBS analysis. The parasitic field contamination of the system was greatly reduced by replacing these components, as confirmed by the grid shadow method, and the microbeam system performance was improved. The minimum beam spot size of 0.4×0.4 μm^2 at a beam current of several tens of pA is obtained, which is the optimum expected from the accelerator performance. The results obtained using the grid-shadow method indicate that a beam spot size of less than 0.4 μm is obtainable in the low-current regime.

While improving the microbeam system, simultaneous in-air/in-vacuum PIXE, RBS, SEM, and STIM analyses, in addition to 3D μ-CT, were developed and are now being applied to biological, environmental, and other fields.

Acknowledgements

This study was partly supported by Grants-in-Aid for Scientific Research, (S) No. 13852017, (B) No. 18360450, (C) No. 16560731, and a Grant-in-Aid for Scientific Research in Priority Areas under Grant No. 14048213 from the Ministry of Education, Culture, Sports, Science and Technology, Japan. The authors would like to thank Prof. Jamieson D.N. of the University of Melbourne, for his valuable suggestions and advice in reducing field contamination and introducing the PRAM and OXTRACE computer codes. The authors would like to acknowledge the assistance of Mr. Sakamoto R. R. and Fujisawa M. for maintenance and operation of the Dynamitron accelerator. The authors would like to thank Mr. Komatsu K., Nagaya T. and Akama C. for their assistance in constructing the microbeam and target system.

References

1) Watt F. and Grime G.W., Principal and Applications of High-energy Ion Microbeams, Adam Hilger, Bristol, 1987.
2) Johansson S.A.E., Campbell J.L. and Malmqvist K.G., Particle-Induced X-ray Emission Spectrometry (PIXE), John Wiley and Sons, N.Y., 1995.
3) Breese M.B.H., Jamieson D.N., and King P.J.C., Materials Analysis using Nuclear Microprobe, John Wiley and Sons, N.Y., 1995.

4) Matsuyama S., Ishii K., Yamazaki H., Sakamoto R., Fujisawa M., Amartaivan Ts., Ohishi Y., Rodoriguez M., Suzuki A., Kamiya K., Oikawa M., Arakawa K., and Matsumoto N., Nucl. Instr. and Meth., **B210** (2003) 59.
5) Jamieson D. N. and Legge G. J. F., Nucl. Instr. and Meth. **B29** (1987) 544.
6) Matsuyama S., Ishii K., Yamazaki H., Barbotteau Y., Amartaivan Ts., Izukawa D., Hotta K., Mizuma K., Abe S., Oishi Y., Rodriguez M., Suzuki A., Sakamoto R., Fujisawa M., Kamiya K., Oikawa M., Arakawa K., Imaseki H., and Matsumoto N., Int. J. of PIXE, **14** (1&2) (2004) 1.
7) Matsuyama S., Ishii K., Abe S., Ohtsu H., Yamazaki H., Kikuchi Y., Amartaivan Ts., Inomata K., Watanabe Y., Ishizaki A., Barbotteau Y., Suzuki A., Yamaguchi T., Momose G., and Imaseki H., Int. J. of PIXE, **15** (1&2) (2005) 41.
8) Matsuyama S., Ishii K., Yamazaki H., Kikuchi Y., Amartaivan Ts., Abe S., Inomata K., Watanabe Y., Ishizaki A., Oyama R., Kawamura Y., Suzuki A., Momose G., Yamaguchi T., and Imaseki H., Int. J. of PIXE, **15** (3&4) (2005) 257.
9) Ishii K., Matsuyama S., Yamazaki H., Watanabe Y., Yamaguchi T., Momose G., Amartaivan Ts., Suzuki A., Kikuchi Y., and Galster W., Int. J. of PIXE, **15** (3&4) (2005) 111.
10) Ishii K., Matsuyama S., Yamazaki H., Watanabe Y., Kawamura Y., Yamaguchi T., Momose G., Kikuchi Y., Terakawa A., and Galster W., Nucl. Instr. and Meth. **B249** (2006) 726.
11) Ishii K., Matsuyama S., Watanabe Y., Kawamura Y., Yamaguchi T., Oyama R., Momose G., Ishizaki A., Yamazaki H., and Kikuchi Y., submitted to Nucl. Instr. and Meth. B.
12) Deves G., Matsuyama S., Barbotteau Y., Ishii K., and Ortega R., Rev. of Sci. Instr., **77** (2006) 056102.
13) Penrice T. W., Int. J. of Refractory Metal and Hard Materials, **15** (1997), 113.

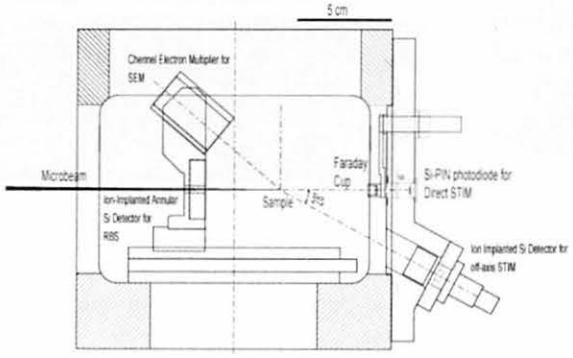

Figure 1. Side cut view of the target chamber.

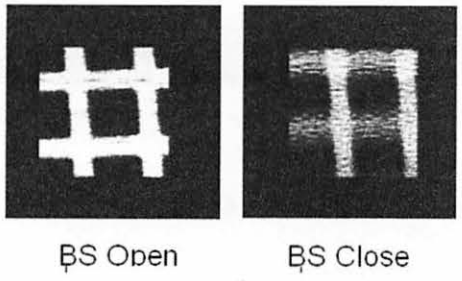

Figure 2. Elemental distribution maps from Cu mesh (1000 lines / inch) measured with the baffle slit open and with the baffle slit closed.

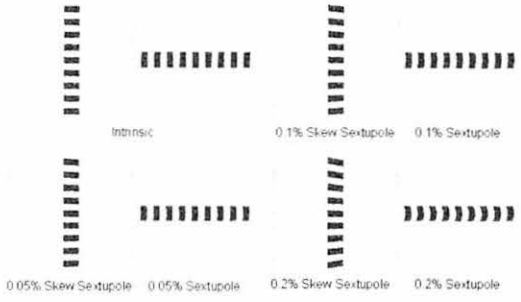

Figure 3. Theoretical grid shadow patterns calculated by PRAM and OXTRACE.

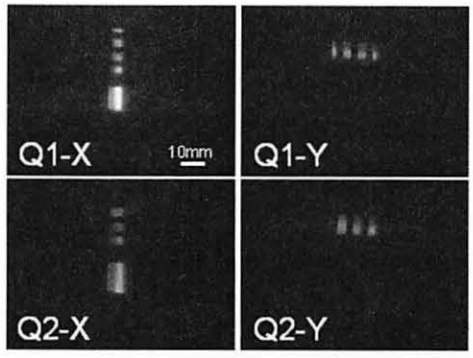

Figure 4. Measured grid shadow patterns of the two quadrupole lenses for vertical (*X*) and horizontal (*Y*) focusing.

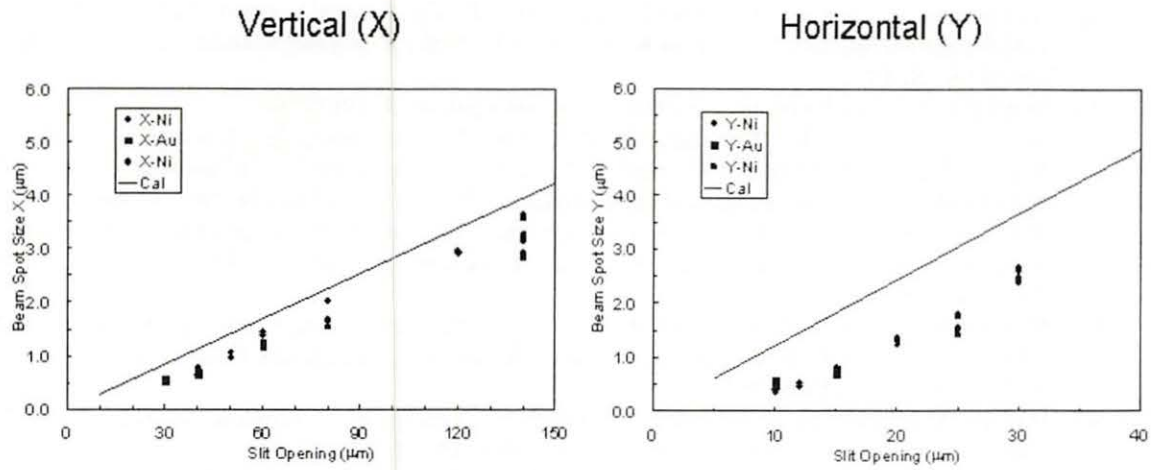

Figure 5. Horizontal and vertical beam spot sizes versus object sizes.

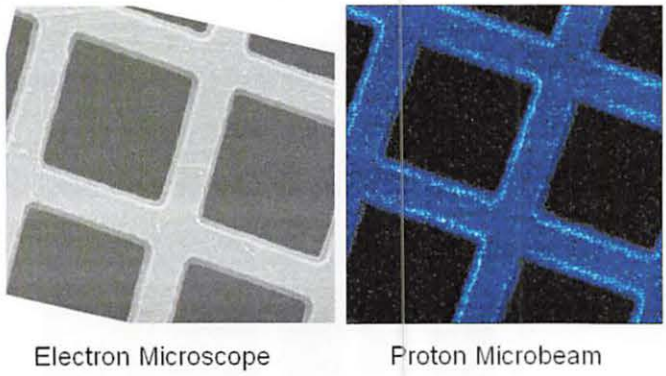

Figure 6. Secondary electron images of Ni mesh (1000 lines/inch) measured using an electron microscope and the microbeam system.

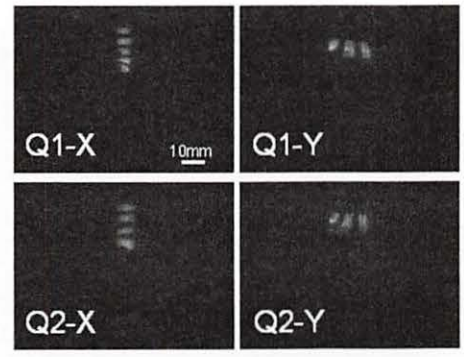

Figure 7. Measured grid shadow patterns with a parasitic field from the annular detector.

V. 2. μ-CT Images of the Egg of Drosophila

Okura S.[1], Ishii K.[1], Matsuyama S.[1], Yamazaki H.[2], Terakawa A.[1], Kikuchi Y.[1], Fujiwara M.[1], Kawamura Y.[1], Tsuboi S.[1], Yamazaki K.[1], Watanabe M.[1], and Fujikawa M.[1]

[1]*Department of Quantum Science and Energy Engineering, Tohoku University*
[2]*Cyclotron Radioisotope Center, Tohoku University*

Introduction

The technology to observe cells in a living body such as a cloning technology and a gene therapy is in progress in the field of biology and medicine. It is very important to develop a drug for a gene therapy and the production of organs for transplant. To observe the cell, one needs a device that can enlarge a microscopic area in the cell (e. g., microscope). For this purpose, we are developing a 3 dimensional micro computed tomography (3D μ-CT) which enables to observe the interior of living small insects[1-5]. The 3D μ-CT uses monoenergetic low-energy X-rays produced by bombarding a target with proton microbeam. Therefore, the contrast of the image for small insects is superior to that of other CT systems which uses continuous X-rays. Furthermore, our system can readily change the X-ray energy to obtain a better contrast depending on the elements contained in the insects[1-4]. In this study, we applied the μ-CT to the egg of drosophila, since the drosophila is used to various basic studies, such as gene research.

μ-CT system using micro-PIXE

The 3D μ-CT comprises a monoenergetic μ-X-ray source, a rotating sample stage and a high-speed X-ray CCD camera. Its technical details were written in Ref. 1. In this system, a sample is encapsulated in a polyimide tube with atmospheric pressure and placed on the rotating stage. This tube is rotated by a stepping motor. An X-ray producing target is set at 30 ~ 45 degrees with respect to the horizontal axis and produces a cone beam of X-ray by microbeam bombardment. In this study, 2.4 MeV proton microbeams were used. The exposure of CCD is begun by an outside trigger and stops when a total beam

charge reaches a constant value; readout of data finishes while the target rotates. A 100 μm Mylar film is placed in front of CCD to prevent recoil protons from entering CCD. 2D transmission data is obtained by the cone beam. 3D image is reconstructed on the basis of an iteration method (Maximum Likelihood-Expectation Maximization method)[5].

Results and discussion

Figure 2 shows the photograph of imagoes and eggs of drosophila melanogaster (Oregon-R). The eggs of drosophila incubate in 24 hr. Considering breeding and measuring times, we used an egg, which was laid 12 hr ago, encapsulated in a polyimide tube (inside diameter of 500 μm and wall thickness of 25 μm). Figure 3 shows the photograph of the tube with the egg. To prevent the egg to dry out, the gelatin was inserted together. The inside is kept in atmospheric pressure with appropriate moisture. Under this treatment, we confirmed that the egg is alive and incubates in the tube[3].

To obtain CT images with a good contrast, The X-ray producing target should be selected in consideration of absorption coefficient of the egg and detection efficiency of the CCD camera. Figure 4 shows the comparison of projection images of an egg for various X-ray targets. It is apparent that the result of Sc target shows the highest contrast.

Figure 5 shows the cross sectional views of the egg; the left figure shows the longitudinal cross sectional view and the other is the vertical view. The experimental conditions are summarized in Table 1. The interior of the egg is uniform. It seems that the egg has grown during the measurement. To confirm this, the cross sectional images reconstructed from the first half and the latter half data in a series measurement are shown in Fig. 6. It is apparent that the shape of the egg changes because of the growth.

CT images of a dried egg were obtained. The egg which was laid about 22 hr before was encapsulated in the tube and was kept for 4 months to dry. Figure 7 shows the cross sectional view and the 3D image of the dried egg. The shell and the interior structure are observed. We recognize a large difference between the image of the dried egg and that of the living egg. It is considered that organs in the living egg have moved thus the interior of the living egg is uniformly seen.

In the previous study, the images of the ant's head fixed by formalin and the one of the living ant's head were compared[3]. There was a difference between them. In the case of the fixed ant, the brain shrank and something was washed out due to formalin-fixation. In the case of the living ant, the interior was uniform. The situation is similar to the

present result.

Conclusion

The CT images of the egg of drosophila were obtained by using the μ-CT. The interior of the living egg was uniform. In the case of the dried egg, the shell and the interior structure were confirmed. It is considered that the living egg has grown during the measurement. The measurement time of 3.5 hr is long enough to change the shape of the living egg because the eggs of drosophila incubate in 24 hr. Therefore, the intensity of the X-ray has to be increased.

Acknowledgements

This study was supported by 21 COE Program "Future Medical Engineering based on Bio-nanotechnology" and a Grant-in-Aid for Scientific Research (S) No. 13852017 (Ishii K.) of the Ministry of Education, Culture, Science, Sports and Technology.

Table 1. Experiment condition (living egg).

X-ray target	Sc
Target angle with respect to the horizontal axis	45°
Beam particles	2.4 MeV protons
Beam spot size	1.33 × 1.00 μ^2m
The number of projection images	250 (250 images/rotation)
Measurement time	12660 sec (about 3.5 hours)

Table 2. Experiment condition (dried egg).

X-ray target	Sc
Target angle with respect to the horizontal axis	30°
Beam particles	2.4 MeV protons
Beam spot size	1.1 × 1.1 μ^2m
The number of projection images	500 (500 images/rotation)
Measurement time	9480 sec (about 2.6 hours)

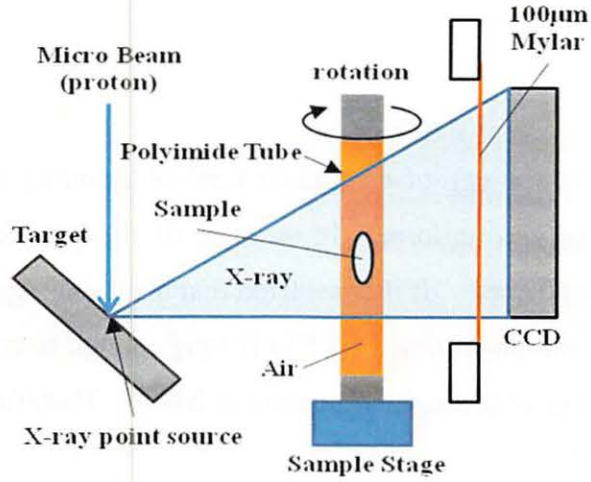

Figue 1. Principle of μ-CT.

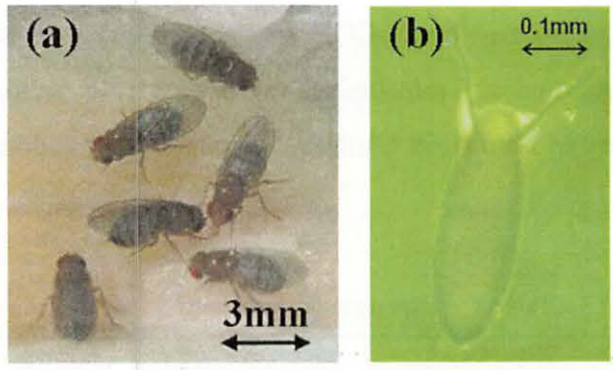

Figure 2. Imagoes of drosophila melanogaster (Oregon-R) (a) and, egg of drosophila (b) observed with an optical microscope.

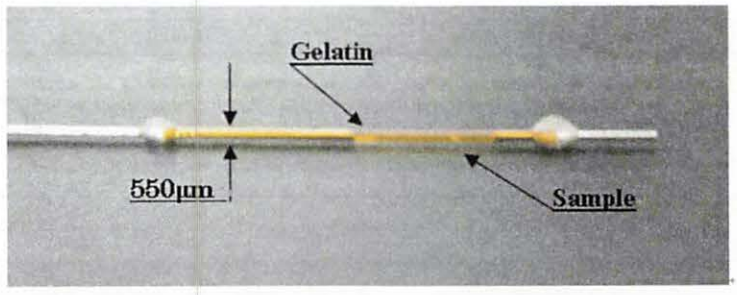

Figure 3. Sample assembly.

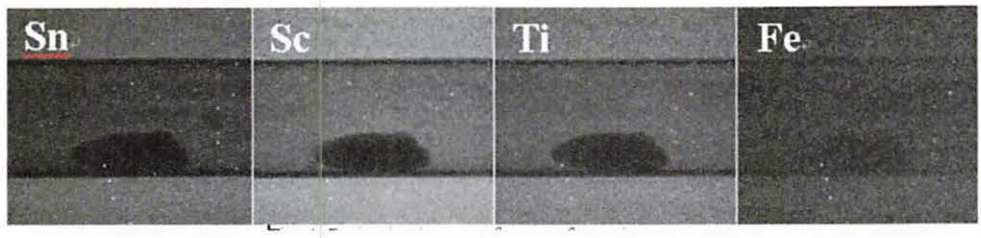

Figure 4. Projection images of an egg for various targets.

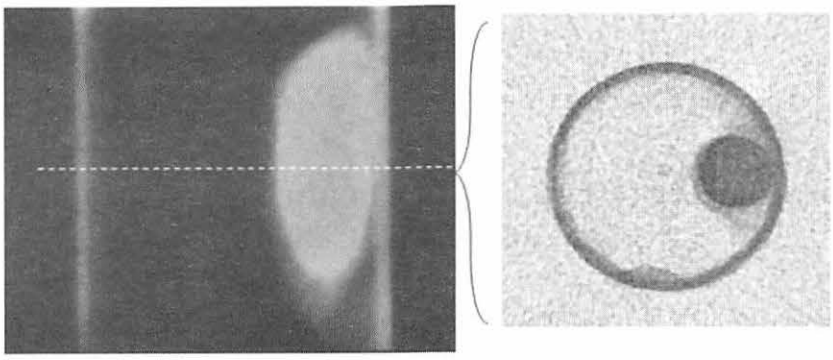

Figure 5. Cross sectional views of the egg (left : longitudinal view, right : vertical view).

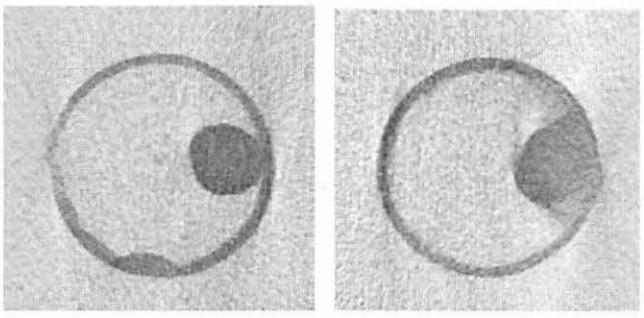

Figure 6. Vertical cross sectional view of the egg (left image is reconstructed from the first half date, right image is reconstructed from the latter half date).

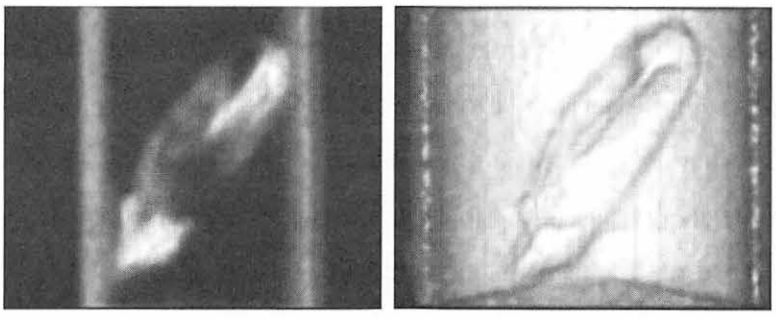

Figyre 7. CT images of the dried egg (left : longitudinal cross sectional view, right : 3D image).

V. 3. Measurement of Elemental Distributions in Mouse Brain by Using Submilli-PIXE Camera

Fujiki K.[1], Matsuyama S.[1], Ishii K.[1], Yamazaki H.[2], Terakawa A.[1], Kikuchi Y.[1], Fujiwara M.[1], Kawamura Y.[1], Okura S.[1], Fujikawa M.[1], Catella G.[1], Hashimoto Y.[2], Hatori Y.[1], Hamada N.[1], Sakurai E.[3,4], and Yanai K.[3]

[1]*Department of Quantum Science and Energy Engineering, Tohoku University*
[2]*Cyclotron Radioisotope Center, Tohoku University*
[3]*Department of Pharmacology, Tohoku University*
[4]*Department of Pharmacology, Iwaki Meisei University*

Introduction

In a biological body, it is well known that trace elements including metallic elements play important roles such as component of hemprotein, detoxication, methabolism and so on. Therefore, knowing their spatial distribution and amounts, we can find out the relation among a physiological role of the trace element *in vivo*, the function, and the disease appearance. We have been analyzing the mouse brain in cell level by using micro-PIXE. In this research, we administered 5'-bromodeoxyuridine (5-BrdU) that was the analogue of the thymidine as a marker to detect a new born cell. 5-BrdU is taken into new born cells in especially the dentate gyrus of the hippocampus where the neuronal cell appears newly in the brain[1]. Because of this, we made mental disease model mice, and investigated the difference of the element distribution in comparison to control mice. We administered Methamphetamine (METH) to mice to make mental disease model. METH is a kind of a typical stimulant. A stimulant acts on a central nerve of a brain, and causes various impaired consciousness, hallucinatory disorder, and the deterioration of memory. The stimulant mental disease is assumed to be a model with animal's schizophrenia[2]. Averaged elemental concentrations of Ca, Fe and Zn over the brain of the mice to which Methamphetamine (METH) had been administrated were higher than those of control mouse. On the other hand, elemental concentration of Br of subject mouse was lower[3].

Due to these facts we needed to investigate, not only the cell level but more wide-ranging images over the brain. In this study, we investigated a method to obtain

elemental distributions in whole brain slice taken from the subject mice, using in-air submilli-PIXE camera at a Dynamitron laboratory of Tohoku University[4,5]. The submilli-PIXE camera is able to measure elemental distribution in the region of several cm^2 with a resolution of submilli-meters.

Sample Preparation

We prepared four mice in this study. Seven weeks old male C57BL6 mice were obtained from the Japan SLC (Hamamatsu, Japan). METH was administered intraperitoneally at a dose of 1 mg/kg/day to the mice, following the schedule as shown in Fig. 1. Saline was injected intraperitoneally to the control mice. 5-BrdU was administered 50 mg/kg to the mice intraperitoneally for 5 consecutive days, as shown in Fig. 1, before the brain was taken out.

After the brain was taken out, it was quickly frozen with dry ice, and it was sliced by a cryomicrotome. While the thickness of the slice is 16 μm in micro-PIXE analysis to get elemental distributions in a single cell, thicker slice is appropriate in this application. In this study, the slice thicknesses were 50, 100 and 200 μm. Thickness of 200 μm is the maximum in our cryomicrotome. The brain slices were put on a Myler film of 2 μm-thickness and dry-fixated on it. The 2 μm-thickness Mylar film used in this study contains less amount of Br compared to the polycarbonate film which is used in the micro-PIXE analysis.

Experiments

Analysis was carried out by using in-air PIXE camera at Tohoku University. Proton beams of 3 MeV were extracted into air through a kapton film of 12.5 μm and irradiated on the target. Samples were fixed to the target holder, and set just after the beam exit window. X-rays were detected two Si(Li) detectors[4,5]. Beam was scanned ca. 10×10 mm^2 on a surface of samples, which covered whole brain slice. Average beam current was around 3 nA and total accumulated charge was around 20-40 μC.

Figure 2 shows a typical photo and elemental images of mouse brain to which METH was administered. Figure 3 shows those of control. Figure 4 shows X-ray spectrum of a sample. Elemental images were produced by using GeoPIXEII software[7]. Brain contains a lot of light elements, such as P, S, Cl and K, which were uniformly distributed over the brain. Brains also contain Fe, Cu, and Zn as a indispensable element.

As shown in Fig. 4, Fe is accumulated in the specific area. Elemental concentration in the area was 10 times higher than that in the other. While some other samples from the subject mice showed similar tendency, accumulation of Fe was not observed in those of control mice. It is suspected that a part of neuronal cells were poisoned by an excitatory action of METH. The similar symptom appears to Alzheimer's disease etc.[4] Zn is accumulated in the vicinity in hippocampus and the side of the brain as shown in Figs. 2 and 3. Other samples showed similar tendency too. Since Zn in neuronal cells of hippocampus is indispensable element to transmit information, it might be related to their activity[5]. Cu is accumulated in the vicinity in third ventricle as shown in Fig. 3. Bromine is uniformly distributed over the brain in all samples.

Conclusion

In order to know the relation among a physiological role of the trace element *in vivo*, the function, and the disease appearance, investigation not only on the cellular level but also on the organ level was carried out. In this study, we investigated a method to obtain elemental distributions in whole brain slice taken from the subject and control mice, using in-air submilli-PIXE camera. Sample thickness more than 200 μm is appropriate in this study. We obtained the elemental distributions of the whole brain of the mice of mental disease model and control mice. Trace elements such as Fe and Zn are accumulated in the brain. Elemental concentration in the area where Fe was accumulated is 10 times higher than that in the other. The accumulation was not observed in the brain of the control mice. It is suspected that a part of neuronal cells were poisoned by an excitatory action of METH. Zn is accumulated in the vicinity in hippocampus. Br was uniformly distributed over the brain for both the administrated and the control mice. In this study, we could obtain the elemental distributions of whole brain slices. The submilli-PIXE camera will provide a powerful tool for this research.

Acknowledgement

We would like to thank Messrs. Sakamoto R. and Fujisawa M. for maintenance and operation of the Dynamitron accelerator.

References

1) Luo C., Xu H., Li X.-M., Brain Res, **1063** (2005) 32.
2) Kubota Y., Ito C., Sakurai E., Watanabe T., Ohtsu H., I J. Neurochem, **83** (2002) 837.
3) Sakurai E. et al., JAEA-review **2008** (2009) 111.
4) Lovell M. A. et al., J Neurol Sci, **158** (1998) 47.
5) Takeda A., Zinc and brain function, Clinical Examination, **53** (2009) 197.

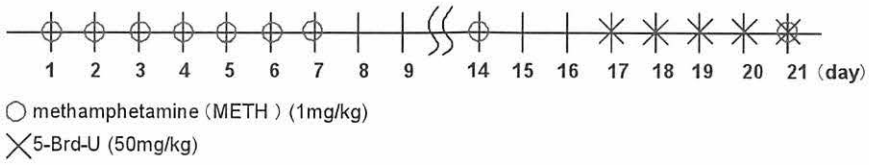

Figure 1. Schedule of administration.

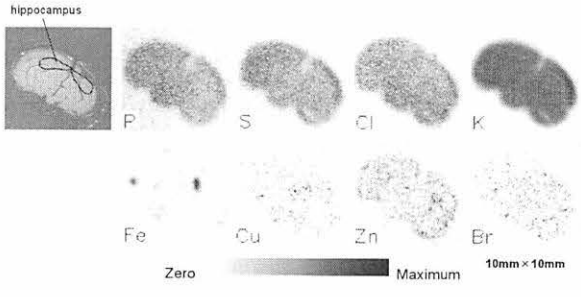

Figure 2. Photo and elemental distributions of the brain of subject mouse.

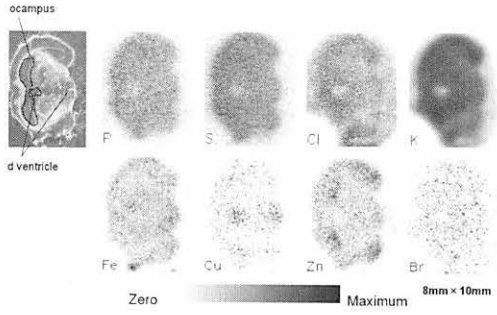

Figure 3. Photo and elemental distributions of the brain of control mouse.

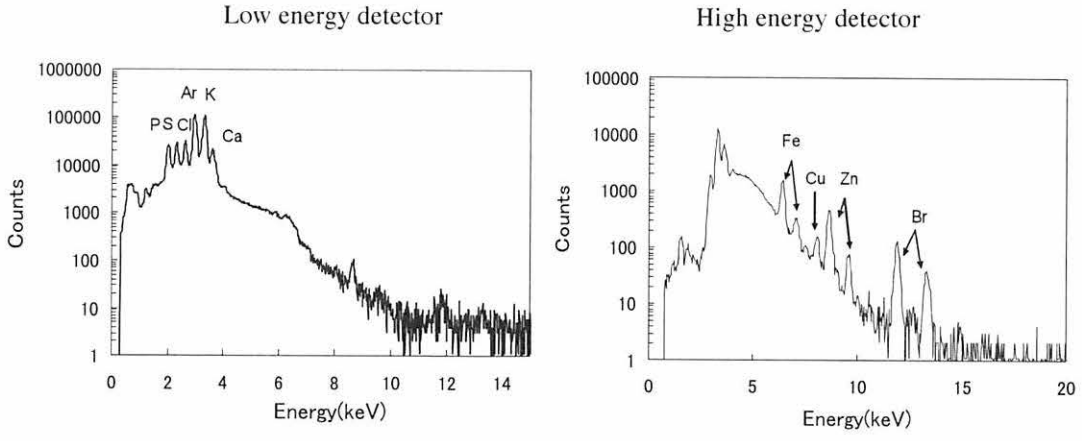

Figure 4. Typical X-ray spectra from a mouse brain slice by the detector for Lowand High energy. Total accumulated charge was 38 μC.

V. 4. 3D Imaging of Human Cells by Using PIXE-μ-CT

Kawamura Y.[1], Ishii K.[1], Matsuytama S.[1], Nakhostin M.[1], Fujiwara M.[1], Watanabe M.[1], Okura S.[1], Hamada N.[1], Tsuboi S.[1], Yamazaki K.[1], Hashimoto Y.[1], Fujikawa M.[1], Catella G.[1], Hatori Y.[1], Fujiki K.[1], Yamazaki H.[2], Ortega R.[3], Deves G.[3], and Carmona A.[3]

[1]*Department of Quantum Science and Energy Engineering, Tohoku University*
[2]*Cyclotron Radioisotope Center, Tohoku University*
[3]*CNAB, CNRS Universite Bordeaux 1*

Introduction

Numerous studies have shown that short-term exposure to particulate matter (PM) can adversely affect human health. For chromium compounds, the main route of exposure is via the respiratory tract by inhalation of dusts, fumes and mists. Human tissues and fluids normally contain low levels of chromium as essential element, but chromium abundance in lung tissues is increased as a result of environmental or occupational exposures and is highly carcinogenic. Some studies were carried out to know the interaction between these particles and human body at a cellular level by using the micro-PIXE/RBS and synchrotron X-ray fluorescence microprobe[1-3]. While the mechanism was suggested in these studies, distribution of chromium particles in the cell is still uncertain because 2D imaging only gives a projection image of the distribution. The 3D distribution of the chromium particles in the cell will give us crucial information on the suggested intracellular interaction mechanism between the particles and human cells. Only few imaging techniques exist that allow *in-situ* quantification and distribution of chromium particles in cell[4]. We are developing a 3D PIXE-μ-CT to observe the interior of small samples with a spatial resolution of less than 10 μm[5-10]. The 3D PIXE-μ-CT has a capability to measure intercellular distribution of Cr particles and is one of the most powerful tools. However, our system has to be optimized to observe the small structures inside a single cell. In this study, we report the 3D μ-CT for intercellular imaging and obtained the intracellular distribution of chromium compound ($PbCrO_4$).

Improvement of 3D μ-CT

The PIXE-μ-CT consists of an accelerator, a proton microbeam system, and a target chamber system equipped with X-ray CCD camera[5-10]. In the PIXE-μ-CT configuration, the X-ray point source and the X-ray CCD are fixed while the sample is placed between them is rotated. In this system, 2D X-ray projection data are obtained for each rotation angle of the sample and therefore a 3D image can be reconstructed. X-ray generated with this system consists mainly of characteristic X-ray of target element which is quasi-monoenergetic[11]. These properties allow getting a high-contrast imaging of cells which makes the system suitable for this biological samples analysis as exemplified in insect studies[7-10].

For intracellular imaging, higher contrast and higher spatial resolution are required in the PIXE-μ-CT system. For this purpose, we have taken the following steps. First, to improve the contrast of CT images, we selected an appropriate X-ray producing target. Second, to obtain higher spatial resolution projection image, we investigated cone beam magnification geometry and also, the precision of sample rotation was improved.

Improvement of the Contrast

In order to visualize microscopic biological sample like cells using PIXE-μ-CT, high contrast X-ray transmission data is needed. Considering the X-ray transmission of the cell and detection efficiency of the CCD camera, X-ray energy of 3 to 5 keV is appropriate for this study. This can be achieved by employing scandium as target.

Improvement of the CT image resolution

In PIXE-μ-CT system, the projection data of the sample is taken by using cone beam magnification geometry. Therefore, the spatial resolution of the CT image is affected by the following two parameters, effective pixel size and blur of the projection data. These parameters are strongly affected by the finite focal spot size and the magnification factor. For the ideal X-ray source that can be considered to be point source, we can obtain higher resolution images as the magnification increases. As shown in the following equation, the image resolution is improved by increasing the magnification:

$$r_{CCD} = \frac{2 \times pixelsize}{m} \qquad (1)$$

where r_{CCD} is the effective pixel size in the object plane and *pixelsize* is the CCD pixel size

(=8 μm) in the image plane and m is the magnification. The magnification was restricted to around 4 to 5 in previous studies[7-10] because of finite sample size and the finite size of CCD. In this study, cell sample is smaller than those used in the previous studies, thus we can obtain better resolution by increasing magnification. However, actual projection data is affected by blurring that surrounds an object. This causes the edge to be reproduced with an optical density gradient by the imaging system. The extent of the blurring is related to the focus size and magnification:

$$Blur = (m-1) \times f \tag{2}$$

where f is the focal spot size. The shape of sample is estimated by the image data projected to the detector screen. Therefore, the spatial resolution distorted by the finite focal spot is as follows:

$$r_{blur} = Blur / m = \frac{(m-1) \times f}{m} \tag{3}$$

Figure 1 shows the relationship between the detector sampling pitch and the image blurring with respect to the magnification. In general, at lower magnification the detector sampling pitch is a limiting factor of the resolution; at higher magnification the blurring caused by focal spot becomes critical for the resolution. In addition, there is an optimal magnification for each focal spot size. In previous study, we obtained the spatial resolution of 4 μm at a magnification of nine with a beam spot size of 1.5×1.5 μm. However, the resolution was worse than the calculated value. This was due to the fact that, in that calculation, the focal spot size was not considered. Thus the calculated resolution was less than the actual one. The present estimation is quite consistent with the experimental results. It shows that resolution will improve as an increase of the magnification and will saturate down to the beam spot size.

Figure 2 shows the CT image of a polyimide tube (inner diameter of 80 μm, wall thickness of 10 μm) and the intensity profile of CT-value, acquired in a condition corresponding to a proton beam energy of 3 MeV, proton beam spot size of 1.1×1.1 μm^2 and magnification of 12.4. The measured profile was fitted by symmetric double Gaussian convolution to obtain the spatial resolution of the system. The resolution of the system was evaluated to be around 3.4 μm, which is consistent with the estimation.

Sample preparation

In this study, we analyzed human epithelial cells exposed *in vitro* to $PbCrO_4$.

Fixation of the cells on the rotating shaft is one of the biggest problems in this study. A micro polycarbonate tube (MicroLumen 030-I; 80 μm inside diameter and 10 μm thickness) was used to fix the cells. The tube is the smallest and thinnest commercially available. Since size of the cell is in the order of 10 to 20 μm, tube thickness is almost same order and not deteriorates the contrast. The cells were fixed in the inner wall of the tube. Then the end of the tube is inserted into the injection needle, and then fixed to rotation shaft. We adopted cryogenic methods to fix the cell in the tube, since they consist of immobilizing the intracellular components by cryofixation and later extraction of the water by freeze drying process. The protocol is almost the same as that for SXRF and PIXE analysis[3], except for encapsulate process. Capillary action was used to insert the cell into the tube. After that, the tube was sealed with formvar and cryofixed at -164°C into isopentane chilled with liquid nitrogen. Then the sample was freeze dried at -35°C for 1 week after removing the seal.

Result and Discussion

Human epithelial cells exposed *in vitro* to 1 μm/cm^2 $PbCrO_4$ for 24 h were analyzed by using the PIXE-μ-CT. Measurement was carried out with 3 MeV proton beam, beam currents of ca. 400 pA, beam spot size of 1.1×1.1 μm^2. Geometric magnification was 12.4. X-ray target is Sc and target was set at 30 degrees with respect to the beam direction. Figure 3 shows the 2D cross sectional view of cell and line profile of pixel value. The image was reconstructed on the basis of image data in the vertical plane by using an iteration method (Maximum Likelihood-Expectation Maximization method). The pixel value of micro tube and cell is different showing a good contrast. While cell density will be similar to that of the tube, higher absorption of X-ray by $PbCrO_4$ particles increased the absorption in the cell. Figure 4 shows the 3D imaging of human epithelial cells from the different angles. The size of the cells is around 20 μm and consistent with microscopic images. The region marked with arrow in the right figure, could be a cell which did not absorb, or absorbed less $PbCrO_4$ than the others. The pixel value is almost same as that of the tube. The region which shows strong absorption means the $PbCrO_4$ particles. Two kind of distribution are seen; one is distributed over the cell area, the other is concentrated in small structures within the cell.

Conclusion

The CT images of the human epithelial cells were obtained by using the PIXE-μ-CT. To observe the microstructure of sample, we improved the existing system. For the image contrast, Sc was selected as an X-ray target and obtained a good contrast of cell projections. For the image resolution, the rotating stage was improved and the magnification geometry was optimized. Thus intracellular distributions of the lead chromate particles could be observed. The PIXE-μ-CT will give us the crucial information on the interaction between the particulate matter and human cells indicating that lead chromate is internalized and that is distribution is both diffused within the all cell volume, and located in small structures inside cells. This result is consistent with the suggested mechanism of action of lead chromate[3] which can be partially soluble in cells, explaining the diffuse distribution, and partially insoluble, explaining the high local concentration within intracellular structures.

Acknowledgements

This study was partly funded by a Grants-in-Aid for Scientific Research, (S) No. 13852017 from the Ministry of Education, Culture, Sports, Science and Technology, Japan. This study was also supported by JSPS and MHEST under the Japan-France Research Cooperative Program (Partenariat Hubert Curien - SAKURA Project).

The authors would like to acknowledge the assistance of Fujisawa M. for maintenance and operation of the Dynamitron accelerator. The authors would like to thank Mr. Nagaya T. and Komatsu K., for their assistance in constructing the system.

References

1) Ortega, R., Devès G., Fayard B., Salomé M., Susini J., Nucl. Instru. Meth. **B210** (2003) 325.
2) Ortega, R., Fayard B., Salomé M., Devès G., Susini J., J. de Physique IV, **104** (2003) 289.
3) Ortega, R., Fayard B., Salomé M., Devès, G.Susini J., accepted in Chemical Research in Toxicology (2005).
4) Ortega R., Sarkar Ed. B., Marcel Dekker Inc., New York (2002) pp.35-68
5) Ishii K., Matsuyama S., Yamazaki H., Watanabe Y., Yamaguchi T., Momose G., Amartaivan Ts., Suzuki A., Kikuchi Y. and Galster W., I. J. PIXE **15** (2005) 111.
6) Yamaguchi T., Ishii K., Yamazaki H., Matsuyama S., Watanabe Y., Abe S., Inomata M., Ishizaki A., Oyama R., Kawamura Y., , I. J. PIXE **15** (2005)195.
7) Ishii K., Matsuyama S., Yamazaki H., Watanabe Y., Kawamura Y., Yamaguchi T., Momose G., Kikuchi Y., Terakawa A., Galster W., Nucl. Instr. Meth., **B249** (2006) 726.
8) Ishii K., Matsuyama S., Watanabe Y., Kawamura Y., Yamaguchi T., Oyama R., Momose G., Ishizaki A., Yamazaki H., Kikuchi Y.. Nucl.Instr. and Meth. **A571** (2007) 64.
9) Kawamura Y., Ishii K., Yamazaki H., Matsuyama S., Kikuchi Y., Yamaguchi T., Watanabe Y., Oyama R., Momose G., Ishizaki A., Tsuboi S., Yamanaka K. and Watanabe M., I. J. PIXE **17** (2007) 41.
10) Ohkura S., Ishii K., Matsuyama S., Yamazaki H., Terakawa A., Kikuchi Y., Fujiwara M.,

Kawamura Y., Tsuboi S., Yamanaka K., Watanabe M. and Fujikawa M., I. J. PIXE **18** (2008) 167.
11) Ishii K., Morita S., I. J. PIXE **1** (1990) 1.

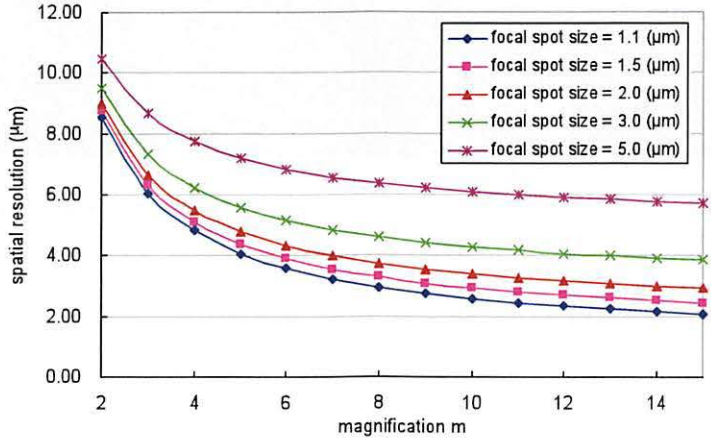

Figure 1. Relationship between spatial resolution and magnification.

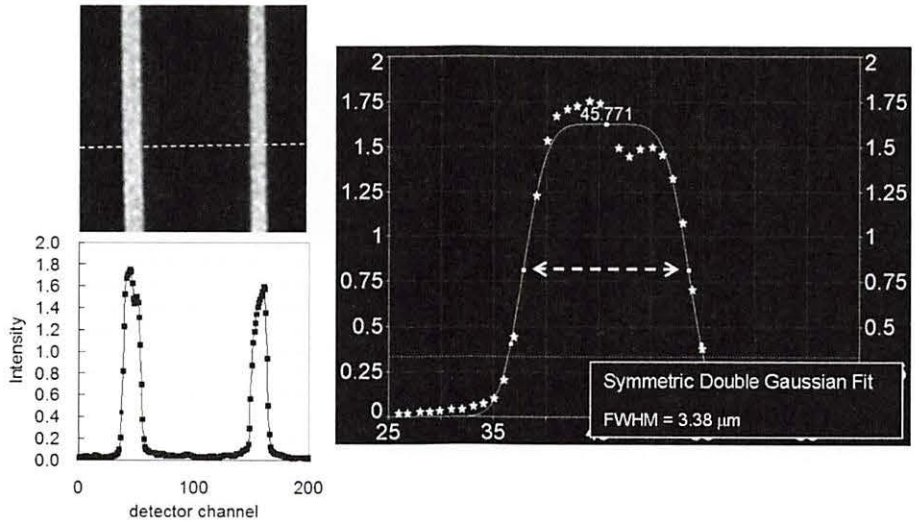

Figure 2. CT image of capillary tube and the profile of the intensity of CT-value.

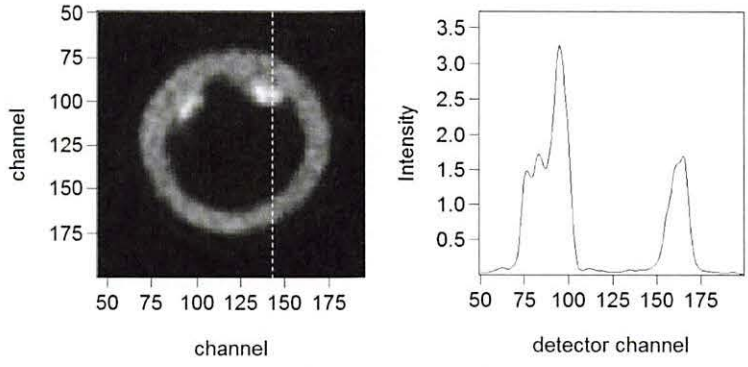

Figue 3. Cross sectional view of cell and Line profile.

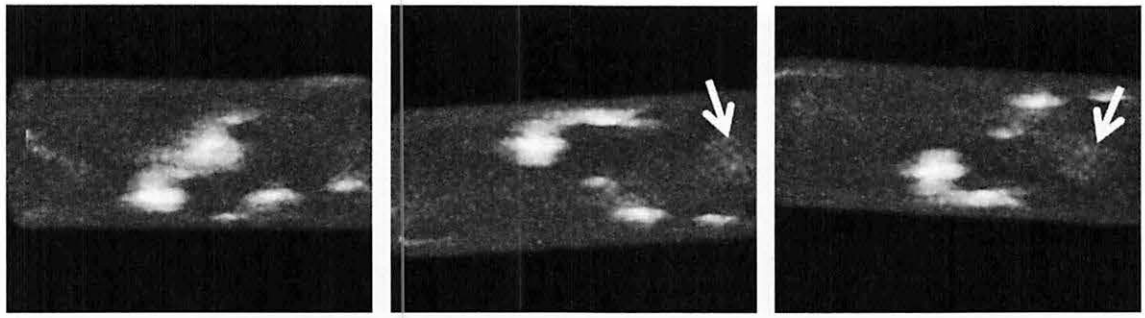

Figure 4. Maximum Intensity Projection (3D imaging from different angles).

V. 5. Characterization of Corrosion Layer of Carbon Steel by Micro-PIXE/RBS Analysis

Matsuyama S.[1], Ishii K.[1], Fujiwara M.[1], Kikuchi Y.[1], Nakhostin M.[1], Kawamura Y.[1], Tsuboi S.[1], Yamanaka K.[1], Watanabe M.[1], Ohkura S.[1], Hashimoto Y.[1], Fujikawa M.[1], Catella G.[1], Fujiki K.[1], Hatori Y.[1], Hamada N.[1], Tanino S.[1], Abe H.[1], Watanabe Y.[1], and Yamazaki H.[2]

[1]Department of Quantum Science and Energy Engineering, Tohoku University
[2]Cyclotron and Radioisotope Center, Tohoku University

Introduction

Piping, vessels and components of nuclear and thermal power plants are made of carbon steel or stainless steel. During plant operation, the protective oxide layer (magnetite or hematite) is formed on the surface of carbon steel where exposed to high temperature water flow and vapor. Wall thinning of piping made of carbon steel results from dissolution of the oxide layer. This phenomenon is a common problem in all types of these power plants and affects their lifetime and safety. Many factors such as flow rate, temperature, pH, dissolved oxygen concentration and composition of carbon steel affect corrosion rate. Especially water flow rate strongly affects the corrosion rate. This phenomenon is known as flow-accelerated corrosion (FAC)[1]. FAC rate depends on many parameters such as water chemistry, temperature, mass transfer coefficient and chromium content in steel. Especially, chromium content is known as an important parameter to reduce the FAC rate. Chromium content higher than 0.05 wt% greatly reduces FAC rate. However, the chromium content is not regulated in carbon steel, or chromium is considered as mere impurity, so far. While the mechanism of this phenomena is not known perfectly yet, the chromium content seems to affect formation and dissolution on the oxide layer. Considering welded part of carbon steel, for examples, in which the segregation of chromium carbide are occurred along grain boundary, the reduction of thickness due to the process of oxide formation and dissolution takes place in the localized area around grain boundary. Therefore, oxide formation and dissolution should be related to the mechanism of corrosion. In order to understand the mechanism of the phenomenon of corrosion, characterization of oxide layer in the localized area is indispensable from this point of view.

For surface analysis of the oxide layer, many techniques such as secondary electron microscopy, X-ray diffraction, and transmission electron microscopy are used. However, complete elemental information, which is important for characterization, is not obtained by these methods. In this study, the simultaneous micro-PIXE/RBS analysis was applied to obtaining elemental characterization on oxide layer formed on the carbon steel.

Analysis system

Analyses of samples were carried out with the microbeam system at Tohoku University. Technical details of the system were presented in previous papers[2,3]. Simultaneous PIXE/RBS analysis was conducted with the proton beam energy of 2.4 MeV and 3 MeV, the beam spot size of 1×1 μm^2 and beam currents of around 50 pA. The beam scanning area was set to 20 x 20 μm^2. The quantitative PIXE analysis was performed using the GeoPIXEII software[5]. Light elements (C,N,O) were quantified by analyzing the extracted RBS spectra using the SIMNRA software[6].

Results of analyses

Samples are plates of carbon steel (1mm thick) with various chromium contents ranging from 0.003 wt% to 1.01 wt% (nominal). These samples were oxidized in water with and without flow in an autoclave. In dynamic oxidation condition, the water was conditioned at pH=9.07 and 9.36 by addition of ammonia under a flow rate of 3 m/sec. Under static condition, the water was conditioned at pH=7.

In the RBS analysis, two layers which correspond to oxide layer and base metal were considered. The corresponding cross sections for carbon, nitrogen, and oxygen were derived from the refs. 7 and 8. Rutherford cross section was used for iron. Figure 1 shows number of atoms in the oxide layer as a function of chromium contents. Nominal chromium and iron ratios are consistent with those obtained by PIXE. Number of atoms in the oxide layer decrease with the increase of chromium content. Thickness of oxide layer is estimated to be 0.3 μm for chromium content of 1.01 wt%. The atomic ratios of O:Fe were around 1:5 and 1.2:1, in the chromium content of 0.003-0.1 wt% and 0.4-1.01 wt%, respectively. In chromium content higher than 0.4 %, the atomic ratio of O:Fe is close to that of Fe_3O_4. The layer formed on the surface is mainly composed of magnetite. Number of oxygen of the oxide layer is lower than that of magnetite for chromium content lower than 0.1 wt%.

X-ray yield maps of chromium and iron are shown in Fig. 2 for carbon steel oxidized with water flow of 3 m/sec. X-ray yields are not uniform over the scanning area, which is related to the changes in the thickness of oxide layer. As well as self-absorption of X-rays in the layer, X-ray production cross section changes corresponding to energy-loss in the oxide layer X-ray yield decreases around 10% correspond to the increase of the magnetite layer of 1 μm. X-ray intensities of iron and chromium vary from 50-100%, which means that thick oxide layer was formed nonuniformly on the surface. In contrast, oxide layer was formed uniformly in the non flow case as mentioned previously. When oxide layer thickness is not uniform over the region, analysis of RBS spectra is impossible. Position dependent oxide layer composition and thickness can be obtained by fitting the RBS spectra derived from each pixel. Considering low counting statistics for each pixel, spectrum fitting is impossible. Thus, we select the region where X-ray yield of iron is similar and obtained RBS spectra from the selected region. Typical RBS spectra are also shown in Fig. 2 together with the simulated result by the SIMNRA for the selected regions. The RBS spectra changes drastically correspond to oxide layer thickness and compositions. In the simulation, three oxide layers have to be considered to fit the spectra. Oxide concentration is highest in the surface layer. Round shape of the edges corresponds to the decrease of oxide concentration toward the inside. While oxygen concentration is the same in the regions 1 and 2, carbon concentration in the region 1 is more than 2 times higher than that in the region 2. Since segregation of chromium carbide occurred along grain boundary, it will be suggested that the region 1 will be the oxide layer along the grain boundary. From the PIXE analysis, chromium and iron ratio is constant in these regions and same as the nominal value. Since PIXE analyze the elements in the ca. 10 μm from the surface when the substrate assumes to be iron for 2.4 MeV protons, it may be difficult to find changes in chromium concentration in the thin layer.

On the other hand, the RBS spectra for chromium content of 1.01 wt% is quite different from the others. In region 1, number of protons scattered from oxygen and iron is quite low, compared to those in region 2 and carbon content is highest. In this simulation, 3 layers are considered and hydrogen must be introduced to fit the spectra. In both regions, hydrous metal oxide layer might be formed. Chromium and iron ratio is more than two times higher than the nominal value. Since layer thickness is thicker than the other case, chromium is concentrated in the layer. In region 1, chromium and iron ratio is 10% higher than that of region 2. It is apparent that chromium carbide is formed in the region 1.

Conclusions

In order to know the mechanism of corrosion in the localized area, we applied the simultaneous micro-PIXE/RBS analysis to characterization of oxide layer. The simultaneous micro-PIXE/RBS system demonstrated the relation between chromium content and numbers of atoms of oxygen and of iron in the oxide layer for carbon steel oxidized under the static condition. T he oxide layer formed at dynamic condition is not uniform even in the narrow area of 20×20 μm^2. In this case, it is difficult to characterize oxide layer by conventional RBS analysis. The simultaneous micro-PIXE/RBS system could characterize the layer by region analysis. By micro-PIXE analysis, a specific area was extracted as a region of interest to be analyzed by RBS. Then an RBS spectrum was extracted and analyzed by using the SIMNRA software so as to obtain the elemental composition of oxide layer. Under the dynamic condition, elemental composition of the oxide layer was strongly affected by chromium content. In the chromium content of 1.01 wt%, hydrous metal oxide layer was formed. Since chromium is concentrated in this layer, chromium carbide is formed and might be related to hydrous metal oxide. These results of this experiment obviously show the simultaneous micro-PIXE/RBS analysis system to be useful for better understanding of the corrosion mechanism.

Acknowledgements

The authors would like to acknowledge the assistance of Fujisawa M. for maintenance and operation of the Dynamitron accelerator. The authors would like to thank Mr. Nagaya T. and Komatsu K., for their assistance in constructing the microbeam and target system.

References

1) Sanchez-Caldera J. E., Griffith P., Rabinowicz E., Trans of the ASME, Engi, for Gas Turbines and Power, **110** (1988) 180.
2) Matsuyama S., Ishii K., Yamazaki H., Barbotteau Y., Amartivan Ts., Izukawa D., Hotta Mizuma K. K., Abe S., Oishi Y., Rodriguez M., Suzuki A., Sakamoto R., Fujisawa M., Kamiya T., Oikawa M., Arakawa K., Imaseki H., and Matsumoto N., *Int. J. PIXE*, **14** (2004) 1.
3) Matsuyama S., Ishii K., Abe S., Ohtsu H., Yamazaki H., Kikuchi Y., Amartaivan Ts., Inomata K., Watanabe Y., Ishizaki A., Barbotteau Y., Suzuki A., Yamaguchi T., Momose G., and Imaseki H., *Int. J. PIXE*, **15** (2005) 41.
4) Matsuyama S., Ishii K., Yamazaki H., Kikuchi Y., Inomata K., Watanabe Y., Ishizaki A., Oyama R., Kawamura Y., Yamaguchi T., Momose G., Nagakakura M., Takahashi M., and Kamiya T., *Nucl. Instr. and Meth.*, **B260** (2007) 55.
5) Ryan C. G., Van Achterbergh E., Yeats C. J., Drieberg S. L., G.Mark, McInnes B. M., Win T. T., Cripps G. and Suter G. F., "Quantitative, high sensitivity, high resolution, nuclear microprobe imaging of fluids, melts and minerals", *Nucl. Instr. and Meth.*, **B188** (2002) 18.
6) Mayer M. SIMNRA Users's Guide, Technical Report IPP 9/113, MPI Plasmaphy.

7) Amirikas R., Jamieson D. N., and Dooley S. P., *Nucl. Instr. and Meth.*, **B77** (1993) 110.
8) Ramos A. R., Paúl A., Rijniers L., F.da Silva M., and Soares J. C., *Nucl. Instr. and Meth.*, **B190** (2002) 95.

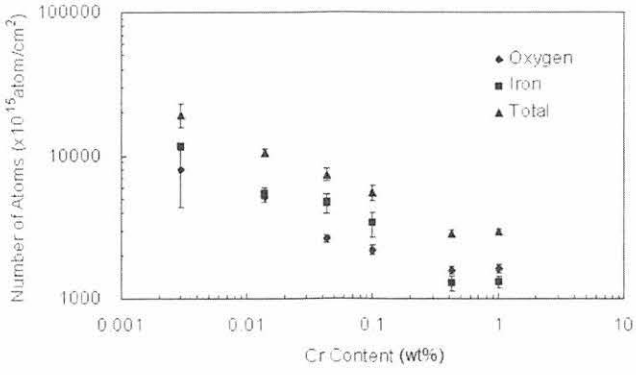

Figure 1. Number of atoms in the Oxide Layer as a Function of Chromium Content.

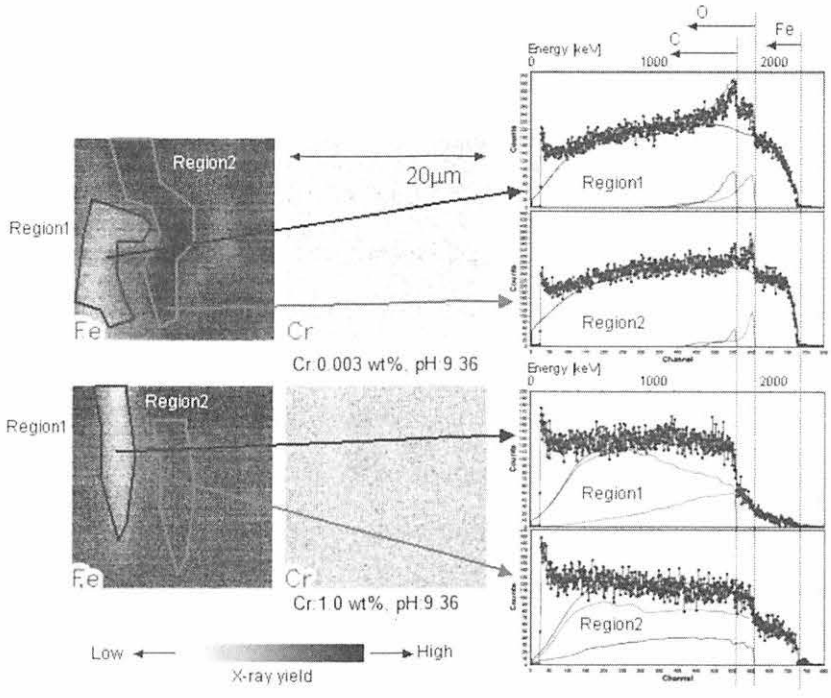

Figure 2. Typical Elemental Maps and RBS spectra of Chromium and Iron for Carbon Steel Oxidized under Dynamic Condition.
Upper : chromium content=0.003 wt% , pH = 9.37 and Lower: chromium content = 1.01 wt%, pH = 9.37

V. 6. PIXE Analysis of Individual Particles in Coal Fly Ash

Hatori Y.[1], Matsuyama S.[1], Ishii K.[1], Terakawa A.[1], Kikuchi Y.[1], Fujiwara H.[1], Kawamura Y.[1], Okura S.[1], Fujikawa M.[1], Hamada N.[1] Fujiki K.[1] Inoue C.[2], Yamazaki H.[3], and Hashimoto Y.[3]

[1]*Department of Quantum Science and Energy Engineering, Tohoku University*
[2]*Department of Environmental Studies, Tohoku University*
[3]*Cyclotron Radioisotope Center, Tohoku University*

Introduction

Coal is the largest source of energy for the generation of electricity. Consumption of coal is increasing as an alternative for petroleum, since the depletion of petroleum has become world wide problem[1]. Coal is pulverized and then combusted in a furnace with a boiler for electricity generation in coal-fired power plants. During the process, waste products such as coal ash residue and flue gas desulfurization sludge are produced. There are two types of coal ash residues, the first is fly ash generated from the boiler, and the second is clinker ash that falls to the bottom of the boiler furnace. The proportion of fly ash is about 80 to 85% of coal ash residues. Although coal ash is partly reused as cement admixture and concrete aggregate, the residuals are disposed as an industrial waste[2]. Coal fly ash contains mercury, arsenic, and other toxic heavy metals, which leads to a concern about the possibility of leakage into environment. While extraction tests of coal fly ash show that coal fly ash is environmentally safe under natural pH condition, some metals are soluble under aggressive pH conditions[3]. Therefore, it could adversely affect humans, animals, plants and living environment. However, it is difficult to investigate a direct correlation between pH of coal fly ash and leakage of elements. The assessment of leakage of toxic elements into the environment and the effect on human beings and animals strongly depend on their spatial distribution in the particles and on their chemical form as well as elemental concentrations[3,4]. Therefore, the physicochemical conditions of the coal fly ash should be investigated. For this purpose, analysis of individual fly ash particle by using microbeam analysis will provide valuable information in this field[5]. In this study, we analyzed coal fly ash from coal-fired power plants with 1 μm spatial resolution by using

the simultaneous micro-PIXE/RBS/off-axis STIM system at Tohoku University. The combination of PIXE, RBS and off-axis STIM methods enabled simultaneous analysis of hydrogen to metal elements and revealed the chemical composition of these particles.

Experimental

Sample preparation

In order to analyze all elements contained in fly ash particles with spatial resolution of 1 μm, it is necessary to attach them on a thin polymer film without using any adhesive. Chemical treatment should not be done because chemical form might change. For this purpose we used an impactor which was developed in aerosol study[6]. Fly ash particles were suspended in a box and were sampled at a flow rate of 1.3 l/min for one hour. The effective 50% cutoff diameter is estimated as ca 2 μm. Fly ash particles were impacted on a 2 μm Mylar ($H_8C_{10}O_4$) film or a 4 μm Prolene (H_6C_3) film. Although particle size of coal fly ash particles ranges from 3 to 20 μm, those of collected particle were 3 to 5 μm in diameter. It was an effect of upper cut-off of the impactor. In order to analyze bigger particles than 5 μm, fly ash particles were put on the Mylar film and were attached by electrostatic force. Number of particles on the film was low, bigger particles than 5 μm could be collected. We analyzed six samples generated in coal-fired power plants in Japan.

Analysis

We performed individual particle analysis of the coal fly ash with a microbeam system at Tohoku University. Technical details of the system were presented in previous publication[7,8]. Simultaneous PIXE/RBS/off-axis STIM analysis was conducted with the proton beam energy of 3 MeV, beam spot size of 1×1 μm^2 and beam currents of 50 to 100 pA. The beam scanning area was 10×10 to 100×100 μm^2.

Quantitative PIXE analyses were performed by using GeoPIXEII software[9]. After generating the elemental maps, individual particles were selected from these maps and corresponding PIXE, RBS, and off-axis STIM spectra were extracted. The elemental concentrations for elements heavier than carbon were then deduced from the fit of the extracted PIXE spectra. For quantitative analysis, yield correction of X-rays was performed for each particle considering the particle size, shape, the changes in X-ray production cross section and self absorption of X-rays. However, the effect of shape is

small even for light elements and is negligible for heavy elements, in particle sizes (<5 μm)[5,10]. In this study, no shape correction did not apply and the changes in X-ray cross section and self absorption effects were considered assuming a flat homogeneous slab. Concentrations of carbon, oxygen, and hydrogen were derived from peak yields of extracted RBS and STIM spectra, which were calibrated by measuring the peak yields from Mylar films of known thickness. Quantitative analysis of hydrogen was carried out by analyzing the extracted off-axis STIM spectra.

Results and Discussion

We analyzed about 80 coal fly ash particles obtained from six coal-fired power plants in Japan and obtained elemental concentrations and elemental distribution images. The coal fly ash particles are mainly composed of O, Si and Al. Sum of the masses of O, Si and Al in each of the particles is 80-95% of the total mass. Figure 1 shows the correlation between number of oxygen atoms and that of metals for the particles. In this analysis, particles collected on the Mylar film and which were bigger than 5 μm were excluded from the analysis. The results on 50 particles are shown in the graph. Number of oxygen atoms increases with that of metals. Atomic ratio is around 2. It is apparent that these particles exist as dioxide. The particles also contain Ca, Ti, Fe, Na, Mg and K. Hydrogen and carbon are not observed in these particles, which implies that coal is completely burned and carbon dioxide and water vapor is dissipated.

Examples of elemental distribution images are shown in Fig. 2 (a), (b) and (c). The oxygen image in Fig. 2 is obtained by RBS. As mentioned previously, Oxygen, silicon and aluminum show similar distributions. As for trace elements, the content of each element is quite different in each particle. Forty percent of the particles contain V and Zn. All of the particles from one of the power plants contain V and Zn. Five to ten percent of these particles contains Sr, Cu, Ni, Mn and Cr. A few particles contain arsenic. These elements distribute homogeneously as shown in Fig. 3 (a) and (b). One exception is shown in Fig. 3 (c). Since the size of the particle is around 20 μm, the yield map of Al and Si is strongly influenced by self absorption, and X-ray intensity of right side is low. While silicon distributes uniformly, Al, Ca, Fe, Zn, As and Zr are distributed on the surface of the particles. It is reported that the elements having boiling points lower than the combustion temperature of the furnace in the power plant condense on the surface of the particle at the low temperature following combustion[4].

Conclusions

Coal fly ash particles contain mercury, arsenic, and other toxic heavy metals, which might lead to leakage into environment. The spatial distribution and chemical form as well as elemental concentrations of the trace elements are important factor in the assessment of leakage into the environment. In this study, we analyzed coal fly ash from coal-fired power plants with 1 μm spatial resolution by using the microbeam analysis system at Tohoku University. Fly ash particles were attached on the Prolene film using impactor. Particle size range collected by the impactor was 3-5 μm in diameter which was smaller than that of fly ash particle. Bigger particles were attached on the Mylar film by electrostatic force. We analyzed about 80 coal fly ash particles obtained from six coal-fired power plants in Japan. The coal ash particles are mainly composed of O, Si and Al and estimated as dioxide. The particles also contain Ca, Ti, Fe, Na, Mg and K. As for trace elements, V, Zn, Sr, Cu, Ni, Mn, Cr and As are contained. Correlation between these elements is not seen. These elements distribute homogeneously. As an exception, Al, Ca, Fe, Zn, As and Zr are distribute on the surface of the particles which might be related to the combustion process. Microbeam analysis of individual fly ash particle will provide valuable information in this field.

References

1) World Energy Council 2007, 2007 Survey of Energy Resources.
2) Baasansuren J., Bolormaa O., Tokunaga R., Kawasaki K. and Watanabe M., Nucl. Instr. Meth. Physi. Res. **B 251** (2006) 209.
3) Jegadeesan G., Souhail R. Al-Abed, Pinto P., Fuel **87** (2008) 1887.
4) Jaksic M., Watt F., Grime G. W., Cereda E., Braga Marcazza G. M. and Valkovic V., Nucl. Instr. Meth. Phys. Res. **B 56/57** (1991) 699.
5) Cereda E., Braga Marcazza G. M., Pedretti M., Grime G. W., Baldacci A., Nucl. Instr. Meth. Phys. Res. **B 104** (1995) 625.
6) Matsuyama S., Katoh K., Sugihara S., Ishii K., Yamazaki H., Satoh T., Martaivan Ts., Tanaka, A. Komori H., Hotta K., Izukawa D., Mizuma K., Int. J. PIXE **13** (2003) 65.
7) Matsuyama S., Ishii K., Yamazaki H., Barbotteau Y., Ts. Martivan, Izukawa D., Hotta K., Mizuma K., Abe S., Oishi Y., Rodriguez M., Suzuki A., Sakamoto R., Fujisawa M., Kamiya T., Oikawa M., Arakawa ., Imaseki H., Matsumoto N., Int. J. PIXE **14** (2004) 1.
8) Matsuyama S., Ishii K., Yamazaki H., Kikuchi Y., Inomata K., Watanabe Y., Ishizaki A., Oyama R., Kawamura Y., Yamaguchi T., Momose G., Nagakura M., Takahashi M., Kamiya T., Nucl. Instr. Meth. Phys. Res. **B 260** (2007) 55.
9) Ryan C. G., Van Achterbergh E., Yeats C. J., Drieberg S. L., Mark G., McInnes B. M., Win T. T., Cripps G., Suter G. F., Nucl. Instr. Meth. Phys. Res. **B 188** (2002) 18.
10) Bogdanovic I., Fazinic S., Jaksic M., Grime G. W., Valkovic V., Nucl. Instr. Meth. Phys. Res. **B 85** (1994) 732.

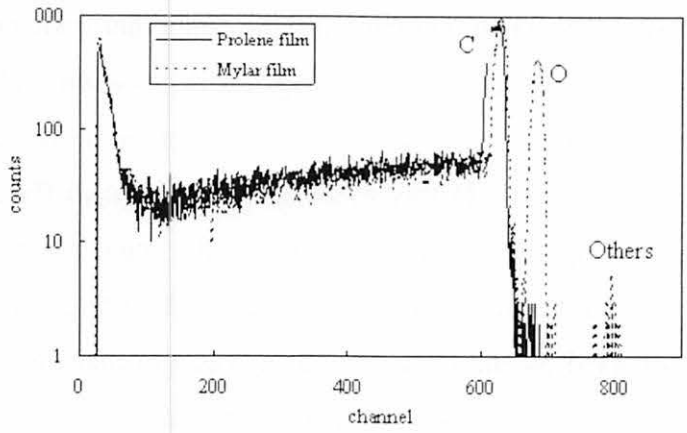

Figure 1. Correlation between Oxygen and sum of Al, Si, Ca, Ti and Fe.

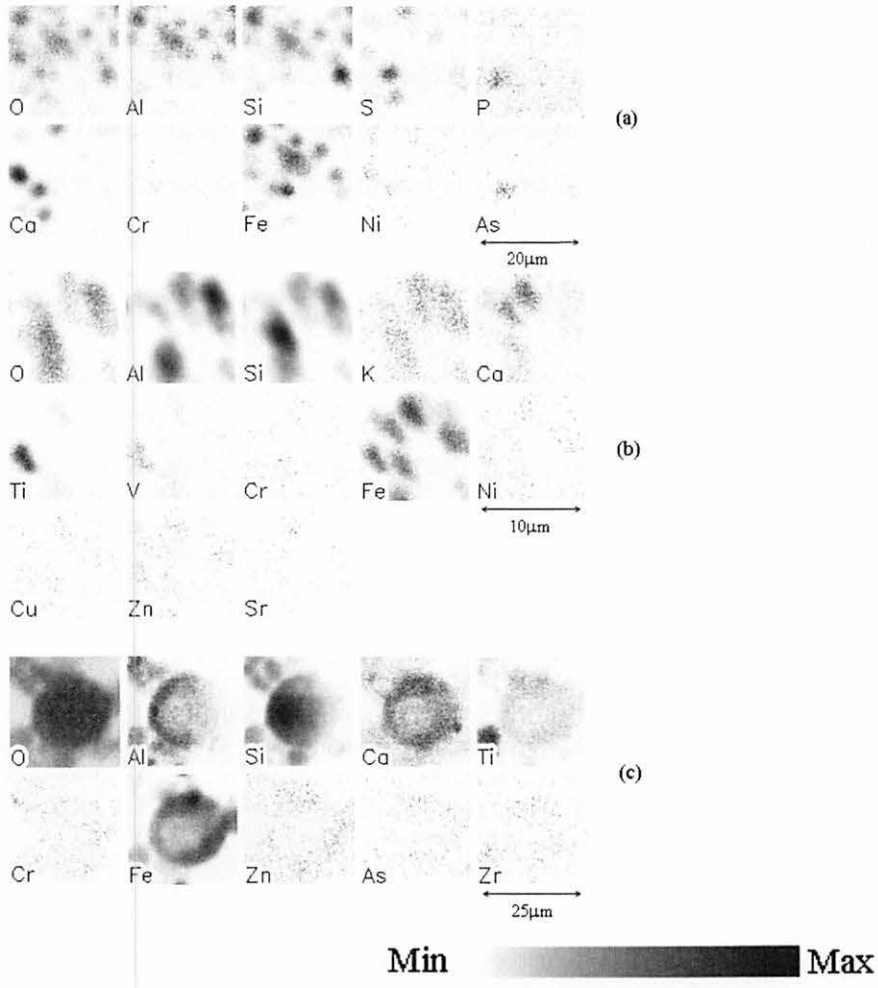

Figure 2. Elemental d istribution maps of the fly ash particles.

V. 7. Microbeam Analysis of Yellow Sand Dust Particles

Matsuyama S.[1], Ishii K.[1], Yamazaki H.[2], Kikuchi Y.[1], Kawamura Y.[1], Oyama R.[1], Yamanaka K.[1], Yamamoto T.[1], Watanabe M.[1], Tsuboi S.[1], and Arao K.[3]

[1]Department of Quantum Science and Energy Engineering, Tohoku University
[2]Cyclotron Radioisotope Center, Tohoku University
[3]Faculty of Environmental Studies, Nagasaki University

Introduction

Yellow sand dust particles from the Asian continent sometimes cause turbid conditions in Japan, especially in spring, which is known as a Kosa event. The particles are carried from the Yellow River basin and deserts, which is known as a natural phenomenon. The particles are principally composed of minerals and their diameters are around 4 μm. Recently, it is regarded as an environmental problem due to forest reduction, soil degradation and desertification rather than a natural seasonal phenomenon. Furthermore, these particles are sometimes deformed by mixing with anthropogenic aerosols during transport and affects agricultural production, climate, living condition and human health. Therefore, physical and chemical changes during transport as well as mechanism of formation, growth and transport have to be known. For better understanding of these mechanisms, analysis of single particles is indispensable. For this purpose, we developed a microbeam analysis system with a spatial resolution better than 1 μm. The combination of PIXE, RBS and off-axis STIM methods enabled simultaneous analysis for hydrogen to metal elements and revealed the chemical composition of these particles. In this study, we applied the system to analyze yellow sand dust particles and investigated their properties.

Sampling

Aerosol particles were collected at the campus of Nagasaki University (32.78°N, 129.87°E; 20 m) on 9,10 and 19 May 2005. Nagasaki University located at Kyusyu Island of western part of Japan, where yellow sand dust particles largely affects the daily life.

Recently, fine particles whose sizes are in the range of 0.3-1.0 μm in diameter occasionally cause significant turbid condition over the Nagasaki area. Since yellow sand dust particles are mostly larger than 1.0 μm, these fine particles are mainly anthropogenic aerosols and not the components of yellow sand dust particles[1,2]. To collect true yellow sand dust particles, sampling was carried out when concentration of coarse particles increases and that of fine particles shows usual atmospheric condition by using an optical particle counter (OPC). On 9 and 10 May, coarse particles showed higher concentration, indicated Kosa events and fine particle showed as usual condition. On 19 May, concentrations of fine and coarse particles were low. Sampling times were 6 hr. In total 3 samples were collected. Aerosol particles were impacted on a thin polycarbonate film[3] at flow rates of 1 *l*/min (face velocity: 530cm/sec). The effective 50% cut-off diameter is estimated to be ~2 μm and sufficient for collection of yellow sand dust particles. Elemental concentrations and ratios in the polycarbonate film were obtained by fitting the RBS spectrum with the SIMNRA software[4]. Thickness of the film was estimated to be less than 1 μm which is thicker than the previous study. The thin polycarbonate film allows analyzing light elements of the particles.

Analysis

Analysis was carried out using the microbeam analysis system at Tohoku University. Technical details of the microbeam and analysis system were presented in previous ppers[5-7] and further development was carried out for the efficient analysis of single aerosol particles. For multimodal analysis, two X-ray detectors for PIXE analysis and three charged particle detectors for RBS and STIM are mounted simultaneously[8].

Results

Simultaneous PIXE/RBS/off-axis STIM analysis employed for scanning areas of 25×25 μm^2 and 100×100 μm^2. Yellow sand dust particles were uniformly distributed, thus direct STIM measurements for defining the analysis area were not needed. Energy of the proton beam was 3 MeV and beam spot size was 1×1 μm^2 with a beam current of 50~100 pA. Total accumulated charge was around 0.2 μC.

Quantitative PIXE analysis was performed using the GeoPIXEII software[9]. After generating the elemental maps, individual particles were selected from these maps and PIXE, RBS and off-axis STIM spectra were extracted. Elemental concentrations of these

particles for elements heavier than Na were deduced from fitting of the extracted PIXE spectra. Carbon and oxygen were quantified by analyzing the extracted RBS spectra. Concentration of carbon and oxygen were derived from peak yields which were calibrated by measuring peak yields from Mylar films of known thickness. Quantitative analysis of hydrogen was carried out by analyzing the extracted off-axis STIM spectra. For the quantitative analysis of hydrogen, intensities of hydrogen were calibrated by measuring hydrogen yields from Mylar films of different thickness. The relation between hydrogen peak yield and hydrogen quantity was linear and was used to calibrate the quantitative analysis of hydrogen. After quantification of these particles, the chemical composition of each particle was obtained.

More than 100 particles were analyzed and Na, Mg, Al, Si, S, Cl, K, Ca, Ti, V, Cr, Mn, Fe, Ni, Cu, Zn and Br elements were quantified. Figure 1 shows typical elemental maps of yellow sand dust particles collected on 11 May, 2005, when high concentration of coarse particles was observed. The scanning area was 100×100 μm^2 and total accumulated charge was 0.21 μC. Distribution of aluminum equals to the one of silicon. Chlorine, potassium, calcium, carbon and hydrogen also show similar distribution. Oxygen distributes on the same part of these particles. Aluminum, silicon, calcium, iron and light elements are major components. Numbers of oxygen atoms of these particles is around eight times higher than that of mineral elements. It is apparent that these particles manly existed as oxide and were mainly originated form soil dust. These particles also contained carbon and hydrogen and might be absorbed organic carbon during transportation. In the contrast, the particles collected on 19 May when atmosphere showed usual condition, two kinds of major elemental groups, which correspond to marine and soil aerosols, were observed. Half of the particles are estimated to be marine aerosols.

Figure 2 shows the ternary diagram for calcium, silicon and aluminum. In this diagram, marine particles, which sodium and calcium are main components, were excluded. The distribution of the particles which were collected on 10 and 11 May were very similar, except for calcium-rich components. On the other hand, the particles collected on 19 May show lower calcium concentration. These facts correspond to the difference of the soil components of Asian continent and Japan Island. Correlation function between calcium and chlorine is shown in Fig. 3 for these particles. As calcium increases, chlorine also increases for the particles collected on 11 May. The particles are supposed to contain $CaCl_2$ particles. Backward trajectory analysis using NOAA HYSPLIT[10] indicated that the

particles which came on 11 May took almost the same route from Chinese coast to Nagasaki with a low velocity as the ones came on 10 May. Amount of sodium on 11 May is also larger than that of 10 May. It implies that the particles came on 11 May deformed by mixing with marine aerosols more than those came on 10 May. These particles collected on 10 and 11 May contained more sulfur and heavier elements such as manganese and zinc than those collected on 19 May. These particles were transported from Asian continent over the industrial area to Japan and might absorb these elements by mixing with anthropogenic aerosols.

Conclusions

The microbeam system was applied to analysis of yellow sand dust particles. Simultaneous PIXE, RBS and STIM analysis enabled to measure the elements from hydrogen to metal elements and revealed the chemical composition of these particles. The major elements of yellow sand dust particles are silicon and calcium and exist as oxide. The ternary diagram of aluminum, silicon and calcium shows the difference of the origin of the soil components of Asian continent and Japan Island. Correlation of calcium and chlorine is different for each Kosa events, which supposed the difference of transport to Japan Island. Yellow sand dust particles contain more sulfur and heavier elements such as manganese and zinc. These particles were transported from Asian continent over the industrial area to Japan and might absorb these elements by mixing with anthropogenic aerosols. These results could be obtained by analyzing single aerosol particles and was not obtained by the bulk analysis which averages over many particles. Single particle analysis of yellow sand dust will lead to a better understanding of their deformation process during transport.

Acknowledgments

This study was partly supported by Grants-in-Aid for Scientific Research, (S) No. 13852017, (B) No. 18360450, (C) No. 16560731, and a Grant-in-Aid for Scientific Research in Priority Areas under Grant No. 14048213 from the Ministry of Education, Culture, Sports, Science and Technology, Japan. The authors would like to acknowledge the assistance of Mr. R. Sakamoto and M. Fujisawa for maintenance and operation of the Dynamitron accelerator. The authors would like to thank Mr. K. Komatsu, T.Nagaya and C. Akama for their assistance in constructing the microbeam and target system. The

authors gratefully acknowledge the NOAA Air Resources Laboratory (ARL) for the provision of the HYSPLIT transport and dispersion model and/or READY website (http://www.arl.noaa.gov/ready.html) used in this publication.

References

1) Arao K., Ishizaka J., Sugimoto N., Matsui I., Shimizu A., Mori I., Nishikawa M., Aoki K., Uchiyama A., Yamazaki A., Togawa H. and Asano J., *SOLA*, **2** (2006) 100.
2) Arao K., Nishizaki M., Hatakeyama S., Takami, A., Matsuyama S., Hayasaka T., *J. of Environmental Studies, Nagasaki University*, **9** (2006) 23.
3) Yamazaki H., Tsutsumi K., Ishii K., Matsuyama S., Murozono K., Inoue J., and Iwasaki S., *Int. J. of PIXE*, **7** (1997) 101.
4) Mayer M., SIMNRA Users's Guide, Technical Report IPP 9/113, MPI Plasmaphysik, Garching, Germany (1997).
5) Matsuyama S., Ishii K., Yamazaki H., Sakamoto R., Fujisawa M., Amartaivan Ts., Ohishi Y., Rodriguez M., Suzuki A., Kamiya T., Oikawa M., Arakawa K. and Matsumoto N., *Nucl. Instr. Meth.* , **B 210** (2003) 59.
6) Matsuyama S., Ishii K., Yamazaki H., Barbotteau Y., Amartaivan Ts., Izukawa D., Hotta K., Mizuma K., Abe S., Oishi Y., Rodriguez M., Suzuki A., Sakamoto R., Fujisawa M., Kamiya T., Oikawa M., Arakawa K., Imaseki H., Matsumoto N., *Int. J. PIXE*, **14** (2004) 1.
7) Matsuyama S., Ishii K., Abe S., Ohtsu H., Yamazaki H., Kikuchi Y., Amartaivan Ts., Inomata K., Watanabe Y., Ishizaki A., Barbotteau Y., Suzuki A., Yamaguchi T., Momose G., and Imaseki H., *Int. J. PIXE*, **15** (2005) 41.
8) Matsuyama S., Ishii K., Yamazaki H., Kikuchi Y., Amartaivan Ts., Abe S., Inomata K., Watanabe Y., Ishizaki A., Oyama R., Kawamura Y., Suzuki A., Momose G., Yamaguchi T., and Imaseki H., *Int. J. PIXE*, **15** (2005) 257.
9) Ryan C. G., Van Achterbergh E., Yeats C. J., Drieberg S. L., Mark G., McInnes B. M., Win T. T., Cripps G., Suter G. F., *Nucl. Instr. Meth.*, **B 188** (2002) 18.
10) Draxler R.R. and Rolph G.D., 2003. HYSPLIT (HYbrid Single-Particle Lagrangian Integrated Trajectory) Model access via NOAA ARL READY Website (http://www.arl.noaa.gov/ready/hysplit4.html). NOAA Air Resources Laboratory, Silver Spring, MD.

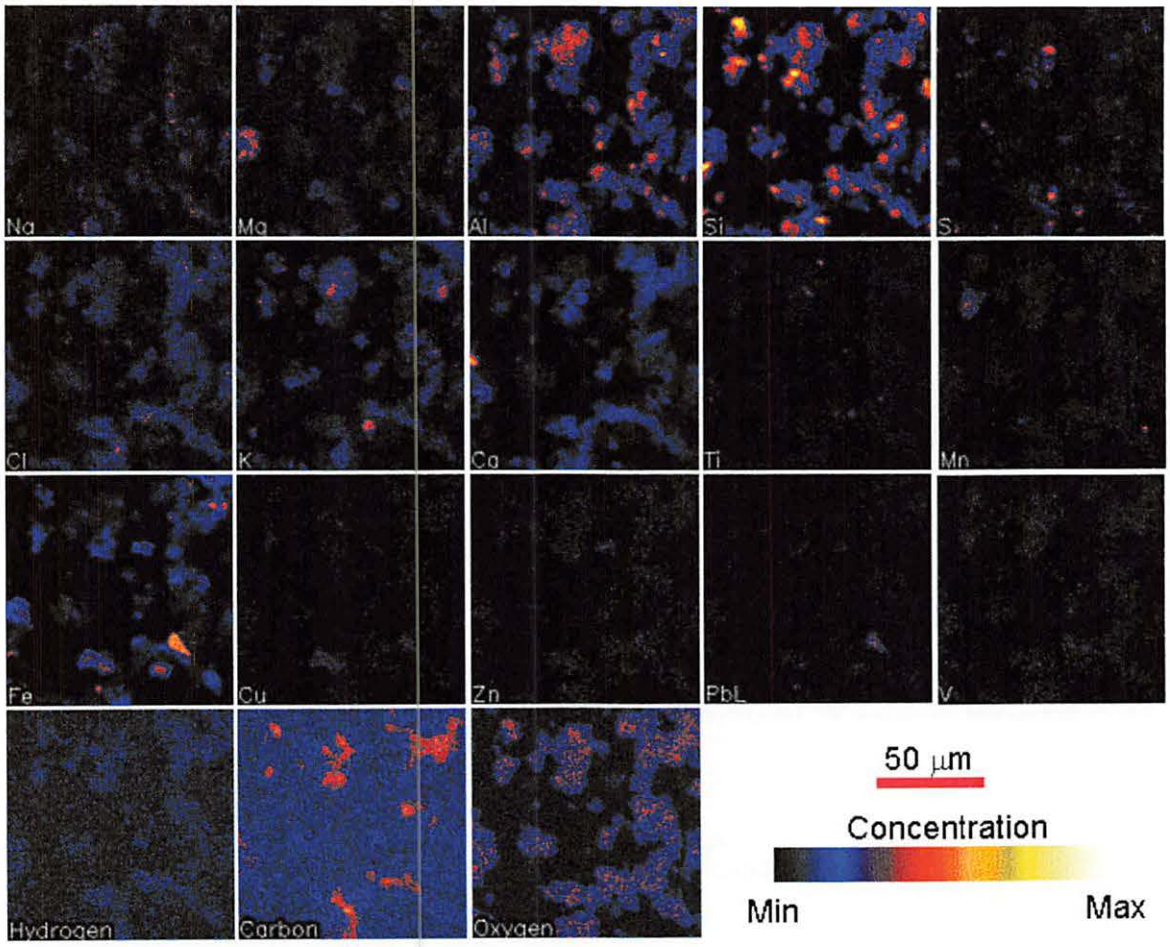

Figure 1. Elemental Distribution images of Yellow Sand Dust Particles collected on 11 May, 2005.

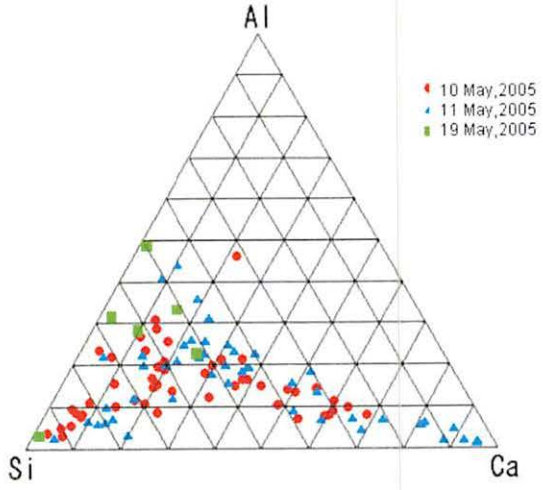

Figure 2. Ternary Diagram of Collected Aerosols.

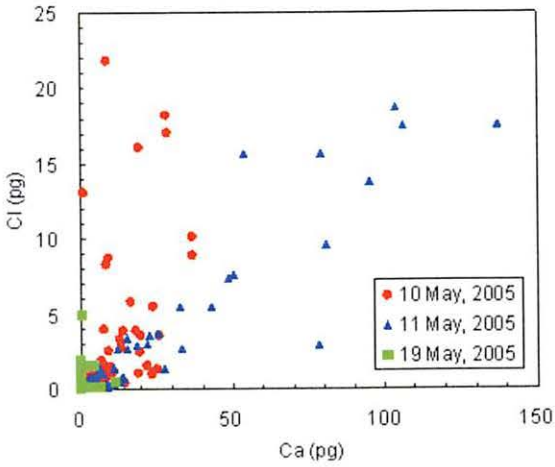

Figure 3. Correlation between Ca and Cl.

V. 8. PIXE Study on Translocation of Arsenate and Arsenite on Arsenic Hyperaccumulating Fern (Pteris Vittata)

Yamazaki H.[1], Ishii K.[2], Matsuyama S.[2], Kikuchi Y.[2], Terakawa Y.[2], Kawamura Y.[2], Fujiki K.[2], Hatori Y.[2], Hamada N.[2], Itoh Y.[2], Fukaya A.[2], Hatayama N.[3], and Inoue C.[3]

[1]*Cyclotoron and Radioisotope Center, Tohoku University*
[2]*Graduate School of Engineering, Tohoku University*
[3]*Graduate School of Environmental Studies, Tohoku University*

Introduction

Phytoremediation is a technology for cleaning metal-contaminated soils using plant physiology. *Pteris vittata* is the first plant to be an arsenic hyper-accumulator[1]. It is reported that arsenate (As(V)) taken-up by the fern root is immediately reduced to arsenite (As(III))[2,3]. And arsenite is then transported to fern fronds by transpiration stream and accumulated in the fronds[4]. It is also revealed that arsenate influx into fern roots is faster than that of arsenite[5]. Different research groups, however, report that arsenate is dominant in the rachis of fern blade and both arsenate and arsenite are contained in xylem vessels of the fern even under the condition of very high concentration of arsenite in a transpiration stream[6-7]. These findings indicate that arsenic is supplied to the fronds by xylem transport as a mixture of arsenite and arsenate.

To develop practical application of *Pteris vittata* to a phytoremediation technique, it is necessary to explicate how arsenic is distributed in fern frond tissues when either arsenite or arsenate is supplied to fern blades separately without an action of the fern root. It is also important to reveal what kinds of elements essential to the fern metabolism are translocated by accumulation of arsenic of either trivalent or pentavalent state in fern tissues. In this study, the distribution of arsenic of different oxidation states and other elements in fern frond tissues were examined in the procedure of separately feeding arsenate or arsenite to fronds through xylem vessels of the fern by using micro-PIXE analysis.

Material and methods

P. vittata L., a perennial and pinnate fern, which grows naturally in the warm district in southern Japan with long sunshine duration, was used throughout the experiment. Fern with several fronds was cultivated for either one week or three months, and the young ferns with not fully opened fronds and the mature ferns with sporophyte were subjected to an arsenic uptake experiment. A piece of the fern fronds was cut from the stipe and dipped in a solution containing either arsenite or arsenate along with 0.2 mM EDTA for preservation of arsenic species[8]. Concentrations of arsenic in test solutions were 7.5 ppm and 200 mM. After a desired period, a fern pinna was plucked and was sectioned around 25 μm in thickness by a microtome after inserted into a radish block. The sliced pinna section was mounted between tow polycarbonate films of 5 μm thickness and was glued on the sample holder for in-air micro-PIXE analysis.

Analyses of samples were carried out with the in-air micro-PIXE system at Tohoku University. Technical details of the system were presented in our previous papers[9-10]. The analysis was conducted with the proton beam energy of 3 MeV, the beam spot size of 1×1 μm^2 and beam currents of around 50 pA. The beam scanning area was set to 20x20 - 600×600 μm^2[2]. X-ray detector was set in vacuum at 125 degrees with respect to the beam axis. A Mylar filter (250 μm thick) was attached in front of the detector to reduce pile-up events and deformation of the spectrum by recoil protons. Quantitative PIXE analysis was performed using the GeoPIXEII software[11]. In the quantification of elements, the major composition and density of the analyzed layer must be set, so the fern matrix was presumed to be uniform composition of 80% H_2O + 20% $C_4H_6O_3$ with a density of 1.25 g/cm^3 [12].

Results and discussion

Fern fronds with sporophyte (mature stage) were subjected to arsenite (7.5 ppm in 7 hr) and arsenate (7.5 ppm in 2 hr) treatments. Although the results are not shown due to the lack of space, arsenic, irrespective of the oxidation state, was brought into a pinna in the concentration of around 800 ppm, indicating higher arsenic concentration in the sporophyte than in the other pinna regions. Arsenic concentration in the pinna veins was less than 200 ppm. These findings suggest that arsenic of different oxidation states is transported to the sporophyte by transpiration stream for the accumulation. In addition to this, the elemental distribution was well correlated between arsenic, potassium and calcium. Hokura et al. reported that arsenic accumulation was well correlated with potassium but was

anti-correlated with calcium for mature fern pinna with sporophyte[13]. The difference in elemental distribution is ascribed to the inconsistency of growth stage.

The young frond without sporophyte was subjected to7.5-ppm arsenate treatment for 3.5 hr. Arsenic concentrations over 35,000 ppm were detected in whole young pinnae. Figure 1 shows the elemental maps on the young pinna section at three positions as indicated ((a): near midrib, (b): between midrib and edge, (c): edge). The maximum value of colour bar was lined up for each element at three positions. In the region (a), arsenic and potassium show similar distribution and their concentrations are higher in the mesophyll. Phosphorus, sulfur, chlorine, and calcium are uniformly distributed over the whole pinna section. Arsenic concentration is considerably high in the region (b), which was consistent with our previous results[12,14]. In the regions (b) and (c), phosphorus, potassium and arsenic show a tendency to distribute more in the mesophyll than in the epidermis. Since the chemical form between orthophosphate and arsenate is similar, the arsenic distribution is accompanied by transportation of elements needed for keeping cell metabolism. It is reported that arsenic and potassium are localized in pinna epidermis of the fern[15], which is not consistent with the present result, while the correlation in distribution between arsenic and potassium are consistent. The rate of elemental transportation from mesophyll to epidermis might be limited at the initial uptake stage, so the time duration in the present study is considered to be shorter than that in ref.15.

Figure 2 shows elemental distributions on the pinna section of young fern subjected to 7.5-ppm arsenite treatment for 3.5 hr. Arsenic distribution is quite different from that of the other elements and only accumulated in the middle region of the pinna mesophyll. The concentration of arsenic decreased one hundredth of arsenate, indicating the slow uptake rate for arsenite by the fern fronds. These findings infer existence of a certain kind of transportation barrier for arsenite in pinna tissues of the fern. The young frond without sporophyte was treated with 200-mM arsenate solution for 60 hours. Figure 3 shows very different distributions of elements on the sliced pinna section from those shown in Fig. 1, which indicates that high arsenic concentration and long transpiration time results in a fatal damage to the fern tissues. Arsenic of ca. 60,000 ppm is distributed in the upper epidermis and correlated with silicon and calcium that are translocated due to the metabolic change in the pinna tissues. Lombi, et al. reported the translocation of silicon in high concentration for the fern sample containing arsenic by EDXA technique[15]. Calcium is also largely required for keeping a structure and a function of plant cell walls at intense growth phase.

Hence, it is highly probable that silicon and calcium are translocated to maintain the morphology of pinna tissues concentrating actively arsenic unnecessary for vital activity of a leaf. The high-concentration spots of sulfur, chlorine and potassium also indicate a metabolism change of the whole pinna tissues exposed to a transpiration flow of high arsenic concentration, although those elements are translocated differently from arsenic.

Conclusion

The micometer-scale area mapping of elements using the in-air micro PIXE system revealed the arsenic accumulation and translocation of elements essential to a plant metabolism in pinna tissues of living *Pteris vittata* that was supplied with arsenate and arsenite to the frond separately via xylem vessel using transpiration flow. The uptake rate was two orders higher for arsenate than for arsenite. Transportation from mesophyll to epidermis was a rather slow process for arsenite uptake. A high loading of arsenate at longer uptake-time caused the translocation of silicon and calcium accompanying by the arsenic accumulation in the epidermis of fern pinnae, and then the morphology of pinna tissue was maintained satisfactorily in discoloured epidermis with the arsenic-accumulation damage. Hence, the in-air micro-PIXE analysis is an effective measure for undertaking a phytoremediation research of hyper-accumulator plants.

References

1) Ma L.Q., Komar K.M., Zhao F.J., et al., Nature **409** (2001) 579.
2) Duan G.L., Zhu Y.G., Tong Y.P., et al., Plant Physiol. **138** (2005) 461.
3) Ellis D.R., Gumaelius L., Indriolo E., Pickering I.J., Banks J.A., Salt D.E., Plant Physiol. **141** (2006) 1544.
4) Webb S.M., Gaillard J.F., Ma L.Q., Tu C., Environmental Science and Technology **37** (2003) 754.
5) Wang J., Zhao F., Meharg A.M., et al., Plant Physiol. **130** (2002) 1552.
6) Pickering I.J., Gumaelius L., Harris H.H., et al., Environmental Science and Technology **40** (2006) 5010.
7) Su Y.H., McGrath S.P., Zhu Y.G., Zhao F.J., New Phytologist **180** (2008) 434.
8) Samanta G., Clifford D.A., Environ. Sci. Technol. **39** (22) (2005) 8877.
9) Matsuyama S., Ishii K., Abe S., et al., Int. J. of PIXE **15** (1&2) (2005) 41.
10) Matsuyama S., Ishii K., Yamazaki H., et al., Nucl. Instr. and Meth. **B260** (2007) 55.
11) Ryan C.G., Van Achterbergh E., Yeats C.J., et al., Nucl. Instr. and Meth. **B188** (2002) 18.
12) Yamazaki H., Ishii K., Matsuyama S., et al., X-ray SPECTROMETRY **37** (2008) 184.
13) Hokura A., Omuma R., Terada Y., et al., J. of Analytical Atomic Spectrometry **21** (2006) 321.
14) Yamazaki H., Ishii K., Matsuyama S., et al., Int. J. of PIXE **18** (3&4) (2004) 241.
15) Lombi E., Zhao F.J., Fuhrmann M., Ma L.Q., McGrath S.P., New Phytologist **156** (2002) 195.

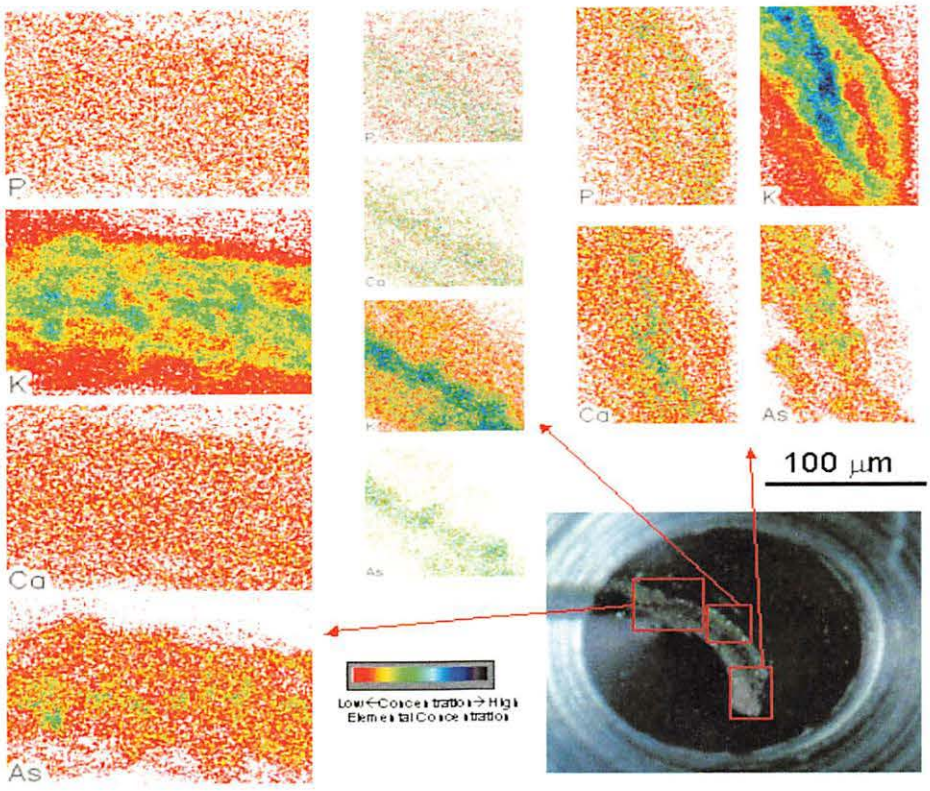

Figure 1. Elemental maps on a young pinna section at three positions, (a):near midrib, (b):between midrib and edge, (c):edge). Young frond was subjected to 7.5-ppm arsenite treatment for 3.5 hours.

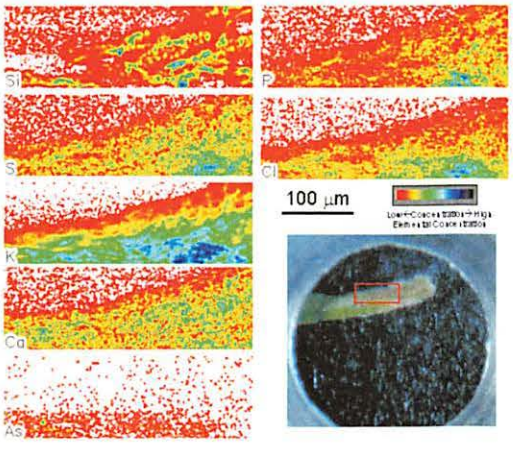

Figure 2. Elemental distributions of pinna section of young frond subjected to 7.5-ppm arsenite treatment for 3.5 hours.

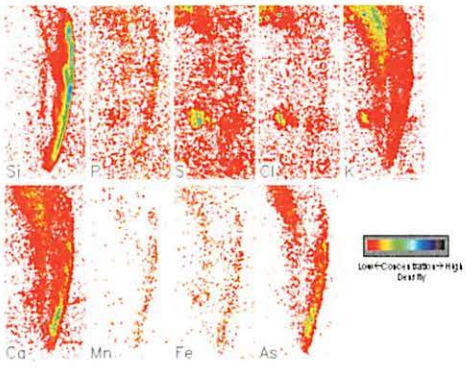

Figure 3. Elemental maps of pinna section treated with 200-mM arsenate solution for 60 hours

VI. RADIOCHEMISRTY AND NUCLEAR CHEMISTRY

VI. 1. Development of a Simplified MA Separation Process Using Novel R-BTP Adsorbents – II

Kuraoka E., Usuda S., Liu R., Xu Y., Kim S.Y., Yamazaki H., and Ishii K.

Cyclotron and Radioisotope Center, Tohoku University

Introduction

In recent years, many soft-donor ligands have been developed for liquid-liquid solvent extraction separation of trivalent minor actinides (MA: Am and Cm) and/or rare earths (RE) from the other fission products (FP) in the high level radioactive liquid waste (HLLW), which is generated by spent fuel reprocessing. Especially, a new type of nitrogen-donor ligand, R-BTP (BTP: 2,6-Bis-(5,6-Dialkyl-1,2,4-Triazin-3-yl)Pyridine, R: alkyl group [C_nH_{2n+1}]), which was discovered by Kolarik *et al.*[1,2], shows high extraction selectivity for Am(III) over RE(III) and attracts a great deal of attention because its constituent elements are C, H, O and N which are combustible after use up. Figure 1 shows the chemical structure of the R-BTP.

On the other hand, to overcome the demerits of solvent extraction method and to advantage the merits of R-BTP, another technology of extraction chromatography for separation of MA(III) has been proposed, which combines the selectivity of solvent extraction with the ease of operation of column chromatography. Kuraoka *et al.* have synthesized several R-BTP adsorbents with different alkyl groups for the extraction chromatography and investigated their fundamental properties such as adsorbability and stability[3-9]. It was found that separation property and stability of the R-BTP adsorbents depended on the structure of alkyls, i.e. number of carbons (length of chain) and different branched chain. Separation factors between Am(III) and Eu(III) are relatively high in the case of normal R-BTP adsorbents with straight 3~7 carbon chain[6,7], and the branched R-BTP (*iso*buthyl-BTP [C=4]) adsorbent is more stable than normal R-BTP adsorbents in $\leq$3 M HNO_3 solution[5,7].

The final object of this work is, by synthesizing novel R-BTP adsorbents (*i.e.*

extraction resins), to establish a simplified MA direct separation process (see Fig. 2). In the fiscal year (FY) 2008, *i) iso*hexyl-BTP [C=6] and *iso*heptyl-BTP [C=7] extraction resins were synthesized by impregnating the R-BTP ligands (*i.e.* extractants) into the macroporous silica/polymer composite support (SiO_2-P particles), then, *ii)* adsorption properties of typical FP including RE(III) with HNO_3 solution onto the resins, and *iii)* chemical and thermal stabilities of the resins were examined[10,11]. In the FY 2009, *(1)* adsorption and desorption properties of Am(III) including typical FP elements and U with HNO_3 solution onto the resins, *(2)* radiolytic stabilities of the resins were examined, and *(3)* another type of novel R-BTP resins (*Cy*heptyl-BTP/SiO_2-P) was prepared and attempted to obtain its fundamental properties.

Experimental

As the novel R-BTP adsorbents, *iso*hexyl-, *iso*heptyl- and *Cy*heptyl-BTP extraction resins were prepared by impregnating the respective R-BTP extractants into the macroporous silica/polymer composite support (SiO_2-P particles), according to the reported procedures[9].

Adsorption and desorption properties were evaluated by batch experiment. The former was obtained by measuring distribution coefficient, K_d[10,11]. The concentration (or radioactivity) of ^{241}Am, which is one of typical MA nuclides, and simulated FP (Cs, Sr, Zr, Mo, Pa, *etc.*) including RE (Y, Ce, Nd, Eu, Dy, *etc.*) in solution was analyzed by γ-ray spectrometer (well-type NaI(Tl) scintillation counter) and ICP-AES (inductively coupled plasma–atomic emission spectrometer), respectively.

Radiolytic stabilities of the resins were examined under relatively low dose (about 40 Gy/h) contacting with various concentration of HNO_3 concentration by irradiating γ-rays from ^{60}Co. Leakage of R-BTP extractants, degradation evalution and thermal stabilities of the resins under γ-ray irradiation were examined with TOC (total organic carbon analyzer), FT-IR (Fourier transform infrared spectrophotometer), and TG-DTA (thermogravimetry-differential thermal analyzer).

Results and Discussion

(1) Adsorption and desorption properties

Figures 3 and 4 show dependence of K_d on HNO_3 concentration onto *iso*hexyl- and *iso*heptyl-BTP resins, respectively, in 3 h at 25°C. In 2~3 M (mol/m^3) HNO_3 solution,

Am(III) seems to be possibly separated from main FP including even heavy RE(III). Separation factor between Am and heavy RE were ≈100 and more. It was found that Am was probably separated from U and Tc, and the separation of Am from Pd required further investigating.

On the other hand, adsorption rate with 3 M HNO_3 solution and desorption rate with H_2O onto *iso*hexyl- and *iso*heptyl-BTP resins at 25°C were extremely slow. Consequently, it was difficult to separate Am from FP by column experiment at 25°C. As compared with two resins, the adsorption and desorption rates onto *iso*hexyl-BTP resin were much higher than those onto *iso*heptyl-BTP resin. Therefore the column experiment using *iso*hexyl-BTP resin at 50°C will be worth performing.

(2) Radiolytic stabilities

In relation to the radiolytic stability, *i)* effects of γ-ray irradiation on adsorbability of RE onto *iso*hexyl- and *iso*heptyl-BTP resins, *ii)* leakage of R-BTP extractants from the resins with TOC, *iii)* degradation of the resins with FT-IR, and *iv)* thermal decomposition of the resins with TG-DTA were investigated during 30~120 d.

The adsorbability of RE (Eu, Gd and Dy) onto the both resins was evaluated by obtaining the K_d values. The values seriously decreased with increasing dose (30~120 kGy) and concentration of HNO_3 (0.01~3 M) except for 0.01 M HNO_3, as compared with those by non-irradiation. As a result of TOC analysis of liquid phase, generally, but not always, increasing irradiation dose and concentration of HNO_3 (0.1~3 M) tended to increase leakage of R-BTP extractants from R-BTP resins. Degradation of the resins examined with FT-IR was observed a little in 0.1 M HNO_3, and it increased with acid concentration. The phenomena seemed to be accelerated by γ-ray irradiation. Concerning thermal stabilities, serious difference between irradiation and non-irradiation was not observed with TG-DTA. Blow about 120 kGy, the resins were decomposed by HNO_3 rather than γ-ray irradiation.

(3) Synthesis of another type of R-BTP resin

Quite recently, similar types of ligands to the R-BTP extractants have been vigorously developed[12-16], which contain plural-pyridine structure and/or plural phenyl groups, and are expected to be improved in hydrolysis (stability of HNO_3) and radiolysis. One of the authors has also designed and synthesized another type of ligand, *Cy*heptyl-BTP (*cyclic*-heptyl-BTP) extractant, as shown in Fig. 5, and then prepared another novel

adsorbent, *Cy*heptyl-BTP/SiO_2-P resin, by impregnating the extractant into the macroporous SiO_2-P particles. Its fundamental properties, except for adsorbability and radiolytic stabilities, were investigated by analyzing the resin with FT-IR, TG-DTA, *etc*. The chemical structure of the resin was verified by analyzing the *Cy*heptyl-BTP extractant, SiO_2-P particles and *Cy*heptyl-BTP/SiO_2-P resins with FT-IR and so on. Table 1 shows the TG-DTA results of *Cy*heptyl-BTP resin, comparing with *iso*hexyl- and *iso*heptyl-BTP resins. It was found that thermal decomposition property of *Cy*heptyl-BTP resin was similar to that of *iso*hexyl- and *iso*heptyl-BTP resins.

Conclusions

Adsorbability of Am in 2~3 M HNO_3 solution onto *iso*hexyl- and *iso*heptyl-BTP adsorbents (*i.e.* extraction resins) showed excellent property for main FP including RE (separation factor ≥100), but adsorption rate with 3 M HNO_3 solution and desorption rate with H_2O were considerably slow at 25°C. In addition, stabilities of the resins against γ-ray irradiation during 30~120 d showed the poor quality in adsorbability of RE, leakage of R-BTP extractants, degradation and thermal decomposition of the resins, as compared with the case of non-irradiation. Therefore, another type of R-BTP resin (Cyheptyl-BTP/SiO_2-P) was synthesized and its evaluation study has started. Batch and column experiments at not only 25°C but also 50°C will be necessary to accelerate the adsorption and desorption rates.

This work has started from October, 2008, and will be over the end of FY2010. More detailed adsorption/desorption (or elution) properties and hydrolytic/radiolytic stabilities will be examined by batch and column experiments in order to construct the simplified MA direct separation process.

Acknowledgments

This study is a part of the result of "Development of a Simplified MA Separation Process Using Novel R-BTP Adsorbents" carried out under the Strategic Promotion Program for Basic Nuclear Research by the Ministry of Education, Culture, Sports, Science and Technology of Japan.

References

1) Kolarik Z., et al., Solv. Extr. Ion Exch. **17** (1999) 23.
2) *idem*, *ibid.* **17** (1999) 1155.
3) Wei Y.Z., et al., Proceedings of 16th Pacific Basin Nuclear Conference (16PBNC), Aomori, Japan, Oct. 13-18, 2008, Paper ID P16P 1033.

4) Zhang A., et al., J. Radioanal. Nucl. Chem. **274** (2007) 455.
5) Hoshi H., et al., J. Alloys Comp. **408-412** (2006) 1274.
6) Wei Y.Z., et al., *ibid.* **374** (2004) 447.
7) Wei Y.Z., et al., J. Nucl. Sci. Technol. **Suppl.3** (2002) 761.
8) Wei Y.Z., et al., *ibid.* **37** (2000) 1108.
9) Wei Y.Z., et al., Nucl. Technol. **132** (2000) 413.
10) Usuda S., et al., J. Ion Exchange **21** (2010) 35.
11) Kuraoka E., et al., CYRIC Annual Report 2008 (2009) 129.
12) Geist A., et al., Solv. Extr. Ion Exch. **24** (2006) 463.
13) Nilsson M., et al., *ibid.* **24** (2006) 299.
14) *idem, ibid.* **24** (2006) 823.
15) Retegan T., et al., *ibid.* **25** (2007) 417.
16) Smirnov I.V., et al., Radiochim. Acta **97** (2009) 593.

Table 1. Comparison with TG-DTA results of three R-BTP/SiO_2-P resins.

R-BTP resins	Weight (mg)	Loss weight (%)					
		<100 °C	100~170 °C	170~234 °C	234~368 °C	368~600 °C	<600 °C (Total)
*Cy*heptyl-BTP	21.2	1.08	2.18	3.88	25.8	17.2	50.1
*iso*hexyl-BTP	35.0	0.96	2.45	6.21	24.8	14.8	49.2
*iso*heptyl-BTP	19.3	0.71	3.17	6.18	25.8	13.8	49.7

Atmosphere gas: O_2, gas flow rate: 30 mL/min, temperature elevating rate: 1 °C/min.

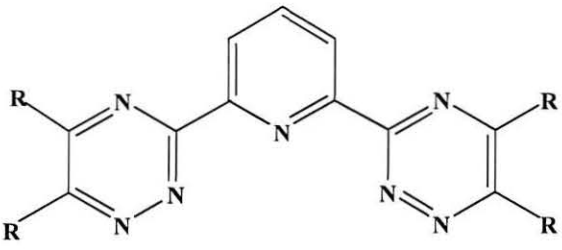

R-BTP

Figure 1. Chemical structure of R-BTP (**BTP**: 2,6-bis-(5,6-dialkyl-1,2,4-triazin-3-yl)pyridine, **R**: alkyl group [C_nH_{2n+1}]).

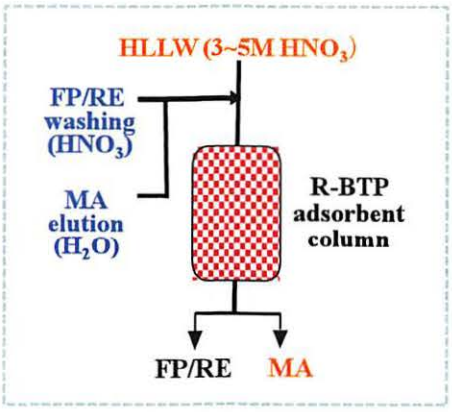

Figure 2. Simplified MA direct separation process by use of novel R-BTP adsorbent column (**MA**: Am, Cm, **RE**: Y, Nd, Eu, *etc.*, **FP**: Cs, Sr, Zr, Mo, Tc, Ru, Rh, RE, *etc.*).

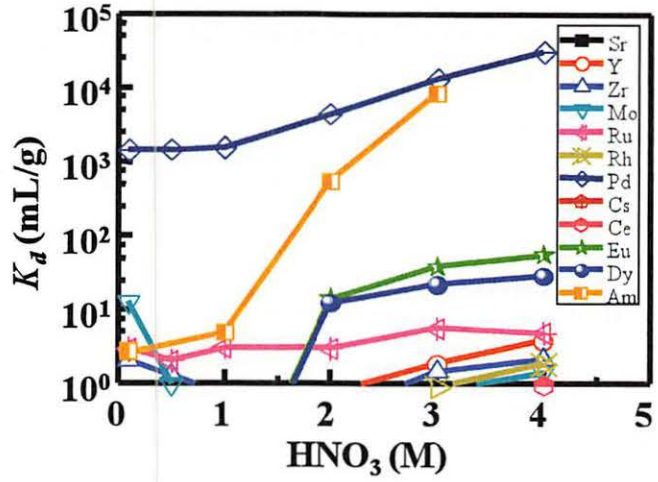

Figure 3. Dependence of K_d on HNO_3 concentration onto *iso*hexyl-BTP/SiO_2-P resin in 3 h at 25°C. [K_d (U): 1~5, K_d (Tc): 3~20, K_d (Cs, Sr, Y, Mo, Ce, Rh)≤10^0].

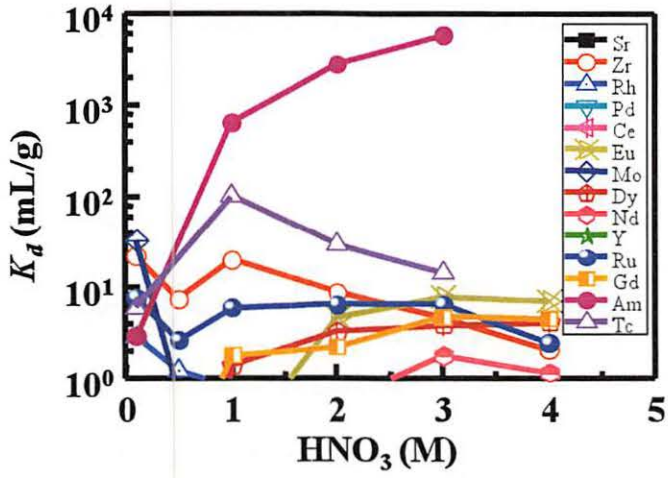

Figure 4. Dependence of K_d on HNO_3 concentration onto *iso*heptyl-BTP/SiO_2-P resin in 3 h at 25°C. [K_d (Pd)>10^4, K_d (U): 2~3, K_d (Cs, Sr, Y, Mo, Ce, Rh)≤10^0] .

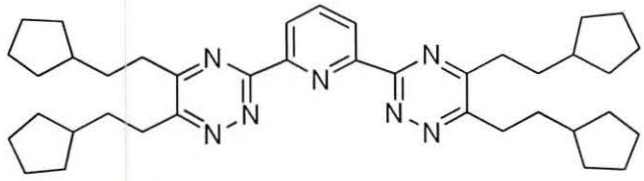

Figure 5. Chemical structure of *Cy*heptyl-BTP.

VI. 2. Study on Selective Separation of Cesium Using a Macroporous Silica-Based Supramolecular Recognition Absorbent

Tozawa D.[1], Wu Y.[2], Ito T.[1], Tada T.[2], Hitomi K.[2], Kuraoka E.[2], Kim S-Y.[2], Yamazaki H.[2], and Ishii K.[1]

[1]*Graduate School of Engineering, Tohoku University*
[2]*Cyclotoron and Radioisotope Center, Tohoku University*

Introduction

Recently, much attention has been given to the selective separation and recovery of Cesium(Cs)-137 from high level liquid waste (HLLW) in relation to the partitioning of radioactive nuclides and their effective utilization[1-3]. Cs-137 having a relatively long half-life of about 30 years exhibits high radioactivity and heat generation. In the HLLW, large amounts of Cs group (~3.6 kg/1tHU, 45 GWd/t) are contained[4]. Therefore, selective separation of Cs-137 from HLLW is an important environmental issue for nuclear waste management. In addition, the purified Cs is also expected for radiation and heat sources in the field of medicine and industry.

Many methods for the separation of Cs(I) such as solvent extraction, ion exchange and co-precipitation have been studied[5-8]. In the liquid-liquid solvent extraction process, supramolecular recognition agents are well known to have selective extraction ability to Cs(I). In order to utilize these extractants having high affinity for Cs(I), the impregnation methods have been proposed to fix the extractant on different supporting matrices[9-12]. 1,3-[(2,4-Diethylheptylethoxy)oxy]-2,4-crown-6-calix[4]arene(Calix[4]arene-R14), a kind of supramolecular recognition composite, which shows high selectivity toward Cs(I) and excellent radiation stability, can act as one of the most promising adsorbent for the uptake of Cs(I) [13]. In this study, we have attempted to loaded the Calix[4]arene-R14 extractant and a molecule modifier 1-dodecanol into the SiO_2 silica based polymer support (SiO_2–P) by using its high immobilizing ability for the selective separation of Cs(I) from HLLW. The present paper deals with the preparation of Calix[4] arene-R14 and dodecanol-loaded

SiO_2-P ((Calix[4] + Dodecanol)/SiO_2-P) , characterization and the evaluation of its uptake abilities.

Experimental

Materials

The 1,3-[(2,4-Diethylheptylethoxy)oxy]-2,4-crown-6-calix[4]arene (Calix[4]arene-R14, 97%) was purchased from Rikoh Kagaku co. ltd. and used without further purification. The Molecular structure of Calix[4]arene-R14 is shown in Fig. 1. 1-dodecanol was procured from Wako Pure Chemical Industries, Ltd. The SiO_2 silica based polymer support (SiO_2–P) was synthesized by following the literature method[14]. Other chemicals such as $CsNO_3$, $Sr(NO_3)_2$, $RE(NO_3)_3 \cdot 6H_2O$ (RE = La, Nd, Sm, and Gd), $ZrO(NO_3)_2 \cdot 2H_2O$ and $(NH_4)_6Mo_7O_{24} \cdot 4H_2O$ were reagent grade supplied by Kanto Chemical Co. Palladium nitrate solution (4.5wt%) and ruthenium nitrosyl nitrate solution (1.5wt%) were purchased from Sigma-Aldrich Chemical Co.

Preparation of (Calix[4] + Dodecanol)/SiO_2-P

The Calix[4]arene-R14 and a molecule modifier 1-dodecanol impregnated on SiO_2-P support ((Calix[4] + Dodecanol)/SiO_2-P) was prepared as follows. First, the Calix[4]arene-R14 and 1-dodecanol were dissolved in dichloromethane and then mixed with the SiO_2-P particles in a glass flask for approximately 0.5 h at 25°C. After that the mixture was stirred gently for 2 h at 40°C under reduced pressure by using rotary evaporator in order to enhance impregnating, and finally vacuum-dried for 1d at 40°C.

Characterization

The surface morphology of (Calix[4] + Dodecanol)/SiO_2-P was observed by scanning electron microscopy (SEM, Hitachi TM-1000). Thermal stability of (Calix[4] + Dodecanol)/SiO_2-P was evaluated by thermal gravimetry and differential thermal analysis (TG-DTA, Shimadzu DTG-60) under the operation conditions of temperature range: 25 ~ 600°C and heating rate: 1°C/min.

Determination of Distribution Coefficient (K_d)

The distribution of metal ions for (Calix[4] + Dodecanol)/SiO_2-P was estimated by batch method. An aqueous solution (4 cm^3) containing 5mM metal ions was contacted with 0.2 g of (Calix[4] + Dodecanol)/SiO_2-P at 25±1°C up to 5 h, which was found to be

sufficient for attaining equilibrium. The concentrations of Cs(I) and other metal ions were measured by atomic absorption spectrophotometry (AAS, Simadzu AA-660) and inductively coupled plasma atomic absorption spectrometry (ICP-AES, Simadzu ICPS-7510). The distribution coefficient (K_d, cm^3/g) of a metal ion on (Calix[4] + Dodecanol)/SiO_2-P is defined as :

$$K_d = ((C_0 - C_f) / C_f) \times V / m \qquad \text{(Eq. 1)}$$

where C_0 and C_f are the concentration of metal ions at initial and at equilibrium, respectively; m (g) the weight of dry (Calix[4] + Dodecanol)/SiO_2-P composite, V (cm^3) the volume of aqueous phase.

Results and Discussion

Surface Morphology and Thermal Stability

The surface morphology of (Calix[4] + Dodecanol)/SiO_2-P was examined by SEM (Fig. 2). Obvious spherical and porous particles are obtained. The particle size of (Calix[4] + Dodecanol)/SiO_2-P was estimated to be 50 μm in diameter by the SEM image. The thermal stability was evaluated by TG/DTA analyses within the temperature range 25°~600°C (Fig. 3). The result of TG and DTA for (Calix[4] + Dodecanol)/SiO_2-P indicates three different weight loss ranges: 20-180°C, 200-330°C and 330-510°C. The first weight loss is due to the desorption of water from SiO_2-P, the second and third weight loss are due to the thermal decomposition of styrene-divinylbenzene(SDB) copolymer and organic solvents(Calix[4] + Dodecanol), respectively. These findings suggest that the (Calix[4] + Dodecanol)/SiO_2-P is thermally stable up to 200°C.

Uptake Rate

In order to evaluate the equilibration time of Cs(I) and other metal ions for (Calix[4] + Dodecanol)/SiO_2-P, the effect of shaking time on K_d value was examined in the presence of 3 M HNO_3 by batch method (Fig. 4). The uptake rate of Cs(I) for (Calix[4] + Dodecanol) /SiO_2-P in 3 M HNO_3 attained equilibrium within 0.5 h, and relatively large K_d value above 70 cm^3/g was obtained. On the other hand, almost no uptake for other metal ions were observed, indicating that (Calix[4] + Dodecanol)/SiO_2-P gel is effective for the selective separation of Cs(I).

Effect of HNO_3 Concentration

As for Cs(I), the K_d value was considerably lowered in the range of 0.1~4 M HNO_3. However, the K_d value tended to increase with increasing HNO_3 concentration of 1 ~ 4 M HNO_3 and relatively large K_d value above 90 cm^3/g were obtained around 4 M HNO_3 (Fig. 5). This effect is due to the extraction of an ion-pair species according to the following related solvent extraction reaction reported earlier[13].

$$Cs^+_{(aq.)} + NO_3^-{}_{(aq.)} + Calix[4]_{(org.)} \Leftrightarrow [Cs \cdot Calix[4] \cdot NO_3]_{(org.)} \quad \text{(Eq. 2)}$$

On the other hand , the K_d values for Sr(II), Pd(II), Ru(III), La(III), Nd(III), Sm(III), Gd(III), Zr(IV) and Mo(VI))were lower than 10 cm^3/g, indicating that the (Calix[4] + Dodecanol)/SiO_2-P had excellent selectivity for Cs(I).

Uptake Isotherm

In order to clarify the uptake mechanism, adsorption isotherms were obtained in a wide range of initial Cs(I) concentrations. The equilibrium amounts of Cs(I) adsorbed on (Calix[4] + Dodecanol)/SiO_2-P approached a constant value with increasing Cs(I) concentration (Fig. 6), suggesting that the uptake of Cs(I) follows a Langmuir-type adsorption equation. A fairly linear relation between C_{eq}/Q_{eq} and C_{eq} was obtained from the Langmuir plots derived from Fig. 6 and the Q_{max} value for (Calix[4] + Dodecanol)/SiO_2-P was estimated to be 0.19 mmol/g.

Conclutions

The uptake properties of Cs(I), characterization and dynamic adsorption properties were investigated by using (Calix[4] + Dodecanol)/SiO_2-P. The uptake of Cs(I) for (Calix[4] + Dodecanol)/SiO_2-P was fairly fast in the initial stage and the uptake equilibrium attained within 0.5 h. The $K_{d,\,Cs}$ was increase with increasing HNO_3 concentration and relatively large K_d values above 90 cm^3/g were obtained around 4 M HNO_3. The uptake isotherm of Cs(I) followed a Langmuir-type adsorption equation. Thus, the Calix[4]arene-R14 and a molecule modifier 1-dodecanol impregnated on SiO_2-P support is effective for the selective separation and recovery of Cs(I).

References

1) Technical Report Series, No. 356, IAEA, Vienna, Austria (1993).
2) Tranter T.J., Herbst R.S., Todd T.A., et al., Advances in Environmental Research **6** (2002) 107 .

3) Riddle C.L., Baker J.D., Law J.D., McGrath C.A., et al., Solvent Extr. Ion Exch. **23** (2005) 449.
4) Ando R., Takano T., JAERI-Rearch 99-004 (1994).
5) Buch R.P., and Acres G.J.K., AERE-R-12830 (1987).
6) Dietz M.L., Horwitz E.P., Rhoads S., Bartsch R.A., et al., Solvent Extr. Ion Exch. **14** (1996) 1.
7) Chiarizia R., Horwitz E.P., Bauvais R.A., et al., Solvent Extr. Ion Exch. **16** (1998) 875.
8) Reguillon A.F., Dunjic B., Lemaiue M., et al., Solvent Extr. Ion Exch. **19** (2001) 181.
9) Gilson C.D., Thomas A., J. Chem. Tech. Biotechnol. **62** (1995) 227.
10) Wei Y.Z., Zhang A., Kumagai M., Watanabe M., et al., J. Nucl. Sci. Technol. **41** (2004) 315.
11) Kozlowski C.A., Kozlowaska J., Pellowaski W., et al., Desalination **198** (2006) 141.
12) Wu Y., Mimura H., Niibori Y., J. Radioanalytical and Nuclear Chemistry **281** (2009) 513.
13) Zhang A., Hui Q., Chemical Engineering Journal **159** (2010) 58.
14) Wei Y.Z., Kumagai M., Takashima Y., et al., Nucl. Technol. **132** (2000) 413.

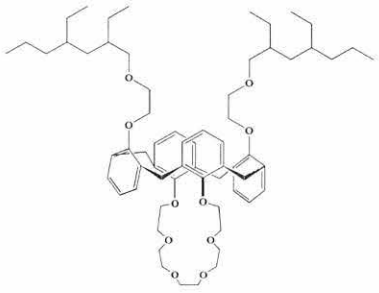

Figure 1. Molecular structure of Calix[4].

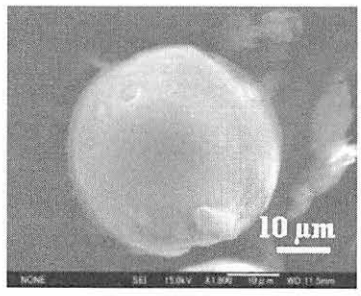

Figure 2. SEM image of the surface of (Calix[4] + Dodecanol)/SiO_2-P.

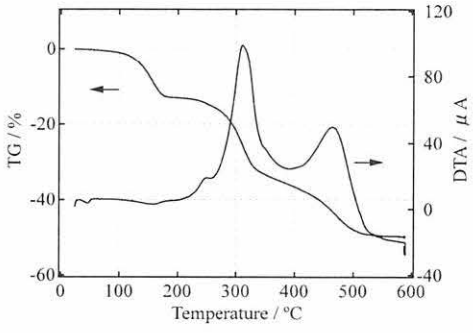

Figure 3. TG / DTA curves for (Calix[4] + Dodecanol)/SiO_2-P.

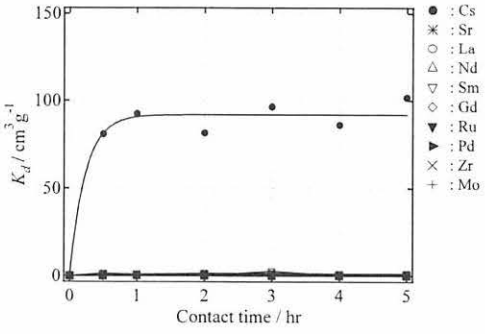

Figure 4. Effects of shaking time on K_d of different metal ions. *V/m*: 20 cm^3/g, [Metal]: 5mM, 3 M HNO_3: 25°C.

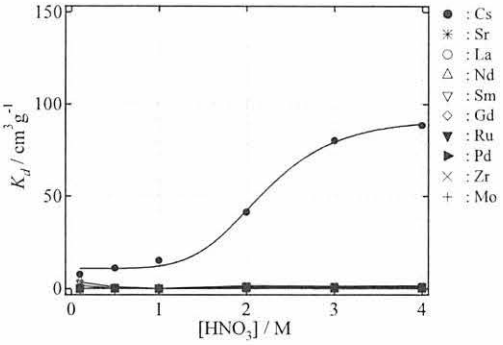

Figure 5. Effects of HNO_3 concentration on K_d of different metal ions. *V/m*: 20 cm^3/g, [Metal]: 5mM, 25°C.

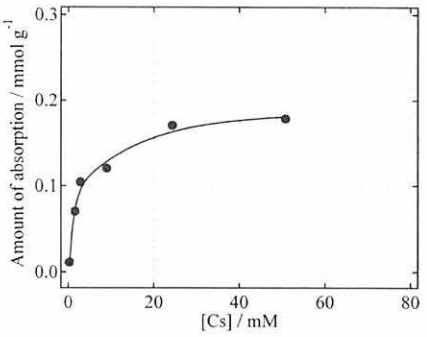

Figure 6. Uptake isotherm of Cs(I) for (Calix[4] + Dodecanol)/SiO_2-P. *V/m*: 20 cm^3/g, 3 M HNO_3: 25°C.

VII. RADIOPHARMACEUTICAL CHEMISTRY AND BIOLOGY

VII. 1. Synthesis and Biological Evaluation of a New Fluorine-18 Labeled MMP-2 Inhibitor for Cancer Imaging by PET

Furumoto S.[1,2], Sakai E.[2], Ishikawa Y.[2], and Iwata R.[2]

[1]*Tohoku University School of Medicine*
[2]*Cyclotron and Radioisotope Center Tohoku University*

Introduction

Matrix metalloproteinases (MMPs) consist of a large family of zinc-dependent endpeptidases that degrade specific components of the extracellular matrix. MMP-2, one of a member of the family, is deeply involved in degradation of type IV collagen (a major component of the basement membrane). Enzymatic activity of MMP-2 is generally low or undetectable in normal tissues but enhanced in pathological processes associated with tissue destruction, such as tumor growth and invasion. Therefore, in vivo evaluation of MMP-2 activity would be helpful for assessing such disease malignancy if we can do that non-invasively. For that purpose, we have been working on the development of PET probes for MMP-2 imaging[1,2]. In this study we designed and synthesized a new F-18 labeled MMP-2 inhibitor and biologically examined the potential for imaging active MMP-2 by PET.

Methods

The newly designed MMP-2 inhibitor, SAV49, was synthesized according to the scheme indicated in Fig. 1. Inhibitory activity of SAV49 was examined by in vitro MMP-2 activity assay. The IC_{50} value was determined from the dose-response curve. In addition to SAV49, its methyl ester derivative was also synthesized because such ester derivative can be a prodrug in vivo. As a precursor for synthesis of ^{18}F-labeled SAV49M, a corresponding nitro pyridine derivative was also prepared according to the scheme indicated in Fig. 2. Radiosynthesis of [^{18}F]SAV49M was carried out by a conventional nucleophilic substitution with [^{18}F]KF/Kryptfix2.2.2. in DMSO at 150°C for 10 min (Fig. 3). The radiolabeled product was isolated by semi-preparative reverse-phase HPLC.

For in vivo evaluation of the utility of [^{18}F]SAV49M, HT-1080 cell line was used for preparing subcutaneous tumor xenograft model mice. HT-1080 cells form tumor mass subcutaneously within a short period, and MMP-2 expression is well enhanced in the tumor mass. Ten days after implantation of HT-1080 the mice were used for biodistribution and metabolite analysis of [^{18}F]SAV49M. Radioactivity uptakes (%ID/g) of major organs and tumor and Radioactive metabolites of were investigated.

Results and Discussion

MMP-2 inhibition assay clearly indicated that SAV49 inhibited MMP-2 activity in a dose-dependent manner (Fig. 4). The IC_{50} value calculated from the inhibition curve was 0.61 μM. Decay corrected radiochemical yield of [^{18}F]SAV49M was about 60% on average with a radiochemical purity over 99% after HLC purification.

Biodistribution study of [^{18}F]SAV49M exhibited no increase of radioactivity uptake in bone over time (Fig. 5). This result suggest that [^{18}F]SAV49M has resistance to in vivo defluorination. Radioactivity uptakes of tumor and muscle showed similar change over time, suggesting non-specific uptake in tumor of [^{18}F]SAV49. Metabolites analysis of plasma samples revealed that 60 to 80 % of radioactive metabolite was identified as a form of SAV49 (Fig. 6). Meanwhile, examination of radioactivity distribution between erythrocytes and plasma clarified that nearly 100 % of radioactivity existed in the fraction of erythrocytes (Fig. 7). These results suggest that the probe in erythrocyte fraction could not move to the tumor tissue through plasma fraction, resulting in low tumor uptake of [^{18}F]SAV49. However, such unsymmetrical distribution of [^{18}F]SAV49 in the blood of rabbit was not observed. In the case of rabbit, unlike mice, radioactivity of plasma was greater than that of erythrocytes throughout 120 min. These results imply that tumor bearing mouse could be an unsuitable animal model for evaluation of [^{18}F]SAV49 in vivo and require further study to draw a conclusion of the utility as a probe for MMP-2 imaging.

Conclusions

In this study we newly designed and synthesized fluorine-18 labeled MMP-2 inhibitor [^{18}F]SAV49 for MMP-2 imaging by PET. Although the prodrug [^{18}F]SAV49M showd biodistribution study using tumor bearing mice indicated that the purpose was satisfactorily accomplished, tumor specific uptake was not observed in the tumor model. Radioactivity analysis of the blood suggested that specific retention of SAV49 in the

erythrocyte fraction caused the low tumor uptake. Such specific retention was not observed in the same study using a rabbit, suggesting that other species of animal would be necessary for evaluation of the utility of SAV49 as a MMP-2 imaging probe.

References

1) Furumoto S., Takashima K., Kubota K., Ido T., Iwata R., Fukuda H., Nucl. Med. Bio. **30** (2003) 119.
2) Furumoto S., Iwata R., Ido T., J. Lab. Comp. Radiopharm. **45** (2002) 975.

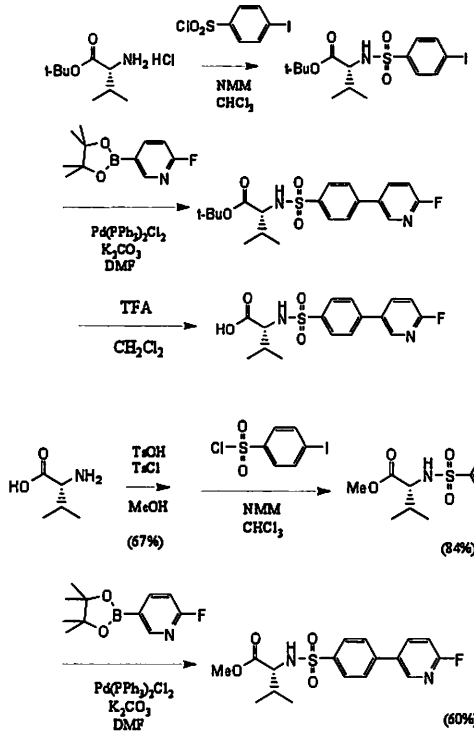

Figure 1. Synthesis of SAV49 and SAV49M.

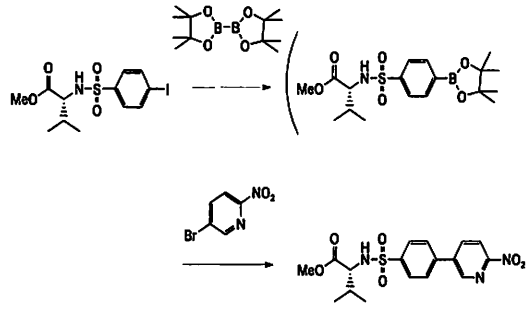

Figure 2. Synthesis of a precursor for [^{18}F]SAV49M.

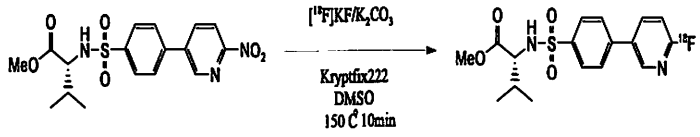

Figure 3. Radiosynthesis of [^{18}F]SAV49M.

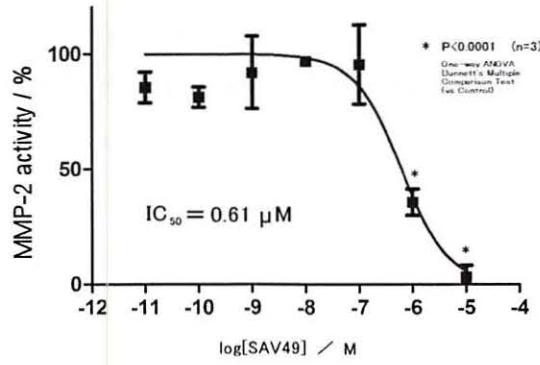

Figure 4. Inhibition curve of MMP-2 with SAV49.

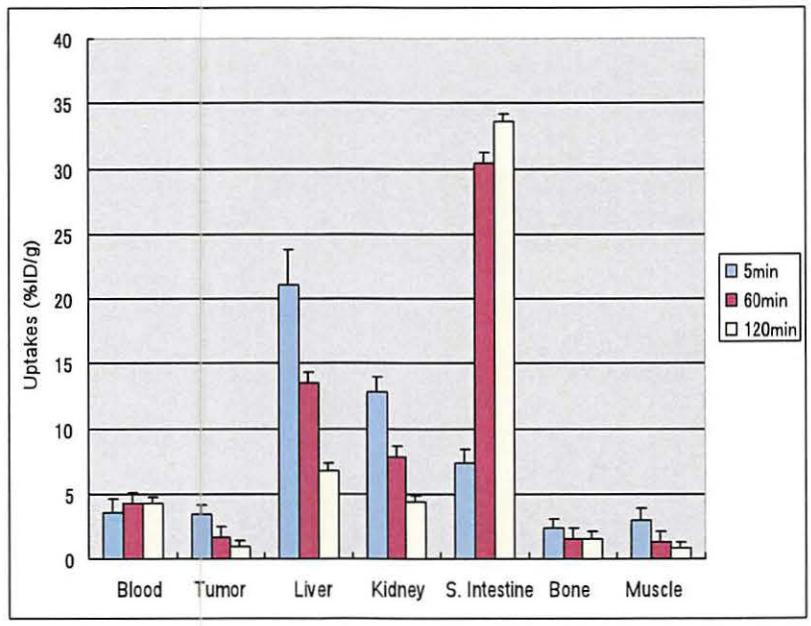

Figure 5. Biodistribution of [^{18}F]SAV49M.

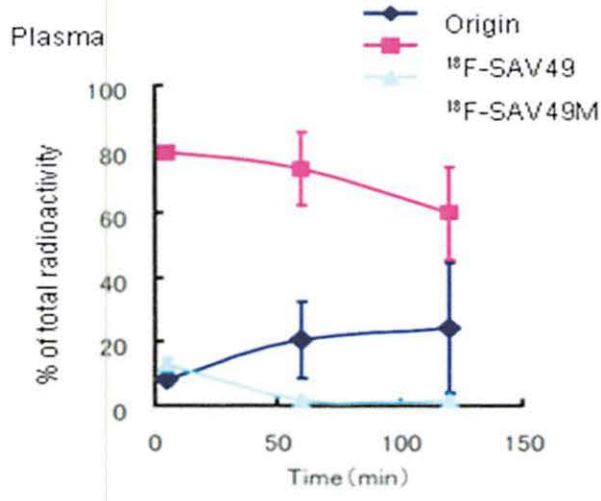

Figure 6. Metabolites of [^{18}F]SAV49M in mouse plasma.

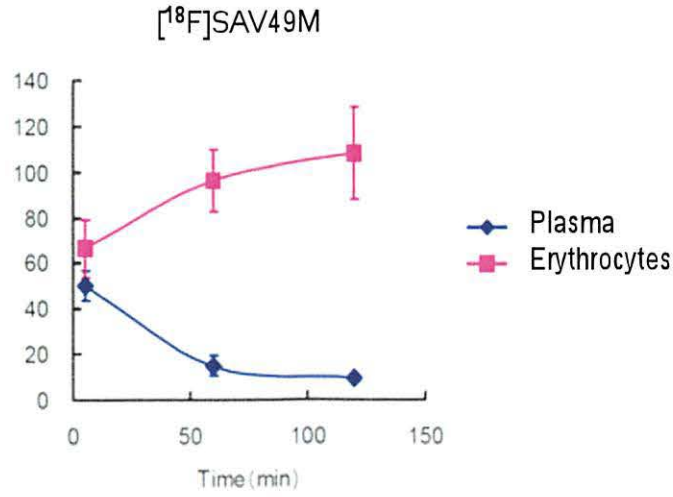

Figure 7. Distribution of [^{18}F]SAV49M in mouse blood.

VIII. NUCLEAR MEDICINE

VIII. 1. Imaging of Hypoxic Tissues in Glioblastoma by PET with [^{18}F]FRP-170, a New ^{18}F-labeled 2-Nitroimidazole Analog

Shibahara I.[1], Kumabe T.[1], Kanamori M.[1], Saito R.[1], Sonoda Y.[1], Watanabe M.[2], Iwata R.[3], Tashiro M.[3], Takanami K.[4], Kaneta T.[4], Takai Y.[5], Fukuda H.[6], and Tominaga T.[1]

Departments of [1]Neurosurgery[2] Pathology, and [4]Diagnostic Radiology, Tohoku University Graduate School of Medicine
[3]Cyclotron and Radioisotope Center, Tohoku University
[5]Department of Radiology, Hirosaki University School of Medicine & Hospital
[6]Department of Nuclear Medicine and Radiology, Institute of Development, Aging and Cancer, Tohoku University

Introduction

Tumor hypoxia arises in solid cancer tissues with inadequate supply of oxygen, and may be important in clinical diagnosis because hypoxia may determine tumor aggressiveness and treatment response[1,2], which are both essential information for treatment selection. The presence of hypoxic condition within brain tumors was confirmed using tube-type pO_2 sensors[3]. The mean intratumoral pO_2 value was 15.3±2.3 mmHg, and pO_2 in brain tissue around the tumor was 59.8±6.5 mmHg. However, these sensing methods are rather invasive, limiting the accessible tumor sites, and not easily applicable for routine clinical usage. A series of 2-nitroimidazoles have been developed as selective radiosensitizers of hypoxic cells, based on the property of selective accumulation and retention in hypoxic cells until the cells die[4]. Therefore, radiolabeled 2-nitroimidazoles have been developed for the direct visualization of tissue hypoxia in tumors[5].

^{18}F-fluoromisonidazole ([^{18}F]FMISO) was the first such radiopharmaceutical developed[6,7], and [^{18}F]FMISO positron emission tomography (PET) has been used to detect hypoxic areas in glioblastoma[8-10]. However, FMISO has failed to gain wider acceptance for routine clinical application because of various limitations, such as slow accumulation in hypoxic tumors, low target-to-background contrast, and significant amounts of radioactive metabolic products. Misonidazole is rather lipophilic, whereas high hydrophilicity is thought to be better for imaging hypoxia because of rapid blood clearance and high

target-to-background ratio. Many 2-nitroimidazole analogs have been developed by modifying the side chain, such as etanidazole with an octanol-water partition coefficient (p value) of 0.046[11]. Fluoroetanidazole (FETA) also has a lower p value (0.16)[12] than FMISO (0.40), so the levels of retention of [^{18}F]FETA in the liver and lung are significantly lower than those of [^{18}F]FMISO[13]. [^{18}F]fluoroerythronitroimidazole and [^{18}F]fluoroazomycin arabinoside have also been developed as hydrophilic hypoxia markers, with lower p value and better tumor-to-blood ratio than [^{18}F]FMISO[14,15].

RP170, 1-(2-hydroxy-1-[hydroxymethyl]ethoxy)methyl-2-nitroimidazole, a 2-nitroimidazole analog with a hydrophilic side chain has a p value of 0.094, much lower than that of misonidazole[16-18]. Recently, a new hypoxia imaging compound, 1-(2-fluoro-1-[hydroxylmethyl]ethoxy)methyl-2-nitroimidazole or [^{18}F]FRP-170, was developed for clinical PET imaging, which is expected to show improvements over [^{18}F]FMISO with regard to higher image contrast and faster clearance[19-21]. Hypoxic lesions of murine tumors, ischemic myocardium of rats, and hypoxic lesions in lung cancer patients have been visualized using this compound[19,20,22].

Here we describe the demonstration of hypoxic tissues in a patient with glioblastoma resistant to radiochemotherapy using [^{18}F]FRP-170 PET, and confirmed the mechanism of radioresistance as the induction of hypoxia-inducible factor 1 (HIF1)-alpha.

Materials and Methods

This study was conducted with the approval of the Ethics Committee of Tohoku University School of Medicine, and written informed consent was obtained from all participants. Three patients, a 53-year-old male with glioblastoma, a 68-year-old male with glioblastoma, and a 53-year-old female with oligodendroglioma, underwent [^{18}F]FRP-170 PET imaging and tissue specimens were obtained by biopsy or surgery.

[^{18}F]FRP-170 was prepared with an automated synthesizer using an on-column basic hydrolysis step as reported previously[23]. The overall radiochemical yield was around 20–30% (decay-corrected) with specific activity of >26 GBq/μmol within 60 minutes. The PET scans for patients were performed 120 minutes after intravenous bolus injection of about 370 MBq of [^{18}F]FRP-170 using a PET scanner (ECAT EXACT HR+; Siemens). Maximum standardized uptake values (SUVmax) were obtained by drawing regions of interest on the PET images covering the tumor and reference tissue in the contralateral normal hemisphere and posterior cervical muscle region.

The tissue specimens were examined by the same neuropathologist (M.W.) and the diagnosis was based on the classification of the World Health Organization[24]. All surgical specimens were examined for the detection of hypoxic tissues. Formalin-fixed, paraffin-embedded tumor tissue was cut into 2 μm sections and mounted on saline-coated slides. After deparaffinization, washing and blocking processes, the sections were incubated with goat polyclonal primary antibody of HIF1-alpha (Santa Cruz Biotechnology, Santa Cruz, CA), which was diluted 1:100, overnight at 4 degrees centigrade. Then sections were washed in phosphate buffered saline, and incubated with biotinylated anti-goat immunoglobulin G diluted 1:100 for 30 minutes at room temperature. Positive immunostaining for HIF1-alpha was judged as brown staining of the cytoplasm.

Illustrative Case

A 53-year-old male, who had previously been healthy, suddenly screamed meaningless words and lost consciousness for 5 minutes. A similar episode happened on the following night, so his family took him to a nearby emergency unit. On admission, he was slightly disoriented with motor aphasia. Computed tomography of the head revealed an edematous lesion in the left hemisphere with midline shift to the right (Fig. 1A). Magnetic resonance (MR) imaging of the head with gadolinium revealed a hypointense lesion mainly in the left insula with spotty enhancement (Fig. 1B). The episodes of the past two nights were diagnosed as symptomatic seizure, and 200 mg of zonisamide per day was prescribed.

The patient underwent a stereotactic needle biopsy, and the histological diagnosis was glioblastoma. He was treated with 60 Gy of radiation therapy combined with intravenous administration of nimustine hydrochloride. However, the tumor kept growing (Fig. 1C). Therefore, he underwent left osteoplastic fronto-temporal craniotomy and partial removal of the tumor. To avoid right hemiparesis, the medial part of tumor involving the left lateral lenticulostriate arteries was not resected (Fig. 1D). Follow-up MR imaging with gadolinium obtained 4 weeks after the surgery revealed progression of the tumor, and [^{18}F]FRP-170 PET showed a marked hypoxic lesion corresponding to the enhanced lesion on MR imaging (Fig. 2A, B). He underwent additional 27 Gy of booster irradiation localized to the enhanced lesion with oral administration of temozolomide. However, follow-up MR imaging revealed further progression of the tumor. Clinical examination showed right hemiparesis and aphasia. The patient was discharged for the best supportive care.

Results

[^{18}F]FRP-170 PET detected hypoxic lesion as high intensity areas, and the relative intensity was calculated by comparison with the control areas. In the illustrative case, the SUVmax values for tumor tissue and posterior cervical muscle were 1.6 and 1.0, respectively (Fig. 2B). The tumor/muscle (T/M) ratio was calculated as 1.6. This indicates that tumor cells were located in the hypoxic lesion. Immunostaining with HIF1-alpha antibody of the tissue obtained from the surgery showed many positive cells, with brown staining of the cytoplasm, indicating induction of HIF1-alpha protein and the presence of hypoxic condition within the tumor (Fig. 3B). Interestingly, the number of HIF1-alpha-positive cells increased in the second specimen obtained from the surgery after 60 Gy of radiation therapy (Fig. 3B) compared to the first tissue specimen from the initial biopsy (Fig. 3A).

In the second patient, a 68-year-old male with glioblastoma (Fig. 4A), SUVmax was 2.3 and T/M ratio was 2.3 (Fig. 4B), indicating the presence of marked hypoxic tissue. In the third patient, a 53-year-old female with oligodendroglioma (Fig. 4D), SUVmax was 1.3 and T/M ratio was 1.2 (Fig. 4E), indicating almost no hypoxic condition within the tumor. In accordance with the PET findings, immunostaining for HIF1-alpha showed many positive cells in the second patient with glioblastoma (Fig. 4C) and almost no positive cells in the third patient with oligodendroglioma (Fig. 4F).

Discussion

The present study showed that [^{18}F]FRP-170 PET could visualize hypoxic lesions in two glioblastoma patients, which were histologically confirmed as hypoxia by upregulation of HIF1-alpha protein (Figs. 3B and 4C), and demonstrated the absence of hypoxia in a patient with oligodendroglioma (Fig. 4E, F). The illustrative case had strong resistance to radiochemotherapy, suggesting that the hypoxic condition might be involved.

Assessment of the hypoxic condition within a tumor is useful to estimate the tumor aggressiveness[25] and prognosis[26] and select the optimum therapy. Pretreatment with nitroglycerin decreased hypoxia-induced resistance to anticancer drugs in lung adenocarcinoma patients[27], and the mechanism involved downregulation of HIF1-alpha[28]. Moreover, inhibition of HIF1-alpha in combination with temozolomide had robust antitumor efficacy in the *in vivo* glioma xenograft model[29]. Therefore, if the degree of hypoxia can be assessed noninvasively, we can take appropriate action to reduce the

hypoxia-induced resistance through downregulation of HIF1-alpha. We may be able to offer more aggressive therapy to patients with poor prognosis, which cannot be accepted for most patients due to the increased side effects[26].

Expression of HIF1-alpha was strong in 12 of 51 cases of oligodendroglioma, moderate in 21, weak in 8, and none in 10[30]. Our case of oligodendroglioma showed no HIF1-alpha immunostaining, possibly because this case was categorized in weak or none subgroup. HIF1-alpha expression correlates to increased risk of treatment failure and death in patients with breast and cervical cancers, despite the low tumor grade[26]. If this is also true in glioma, applying this imaging to glioma patients may be very important for treatment selection.

A significant difference was detected in the positive rate of HIF1-alpha immunostaining between the first and second tumor tissues obtained in the illustrative case (Fig. 3A, B). The patient was treated with 60 Gy of radiation therapy with nimustine hydrochloride between these two time points. Radiosensitive cells and/or cells in normoxia may have been eradicated by such treatments, whereas unresponsive cells or cells in hypoxia may have survived. This finding suggests that both the histopathology and hypoxic condition are important factors for treatment sensitivity.

Conclusion

[^{18}F]FRP-170 PET could visualize the hypoxic tissues within glioblastoma with relatively high T/M ratio, as confirmed by HIF1-alpha immunohistochemistry. Such findings can provide noninvasive indications of the aggressiveness and prognosis of glioma.

References

1) Brizel D.M., Dodge R.K., Clough R.W., Dewhirst M.W., Radiother Oncol. **53** (1999) 113.
2) Brown J.M., Int. J. Radiat. Oncol. Biol. Phys. **49** (2001) 319.
3) Kayama T., Yoshimoto T., Fujimoto S., Sakurai Y., J. Neurosurg. **74** (1991) 55.
4) Nunn A., Linder K., Strauss H.W., Eur. J. Nucl. Med. **22** (1995) 265.
5) Chapman J., Franko A., Sharplin J., Br. J. Cancer **43** (1981) 546.
6) Jerabek P.A., Patrick T.B., Kilbourn M.R., Dischino D.D., Welch M.J., Int. J. Rad. Appl. Instrum. **A37** (1986) 599.
7) Martin G.V., Caldwell J.H., Graham M.M., Grierson J.R., Kroll K., Cowan M.J., et al., J. Nucl. Med. **33** (1992) 2202.
8) Cher L.M., Murone C., Lawrentschuk N., Ramdave S., Papenfuss A., Hannah A., et al., J. Nucl. Med. **47** (2006) 410.
9) Spence A.M., Muzi M., Swanson K.R., O'Sullivan F., Rockhill J.K., Rajendran J.G., et al., Clin. Cancer Res. **14** (2008) 2623.
10) Tochon-Danguy H.J., Sachinidis J.I., Chan F., Chan J.G., Hall C., Cher L., et al., Nucl. Med. Biol. **29** (2002) 191.
11) Brown J.M., Workman P., Radiat. Res. **82** (1980) 171.

12) Barthel H., Wilson H., Collingridge D.R., Brown G., Osman S., Luthra S.K., et al., Br. J. Cancer **90** (2004) 2232.13) Rasey J.S., Hofstrand P.D., Chin L.K., Tewson T.J., J. Nucl. Med. **40** (1999) 1072.
13) Rasey J.S., Hofstrand P.D., Chin L.K., Tewson T.J., J. Nucl. Med. **40** (1999) 1072.
14) Kumar P., Stypinski D., Xia H., McEwan A., Machulla H., Wiebe L.I., J. Labelled. Comp. Radiopharm. **42** (1999) 3.
15) Yang D.J., Wallace S., Cherif A., Li C., Gretzer M.B., Kim E.E., et al., Radiology **194** (1995) 795.
16) Murayama C., Suzuki A., Sato C., Tanabe Y., Miyata Y., Shoji T., et al., Int. J. Radiat. Oncol. Biol. Phys. **22** (1992) 557.
17) Murayama C., Suzuki A., Suzuki T., Miyata Y., Sakaguchi M., Tanabe Y., et al., Int. J. Radiat. Oncol. Biol. Phys. **17** (1989) 575.
18) Sasai K., Shibamoto Y., Takahashi M., Abe M., Wang J., Zhou L., et al., Jpn. J. Cancer Res. **80** (1989) 1113.
19) Kaneta T., Takai Y., Iwata R., Hakamatsuka T., Yasuda H., Nakayama K., et al., Ann. Nucl. Med. **21** (2007) 101.
20) Kaneta T., Takai Y., Kagaya Y., Yamane Y., Wada H., Yuki M., et al., J. Nucl. Med. **43** (2002) 109.
21) Wada H., Iwata R., Ido T., Takai Y., J. Labelled. Comp. Radiopharm. **43** (2000) 785.
22) Takai Y., Kaneta T., Hakamatsuka T., Nemoto K., Ogawa Y., Yamada S., et al., Int. J. Radiat. Oncol. Biol. Phys. **63** (Suppl) (2005) S465-S466.
23) Ishikawa Y., Iwata R., Furumoto S., Takai Y., Appl. Radiat. Isot. **62** (2005) 705.
24) Louis D.N., Ohgaki H., Wiestler O.D., Cavenee W.K., Burger P.C., Jouvet A., et al., (eds) Lyon: IARC, 2007.
25) Evans S.M., Judy K.D., Dunphy I., Jenkins W.T., Hwang W.T., Nelson P.T., et al., Clin. Cancer Res. **10** (2004) 8177.
26) Semenza G.L., Trends Mol. Med. **8** (4 Suppl) (2002) S62-67.
27) Yasuda H., Nakayama K., Watanabe M., Suzuki S., Fuji H., Okinaga S., et al., Clin. Cancer Res. **12** (2006) 6748.
28) Huang L.E., Willmore W.G., Gu J., Goldberg M.A., Bunn H.F., J. Biol. Chem. **274** (1999) 9038.
29) Li L., Lin X., Shoemaker A.R., Albert D.H., Fesik S.W., Shen Y., Clin. Cancer. Res. **12** (2006) 4747.
30) Birner P., Gatterbauer B., Oberhuber G., Schindl M., Rossler K., Prodinger A., et al., Cancer **92** (2001) 165.

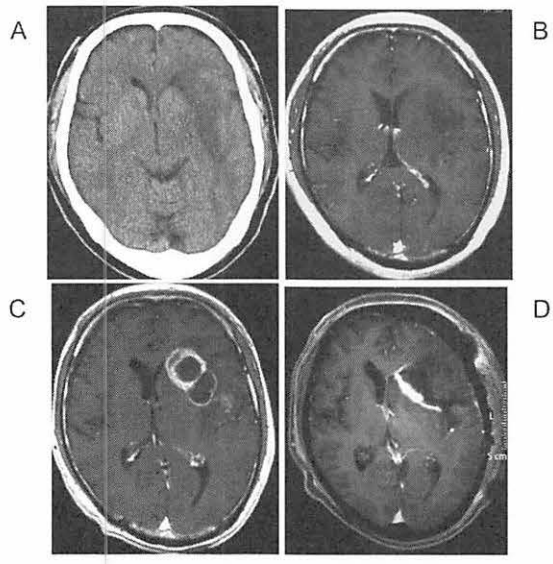

Figure 1. Illustrative case. Axial computed tomography scan (A) and T1-weighted magnetic resonance (MR) image with gadolinium (B) on admission, showing a diffuse infiltrative tumor in the left insulo-opercular region. Axial T1-weighted MR image with gadolinium after 60 Gy of irradiation (C), demonstrating tumor progression. Axial T1-weighted MR image with gadolinium after surgery (D), depicting partial resection of the tumor.

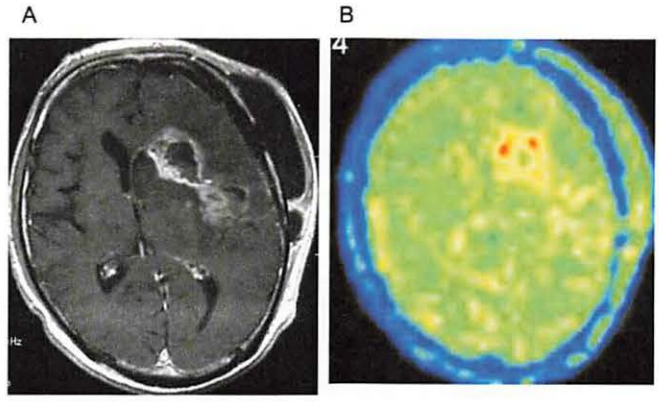

Figure 2. Illustrative case. Axial T1-weighted MR image with gadolinium obtained 4 weeks after the surgery (A), demonstrating further progression of the tumor. [^{18}F]FRP-170 positron emission tomography (PET) image(B), depicting high uptake corresponding to the enhanced lesion on MR imaging.

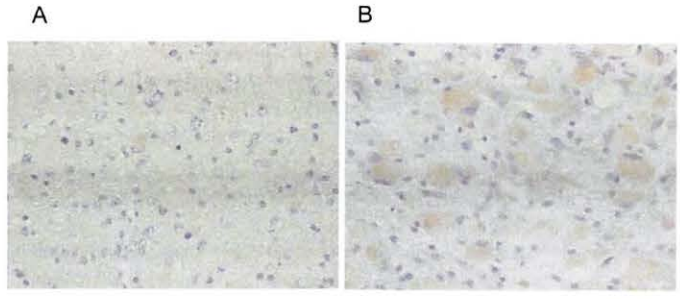

Figure 3. Photomicrographs of the glioblastoma from the illustrative case. HIF1-alpha-positive cells can be seen as brown staining of cytoplasm. The first tissue from the stereotactic biopsy contains fewer positive cells (A) compared to the second tissue from the surgery, which was performed after 60 Gy of irradiation with chemotherapy (B) (original magnificationx400).

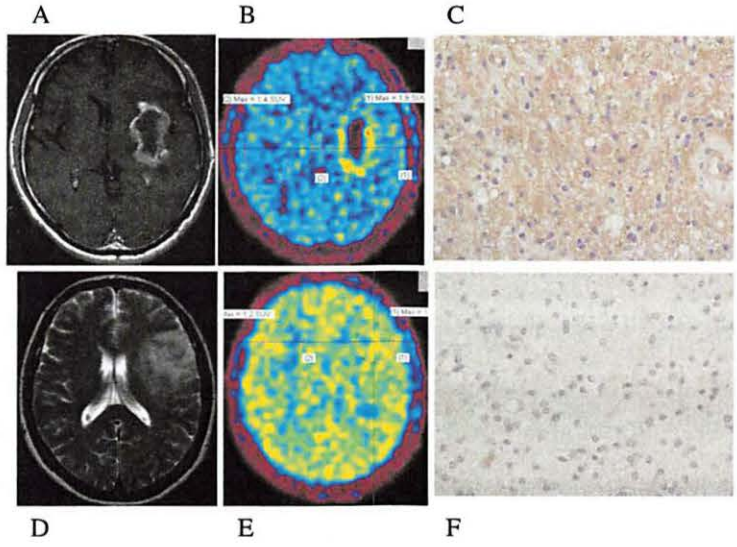

Figure 4. Axial T1-weighted MR image with gadolinium from a 68-year-old male with glioblastoma, showing an enhanced lesion in the left insula (A). [^{18}F]FRP-170 PET image showing high uptake (B), corresponding to the enhanced lesion on MR imaging. Photomicrograph of the surgical specimen showing many strongly HIF1-alpha-positive cells (original magnificationx400) (C). Axial T2-weighted MR image from a 53-year-old female with oligodendroglioma, showing a diffuse infiltrative lesion in the left insulo-operculum (D). [^{18}F]FRP-170 PET image showing no high uptake lesions (E). Photomicrograph showing no HIF1-alpha immunostaining (original magnificationx400) (F).

VIII. 2. Imaging Prion Amyloid Plaques Using [^{11}C]BF-227

Okamura N.[1], Shiga Y.[2], Furumoto S.[1,3], Tashiro M.[4], Tsuboi Y.[5], Furukawa K.[6], Yanai K.[1], Iwata R.[3], Arai H.[6], Kudo Y., Y[7] Itoyama Y.[2], and Doh-ura K.[8],

[1]*Department of Pharmacology, Tohoku University School of Medicine*
[2]*Department of Neurology, Tohoku University School of Medicine*
[3]*Division of Radiopharmaceutical Chemistry, Cyclotron and Radioisotope Center, Tohoku University*
[4]*Division of Cyclotron Nuclear Medicine, Cyclotron and Radioisotope Center, Tohoku University*
[5]*Department of Neurology, Fukuoka University School of Medicin,*
[6]*Department of Geriatrics and Gerontology, Division of Brain Sciences, Institute of Development, Aging, and Cancer, Tohoku University*
[7]*Innovation of New Biomedical Engineering Center, Tohoku University*
[8]*Department of Prion Research, Tohoku University School of Medicine*

Introduction

Prion diseases are a group of fatal neurodegenerative disorders, including Creutzfeldt-Jakob disease (CJD), Gerstmann-Sträussler-Scheinker disease (GSS), and kuru[1)]. These diseases are characterized by progressive deposition of abnormal prion protein (PrP) in the brain. CJD is the most common type of human prion disease. GSS is a familial neurodegenerative disorder associated with mutations of the PrP gene. Abnormal PrP deposition in the brain is suggested to start before the occurrence of clinical symptoms. Thus, preclinical diagnosis and early disease-specific therapeutic interventions can be beneficial for people affected by prion diseases.

Several positron emission tomography (PET) imaging agents have been recently developed and used for in vivo detection of brain amyloid-β (Aβ) plaques in patients with Alzheimer's disease (AD). Most of these PET agents show high binding affinity to PrP amyloid because PrP aggregates form β-pleated sheet structures and share a common secondary structure with Aβ deposits in AD brain. Therefore, these agents would be useful for the in vivo detection of PrP amyloid in the brain. We have demonstrated in vitro and in vivo binding of benzoxazole derivatives to both Aβ and PrP amyloids[2,3)]. One of these derivatives, BF-227, was used for a clinical PET study where it successfully visualized amyloid deposits in the brain of AD patients in vivo. Therefore, [^{11}C]BF-227 appears to be a promising candidate for PET imaging of PrP deposits. The purpose of this study was to

evaluate the clinical utility of [^{11}C]BF-227 PET for the noninvasive detection of abnormal PrP deposits.

Subject and Methods

Two sporadic CJD patients [63-year-old female (CJD1) and 58-year-old male (CJD2)] and 3 GSS patients [69-year-old female (GSS1), 61-year-old male (GSS2), and 30-year-old female (GSS3)] underwent PET scans with [^{11}C]BF-227. For comparison, [^{11}C]BF-227 PET studies were also performed in AD patients and aged normal controls. CJD1 health was unremarkable until the manifestation of depressive symptoms at the age of 62 years. The patient then developed subacutely progressive dementia, motor disturbances, and myoclonus. CJD2 showed subacutely progressive dementia and gait disturbance and then developed psychotic symptoms, dysarthria, and myoclonus. Both CJD patients had no mutations and showed methionine homozygosity at codon 129 of the PrP gene. PET studies in CJD1 and CJD2 were performed when they reached grade 4 of the modified Rankin scale at a 3- and 4-month after onset of symptoms, respectively. Both patients showed periodic synchronous discharges in electroencephalograms and hyperintensity in the caudate, putamen, and cerebral cortex on diffusion-weighted magnetic resonance (MR) images. Diagnosis of probable CJD was made according to the WHO criteria. Each GSS patient was from a different pedigree and had a family history of the same disease, carrying a proline-to-leucine mutation at codon 102 and methionine homozygosity at codon 129 of the PrP gene. GSS1 and GSS2, having a 9- and 20-month clinical duration from the onset, respectively, showed signs of moderate cerebellar ataxia, such as gait disturbance and slurred speech; however, they could walk unassisted and had slight or no cognitive impairment. GSS1 and GSS2 scored 22 and 26 points, respectively, on the Mini-Mental State Examination. GSS3, having a 27-month clinical duration, showed severe gait disturbance and slurred speech and was unable to walk unassisted; however, she had no cognitive impairment (30 points on the Mini-Mental State Examination) at the time of this study. This study was approved by the ethics committee on clinical investigations of Tohoku University School of Medicine and performed in accordance with the Declaration of Helsinki. Written informed consent was obtained after complete description of the study to the patients and subjects.

PET scans were performed using a SET-2400W (Shimadzu Inc., Japan). After intravenous injection of 211–366 MBq of [^{11}C]BF-227, dynamic PET images were obtained for 60 min with the subjects' eyes closed. Standardized uptake value (SUV)

images of [^{11}C]BF-227 were obtained by normalizing tissue concentration by injected dose and body weight. Average summations of SUV images were created from late frames (40–60 min post injection) of dynamic PET images. Deposition of PrP plaques is reportedly frequent in the cerebellum but scarce in the pons of GSS brain. Furthermore, BF-227 retention in the pons does not differ between AD patients and normal controls. Therefore, we used the pons as a reference region and calculated the regional to pons SUV ratio (SUVRp) as an index of BF-227 retention.

Results

GSS patient showed obvious retention of [^{11}C]BF-227 in the cerebellum, and lateral and medial temporal cortices. The three GSS patients showed significantly higher SUVRp in the lateral temporal cortex, thalamus, and cerebellum (Figure) when compared to aged normal controls. Furthermore, when compared to the AD group, the GSS group showed significant elevation of SUVRp in the medial temporal cortex, thalamus, and cerebellum. Although 2 GSS patients showed retention of BF-227 in most brain regions, the youngest GSS patient showed BF-227 retention only in the cerebellum, thalamus, and medial temporal cortex, but not in the neocortex. Furthermore, 2 sporadic CJD patients showed no obvious BF-227 retention in any of the brain regions examined[4)].

Discussion

GSS is a rare form of prion disease occurring in only about 3% of prion disease cases in Japan. However, GSS is probably one of the prion diseases most likely to benefit from early therapeutic interventions because the disease can be confirmed earlier using PrP gene analysis and progression occurs much slower than that in sporadic CJD, which comprises the majority of prion disease cases. Recently such compounds as pentosan polysulfate and doxycycline have been clinically used for experimental treatments for prion diseases to prevent deposition of abnormal PrP in the brain, because these compounds slowered the disease progression in animal disease models when administered in an earlier stage of the disease. Reliable surrogate markers are also required to evaluate the efficacy of these experimental interventions. [^{11}C]BF-227 PET might be one of the best candidates to assess PrP amyloid deposition in GSS.

References

1) DeArmond S.J., Kretzschmar H.A., Prusiner S.B., Prion diseases. In Greenfield's Neuropathology

eds Graham D.I., & Lantos P.L., (Hodder Arnold, London), 7th Ed. pp. 273-323.
2) Okamura N., Suemoto T., Shimadzu H., Suzuki M., Shiomitsu T., Akatsu H., et al., J. Neurosci. **24** (2004) 2535.
3) Ishikawa K., Kudo Y., Nishida N., Suemoto T., Sawada T., Iwaki T., et al., J. Neurochem. **99** (2006) 198.
4) Okamura N., Shiga Y., Furumoto S., Tashiro M., Tsuboi Y., Furukawa K., Yanai K., Iwata R., Arai H., Kudo Y., Itoyama Y., Doh-ura K., Eur. J. Nucl. Med. Mol. Imaging. **37** (2010) 934.

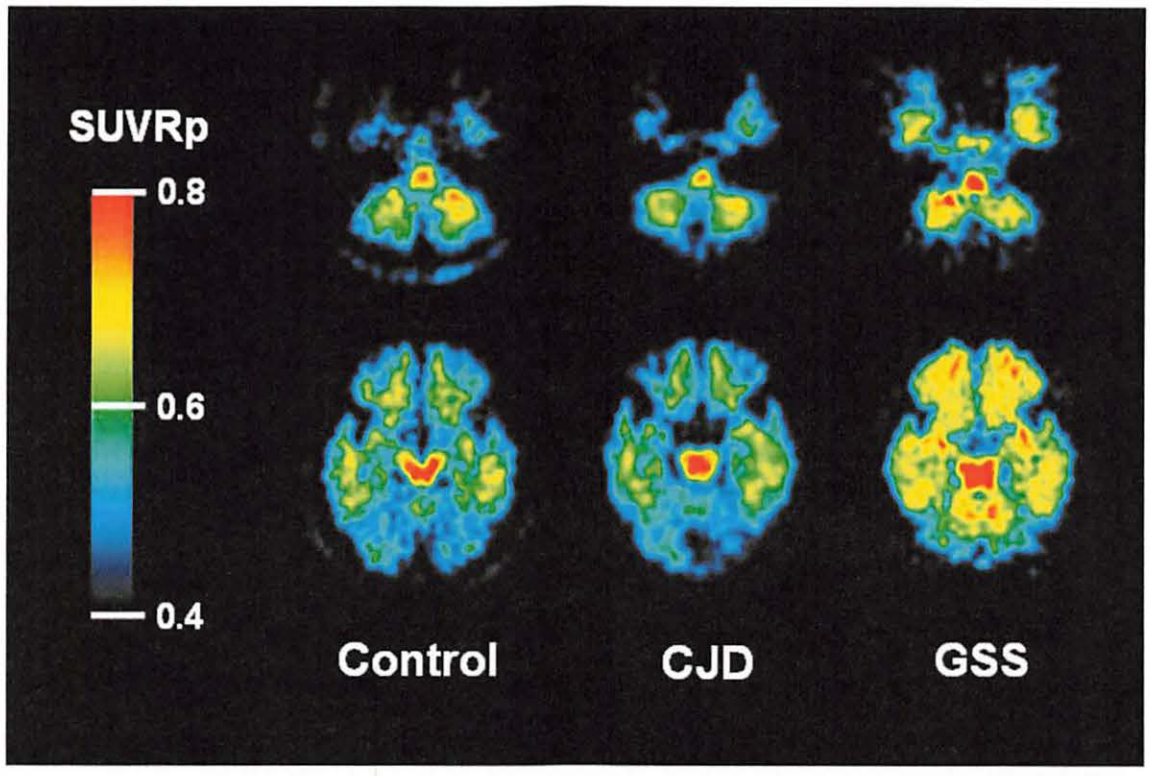

Figure 1. Regional to pons standardized uptake value ratio (SUVRp) images between 40 and 60 min post injection of [^{11}C]BF-227 in an aged normal subject (64-year-old male), a sporadic CJD patient (63-year-old female), a GSS patient (61-year-old male).

VIII. 3. *In vivo* Visualization of α-Synuclein Deposition by [^{11}C]BF-227 PET in Multiple System Atrophy

Kikuchi A.[1], Takeda A.[1], Okamura N.[2], Tashiro M.[3], Hasegawa T.[1], Furumoto S.[2,5], Kobayashi M.[1], Sugeno N.[1], T Baba.[1], Miki Y.[4], Mori F.[4], Wakabayashi K.[4], Funaki Y.[5], Iwata R.[5], Takahashi S.[6], Fukuda H.[7], Arai H.[8], Kudo Y.[9], Yanai K.[2], and Itoyama Y.[1]

[1]*Department of Neurology, Graduate School of Medicine, Tohoku University*
[2]*Department of Pharmacology, Graduate School of Medicine, Tohoku University*
[3]*Division of Cyclotron Nuclear Medicine, Cyclotron and Radioisotope Center, Tohoku University*
[4]*Division of Radiopharmaceutical Chemistry, Cyclotron and Radioisotope Center, Tohoku University*
[5]*Department of Neuropathology, Institute of Brain Science, Hirosaki University Graduate School of Medicine*
[6]*Departments of Diagnostic Radiology, Graduate School of Medicine, Tohoku University*
[7]*Department of Nuclear Medicine and Radiology, Institute of Development, Aging and Cancer, Tohoku University*
[8]*Department of Geriatric and Gerontology, Institute of Development, Aging and Cancer, Tohoku University*
[9]*Innovation of New Biomedical Engineering Center, Tohoku University*

To confirm *in vivo* visualization of α-synuclein deposition in glial cytoplasmic inclusion (GCI) in multiple system atrophy (MSA), we compared the carbon-11-labeled 2-(2-[2-dimethylaminothiazol-5-yl]ethenyl)-6-(2-[fluoro]ethoxy) benzoxazole ([^{11}C] BF-227) PET findings of eight MSA cases to those of age-matched normal controls. The PET data demonstrated significantly high distribution volumes in the GCI-rich brain areas in the MSA. The [^{11}C]BF-227 PET is a promising surrogate marker for monitoring intracellular α-synuclein deposition in the living brains[1)].

Multiple system atrophy (MSA) is a sporadic, progressive neurodegenerative disease characterized by variable severity of parkinsonism, cerebellar ataxia, autonomic failure, and pyramidal signs. MSA is currently classified into a single disease, which consists of MSA with predominant parkinsonism (MSA-P) and MSA with predominant cerebellar ataxia (MSA-C)[2)]. The histopathological hallmark of MSA is the appearance of intracellular inclusion bodies, named glial cytoplasmic inclusions (GCIs), which are mainly composed of α-synuclein fibrils[3)]. Previous neuropathological studies indicated that the appearance of GCIs preceded the clinical onset of MSA[4)] and the amount of α-synuclein deposition correlated with the disease progression[5)]. Therefore, it is plausible that the

formation of α-synuclein deposits plays a key role in the neurodegeneration and that compounds that inhibit this process may be therapeutically useful for MSA and other synucleinopathies such as Parkinson's disease and dementia with Lewy bodies. In fact, some compounds including antioxidants[6] and non-steroidal anti-inflammatory drugs [7] were reported to have potent anti-fibrillogenic and fibril-destabilizing effects on aggregated α-synucleins and received much attention as possible new therapeutic agents[6,7]. Detection of α-synuclein deposition *in vivo* could theoretically allow early diagnosis even at the presymptomatic stage, as well as assess disease progression and possible therapeutic effects in the living brain of MSA patients.

Although the Pittsburgh Compound B and other compounds were reported to be useful in detecting senile plaques *in vivo*, there were no imaging probes currently available for *in vivo* detection of α-synuclein deposition. Recently, 2-(2-[2-dimethylaminothiazol-5-yl]ethenyl)-6-(2-[fluoro]ethoxy)benzoxazole (BF-227), known as a PET probe for *in vivo* detection of dense β-amyloid (Aβ) deposits in humans[8], was reported to bind with synthetic α-synuclein aggregates as well as Aβ fibrils *in vitro*[9].

To demonstrate that BF-227 could bind to α-synuclein-containing GCIs in postmortem tissues, we stained brain tissues taken from 3 autopsy cases with MSA, using BF-227 and anti-phosphorylated α-synuclein antibody. The above diagnosis was confirmed both clinically and histopathologically. Double-labeling experiments using BF-227 and anti-phosphorylated α-synuclein antibody demonstrated that BF-227 fluorescent signal in the most of GCIs in the pontine base (Fig. 1a, b). Not all GCIs stained by anti-phosphorylated α-synuclein antibody were always positive for BF staining (Fig. 1a, b). In the process of oligodendroglial pathology, it was believed that α-synuclein deposits as amorphous state and then forms fibrillar structures[10,11]. In fact, part of GCIs were reported to be ubiquitin-negative[12] and therefore, it seems reasonable that some of GCIs were not composed of β-sheet fibrils and were negative for BF-227 staining.

To confirm *in vivo* visualization of α-synuclein deposits by carbon-11-labeled BF-227 ([^{11}C]BF-227) PET in the living brains of patients with MSA, we compared the distribution volume (DV) of [^{11}C] BF-227 of eight MSA cases to those of age-matched controls. All probable MSA patients were diagnosed on the second consensus criteria for probable MSA[13]. The clinical features of these patients are summarized (Table 1). There were no significant differences in age, disease duration, and unified MSA rating scale score between MSA-P and MSA-C subgroups. The normal control group comprised volunteers without impairment of cognitive and motor functions who had no cerebrovascular lesions

on magnetic resonance images. Tissue time activity curves of [^{11}C]BF-227 in the brain indicated more gradual clearance from the brain in MSA patients compared to normal subjects following initial rapid uptake of radioactivity. Relatively high concentrations of [^{11}C]BF-227 radioactivity were observed in the subcortical white matter and lenticular nucleus in MSA, in which relatively intense α-synuclein deposits were found in the postmortem brain. [^{11}C]BF-227 exhibited linear regression curves on Logan plot analysis in all brain regions examined. Since the slopes of the regression lines represent the DV of the tracer, these findings indicated a higher DV of [^{11}C]BF-227 in MSA than in normal control (Fig. 2). The regional DV values were significantly high in the subcortical white matter ($p<0.001$), putamen and posterior cingulate cortex ($p<0.005$), globus pallidus, primary motor cortex and anterior cingulate cortex ($p<0.01$), and substantia nigra ($p<0.05$) in MSA patients compared to the normal controls. The regional DV of [^{11}C]BF-227 was increased in the subcortical white matter and lentiform nucleus, in which GCIs were densely distributed in the postmortem brains[5], suggesting specific binding of [^{11}C]BF-227 to the α-synuclein deposits *in vivo*. On the other hand, regional DV in other brain regions, such as the cerebellum and pons, did not show significant increases relative to the normal control group. Due to the remarkable cerebellar and pontine atrophy, the DV in these regions might be underestimated. Correction for partial volume loss is therefore needed to improve the accuracy of quantification in the cerebellum and brainstem of MSA.

In conclusion, the BF-227 could bind to α-synuclein-containing GCIs (Fig. 1a, b) in the postmortem brain, and the [^{11}C]BF-227 PET demonstrated significantly high signals in the GCI-rich brain regions including subcortical white matter, putamen, globus pallidus, primary motor cortex, and anterior and posterior cingulate cortex. These results suggest that [^{11}C]BF-227 PET is a suitable surrogate maker for monitoring α-synuclein deposits in living brains with MSA and could be a potential tool to develop neuroprotective therapy for MSA. Further studies are warranted to verify whether Lewy bodies in other synucleinopathies as well as GCIs can be detected by [^{11}C]BF-227 PET.

References

1) Kikuchi A., Takeda A., Okamura N., Tashiro M., Hasegawa T., Furumoto S., Kobayashi M., Sugeno N., Baba T., Miki Y., Mori F., Wakabayashi K., Funaki Y., Iwata R., Takahashi S., Fukuda H., Arai H., Kudo Y., Yanai K., Itoyama Y., Brain **133** (2010) 1772.
2) Gilman S., Low P.A., Quinn N., Albanese A., Ben-Shlomo Y., Fowler C.J., Kaufmann H., Klockgether T., Lang A.E., Lantos P.L., Litvan I., Mathias C.J., Oliver E., Robertson D., Schatz I., Wenning G.K., J. Neurol. Sci. **163** (1999) 94.
3) Wakabayashi K., Yoshimoto M., Tsuji S., Takahashi H., Neurosci. Lett. **249** (1998) 180.

4) Fujishiro H., Ahn T.B., Frigerio R., DelleDonne A., Josephs K.A., Parisi J.E., Eric Ahlskog J., Dickson D.W., Acta. Neuropathol. **116** (2008) 269.
5) Wakabayashi K., Takahashi H., Neuropathology. **26** (2006) 338.
6) Ono K., Yamada M., J. Neurochem. **97** (2006) 105.
7) Hirohata M., Ono K., Morinaga A., Yamada M., Neuropharmacology **54** (2008) 620.
8) Kudo Y., Okamura N., Furumoto S., Tashiro M., Furukawa K., Maruyama M., Itoh M., Iwata R., Yanai K., Arai H., J. Nucl. Med. **48** (2007) 553.
9) Fodero-Tavoletti M.T., Mulligan R.S., Okamura N., Furumoto S., Rowe C.C., Kudo Y., Masters C.L., Cappai R., Yanai K., Villemagne V.L., Eur. J. Pharmacol. **617** (2009) 54.
10) Gai W.P., Pountney D.L., Power J.H., Li Q.X., Culvenor J.G., McLean C.A., Jensen P.H., Blumbergs P.C., Exp. Neurol. **181** (2003) 68.
11) Stefanova N., Reindl M., Neumann M., Haass C., Poewe W., Kahle P.J., Wenning G.K., Am. J. Pathol. **166** (2005) 869.
12) Sakamoto M., Uchihara T., Nakamura A., Mizutani T., Mizusawa H., Acta. Neuropathol. **110** (2005) 417.
13) Wood N.W., Colosimo C., Dürr A., Fowler C.J., Kaufmann H., Klockgether T., Lees A., Poewe W., Quinn N., Revesz T., Robertson D., Sandroni P., Seppi K., Vidailhet M., Neurology **71** (2008) 670.

Table 1. Subject profiles.

	Normal	MSA		
	control	Total	MSA-P	MSA-C
n	8	8	4	4
Gender (F/M)	4/4	4/4	1/3	3/1
Age (years)	64.3±5.90	57.4±10.1	60.5±11.1	54.3±9.50
Duration (years)		1.50±0.54	1.75±0.50	1.25±0.50
UMSARS score		36.1±8.87	41.5±9.39	30.8±4.27

Data are mean ± SD.
MSA: multiple system atrophy, UMSARS: unified MSA rating scale

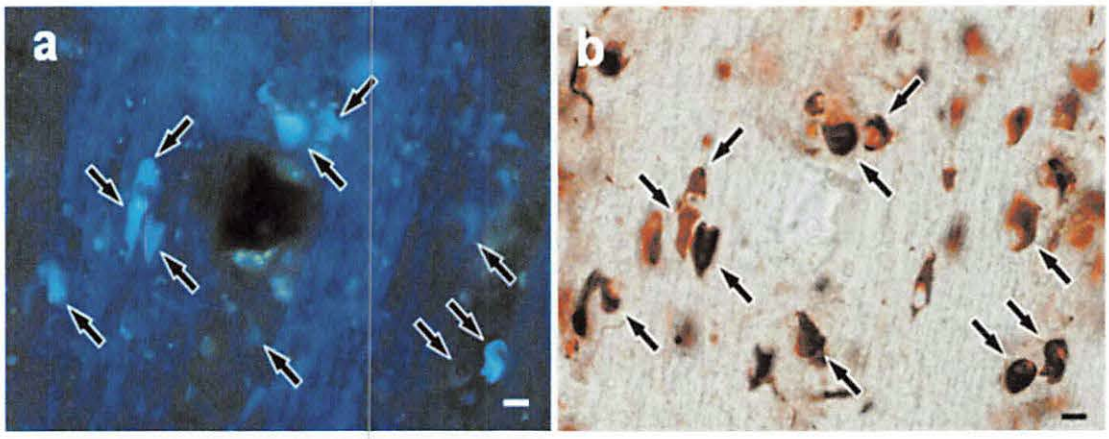

Figure 1. Neuropathological findings of BF-227 fluorostaining and anti-phosphorylated α-synuclein antibody immunostaining (a quotation from reference 1).
BF-227 fluorostaining (a) and anti-phosphorylated α-synuclein antibody immunostaining (b) were codetected in GCIs in the pontine base of a patient with MSA. BF-227 histofluorescence was observed in the most of GCIs (arrows). Bars = 10 μm.

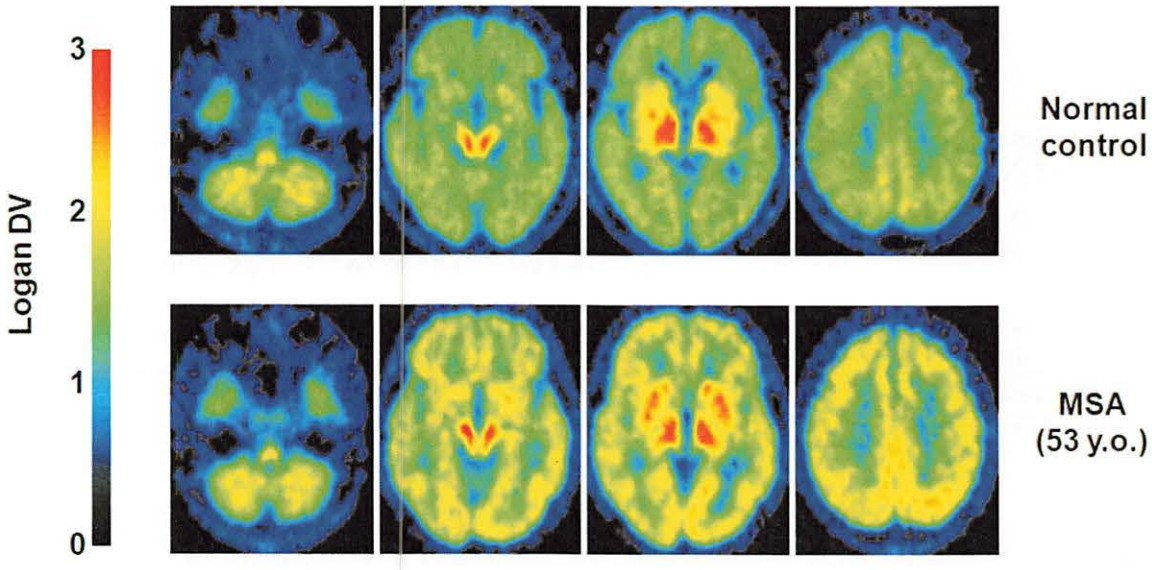

Figure 2. [^{11}C]BF-227 PET findings in MSA (a quotation from reference 1).
In a representative patient with MSA-C, the regional DVs were mapped to the subcortical white matter and lentiform nucleus compared to normal control.

VIII. 4. Amyloid Imaging in MCI and Alzheimer's Disease with BF-227, a New PET Tracer: Comparison to FDG-PET

Furukawa K.[1], Okamura N.[2], Tashiro M.[3], Waragai M.[1], Furumoto S.[2], Iwata R.[4], Yanai K.[2], Kudo Y.[5], and Arai H.[1]

[1] Department of Geriatrics and Gerontology, Division of Brain Sciences, Institute of Development, Aging and Cancer, Tohoku University
[2]Department of Pharmacology, Tohoku University Graduate School of Medicine
[3]Division of Cyclotron Nuclear Medicine, Cyclotron and Radioisotope Center
[4]Division of Radiopharmaceutical Chemistry, Cyclotron and Radioisotope Center
[5]Department of NeuroImaging Research, Innovation New Biomedical Engineering Center

Introduction

In recent years several laboratories, including ours, have succeeded in visualizing Ab deposition in living patients' brains with AD using PET probes[1,2]. Ronald Petersen addressed the concept of mild cognitive impairment (MCI), which is an intermediate state between normal aging and AD[3].

Regional cerebral glucose metabolism (rCMRglu) has been investigated by several investigators[4] using 2-[^{18}F]fluoro-deoxy-D-glucose (FDG) and PET in AD. We used [^{11}C]BF-227-PET as well as FDG-PET on the same subjects (AN, MCI, and AD) and carefully analyzed and compared the results with these two kinds of PET.

Method

The diagnosis for MCI and probable AD followed the MCI clinical criteria presented by "Petersen et al."[3] and "the National Institute of Neurological and Communicative Disorders and Stroke - Alzheimer's Disease and Related Disorders Association"[5], respectively. The study protocol was approved by the Committee on Clinical Investigation at Tohoku University School of Medicine and the Advisory Committee on Radioactive Substances at Tohoku University. After a complete description of the study to the patients and subjects, written informed consent was obtained.

The PET procedure for [^{11}C]BF-227 was described precisely before[1]. [^{11}C]BF-227 and its *N*-desmethylated derivative (a precursor of [^{11}C]BF-227) were custom-synthesized

by Tanabe R&D Service Co. After intravenous injection of 211-366 mBq of [^{11}C]BF-227, dynamic PET images were obtained for 60 min with each subject's eyes closed. Standardized uptake value (SUV) images of [^{11}C]BF-227 were obtained by normalizing tissue radioactivity concentration by injected dose and body weight. The FDG-PET procedure was described previously[6]. Subjects were scanned in a quiet and dimly-lit room with their eyes closed after at least four hours of food restriction. The emission data were corrected for tissue attenuation using the transmission data. Regions of interest (ROIs) were placed on individual axial magnetic resonance (MR) images. Because there were neither senile plaques nor glucose hypometabolism in the cerebellum of AD, ratios of regional SUV to cerebellar SUV (SUVR) were calculated as an index of [^{11}C]BF-227 retention and CMRglu.

Results

BF-227 retention in MCI

First, we analyzed PET images with [^{11}C]BF-227 among the three groups (AN, MCI, and AD), and representative brain PET images are shown in Fig. 1. As indicated in the figure, some MCI subjects showed strong retention of [^{11}C]BF-227, but other MCI subjects did not. Most AD cases, however, indicated strong accumulation of [^{11}C]BF-227 especially in frontal, temporal and parietal cortices. If the retention pattern of [^{11}C]BF-227 is compared to that of PIB, the accumulation of [^{11}C]BF-227 in the frontal lobe looks much weaker than that of PIB.

Figure 2 shows the mean neocortical and regional SUVRs of [^{11}C]BF-227 for the three groups. Both the mean neocortical SUVRs for MCI and AD are significantly higher than that for AN. As we previously reported[1], significantly higher SUVRs were observed in most cerebral regions in AD compared to AN except for the medial temporal lobe. A significantly lower SUVR in MCI was observed in the parietal cortex compared to AD. In the other neocortical regions, MCI subjects showed a tendency towards milder retention of [^{11}C]BF-227 than that in AD.

Cerebral glucose metabolism in AN, MCI and AD

A significant reduction of neocortical SUVR was observed in both MCI and AD patients compared to AN in FDG-PET (Table 1, Fig. 3). Neocortical SUVR of FDG-PET for each subject was plotted against neocortical SUVR of BF-227-PET (Fig. 4A). ROC

analysis was performed for the lateral temporal SUVR of BF-227 and posterior cingulate SUVR of FDG (Fig. 4B). The AUC for BF-227 (0.994) is much higher than that for FDG (0.839).

Discussion

It was presented that FDDNP can detect a high signal in MCI by binding not only for amyloid plaques but also tau neurofibrillary tangles[7], and the retention level for MCI is between AN and AD. On the other hand, several groups reported that about a half of the MCI subjects showed PIB uptake in the AD range, and other MCI subjects indicated retention levels lower than the AD range[8]. The present study also revealed higher retention of BF-227 in 60-70% of MCI subjects and in almost all the AD patients. Therefore, the amyloid PET technique is considered to be a highly useful and strong method for early detection of AD patients in the MCI stage.

FDG-PET has been used in investigations for MCI, and low rCMRglu in the temporo-parietal and medial frontal cortices and hippocampus was reported as the most prominent predictor of subsequent cognitive decline[9]. Our results indicate, however, that amyloid retention detected by BF-227 is more sensitive and specific than FDG-PET for AD diagnosis. Therefore it is reasonable that amyloid PET is more sensitive than FDG-PET for detecting MCI, which is regarded as a prodromal state of dementia or early AD.

References

1) Kudo Y., Okamura N., Furumoto S., et al., J. Nucl. Med. **48** (2007) 553.
2) Klunk W.E., Engler H., Nordberg A., et al., Ann. Neurol. **55** (2004) 306.
3) Petersen R.C., Smith G.E., Waring S.C., et al., Arch. Neurol. **56** (1999) 303.
4) Herholz K., Carter S.F., Jones M., Br. J. Radiol. **80** (2007) S160.
5) McKhann G., Drachman D., Folstein M., et al., Neurology **34** (1984) 939.
6) Okamura N., Arai H., Higuchi M., et al., Prog. Neuropsychopharmacol. Biol. Psychiatry **25** (2001) 447.
7) Small G.W., Kepe V., Ercoli L.M., Siddarth P., et al., N. Engl. J. Med. **355** (2006) 2652.
8) Kemppainen N.M., Aalto S., Wilson I.A., et al., Neurology **68** (2007) 1603.
9) Chételat G., Desgranges B., Sayette V., Neurology **60** (2003) 1374.

Table 1. Demographic details of the subjects in this study. AN aged normal, MCI mild cognitive impairment, AD Alzheimer's disease. MMSE scores are significantly different between "AN and MCI", "AN and AD", and "MCI and AD".

	N	Gender	Age	MMSE
AN	12	M/F=7/5	66.3 ± 3.3	29.9 ± 0.3
MCI	15	M/F=8/7	78.3 ± 3.8	25.5 ± 2.5
AD	15	M/F=5/10	72.5 ± 6.9	19.5 ± 3.7

Table 2. Box plots of SUVR values with BF-227 PET for AN, MCI and AD. Each dot indicates the mean SUVR from "the mean neocortex" and "the eight regions", that is, frontal, temporal, parietal, occipital, anterior cingulate, posterior cingulated, striatum and medial temporal cortex. Box indicates interquartile range. Vertical bars indicate minimum aximum range.

		Mean neocortex	Frontal	Lateral temporal	Parietal	Occipital	Anterior cingulate	Posterior cingulate	Striatum	Medeial temporal
BF-227	AN	1.05 ± 0.04	1.00 ± 0.06	1.03 ± 0.04	1.08 ± 0.05	1.08 ± 0.05	1.04 ± 0.03	1.11 ± 0.07	1.34 ± 0.06	1.16 ± 0.06
	MCI	1.16 ± 0.10*	1.10 ± 0.11*	1.17 ± 0.10*	1.18 ± 0.10*	1.16 ± 0.08*	1.15 ± 0.11*	1.20 ± 0.11	1.41 ± 0.11	1.18 ± 0.10
	AD	1.22 ± 0.06*	1.13 ± 0.07*	1.24 ± 0.07*	1.25 ± 0.09*†	1.19 ± 0.06*	1.16 ± 0.09*	1.25 ± 0.06*	1.47 ± 0.09*	1.19 ± 0.09
FDG	AN	1.18 ± 0.10	1.10 ± 0.11	1.10 ± 0.10	1.15 ± 0.09	1.24 ± 0.12	1.10 ± 0.10	1.39 ± 0.13	1.29 ± 0.13	0.90 ± 0.06
	MCI	1.10 ± 0.06*	1.05 ± 0.06	1.03 ± 0.07	1.08 ± 0.08	1.23 ± 0.14	0.99 ± 0.08*	1.24 ± 0.09*	1.27 ± 0.13	0.82 ± 0.06*
	AD	1.06 ± 0.08*	1.05 ± 0.14	0.98 ± 0.11*	1.01 ± 0.09*	1.25 ± 0.15	1.00 ± 0.12	1.20 ± 0.13*	1.31 ± 0.11	0.81 ± 0.07*

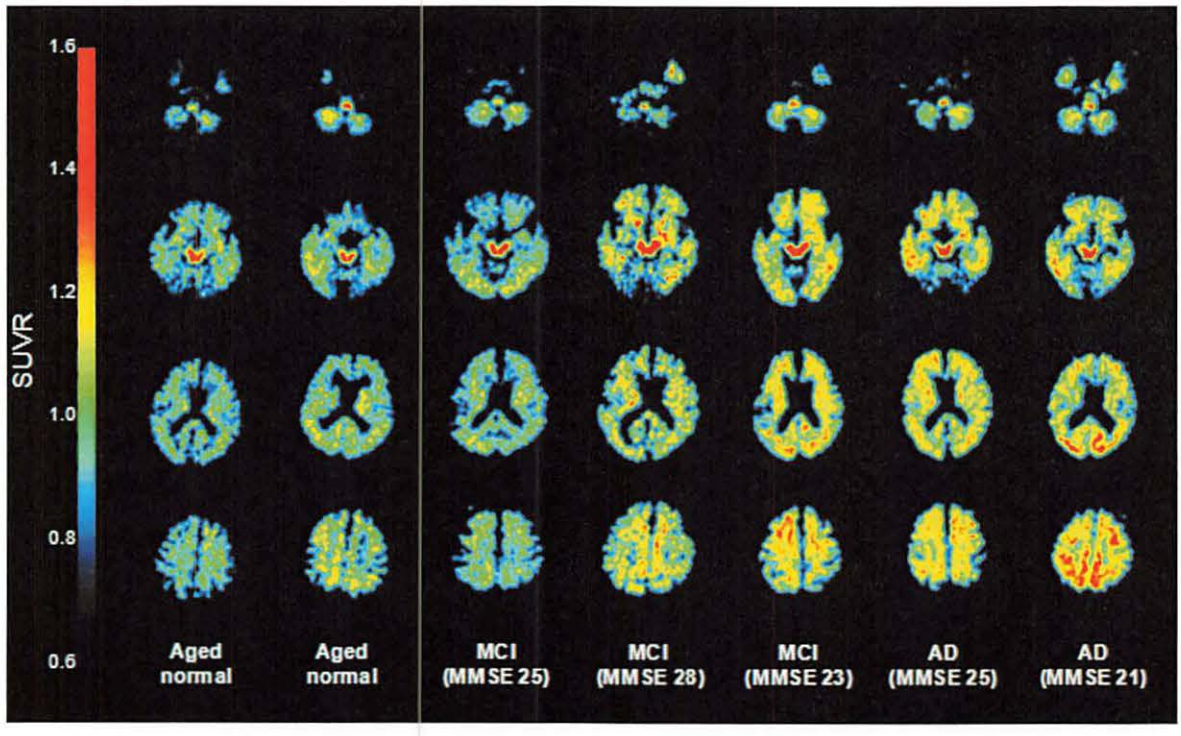

Figure 1. Representative axial brain PET images with [^{11}C]BF-227.

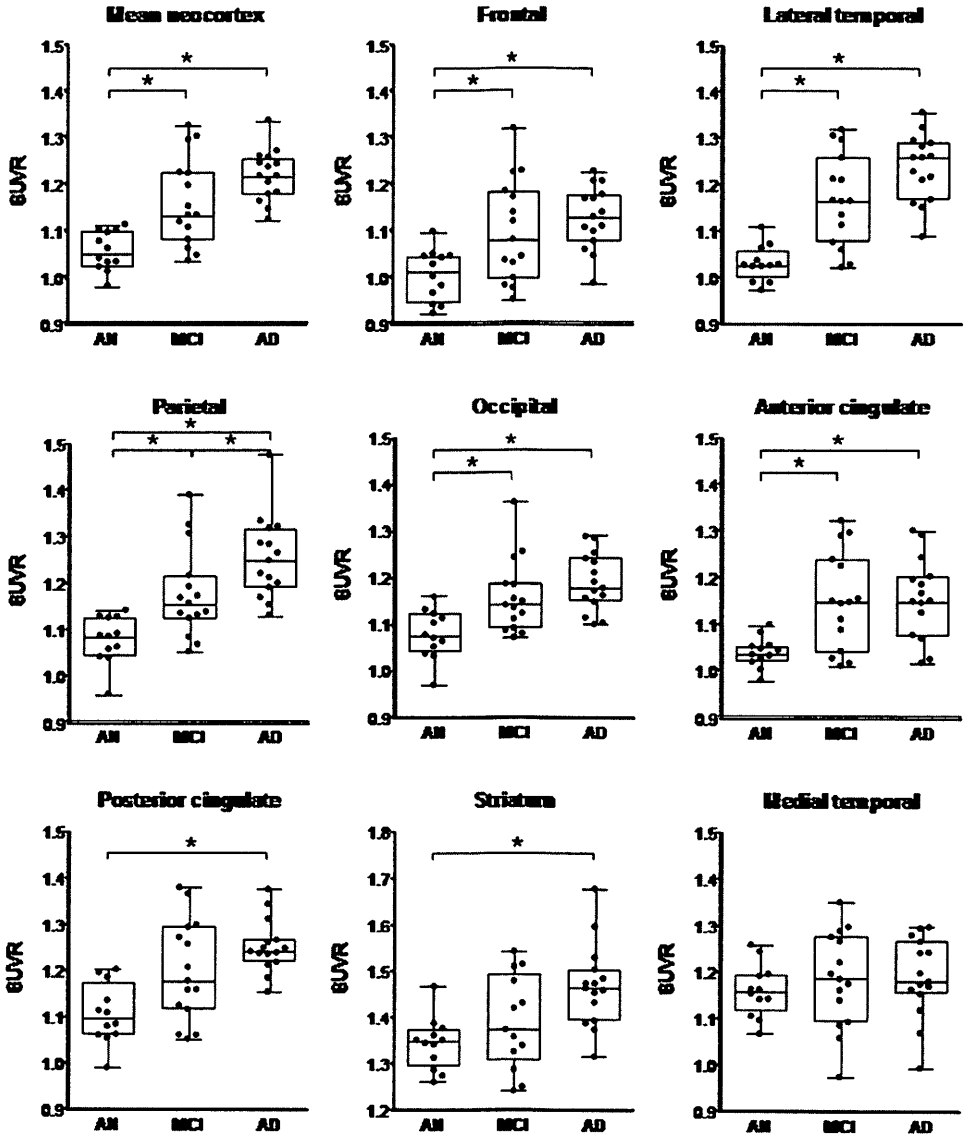

Figure 2. Box plots of SUVR values with [^{11}C]BF-227 PET for AN, MCI and AD.

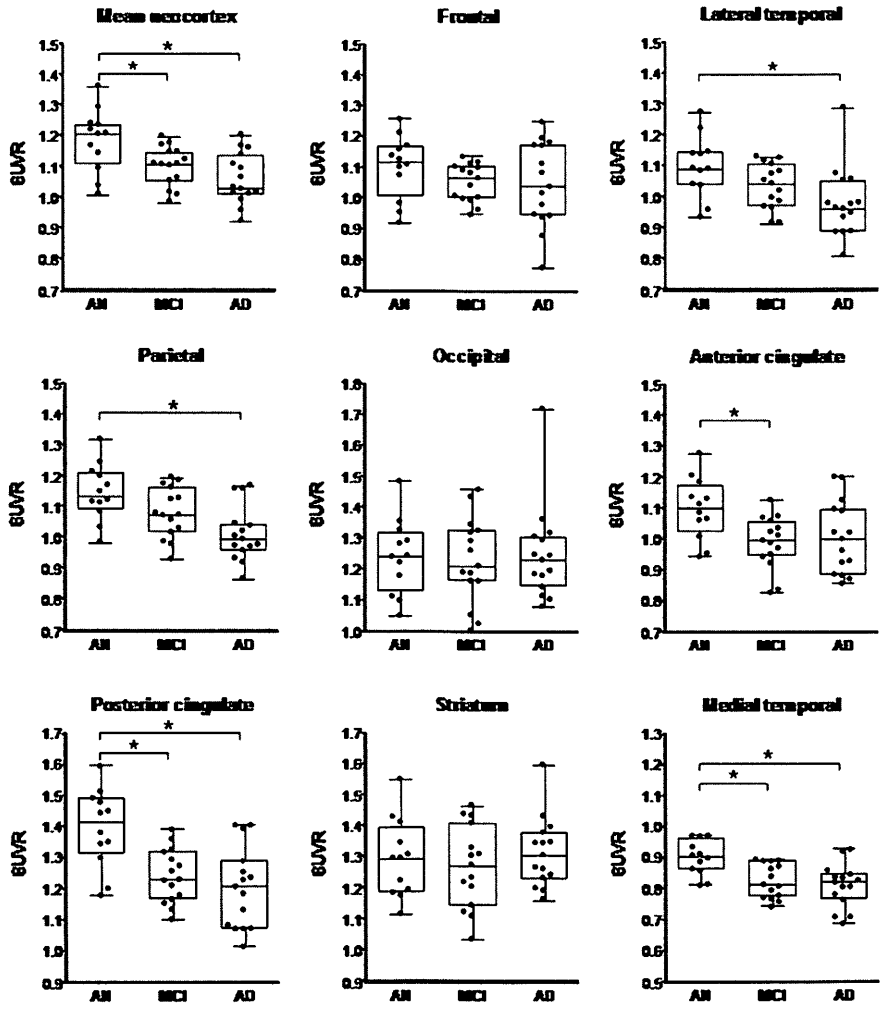

Figure 3. Box plots of SUVR values with FDG-PET for AN, MCI and AD.

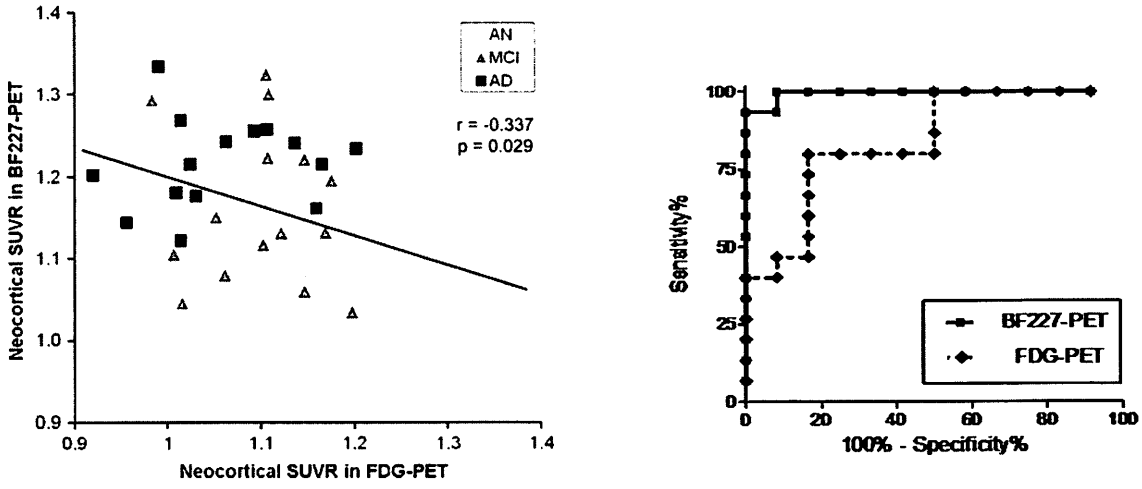

(A) (B)

Figure 4. (A) Relationship between neocortical SUVRs in FDG-PET and BF-227-PET. White, gray and black dots indicate AN, MCI and AD, respectively. (B) Receiver operating characteristic (ROC) curves of BF-227 and FDG-PET. BF-227-PET SUVR in the lateral temporal cortex and FDG-PET SUVR in the posterior cingulate cortex for differentiation between AD and AN.

VIII. 5. Voxel-Based Analysis of Cerebral Amyloid Deposition Using [^{11}C]BF-227 PET

Shao H.[1], Okamura N.[1], Furukawa K.[2], Furumoto S.[1], Tashiro M.[3], Iwata R.[3], Kudo Y.[4] Arai H.[2], and Yanai K.[1]

[1]Department of Pharmacology, Tohoku University Graduate School of Medicine
[2]Department of Geriatrics and Gerontology, Division of Brain Sciences, Institute of Development, Aging and Cancer, Tohoku University
[3]Cyclotron and Radioisotope Center, Tohoku University
[4]Innovation of New Biomedical Engineering Center, Tohoku University

A PET study using ^{11}C-labeled BF-227 successfully detected amyloid plaques in living Alzheimer's disease (AD) patients. AD patients showed the preferential [^{11}C]BF-227 retention in the posterior neocortical region of the brain, which corresponded with an area containing a high density of neuritic plaques. In the previous studies, data analysis has been mainly based on region of interest (ROI) analysis. To eliminate any a priori hypothesis about ROI selection, we performed a voxel-based analysis of whole brain regions for the comparison between the groups. The purpose of this study is to understand the pattern of neocortical BF-227 uptake for early diagnosis of AD.

[^{11}C]BF-227 PET scans were performed in 12 normal healthy control subjects and 19 probable AD patients. AD patients were recruited through the Tohoku University Hospital Dementia Patients Registry. The diagnosis of AD was made according to the National Institute of Neurological and Communicative Diseases and Stroke/Alzheimer's Disease and Related Disorders Association (NINCDS–ADRDA) criteria.

Voxel-by-voxel comparisons between images from normal controls and AD patients were performed using SPM5 software. SUV summation images 20 to 40 min post injection were stereotaxically normalized using individual MR images into a standard space of Talairach and Tournoux. The normalized images were smoothed using a 12 mm×12 mm×12 mm Gaussian filter. The count of each voxel was normalized to the cerebellar ROI value. Images of AD patients were compared with those of aged normal controls for between-group analysis ($P < 0.05$ with false discovery rate (FDR) correction). For the

group analysis, a two sample t-test was used to detect differences between the groups.

We additionally created a Z score map by comparison with mean and standard deviation PET images of the aged normal controls for each voxel. A software program named the easy Z score imaging system (eZIS)[1] was used for this analysis. Each PET SUV image of AD patients was compared with the mean and standard deviation (SD) of PET SUV images of 12 aged normal controls using voxel-by-voxel Z score analysis after voxel normalization to cerebellar ROI values; Z score = ([control mean]–[individual value])/(control SD). These Z score maps were displayed by projection with an averaged Z score of 14 mm thickness to surface rendering of the anatomically standardized MRI template.

SPM analysis of [^{11}C]BF-227 PET images demonstrated that patients with AD had significantly higher [^{11}C]BF-227 uptake in the neocortical region than aged normal controls (Fig. 1). Bilateral temporoparietal BF-227 uptake was evident in AD group. Compared to the lateral temporoparietal region, difference in the lateral frontal cortex was less evident. The Z-score maps of PET images were created by comparison with aged normal controls (Fig. 2). Most patients with AD showed a Z-score greater than 2 in the bilateral temporal and posterior cingulate cortices[2].

[^{11}C]BF-227 PET can detect early Aβ load in the lateral temporal cortex of patients with AD. BF-227 would be less subjective to amyloid pathology during the process of aging since this probe is considered to bind selectively to dense Aβ plaques. Thus, [^{11}C]BF-227 PET offers unique information concerning AD pathology that cannot be obtained by other PET tracers.

References

1) Kanetaka H., Matsuda H., Asada T., Ohnishi T., Yamashita F., Imabayashi E., Tanaka F., Nakano S., Takasaki M., Eur. Nucl. Med. Mol. Imaging **31** (2004) 975.
2) Shao H., Okamura N., Sugi K., Furumoto S., Furukawa K., Tashiro M., Iwata R., Matsuda H., Kudo Y., Arai H., Fukuda H., Yanai K., Dement. Geriatr. Cogn. Disord. **30** (2010) 101.

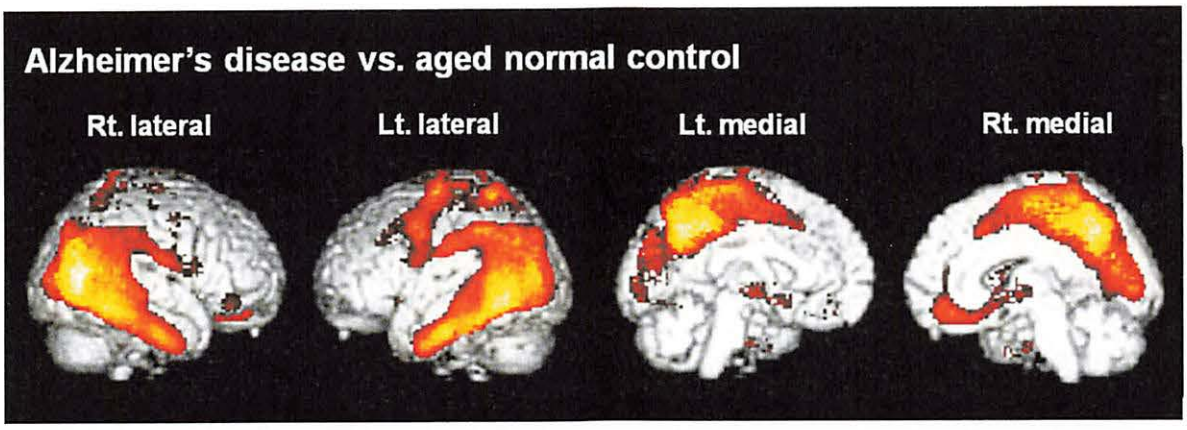

Figure 1. Brain regions showing significantly higher uptake of [^{11}C]BF-227 in patients with AD.

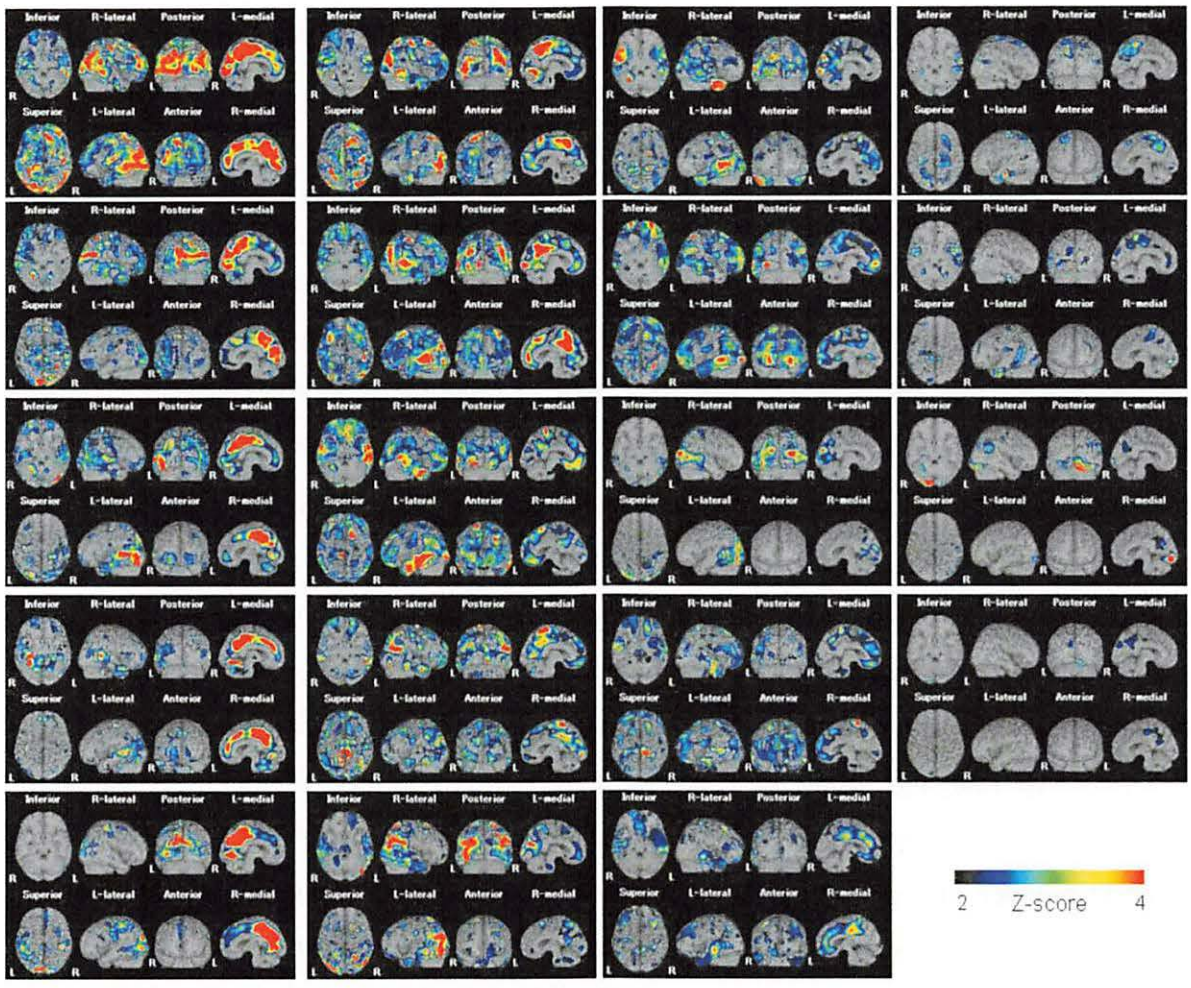

Figure 2. Voxel-by-voxel Z-score analysis by comparison of [^{11}C]BF-227 PET images for 19 patients with AD with the mean and SD of PET images of the 12 aged normal controls.

VIII. 6. Quantification of Amyloid β Deposition in Alzheimer's Disease Patients Using PET and [^{11}C]BF-227

Tashiro M.[1], Okamura N.[3], Watanuki S.[1], Furumoto S.[2,3], Furukawa K.[4], Funaki Y.[2], Iwata R.[2], Kudo Y.[5], Arai H.[4], Watabe H.[6], and Yanai K.[1,2]

[1]Divisions of Cyclotron Nuclear Medicine and [2]Radiopharmaceutical Chemistry, Cyclotron and Radioisotope Center, Tohoku University
[3]Department of Pharmacology, Tohoku University Graduate School of Medicine
[4]Department of Geriatrics and Gerontology, Institute of Development, Aging and Cancer, Tohoku University
[5]Innovation of New Biomedical Engineering Center, Tohoku University
[6]Department of Molecular Imaging in Medicine, Osaka University Graduate School of Medicine

Introduction

In Japan, incidence of cognitive disorders has been increasing and clinical studies on dementia have been very important. Functional neuroimaging of early Alzheimer's disease (AD) using PET and [^{18}F]fluorodeoxyglucose ([^{18}F]FDG) has demonstrated that a decrease in the cerebral metabolic rate of glucose (CMR_{glc}) often starts in the posterior cingulate gyrus and further propagates to the temporo-parietal regions and others. But the regional metabolic reduction is not so obvious and widespread in the early stage of disease course including mild cognitive impairment (MCI)[1]. Neuronal damage is associated with high deposition of amyloid β (Aβ) protein in the brain, and massive neuronal loss is often preceded by high Aβ deposition. An early diagnosis of mild AD can be established if we use a proper tracer that specifically-binds to Aβ proteins in the brain of patients.

"Aβ imaging" using PET has been recognized as one of the most important methods for diagnosing early AD partly because of excellent sensitivity of PET technique[2]. A large number of candidate compounds have already been tested in basic studies and several compounds were selected for clinical studies[3]. Clinical PET studies have been conducted using several probes such as [^{18}F]FDDNP[4], [^{11}C]SB-13[5] and [^{11}C]Pittsburgh compound-B ([^{11}C]PIB) [6], among which [^{11}C]PIB has been used the most widely in the world[6-8]. Many studies have clearly demonstrated that the [^{11}C]PIB binds to Aβ fibrils, enabling noninvasive assessment of Aβ deposition in the brain of AD patients as a biomarker for AD[6].

Considering the importance of Aβ imaging, our group also developed a novel PET tracer, 2-(2-[2-demethylaminothiazol-5-yl]ethenyl)-6-(2-[fluoro]ethoxy)benzoxazole (BF-227), probably the first original compound used for human study in Japan[9]. Our clinical study has demonstrated that this compound is able to finely detect Aβ deposition primarily in the posterior association area of AD patients and accumulation in the frontal area is not prominent . In contrast to [^{11}C]PIB, interestingly, [^{11}C]BF-227 seems to be able to detect senile plaques containing dense amyloid fibrils preferentially, providing unique and specific information regarding the Aβ pathology in AD patients[9]. In addition, we compared the [^{11}C]BF-227 PET to structural MRI and FDG PET for diagnosing and tracking the severity of AD, to demonstrate that [^{11}C]BF-227 PET was more sensitive than MRI in diagnosing AD and detecting converters from MCI to AD[10]. These studies have indicated that [^{11}C]BF-227 PET is a useful method for early diagnosis of AD and for predicting potential converters from MCI to AD[10,11].

Though these above PET studies have succeeded in demonstrating [^{11}C]BF-227 is a useful tracer, they have used standardized uptake values (SUV) as a tool for clinical evaluation, that is a semi-quantitative measure, simply corrected for the injected dose and the body size of the subject. Precise quantitative examination may give a better rational to the use of such a simple method as a clinical tool, as experienced with [^{11}C]PIB[7,8]. However, we have not conducted the precise examination of pharmacokinetics of [^{11}C]BF-227 in the human brain using arterial sampling data. In this paper, quantification methods for Aβ imaging with PET is briefly overviewed and preliminary results of [^{11}C]BF-227 PET are discussed.

Matrials and Methods

For the present study, 6 AD patients (mean age: 73 years old) and 6 healthy volunteers (mean age: 61 years old) were recruited. PET scan was initiated simultaneously to the [^{11}C]BF-227 injection, in order to obtain dynamic data of 23 time frames. Serial arterial blood sampling was also done. Metabolite fraction was also examined using the blood data at 5, 15, 30 and 60 min post-injection and the fraction data were used for correction of input functions. The dynamic PET data were coregistered to the individual MRI T1 images for defining regions of interest (ROIs) in the cortex and subcortical deep nuclei (Figs. 1a and 1b). This study was approved by the ethics committee of Tohoku University Graduate School of Medicine, and informed consent was obtained from each

subject. In analysis, distribution volume (DV) and binding potential (BP) values of [^{11}C]BF-227 were estimated based on full kinetic compartmental model based on the 1-tisssue (1TM) and 2-tissues models (2TM) (Fig. 1d). Graphical analysis methods were also applied using 2 types of Logan graphical analysis methods; one using the time-activity curve (TAC) of arterial plasma data as an input function for analysis (LGA)[12] and the other using the TAC of the reference brain tissue (cerebellum) (LGAR)[13] (Fig. 1c). PMOD software ver. 3.0 (PMOD Technologies, Zurich, Switzerland) was used for calculation. The results of compartmental model analysis and graphical analysis were compared to the SUV and the SUV ratios to the cerebellar SUV (cerebellar SUVR). Correlations among these different methods were examined one another [14].

Results

No clear difference was observed in the plasma TAC between AD patients and controls. But, clear difference was observed in the tissue TAC between AD patients and controls. [^{11}C]BF-227 accumulation was significantly higher in the cerebral cortex than in the cerebellum of AD patients, while there was no difference in Control. In the analysis results, it turned out that 2TM better described the pharmacokinetics of [^{11}C]BF-227 than 1TM (Fig. 2). The DV and BP values of [^{11}C]BF-227 showed significantly higher in AD patients than in controls, and the most prominent difference was observed in the temporo-occipital and lateral temporal regions[14]. Next, both the DV values correlated well between the two methods such as 2TM and LGA (r^2>0.95 in all regions). In addition, results of LGA and LGAR also correlated well. The LGA values also correlated well to the SUV and SUVR (r^2>0.94 in all regions) [14].

Discussion

Nowadays, Aβ imaging using PET has been recognized as one of the most effective methods for diagnosing early AD and for predicting potential converters from MCI to AD[2,6]. Several promisin[5] and [^{11}C]PIB[6], among which [^{11}C]PIB has been regarded as the most successful Aβ imaging probe. Though an initial study was done without arterial blood sampling and mainly used SUV for clinical evaluation[6], the results of quantitative study was reported in the details[8].

Initial studies using [^{11}C]BF-227 have been conducted in a similar manner. Kudo and colleagues reported that this compound was able to finely detect Aβ deposition

primarily in the posterior association area of AD patients, suggesting that [^{11}C]BF-227 might be able to detect senile plaques containing dense amyloid fibrils preferentially, in contrast to [^{11}C]PIB, providing unique and specific information regarding the Aβ pathology in AD patients[9]. In addition, we performed the comparative study between [^{11}C]BF-227 PET and structural MRI for the diagnosis and tracking the severity of AD. The results demonstrated that PET and [^{11}C]BF-227 was more sensitive than the result of MRI voxel-based morphometry (VBM)[10]. Another study demonstrated that [^{11}C]BF-227 was more sensitive than FDG PET in diagnosing AD and detecting converters from MCI to AD[11]. Thus, these studies may suggest that Aβ PET imaging is more sensitive than the detection of hippocampal atrophy using MRI and the glucose metabolic reduction measured by PET, in diagnosing early AD and predicting potential converters from MCI to AD.

The pharmacokinetics of [^{11}C]PIB has been thoroughly examined using various quantification methods such as full kinetic analysis and graphical analysis[7,8]. In their full kinetic analyses, commonly-used compartmental models are the 3 compartmental model (2-tissue compartmental model: 2TM), where one blood compartment and 2 tissue compartments with specific and non-specific binding are assumed, and the 2 compartmental model (1-tissue compartmental model: 1TM), where one tissue compartment represents both the specific and non-specific binding[7,8]. When the tracer penetrates the blood-brain barrier (BBB) into the tissue compartment very rapidly, 1-tissue compartmental model might better describe the kinetics of the tracer. In the analysis of [^{11}C]PIB, it seems that the 2TM better described the kinetics of tracer binding to the Aβ in the human brain[7,8]. Price and colleagues reported that Logan graphical analysis (LGA) were more useful and robust than the result of analysis using 2TM. However, interesting point is that the cerebellum itself, the reference regions that is thought to be free of mature Aβ plaques, was better described based on the 2TM[8]. Though many [^{11}C]PIB papers employ the use of DVR values for clinical evaluation, the use of BP was also proposed in the paper by Mintun and colleagues[7].

As for [^{11}C]BF-227, the results of compartmental analysis indicated that 2TM showed better fitting than 1TM likely in the case of [^{11}C]PIB[8]. Linearization by LGA method was also successful, likely in the case of [^{11}C]PIB. Significant correlation between the DV values calculated by 2TM and LGA (and LGAR, as well) may suggest that Logan methods are fully applicable to the quantification of [^{11}C]BF-227. Significant correlation of the results of Logan methods to the SUV (and SUVR) may suggest that clinical evaluation

of Aβ deposition using [^{11}C]BF-227 PET can be done by using LGA (and LGAR, as well) and SUV and SUVR. These results can reconfirm the reliability of the results of our recent studies[9-11].

In summary, it is demonstrated that [^{11}C]BF-227 is a promising tracer for Aβ imaging; diagnosing AD patients and detecting potential converters from MCI to AD. In addition to the study on AD diagnosis, recently, further clinical applications of [^{11}C]BF-227 PET have been tried and successful, for instance, to visualize pathological prion protein in prion diseases[15] and to imaging of a-synuclein deposition in multiple system atrophy[16].

For future prospects, in order to obtain more accurate examination, however, correction for partial volume effect should be considered. This partial volume correction (PVC) is important because of the following 2 reasons; one due to local atrophy in AD patients, and the other reason due to relatively high accumulation of [^{11}C]BF-227 in the white matter, as experienced in the analysis of [^{11}C]PIB PET[8].

Acknowledgments

This study was partly supported the grant-in-aids from the Ministry of Health, Welfare and Labor for Amyloid imaging, JST grant for education and research for molecular imaging. The authors thank to all the staffs of Cyclotron and Radioisotope Center, Tohoku University, for the operation of cyclotron and patients care.

References

1) Minoshima S., Foster N.L., Kuhl D.E., Lancet **344** (1994) 895.
2) Nordberg A., Lancet Neurol. **3** (2004) 519.
3) Furumoto S., Okamura N., Iwata R., Yanai K., Arai H., Kudo Y., Curr. Top. Med. Chem. **7** (2007) 1773.
4) Shoghi-Jadid K., Small G.W., Agdeppa E.D., Kepe V., Ercoli L.M., Siddarth P., Read S., Satyamurthy N., Petric A., Huang S.C., Barrio J. R., Am. J. Geriatr. Psychiatry **10** (2002) 24.
5) Verhoeff N.P., Wilson A.A., Takeshita S., Trop L., Hussey D., Singh K., Kung H.F., Kung M.P., Houle S. Am. J. Geriatr. Psychiatry **12** (2004) 584.
6) Klunk W.E., Engler H., Nordberg A., Wang Y., Blomqvist G., Holt D.P., Bergstrom M., Savitcheva I., Huang G.F., Estrada S., Ausen B., Debnath M.L., Barletta J., Price J.C., Sandell J., Lopresti B.J., Wall A., Koivisto P., Antoni G., Mathis C.A., Langstrom B., Ann. Neurol. **55** (2004) 306.
7) Mintun M.A., CNS Spectr. **10** (2005) 13.
8) Price J.C., Klunk W.E., Lopresti B.J., Lu X., Hoge J.A., Ziolko S.K., Holt D.P., Meltzer C.C., DeKosky S.T., Mathis C.A., J. Cereb. Blood Flow Metab. **25** (2005) 1528.
9) Kudo Y., Okamura N., Furumoto S., Tashiro M., Furukawa K., Maruyama M., Itoh M., Iwata R., Yanai K., Arai H., J. Nucl. Med. **48** (2007) 553.
10) Waragai M., Okamura N., Furukawa K., Tashiro M., Furumoto S., Funaki Y., Kato M., Iwata R., Yanai K., Kudo Y., Arai H., J. Neurol. Sci. **285** (2009) 100.
11) Furukawa K., Okamura N., Tashiro M., Waragai M., Furumoto S., Iwata R., Yanai K., Kudo Y.,

Arai H., J. Neurol. **257** (2010) 721.
12) Logan J., Fowler J.S., Volkow N.D., Wang G.J., Ding Y.S., Alexoff D.L., J. Cereb. Blood Flow Metab. **16** (1996) 834.
13) Logan J., Fowler J.S., Volkow N.D., Wolf A.P., Dewey S.L., Schlyer D.J., MacGregor R.R., Hitzemann R., Bendriem B., Gatley S.J., et al., J. Cereb. Blood Flow Metab. **10** (1990) 740.
14) Tashiro M., Okamura N., Watanuki S., Furumoto S., Furukawa K., Funaki Y., Iwata R., Kudo Y., Arai H., Watabe H., Yanai K., Quantitative Analysis of Amyloid β Deposition in Patients with Alzheimer's Disease Using Positron Emission Tomography. IN: Early Detection and Rehabilitation Technologies for Dementia: Neuroscience and Biomedical Applications, Editor: WU JINGLONG. Publisher: IGI Global. Philadelphia, USA (in press).
15) Okamura N., Shiga Y., Furumoto S., Tashiro M., Tsuboi Y., Furukawa K., Yanai K., Iwata R., Arai H., Kudo Y., Itoyama Y., Doh-ura K., Eur. J. Nucl. Med. Mol. Imaging **37** (2010) 934.
16) Kikuchi A., Takeda A., Okamura N., Tashiro M., Hasegawa T., Furumoto S., Kobayashi M., Sugeno N., Baba T., Miki Y., Mori F., Wakabayashi K., Funaki Y., Iwata R., Takahashi S., Fukuda H., Arai H., Kudo Y., Yanai K., Itoyama Y., Brain **133** (2010) 1772.

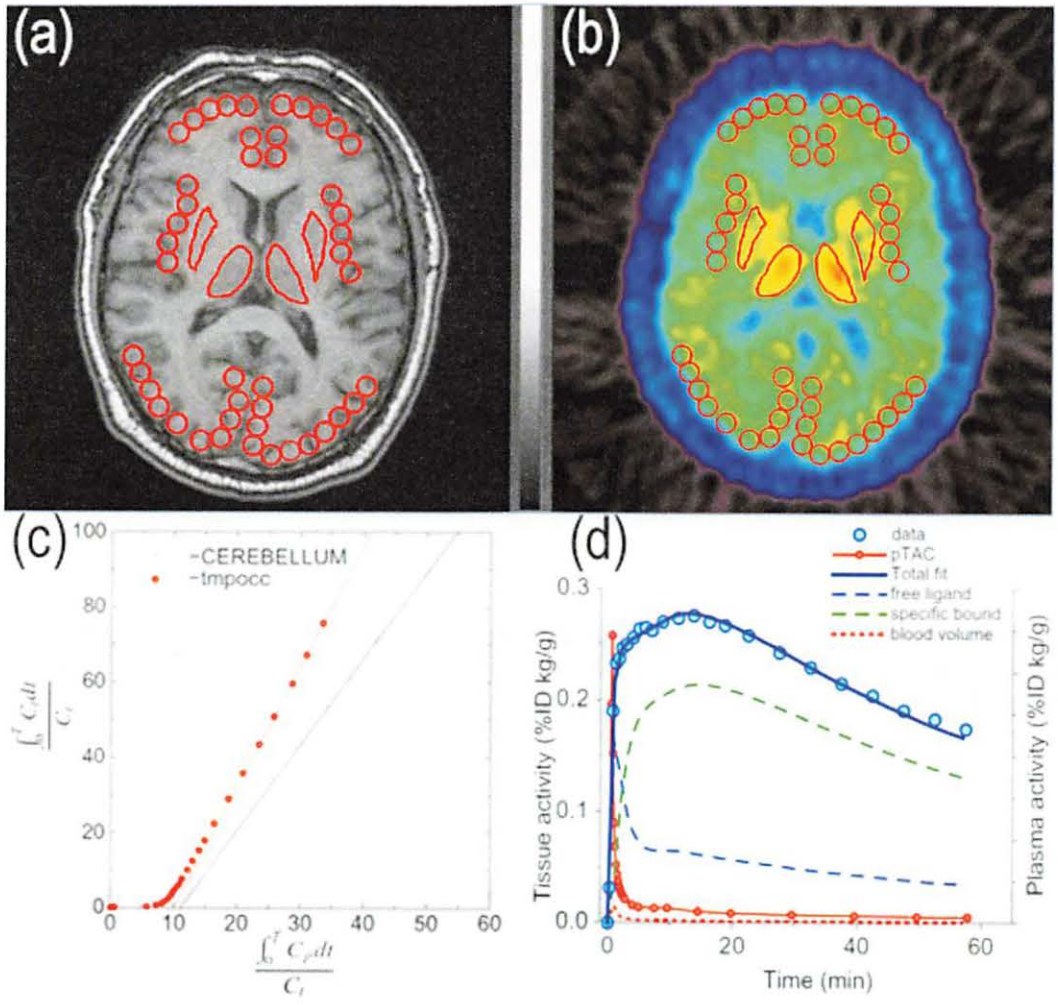

Figure 1. Regions of interest (ROIs) defined in the cerebral cortex and subcortical deep nuclei in the MRI (a) and the co-registered PET image taken from a healthy volunteer subject (b); result of linearization using Logan graphical analysis (c); and time activity curves in plasma and brain tissue for compartmental model analysis (d) are demonstrated.

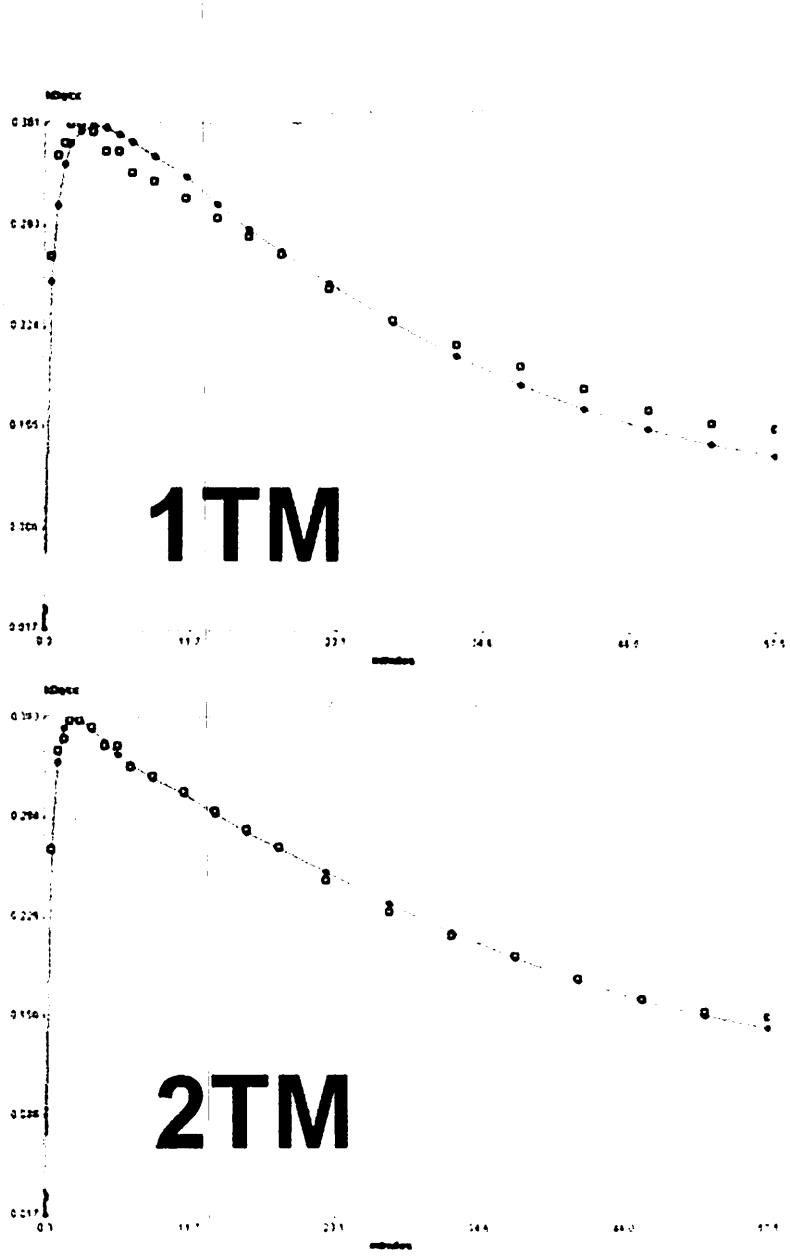

Figure 2. Results of fitting for the time activity curve in the temporoparietal cortex of an Alzheimer's disease patient based on 1-tissue (LEFT) and 2-tissue compartmental models (RIGHT). 2-tissue model gives better fitting result.

VIII. 7. Quantitative Analysis of Donepezil Binding to Acetylcholinesterase Using PET and [5-^{11}C-*methoxy*]Donepezil

Hiraoka K.[1], Okamura N.[2], Funaki Y.[3], Watanuki S.[1], Tashiro M.[1], Kato M.[2], Hayashi A.[4], Hosokai Y.[4], Yamasaki H.[4], . Fujii.[4], Mori E.[4], Yanai K.[2], and Watabe H.[5]

[1]Division of Cyclotron Nuclear Medicine, Cyclotron and Radioisotope Center, Tohoku University
[2]Department of Pharmacology, Tohoku University Graduate School of Medicine
[3]Division of Radiopharmaceutical Chemistry, Cyclotron and Radioisotope Center, Tohoku University
[4]Department of Behavioral Neurology and Cognitive Neuroscience, Tohoku University Graduate School of Medicine
[5]Department of Molecular Imaging in Medicine, Osaka University Graduate School of Medicine

The cholinergic system is one of the most crucial neurotransmitter systems in the brain, and it has very profound links with the manifestations of dementia. The activity of choline acetyltransferase, the enzyme catalyzing acetylcholine synthesis, and of acetylcholinesterase (AChE), the enzyme degrading brain acetylcholine, are both reported to be decreased in the neocortex and the hippocampus of patients with Alzheimer's disease (AD) and dementia with Lewy bodies (DLB), and this decreased activity correlates with the severity of cognitive impairment. Significant loss of cholinergic neurons in the nucleus basalis of Meynert has been reported in the brains of patients with both diseases. Based on these pathological findings, the rational use of reversible AChE inhibitors was proposed as means for potentiating cholinergic neurotransmission, with an aim to improve cognitive function. Currently, several AChE inhibitors are prescribed to improve the cognitive function of patients with dementia. Donepezil hydrochloride is an AChE inhibitor that has been proved to be effective in ameliorating the cognitive impairment of patients with AD and DLB, and it is widely prescribed for the treatment of the diseases.

[5-^{11}C-*methoxy*]Donepezil ([^{11}C]donepezil) was developed for the in-vivo visualization of donepezil binding to AChE using positron emission tomography (PET)[1]. We established the kinetic analysis of [^{11}C]donepezil by a dynamic study involving 60-min PET scans after intravenous injection of [^{11}C]donepezil to six healthy subjects[2]. The rank order of the mean total distribution volume (tDV) values of cerebral regions (cerebral cortices < hippocampus < thalamus < cerebellum < putamen) was consistent with that of

AChE activity reported in a previous post-mortem study (Fig. 1).

Logan graphical analysis[3] generated voxel-wise images of tDV, revealing the overall distribution pattern of AChE in individual brains (Fig. 2).

Subsequently, donepezil-PET imaging was applied to patients with AD[4] and DLB. Compared with elderly normal subjects, patients with mild AD exhibited about 18–20% reduction of donepezil binding in the neocortex and hippocampus, while patients with moderate AD exhibited about 24–30% reduction of donepezil binding throughout the brain. Orally administered donepezil (5mg/day) induced 61.6–63.3% reduction of donepezil binding in AD brains. Patients with DLB exhibited about 19–26% reduction of donepezil binding throughout the brain compared with age- and sex-matched controls (Fig. 3).

In conclusion, [^{11}C]donepezil-PET enables pharmacokinetic study of donepezil and quantitative analysis of AChE in the human brain, which is useful in various situations for patients with dementia.

References

1) Funaki Y., Kato M., Iwata R., Sakurai E., Tashiro M., Ido T., Yanai K., J. Pharmacol. Sci. **91** (2003) 105.
2) Hiraoka K., Okamura N., Funaki Y., Watanuki S., Tashiro M., Kato M., Hayashi A., Hosokai Y., Yamasaki H., Fujii T., Mori E., Yanai K., Watabe H., Neuroimage **46** (2009) 616.
3) Logan J., Fowler J., Volkow N., Wolf A., Dewey S., Schlyer D., MacGregor R., Hitzemann R., Bendriem B., Gatley S., J. Cereb. Blood Flow Metab. **10** (1990) 740.
4) Okamura N., Funaki Y., Tashiro M., Kato M., Ishikawa Y., Maruyama M., Ishikawa H., Meguro K., Iwata R., Yanai K., Br. J. Clin. Pharmacol. **65** (2008) 472.

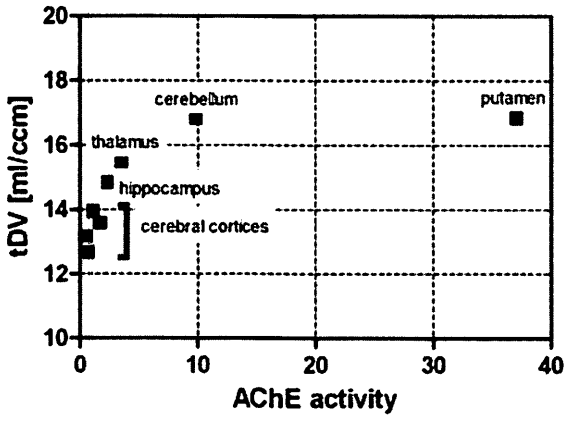

Figure 1. Mean total distribution volume (tDV) values of cerebral regions and post-mortem acetylcholinesterase (AChE) values in human brain obtained from the literature. Post-mortem AChE values are expressed as ratios to the mean AChE value of cerebral cortices.

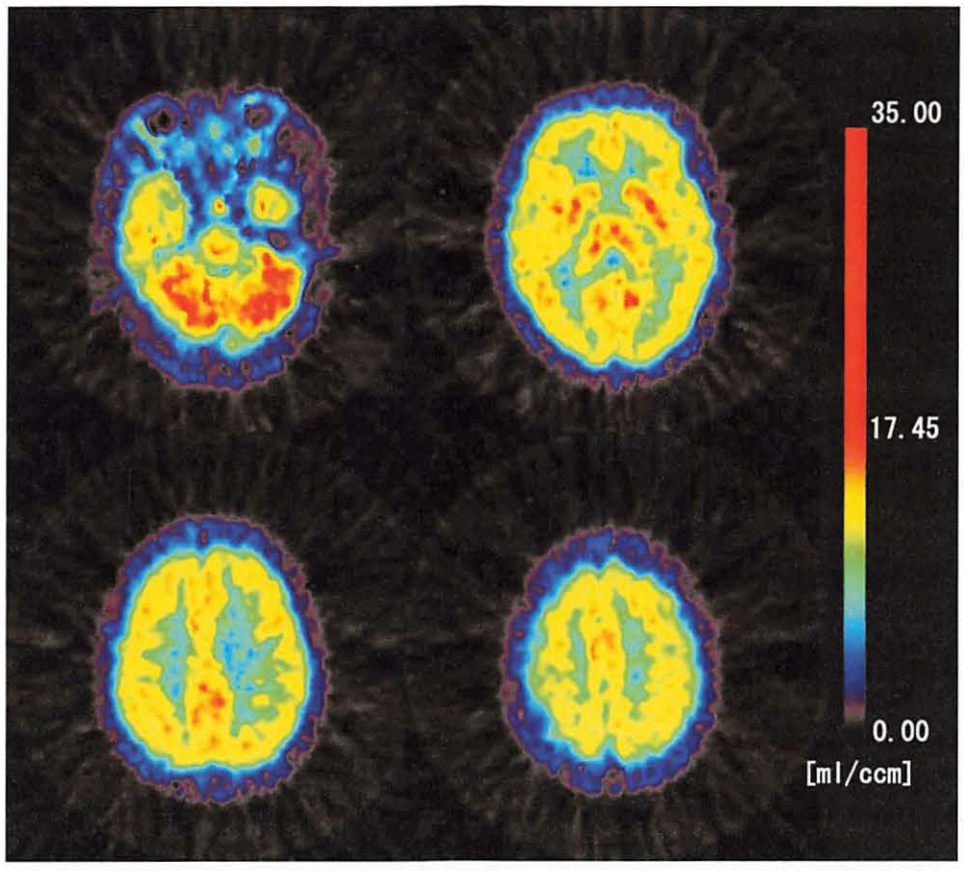

Figure 2. Image of total distribution volumes (tDVs) derived with a Logan plot. tDV values were large in the thalamus, basal ganglia, and cerebellar hemispheres, and small in the cortices.

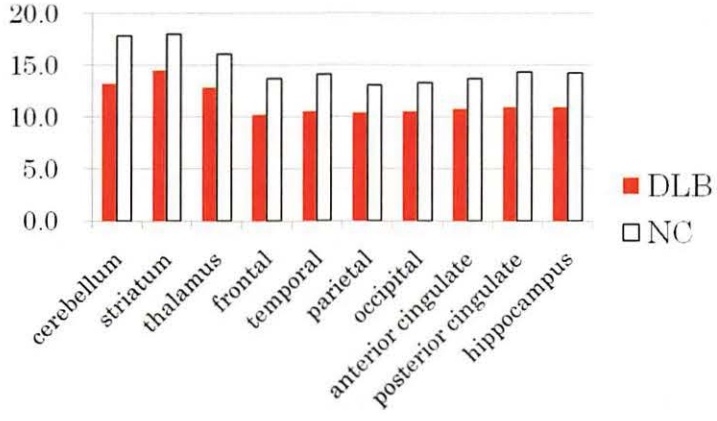

Figure 3. Regional distribution volume data in elderly normal controls (NC) and dementia with Lewy bodies (DLB) patients.

VIII. 8. Hangover Effect of Orally Administered Antihistamines Measured by Brain Histamine H_1 Receptor Occupancy Using PET and ^{11}C-doxepin: A Comparison between Diphenhydramine and Bepotastine in Healthy Subjects

Zhang D.[1,2], Tashiro M.[3], Okamura N.[1], Shibuya K.[1,3], Funaki Y.[4], Watanuki S.[3], and Yanai K.[1,3]

[1]Department of Pharmacology, Graduate School of Medicine, Tohoku University,
[2]Department of Anesthesiology, the First Hospital, China Medical University
[3]Division of Cyclotron Nuclear Medicine and [4]Radiopharmaceutical Chemistry, Cyclotron and Radioisotope Center, Tohoku University

Introduction

Most of us have, at least once, received antihistamine medication for treatment of allergic diseases, common cold, cough, fever, or motion sickness. The most undesirable central nervous system side-effect of antihistamines is sedation[1)], which is considered to be attributed to their penetration across the blood-brain-barrier (BBB) and blockage of the brain histamine H_1 receptors (H_1Rs) which promotes wakefulness and cognition[2)]. To avoid daytime sedation, antihistamines are often administrated at night. However, the residual sedative effect of antihistamines, so-called "hangover effect", has poorly been evaluated, although it can negatively affect daily activities as the actual acute effects do. Subjective questionnaires or psychomotor-task-based evaluations of antihistamines-induced hangover effects[3-5)] have so far failed to provide a quantitative index, making it difficult to compare inter-drugs differences obtained from different experiments.

Using positron emission tomography (PET), antihistamines ability to penetrate across the BBB and cause sedation could be evaluated in terms of brain H_1R occupancy (H_1RO)[6)]. In this study, we evaluated the next-day hangover effect of two antihistamines, specifically, diphenhydramine and bepotastine, the first- and second-generation an

Methods

This study was approved by the Committee on Clinical Investigation at Tohoku

University Graduate School of Medicine and was performed according to the criteria of the Declaration of Helsinki. All experiments were performed at the Cyclotron and Radioisotope Centre, Tohoku University. Eight healthy male volunteers (mean age ± SD: 22.6±2.1 yrs old) received a single dose of diphenhydramine 50 mg (DREWELL®), bepotastine 10 mg (TALION®) or a placebo orally at bedtime (11 p.m.) in a double-blinded, crossover manner with minimum washout-time of 7 days. PET measurement was performed at 11 a.m. the next morning (12 hr post-drug). Blood samples were collected for measuring plasma drug concentration and individual subjective sleepiness is measured using Line Analogue Rating Scale (LARS) and Stanford Sleepiness Scale (SSS). PET brain images, after being corrected and reconstructed, was considered to reflect the distribution volume (DV) according to our previous investigation on static scan protocol[7]. PET brain images obtained from each subject were then co-registered using their T1-weighted magnetic resonance images (MRI) using Statistical Parametric Mapping software (SPM2). Regions of interest (ROIs) were defined in the cortical regions and binding potential ratio (BPR) and H_1R occupancy (H_1RO) values were calculated using placebo data, and were compared between bepotastine and diphenhydramine.

For visualization at a whole-brain level, DV brain images were also analyzed statistically on a voxel-by-voxel basis using SPM2. Differences in parameter values between bepotastine, diphenhydramine and placebo were statistically examined, and regional maxima of statistical significance ($P<0.001$) were projected onto the surface-rendered MRI-T1 standard brain images.

Results

^{11}C-Doxepin radioactivity distribution patterns were similar in the subjects treated with bepotastine or placebo. However, in the subject treated with diphenhydramine, ^{11}C-doxepin radioactivity distribution appeared much lower than that in bepotastine or placebo, reflecting a much lower specific binding density at 12 hr post-dosing with diphenhydramine. Parametric brain BPR images following treatment with diphenhydramine or bepotastine were statistically compared with those obtained following treatment with the placebo. Brain regions with statistically lower BPRs ($P<0.001$) are found in most brain regions, including ACG, PFC, TC and OC, on the other hand, the difference in BPRs between the subjects treated with bepotastine and those treated with the placebo was negligible. Calculation of BPR in the different ROIs revealed significantly

lower values in the case of diphenhydramine than in the case of bepotastine or the placebo ($P<0.05$) in all cortical regions studied, although no significant difference between bepotastine and the placebo was observed. Overall cortical mean H_1RO of bepotastine and diphenhydramine were 16.6% and 44.7%, respectively. H_1RO of both antihistamines are not correlated with their respective subjective sleepiness.

Discussions

Though the hangover effect of antihistamines has been noticed almost simultaneously as their acute sedative effect as established in some early papers showing that promethadine, diphenhydramine, and chlorpheniramine, induce after-morning drowsiness after single or repeated administration[3, 8], the Objective assessments are rare. Alford C. *et al.* reported that the hangover effect of hydroxyzine (50 mg) can be detected by continuous electroencephalography (C-EEG), which reveals increased total drowsiness scores[4]. Boyle J. *et al.* clearly differentiated the hangover effect of first- and second-generation products, specifically, chlorpheniramine and fexofenadine, using polysomnography and performance tasks in a normal-volunteers-involved, placebo-controlled study[5]. However, these assessments have so far failed to provide a quantitative index which can compare inter-drugs differences obtained from different experiments. In this study, the hangover effect of diphenhydramine and bepotastine are quantitatively evaluated in terms of H_1RO at 12 hr post-dose (45% and 17%, respectively). Since we have previously confirmed that H_1RO at Tmax of non-sedating antihistamines is less than 20%[9]. Once H_1RO reaches 50%, sedation is almost inevitable, as seen in many original products[10-12]. These results are agree with the results of proportional impairment ratios (PIRs)[1] and psychomotor study. In this study, the relatively high H_1RO of diphenhydramine, i.e. 45% at 12 hr post-dose suggests a predominant residual sedative effect and therefore increased possibility of sedation. On the other hand, the low H_1RO of bepotastine (less than 20%) supports its non-sedative effect at standard oral dose (10 mg), suggesting that second-generation antihistamine, being free of hangover, may be superior to the classical antihistamines in treating allergic diseases.

In contrast to the highly sensitive PET measurement, it is widely accepted that subjective sleepiness is not a reliable mean for assessing the sedative effect of antihistamines because this parameter is affected by many internal and environmental factors. It is thus not surprising in this study that no inter-drug difference in subjective

sleepiness at 12 hr post-dose was observed. To that end, impairment of objective performance has in some cases been established in the absence of subjective sleepiness following treatment with antihistamines[13,14]. Therefore, those who believe that lack of sleepiness means a better response are probably mistaken and are prone to have a higher sedation-related detrimental risk than those who feel sleepy. The lack of correlation between H_1RO and sleepiness scores in this study further suggests that assessment of antihistamines hangover effect should not be made based on subjective feelings alone.

In summary, we have demonstrated that nighttime-administrated diphenhydramine results in a hangover effect, whereas the non-sedative bepotastine is hangover free the next day. To the authors' knowledge, this is the first study evaluating the residual sedative effect of antihistamines using PET. It must be emphasized that sedating OTC-antihistamines, including diphenhydramine, are often self-administrated by active, healthy individuals during their important years of middle life. The clinical benefits of this treatment need to be weighed carefully against the risks, taking into account drug hangover effect. Further work is encouraged to reaffirm the findings of the present study in repeated dose studies or in patients with chronic allergic conditions.

References

1) McDonald K., et al., Hum Psychopharmacol **23** (2008) 555.
2) Haas H.L., et al., Physiol. Rev. **88** (2008) 1183.
3) Hindmarch I., et al., Arzneimittelforschung **28** (1978) 483.
4) Alford C., et al., Hum. Psychopharmacol. **7** (1992) 25.
5) Boyle J., et al., Curr. Med. Res. Opin. **22** (2006) 1343.
6) Yanai K., Tashiro M., Pharmacol. Ther. **113** (2007) 1.
7) Mochizuki H., et al., Nucl. Med. Biol. **31** (2004) 1005.
8) Risberg A.M., et al., Psychopharmacologia **43** (1975) 279.
9) Tashiro M., et al., Br. J. Clin. Pharmacol. **65** (2008) 811.
10) Tashiro M., et al., J. Clin. Pharmacol. **44** (2004) 890.
11) Yanai K., et al., Br. J. Pharmacol. **116** (1995) 1649.
12) Tashiro M., et al., Br. J. Clin. Pharmacol. **61** (2006) 16.
13) Weiler J., et al., Ann. Intern. Med. **132** (2000) 354.
14) Okamura N., et al., Br. J. Pharmacol. **129** (2000) 115.

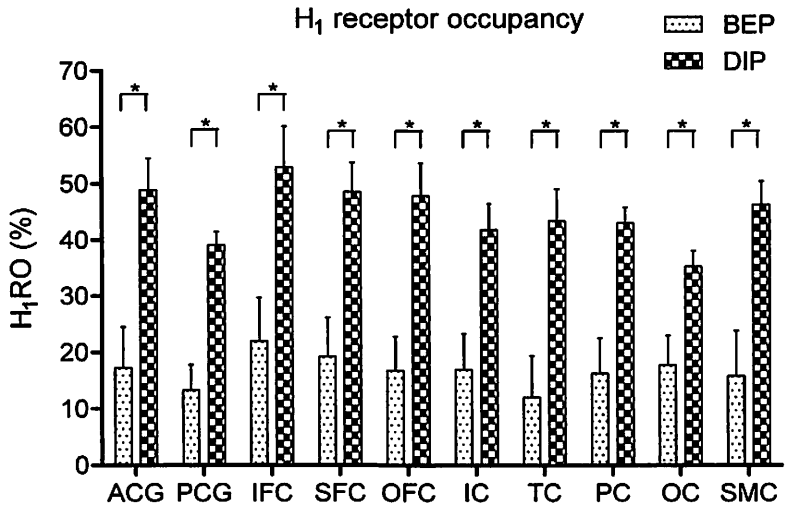

Figure 1. Region of interest (ROI) -based analyses of histamine H_1 receptor occupancy (H_1RO) in the cortex region. *P<0.01, paired-t test. Error bars represent inter-individual variability (S.E.M.). ACG and PCG, anterior and posterior cingulate gyri, respectively; PFC, prefrontal cortex; OFC, orbitofrontal cortex; IC, insular cortex; TC, temporal cortex; PC, parietal cortex; OC, occipital cortex; SMC, sensorimotor cortex.

VIII. 9. Impact of Serotonin Transporter Gene Polymorphism on Brain Activation by Colorectal Distention

Fukudo S.[1], Kanazawa M.[1], Mizuno T.[1], Hamaguchi T.[1], Kano M.[1], Watanabe S.[1], Sagami Y.[2], Shoji T.[2], Endo Y.[2], Hongo M.[3], Itoyama Y.[4], Yanai K.[5], Tashiro M.[6], and Aoki M.[5]

[1]*Departments of Behavioral Medicine,*
[2]*Psychosomatic Medicine,*
[3]*Comprehensive Medicine,*
[4]*Neurology,* [5]*Pharmacology, Tohoku University Graduate School of Medicine*
[6]*Cyclotron and Radioisotope Center*

Visceral Perception and Cingulate Cortex

Our previous study using positron emission tomography (PET) demonstrated that colonic stimulation increases regional cerebral blood flow (rCBF) in the anterior cingulate cortex (ACC) and prefrontal cortex (PFC), showing correlation with increased anxiety[1)]. In a functional magnetic resonance imaging (fMRI) study, patients with irritable bowel syndrome (IBS) showed stronger activation of the ACC in response to intense rectal distention than control subjects[2)]. Imaging data on depressive disorders suggest that one of the common regions of brain activation is the ACC[3)]. Subjects with major depressive disorder compared with healthy controls have also shown increased activation of the ACC during anticipation of pain relative to nonpainful stimuli. With regard to intrinsic functional connectivity, a significant difference for dorsal to rostral ACC connectivity between patients with depressive disorder and controls in terms of higher connectivity in patients has also been reported[4)]. Therefore, increased activity of the ACC is one of the key features of interoception-induced negative emotion.

Serotonin (5-hydroxytryptamine; 5-HT) plays a crucial role in multiple brain function including negative emotion[5)]. Serotonin is released from serotonergic nerve terminals which distribute almost throughout the brain and mainly originate from the raphe nuclei in the brain stem. Among the brain regions, the limbic system (i.e., cingulate cortex, hippocampus, amygdala, orbitofrontal cortex (OFC), and hypothalamus) are densely innervated by serotonergic neurons. The human serotonin transporter (5-HTT) gene

(SLC6A4) is located on chromosome 17q12, and a variant in the upstream promoter region of the 5-HTT gene has been identified[6]. The 5-HTT linked promoter region (5-HTTLPR) polymorphism with long (*l*, 528 bp) and short (*s*, 484 bp) forms affect the expression and function of 5-HTT. Those with the *s* allele of this polymorphism are associated with lower transcriptional efficiency of the promoter than the *l* allele, leading to a lower 5-HTT expression and a lower cellular uptake of serotonin in the presynaptic nerve terminals of serotonergic neurons. This results in a higher serotonin concentration in the synaptic cleft and increases susceptibility to negative mood in individuals with the *s* gene. Individuals with the *s* gene are at significantly greater risk for major depressive disorder following repeated adult stress or childhood trauma[7]. Hariri et al.[8] reported that individuals with the *s* allele show greater amygdala neuronal activity in response to fearful stimuli than individuals homozygous for the *l* allele. Functional analysis of the ACC and amygdala during perceptual processing of fearful stimuli demonstrated tight coupling as a feedback circuit implicated in the extinction of negative effect, and *s* allele carriers showed relative uncoupling of this circuit[9]. These data suggest that 5-HTTLPR at least in part may predict the function of prefrontal-limbic circuits, especially of the ACC and amygdala, during emotional formation.

Although interoception is the essential process of emotional formation, most previous studies used visual and cognitive tasks to demonstrate brain processing. No studies on the influence of 5-HTTLPR on brain processing of visceral perception have been reported. We therefore tested our hypothesis that 5-HTTLPR differentially activates brain regions with colorectal distention in humans[10].

Serotonin Transporter Gene Polymorphism and Positron Emission Tomography

Twenty-eight adult Japanese subjects without organic diseases or psychiatric disorders were enrolled in the study. Subjects were genotyped as described below. Individuals with the *s/s* genotype (n = 14, *s* group) and those with the *l* allele (genotype *l/s*, n = 10; genotype *l/l*, n = 2; genotype *l/extra-l*, n = 2; total n = 14, *l* group) were compared. All subjects were right-handed. Age, sex, gastrointestinal symptoms, and the stimulated site did not differ among groups (Table 1). Each group was composed of 11 healthy subjects and 3 IBS subjects who fulfilled the Rome III criteria[11]. This study was approved by the Tohoku University Ethics Committee and subjects provided written informed consent.

Peripheral blood was sampled with a heparinized syringe. Genotyping of 5-HTTLPR was performed using the same methods as in our previous report[12]. Colorectal stimulation was performed using the same methods as previously described[1,13]. On the experimental day, a catheter with a barostat bag (700 ml in volume) was inserted into the rectum or the upper part of the descending colon by colonoscopy. Colorectal distention stimuli were provided with a computerized barostat equipment (Medtronics Synectics, Shoreview, MN, USA), which inflated the bag at a rate of 38 ml/s. First, each subject underwent a baseline PET scan without bag stimulation. Thereafter, the colorectum was stimulated with bag pressures of 0, 20 and 40 mmHg for 80 s. The intensity of each stimulus was randomly chosen to avoid stimulation order effect, and the time interval between two stimuli was 15 min. After each stimulation, the subjects were asked to report the following 7 items of visceral perception or emotion: abdominal discomfort, abdominal distention, abdominal pain, urgency for defecation, perceived stress, sleepiness, and anxiety. Each sensation was evaluated on an ordinate scale from 0 (no sensation) to 10 (maximal sensation).

Scans of the distribution of $H_2{}^{15}O$ were obtained using a SET-2400W PET scanner (Shimadzu, Japan) operated on a high sensitivity three-dimensional mode with an average axial resolution of 4.5 mm at maximum strength and sensitivity for a 20-cm cylindrical phantom of 48.6 k.c.p.s.kBq^{-1}ml^{-1} [1,13]. For each scan, a subject received approximately 5 mCi (185 MBq) of $H_2{}^{15}O$ intravenously through the forearm vein and underwent colorectal distention during rCBF measurement. The radioactivity peak to the scan onset was about 10 s after the start of colorectal distention at which both the radioactivity peak and peak pressure of the bag simultaneously reached a plateau. The PET scanning room was darkened and the subjects, while awake, were instructed to keep their eyes closed for the whole period of scanning (70 s).

Statistical parametric mapping software (SPM2, Wellcome Department of Cognitive Neurology, London, UK) was used for PET image realignment, normalization, smoothing, and to create statistical maps of significant rCBF changes[14,15]. All rCBF images were stereotaxically normalized into the standard space defined by Talairach & Tournoux[16] using an rCBF template image supplied with SPM2. The normalized images were smoothed using a 12×12×12-mm Gaussian filter, and the rCBF values were expressed in ml dl^{-1} min^{-1}, adjusted for individual global CBF values using ANCOVA, and scaled to a mean of 50. The contribution of each parameter of interest to changes in rCBF was estimated by SPM2

according to the general linear model at the voxel level. Estimates were made using linear compounds of contrasts, and the resulting set of voxel values constituted a parametric map for each contrast. To examine whether specific brain regions differ between the *s* group and the *l* group, we performed subtraction analysis between rCBF changes at stimulation. Brain regions with significant cluster level ($p < 0.05$) and significant voxel level ($T > 4.0$ and $p < 0.0001$) were demonstrated.

The brain image with 0 mmHg was subtracted from the brain image with 40 mmHg. The *s* group showed a significantly larger increase in rCBF in the left ACC (BA 32, x, y, z = -8, 40, -2) by moderate colorectal distention than the *l* group ($p < 0.0001$)(Fig. 1)[10]. The spatial distribution of the more activated area in the *s* group than in the *l* group was mainly the perigenual ACC including the supragenual ACC and subgenual ACC. The *s* group also showed a significantly larger increase in rCBF in the right hippocampus (x, y, z = 32, -42, -4) by mild colorectal distention than the *l* group ($p < 0.0001$) (Fig. 2)[10]. The brain image with 0 mmHg was then subtracted from the brain image with 20 mmHg. The increase in rCBF by mild colorectal distention in the *s* group was significantly larger in the left OFC (BA 47, x, y, z = -38, 24, -20) than that in the *l* group ($p < 0.0001$) (Fig. 3)[10]. Table 2 shows a summary of the significantly more activated brain regions in response to colorectal stimulation in the *s* group than in the *l* group[10]. There were no other regions which differentiate the brain response to colorectal distention between the *s* group and the *l* group.

Colorectal distention significantly and intensity dependently increased the ordinate scale of abdominal discomfort, abdominal distention, abdominal pain, urgency for defecation, perceived stress, and anxiety, and significantly reduced sleepiness in both groups (data not shown). However, the effect of 5-HTTLPR genotype on the changes in the ordinate scale was not significant.

Serotonin, Cingulate and Negative Emotion

Colorectal distention in individuals with the *s/s* genotype activated the ACC, hippocampus, and OFC more than in individuals with the *l* allele[10]. This study[10] are in line with those of Hariri et al.[8] and Pezawas et al.[9] Therefore, our study[10], together with earlier studies, suggests that the *s* allele and *l* allele of 5-HTTLPR exhibit dysfunction of the prefrontal-limbic circuits in response to stimuli that usually evoke negative emotion. The advantage of this study is that the stimulus we used (visceral stimulation) is known to

directly activate the raphe nuclei in the brain stem[17]. Serotonergic neurons originate from the dorsal raphe nucleus and innervate the limbic system (i.e., cingulate cortex, hippocampus, amygdala, OFC, and hypothalamus)[5]. In our study of these brain regions, the differentially activated areas in individuals with the *s/s* genotype from those with the *l* allele were the ACC, hippocampus, and OFC[10]. This implies that our study[10] presents more reliable neuroanatomical evidence than earlier studies.

Individuals with the *s* allele of 5-HTTLPR are associated with lower transcriptional efficiency of the promoter than those with the *l* allele, leading to a lower 5-HTT expression and a lower cellular uptake of serotonin to presynaptic nerve terminals in serotonergic neurons[6]. In our study[10], serotonin neurons in the dorsal raphe nucleus stimulated by colorectal distention would release serotonin from nerve terminals and consequently a higher serotonin concentration may remain in the synaptic cleft of the ACC, hippocampus, and OFC in individuals with the *s/s* genotype. Endogenously released serotonin could therefore change the probability or duration (or both) of neuronal firing in human brain regions in different ways to produce excitatory, inhibitory, or mixed effects. The ACC, hippocampus, and OFC are more activated in individuals with the *s/s* genotype than in those with the *l* allele in our study[10], which could therefore be attributed to the local serotonin action on conductance and the receptors.

The ACC, hippocampus, and OFC are key areas of the emotional circuit as well as serotonergic neurotransmission. The perigenual part of the ACC is related to negative emotion and conflict monitoring[3]. The perigenual ACC is divided into two parts, namely, the supragenual ACC and subgenual ACC. The function of the supragenual ACC negatively correlates with amygdala activity, while that of the subgenual ACC positively correlates with amygdala function[9]. 5-HTTLPR *s* allele carriers show less coupling between the amygdala and the perigenual ACC than *l/l* individuals, particularly in the subgenual ACC[18]. The influence of 5-HTTLPR on coupling between the ACC and amygdala during visceral perception processing warrants future study. The hippocampus is the key region for explicit and implicit memory[5]. In this case, the hippocampus may work to recall possible noxious visceral stimuli as a negative somatic marker. On the other hand, the OFC evaluates reward, punishment and unavoidable sensation[19]. It is also implicated in emotion and emotion-related learning. Distinct areas of the OFC were shown to be activated by monetary rewards and punishments. Moreover, these areas are reported to be correlated with the magnitude of brain activation and the magnitude of rewards and

punishments received. Further, medial OFC activity is related to monitoring the reward value of many different reinforcers, whereas lateral OFC activity is related to the evaluation of punishers which may lead to a change in ongoing behavior[20]. A posterior-anterior distinction exists with more complex or abstract reinforcers (such as monetary gain and loss) represented more anteriorly in the OFC than simpler reinforcers such as taste or pain. Our data showing more activation of the lateral and posterior OFCs suggest that individuals with the *s/s* genotype tend to evaluate mild visceral activation as a punishment marker.

In conclusion, the present data suggest that individuals with a weak function of serotonin transporter respond to gut signals more in emotion-regulating brain regions. Functional gene polymorphism may partially predict the individual effects of long-lasting neural processing from visceral organs.

Acknowledgments

This work was supported by Grants-in-Aid from the Ministry of Education, Culture, Sports, Science and Technology and Grants-in-Aid from the Ministry of Health, Welfare, and Labor, Japan. The authors have no conflict of interest and have nothing to disclose financially regarding the study.

References

1) Hamaguchi T., Kano M., Rikimaru H., Kanazawa M., Itoh M., Yanai K., Fukudo S., Neurogastro. Motil. **16** (2004) 299.
2) Mertz H., Morgan V., Tanner G., Pickens D., Price R., Shyr Y., Kessler R., Gastroenterology **118** (2000) 842.
3) Ressler K.J., Mayberg H.S., Nat. Neurosci. **10** (2007) 1116.
4) Schlösser R.G., Wagner G., Koch K., Dahnke R., Reichenbach J.R., Sauer H., Neuroimage **43** (2008) 645.
5) Kandel E.R., Disorders of mood: depression, mania, and anxiety disorders. In: Kandel E.R., Schwartz J.H., Jessell T.M., (Eds.) Principles of neural science. McGraw-Hill, New York, (2000) 1209.
6) Lesch K.P., Bengel D., Heils A., Sabol S.Z., Greenberg B.D., Petri S., Benjamin J., Müller C.R., Hamer D.H., Murphy D.L., Science **274** (1996) 1527.
7) Caspi A., Sugden K., Moffitt T.E., Taylor A., Craig I.W., Harrington H., McClay J., Mill J., Martin J., Braithwaite A., Poulton R., Science **301** (2003) 386.
8) Hariri A.R., Mattay V.S., Tessitore A., Kolachana B., Fera F., Goldman D., Egan M.F., Weinberger D.R., Science **297** (2002) 400.
9) Pezawas L., Meyer-Lindenberg A., Drabant E.M., Verchinski B.A., Munoz K.E., Kolachana B.S., Egan M.F., Mattay V.S., Hariri A.R., Weinberger D.R., Nat. Neurosci. **8** (2005) 828.
10) Fukudo S., Kanazawa M., Mizuno T., Hamaguchi T., Kano M., Watanabe S., Sagami Y., Shoji T., Endo Y., Hongo M., Itoyama Y., Yanai K., Tashiro M., Aoki M., Neuroimage **47** (2009) 946.
11) Longstreth G.F., Thompson W.G., Chey W.D., Houghton L.A., Gastroenterology **130** (2006) 1480.
12) Mizuno T., Aoki M., Shimada Y., Inoue M., Nakaya K., Takahashi T., Itoyama Y., Kanazawa

M., Utsumi A., Endo Y., Nomura T., Hiratsuka M., Mizugaki M., Goto J., Hongo M., Fukudo S., J. Psychosom. Res. **60** (2006) 91.
13) Suzuki H., Watanabe S., Hamaguchi T., Mine H., Terui T., Kanazawa M., Oohisa N., Maruyama M., Yambe T., Itoh M., Fukudo S., Psychosom. Med. **71** (2009) 619.
14) Friston K., Ashburner J., Frith C.D., Poline J.B., Frith C., Frackowiak, R.S.J., Hum. Brain. Mapp. **2** (1995) 165.
15) Friston K., Holmes A.P., Worsley K.J., Poline J.B., Frith C.D., Frackowiak R.S.J., Hum. Brain. Mapp. **2** (1995) 189.
16) Talairach J., Tournoux P., Co-planar stereotaxic atlas of the human brain. Thieme Medical, New York, 1988.
17) Brink T.S., Mason P., J. Neurophysiol. **92** (2004) 2302.
18) Shah M.P., Wang F., Kalmar J.H., Chepenik L.G., Tie K., Pittman B., Jones M.M., Constable R.T., Gelernter J., Blumberg H.P., Neuropsychopharmacology, Epub ahead of print (Nov 26), 2008.
19) O'Doherty J., Kringelbach M.L., Rolls E.T., Hornak J., Andrews C., Nat. Neurosci. **4** (2001) 95.
20) Kringelbach M.L., Rolls E.T., Prog. Neurobiol. **72** (2004) 341.

Table 1. Subject characteristics of *s* group and *l* group[10]. *s* group: individuals with the *s/s* genotype; *l* group: individuals with the *l* allele (*l/s, l/l,* or *l/extra-l* genotype).

Group		*s*	*l*
Number		14	14
Age (Mean ± SD)		23.9 ± 3.5	22.1 ± 1.4
Sex (Male/Female)		11/3	10/4
Protocol (Colon/Rectum)		8/6	8/6
Diagnosis (Normal/IBS)		11/3	11/3
5-HTTLPR Genotype	*s/s*	14	0
	l/s	0	10
	l/l	0	2
	l/extra-l	0	2

Table 2. Summary of differential brain activation between *s* group and *l* group[10]. Side: R: right, L: left; BA: Brodmann's area: regions with $p < 0.0001$ were shown.

Main Effect	Region	Side	BA	Cluster	p	x	y	z	T
s > *l* (40mmHg − 0 mmHg)									
	Hippocampus	R		215	0.012	32	-42	-4	5.05
	Anterior Cingulate Cortex	L	32	183	0.019	-8	40	-2	4.93
s > *l* (20mmHg − 0 mmHg)									
	Orbitofrontal Cortex	L	47	215	0.012	-38	24	-20	4.32
l > *s*									
	No Suprathreshold Brain Regions								

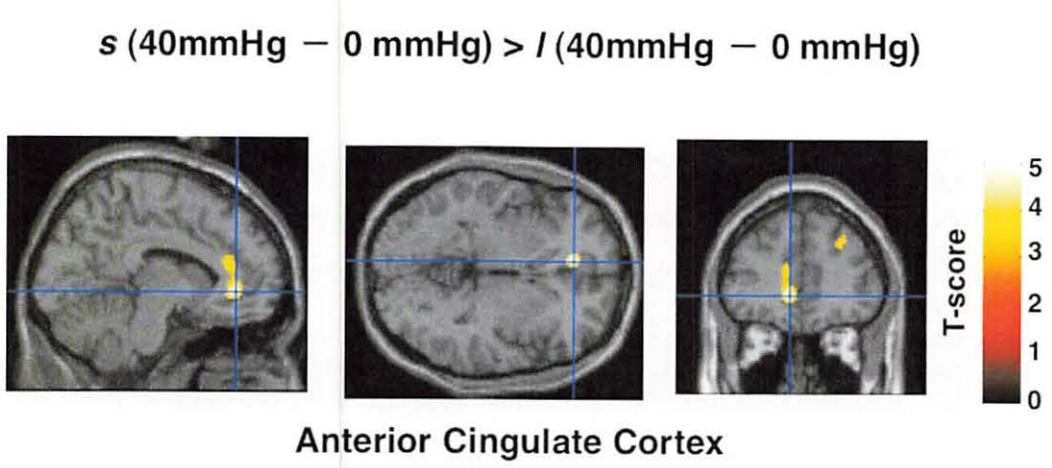

Figure 1. Moderate colorectal distention in the *s* group significantly activated more the left anterior cingulate cortex than that in the *l* group[10]. The image with 40 mmHg was subtracted by that with 0 mmHg. BA 32, x, y, z = -8, 40, -2, $p < 0.0001$.

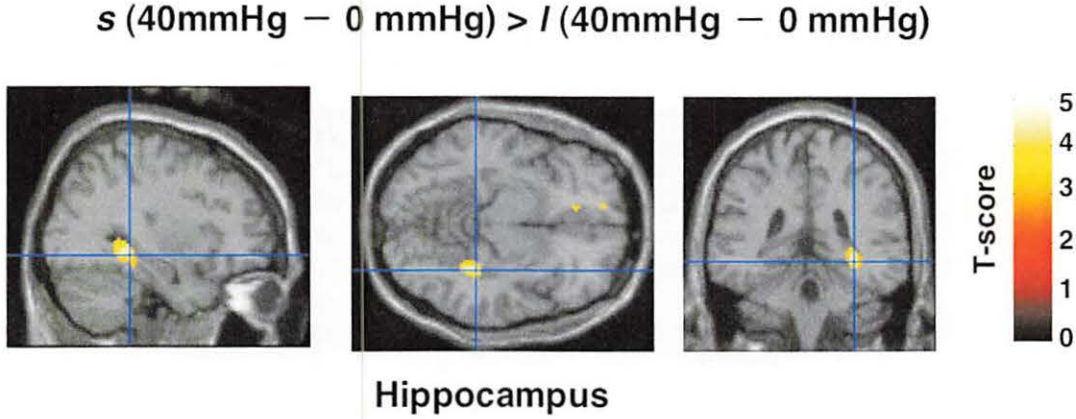

Figure 2. Moderate colorectal distention in the *s* group significantly activated more the right hippocampus than that in the *l* group[10]. The image with 40 mmHg was subtracted by that with 0 mmHg. x, y, z = 32, -42, -4, $p < 0.0001$.

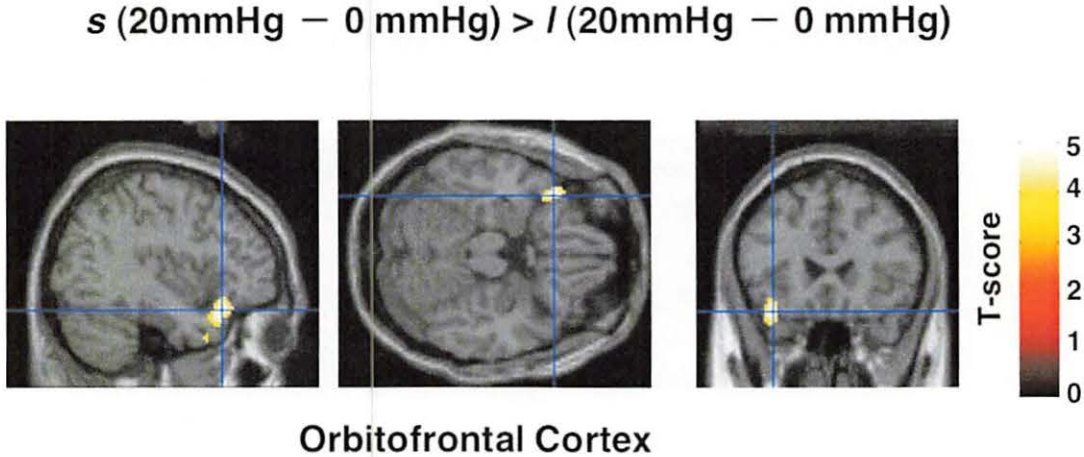

Figure 3. Mild colorectal distention in the *s* group significantly activated more the left hippocampus than that in the *l* group[10]. The image with 20 mmHg was subtracted by that with 0 mmHg. BA 47, x, y, z = -38, 24, -20, $p < 0.0001$.

VIII. 10. Right Temporal-Lobe Contribution to the Retrieval of Family Relationships in Person Identification

Abe N.[1], Fujii T.[1], Ueno A.[1], Shigemune Y.[1], Suzuki M.[2], Tashiro M.[2], and Mori E.[1]

[1]Department of Behavioral Neurology and Cognitive Neuroscience, Tohoku University Graduate School of Medicine
[2]Division of Cyclotron Nuclear Medicine, Cyclotron and Radioisotope Center, Tohoku University

We previously reported a patient who exhibited a peculiar form of delusional misidentification[1]. She had a selective deficit in retrieving family relationships between herself and her daughters and husband (i.e., she misidentified her daughters as her sisters and her husband as her father) despite being able to retrieve their names and faces and some person-specific semantic information (e.g., occupation). Based on this finding, the present positron emission tomography study (PET) was designed to elucidate the brain mechanisms underlying the retrieval of family relationships in healthy individuals.

Fifteen male volunteers who had no history of neurological or psychiatric disease were paid for their participation in this study. Before the analysis of imaging data, three participants were excluded due to excessive head motion during PET scanning (approximately 5 mm). Thus, the results of the present study are based on the data from the remaining 12 subjects (age range 20-24 years, mean age 21.6 years). There were no pathological findings during magnetic resonance imaging (MRI) of any of the subjects' brains. All of the subjects were right-handed. The subjects gave their written informed consent in accordance with the Declaration of Helsinki and the guidelines were approved by the Ethical Committee of Tohoku University.

For each subject, we collected 6 photographs of the faces of the subject's family members. These 6 photographs consisted of different family members, and each photograph of a face represented one of the following: mother, father, grandmother, grandfather, elder brother, younger brother, elder sister, younger sister, aunt, uncle, niece, and nephew. All of the photographs had been taken within the past few years. During PET

imaging, the subjects performed three tasks: (1) a name task in which subjects were presented with photographs of the faces of family members and were asked to retrieve names and answer them orally; (2) an occupation task in which subjects were presented with photographs of the faces of family members and were asked to retrieve occupations and answer them orally; and (3) a relation task in which subjects were presented with photographs of the faces of family members and were asked to retrieve family relationships and answer them orally. In addition to these three tasks, subjects also performed two control tasks, a judgment of the gender of family members in one task and of unfamiliar people in the other task.

Regional cerebral blood flow (rCBF) was measured using PET (SET2400W Shimadzu, FWHM 4.0 mm) and ^{15}O-labeled water (approximately 180 MBq per injection). The transaxial sampling field of view (FOV) was 256 mm, and the axial FOV was 190 mm. The thickness of the slices measured was 3.125 mm. Before the PET experiments, a catheter was inserted into the subject's right brachial vein for tracer administration, and the subject's head was fixed in an air-cushioned headrest apparatus. Each task started 1.5 s before PET data acquisition, and PET data acquisition lasted 60 s. A transmission scan was followed by the experiment, and the data were used to obtain corrected emission images. The PET data were analyzed with SPM8 (Wellcome Department of Imaging Neuroscience, London, UK). The threshold of significance was set at $p<0.001$ (uncorrected for multiple comparisons) with an extent threshold of 10 contiguous voxels.

Behaviorally, all of the subjects were 100% correct in each task; they could completely retrieve names, occupations, and relations in response to each stimulus. As for the imaging data, to identify the neural activity specifically associated with the retrieval of names of family members, we performed a conjunction analysis of name vs. occupation and name vs. relation. We did not find a significant difference in the neural activity of any brain region. Then, to identify the neural activity specifically associated with the retrieval of the occupations of family members, we performed a conjunction analysis of occupation vs. name and occupation vs. relation. This analysis detected a significant activation in the left middle temporal gyrus. Next, to identify the neural activity specifically associated with the retrieval of family relationships, we performed a conjunction analysis of relation vs. name and relation vs. occupation. This analysis detected a significant activation in the right inferior temporal gyrus. These results are summarized in Table 1 and Fig. 1.

In the present study, we used PET to identify the neural correlates of the retrieval of

family relationships in person identification. We found that the retrieval of family relationships was specifically associated with activity in the right inferior temporal gyrus. The right inferior temporal gyrus was one of the regions showing prominent hypoperfusion in our previously reported patient who showed a selective deficit in the retrieval of family relationships in person identification[1]. The present findings, together with our case report, support the view that the retrieval of the relationships between oneself and family members may require a special cognitive process dissociated from the retrieval of names and other person-specific semantic information.

Most importantly, we found that right inferior temporal activation was specifically associated with the retrieval of family relationships. This finding is partially consistent with our a priori hypothesis that the activation relevant to the retrieval of family relationships could be found in the right fronto-temporal region. However, we did not find right frontal activation in this study, suggesting the possibility that the right frontal lobe is not associated with the retrieval of family relationships per se. It is difficult to say what roles the right inferior temporal gyrus plays in the retrieval of family relationships, but we should note the special nature of the conceptual knowledge of family relationships. Basically, knowledge about family relationships is 'relative' semantic information determined by the relationship between oneself and a partner, whereas other knowledge, including names, faces, and some person-specific information (e.g., occupation), is 'absolute' semantic information, which does not depend on the relationship between oneself and a partner. Thus, the process of retrieving family relationships between oneself and one's partner is likely to require an additional cognitive process that monitors 'relative' semantic information, which might be associated with the right inferior temporal gyrus.

Together with the findings of our case study[1], the present imaging findings support the view that the retrieval of the relationships between oneself and family members may require a special cognitive process dissociated from the retrieval of names and other person-specific semantic information. The present study also suggests that the right inferior temporal gyrus may play an important role in the retrieval of family relationships in person identification. One major limitation in the current study is that we could not dissociate the brain activations in response to highly intimate family members (e.g., mother and father) and less intimate family members (e.g., aunt and uncle). The effect of familiarity feeling on brain activations during the retrieval of relations is an important issue to be pursued. Psychological data regarding the subjective feeling of familiarity to family members,

combined with an event-related design using fMRI, could have been informative. It should be also noted that the present findings can be specified only in semantic representations of family members and cannot be generalized in person-related semantics including famous or newly learned people, since the family relationships for an individual exist only between the individual and his/her family members. Although more data collection concerning the neural mechanisms underlying the retrieval of family relationships (e.g., neuropsychological study of sizable series of patients) is required, the present findings provide further insight into the neural mechanisms underlying person identification and theoretically stimulate the updating of neurobiologically-based models of person identification.

Reference

1) Abe N., Neuropsychologia **45** (2007) 2902.

Table 1. Brain regions showing specific responses across name occupation and relation tasks.

Regions (Brodmann's area)	Coordinates			Z value	Cluster size
	x	y	z		
Conjunction analysis of name vs. occupation and name vs. relation No suprathreshold activations					
Conjunction analysis of occupation vs. name and occupation vs. relation Left middle temporal gyrus (21)	-62	-28	-12	3.40	13
Conjunction analysis of relation vs. name and relation vs. occupation Right inferior temporal gyrus (20)	62	-26	-20	3.72	21

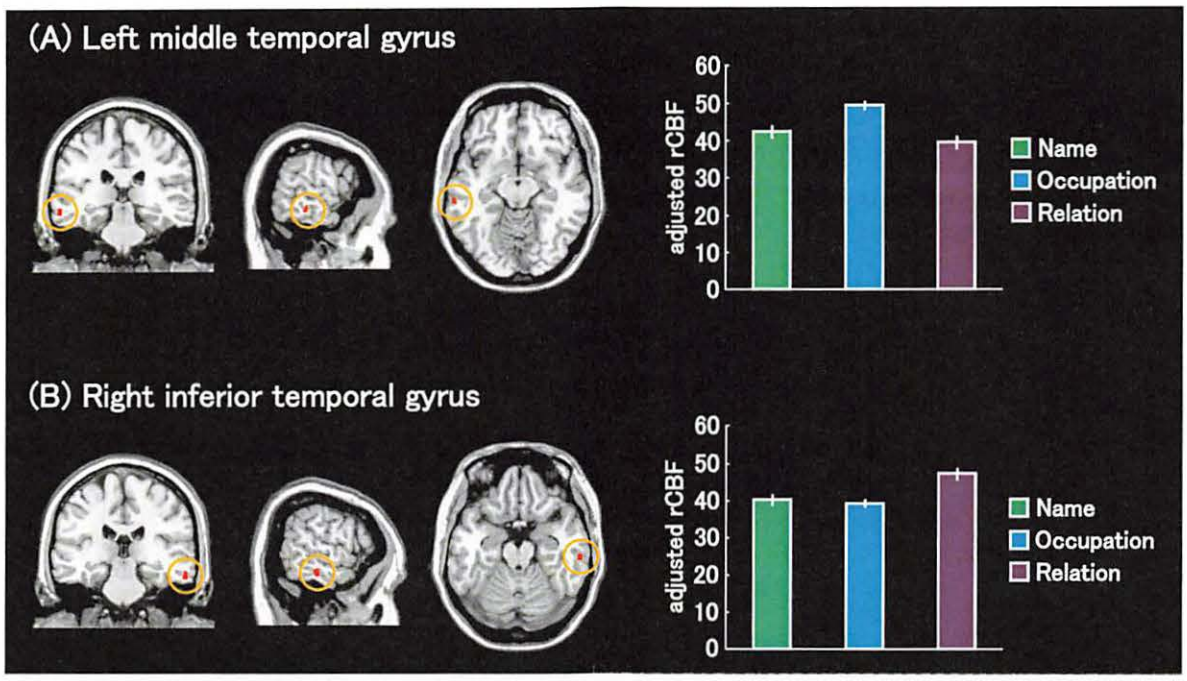

Figure 1. Significant activations detected in SPM whole-brain analyses. The activations are superimposed onto the standard brain. The rCBF values of the following two regions are depicted (error bars represent S.E.M.). (A) The left middle temporal gyrus is activated during the retrieval of occupation compared with the retrieval of name and relation. (B) The right inferior temporal gyrus is activated during the retrieval of relation compared with the retrieval of name and occupation.

VIII. 11. Effects of Emotion and Reward Motivation on Neural Correlates of Episodic Memory Encoding: a PET Study

Shigemune Y.[1], Abe N.[1], Suzuki M.[2], Ueno A.[1], Mori E.[1], Tashiro M.[2], Itoh M.[2], and Fujii T.[1]

[1]Department of Behavioral Neurology and Cognitive Neuroscience, Tohoku University Graduate School of Medicine
[2]Division of Cyclotron Nuclear Medicine, Cyclotron and Radioisotope Center, Tohoku University

Emotional items are better recalled than neutral ones[1]. Previous neuroscientific studies have reported that the enhancement of memory by emotion could be modulated by interaction between the amygdala and hippocampus[2]. In addition, reward motivation also enhances learning and memory processes[3]. Functional neuroimaging studies have demonstrated that interaction between reward-related regions including the orbitofrontal or ventral tegmental areas, and memory-related regions including the medial temporal lobe (MTL) structures, could contribute to the memory enhancement by reward motivation[4,5]. However, little is known about the neural mechanisms how both processes of emotion and reward affect encoding-related processes in episodic memories. In this study[6], by using the positron emission tomography (PET), we investigated neural activations reflecting the effects of emotion and reward during the encoding of episodic memories. Healthy right-handed subjects (mean age: 21.2 years) recruited from the Tohoku University community were required to encode photographs under four conditions, which were categorized by two factors of emotion (negative or neutral) and monetary reward value (high or low reward for subsequent retrieval success). Encoding-related activations were measured by $H_2{}^{15}O$ PET scanning. Behaviorally, emotional valence (negative > neutral) and reward value (high-value > low-value) enhanced retrieval performance of memory, but the interaction between the two factors was not significant (see Fig. 1). In functional neuroimaging data, the left amygdala showed greater activity during the encoding of negative pictures than that of neutral pictures, whereas the left orbitofrontal cortex activity was greater for pictures encoded with high reward value than with low reward value.

Moreover, the conjunction analysis between the two factors of emotional valence and reward value demonstrated significant activations in the right hippocampus (see Fig. 2). The present findings suggest that emotion, which is associated with the amygdala activity, and monetary reward, which is associated with the orbitofrontal cortex activity, could independently affect encoding-related activations in the hippocampus, in which the information of both processes could be integrated during the encoding of episodic memories.

References

1) Stratton G.M., Psychol. Rev. **26** (1919) 474.
2) Cahill L., Haier R.J., Fallon J., Alkire M.T., Tang C., Keator D., Wu J., McGaugh J.L., Proc. Natl. Acad. Sci. U. S. A. **93** (1996) 8016.
3) Stein L., Belluzzi J.D., Fed. Proc. **38** (1979) 2468.
4) Adcock R.A., Thangavel A., Whitfield-Gabrieli S., Knutson B., Gabrieli J.D., Neuron **50** (2006) 507.
5) Tsukiura T., Cabeza R., Neuropsychologia **46** (2008) 2310.
6) Shigemune Y., Abe N., Suzuki M., Ueno A., Mori E., Tashiro M., Itoh M., Fujii T., Neurosci. Res. **67** (2010) 72.

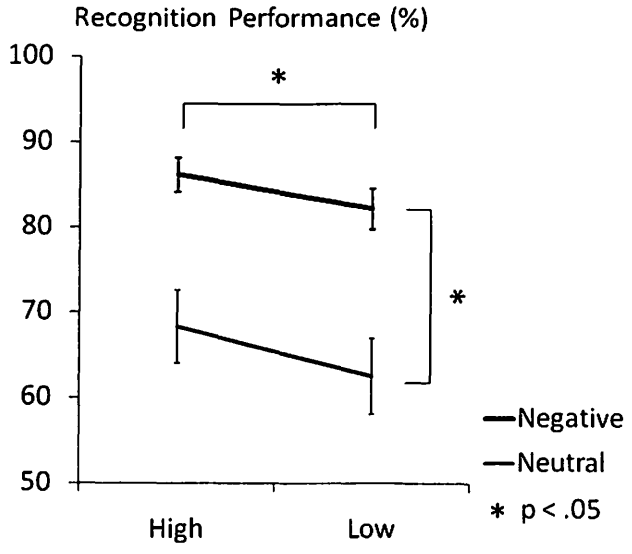

Figure 1. Performance on recognition memory task.

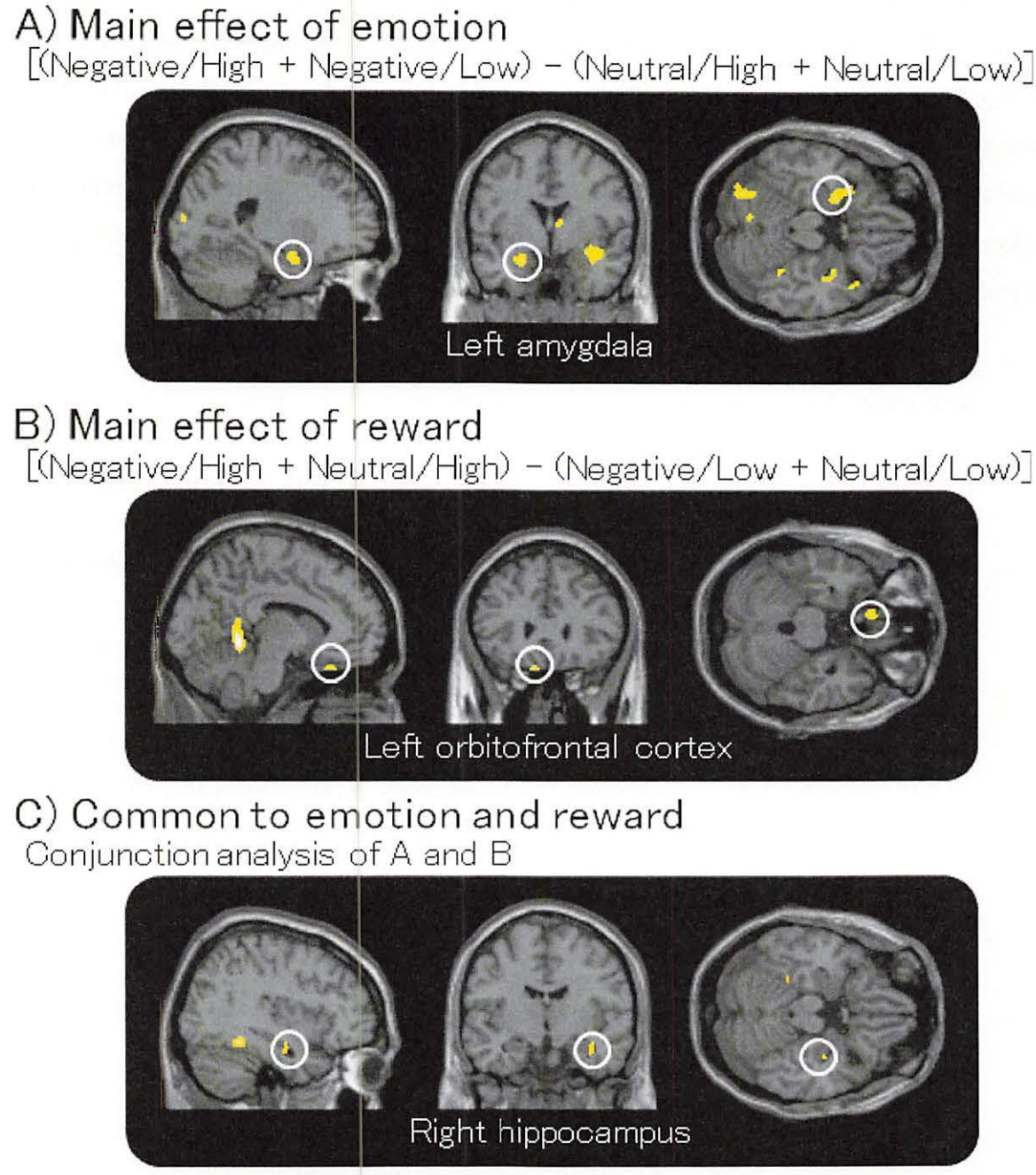

Figure 2. Sagittal, coronal, and axial projections of the regions associated with negative emotion, high monetary reward, and both.

VIII. 12. Neural Correlates of Forgiveness for Moral Transgressions Involving Deception

Hayashi A.[1], Abe N.[1], Ueno A.[1], Shigemune Y.[1], Mori E.[1], Tashiro M.[2], and Fujii T.[1]

[1]Department of Behavioral Neurology and Cognitive Neuroscience, Tohoku University Graduate School of Medicine
[2]Division of Cyclotron Nuclear Medicine, Cyclotron and Radioisotope Center, Tohoku University

Introduction

In human social interactions, there are many types of complex social behaviors that inevitably involve forgivability or moral judgments. Previous neuroimaging studies have shown that ventromedial prefrontal cortex plays a key role in forgivablity judgments[1)] and moral judgments[2)]. Recently, Harada et al. assessed the unique hypothesis that the judgment of deception, a human immoral social behavior, is mediated by the neural substrates of moral judgment[3)]. However, they were not required to judge whether or not the deception was morally acceptable. It therefore remains to be determined whether deception has an effect on forgivability judgments at the behavioral and the neural levels. We used positron emission tomography (PET) to investigate the neural mechanisms underlying the willingness to forgive another person's moral transgression involving deception[4)].

Experimental procedures

a) Participants

Twelve male volunteers with no history of neurological or psychiatric disease were paid for their participation in this study (age range 20-24 years, mean age 21.9 years).

b) Stimuli and tasks

Stimuli consisted of four variants of eight scenarios (a total of 32 stories). A 2×2 factorial design was used to make four variants for each scenario: (i) perpetrators showing either a dishonest or an honest attitude (dishonest or honest) and (ii) perpetrators causing

either serious or minor moral transgressions (serious or minor). Thus, during PET scanning, the subjects were asked to judge the forgivability of each scenario under the following four conditions: (a) a dishonest/serious (DS) condition, (b) a dishonest/minor (DM) condition, (c) an honest/serious (HS) condition, and (d) an honest/minor (HM) condition (Fig. 1). They made forgivability judgments on a 4-point scale ranging from 1 (completely forgivable) to 4 (completely unforgivable) by pressing a button. Eight different stories were presented for each condition, lasting a total of 80 sec. Stories were presented in a randomized order, and the order of the conditions was counterbalanced across subjects.

c) Image acquisition and data analysis

Regional cerebral blood flow (rCBF) was measured using PET (SET2400W Shimadzu, Kyoto, Japan; FWHM = 4.0 mm) and ^{15}O-labeled water. The PET data were analyzed with Statistical Parametric Mapping (SPM5) software (Wellcome Department of Imaging Neuroscience, London, UK). The threshold of significance was set at $p < 0.001$ (uncorrected for multiple comparisons) with an extent threshold of 30 contiguous voxels.

Result

a) Behavioral data

The mean scores for forgivability were 3.65 (SD = 0.33) for the DS condition, 2.36 (SD = 0.52) for the DM condition, 3.10 (SD = 0.44) for the HS condition, and 1.66 (SD = 0.34) for the HM condition. A Friedman test revealed a significant difference ($p < 0.001$). Behavioral data revealed that the perpetrator's dishonesty and the seriousness of the scenario decreased the subjects' forgiveness of the moral transgression.

b) Brain activation

First, to investigate the effect of deception on the neural correlates of forgivability judgments of moral violation, the functional imaging data were analyzed to determine the main effect of the attitude of the perpetrator [(DS + DM) vs. (HS + HM)]. This analysis revealed significant activation in the right ventromedial prefrontal cortex. The opposite contrast [(HS + HM) vs. (DS + DM)] did not reveal significant activation in any brain region.

Second, to investigate the effect of the seriousness of the scenarios on the neural correlates of forgivability judgments of moral violation, the functional imaging data were analyzed to gauge the effect of the severity of the moral violation [(DS + HS) vs. (DM + HM)]. Contrary to our hypothesis, this analysis revealed no significant activation in any brain region. Instead, the opposite contrast [(DM + HM) vs. (DS + HS)] revealed

significant activation in the right middle frontal gyrus, the right caudate nucleus, the right middle occipital gyrus, the right cerebellum, and the left ventromedial prefrontal cortex.

Third, to determine whether an interaction occurred in each of the activated regions, the regional cerebral blood flow (rCBF) values (averaged across all voxels in a given cluster) were analyzed using a two-way repeated-measures ANOVA using the attitude of the perpetrator (dishonest or honest) and the severity of the moral violation (serious or minor) as factors. This analysis revealed that only the left ventromedial prefrontal cortex showed a significant interaction between the two factors. The results for the bilateral ventromedial prefrontal cortex, the right dorsolateral prefrontal cortex, and the right caudate nucleus are illustrated in Fig. 2.

Discussion

The right ventromedial prefrontal activity can be interpreted as the neural correlate of the subject's identification of the perpetrator's deception. In a previous fMRI study, Lissek et al. demonstrated that understanding the mental state of a character in a situation involving deception activates the orbitofrontal and medial prefrontal regions[5]. In a neuropsychological study, Stuss et al. showed that bilateral, particularly right, orbitofrontal lesions impair the ability to detect deception[6]. Expanding on these findings, the present study demonstrates the relationship between the detection of another person's lies and right ventromedial prefrontal activity in the context of forgivability judgments.

Further analysis revealed that only the left ventromedial prefrontal cortex had a significant interaction between the two factors, indicating that this region functions as a mediator of the two factors and modulates judgments regarding the forgivability of moral transgressions.

In conclusion, the present study expands on previous studies[1,7] and sheds additional light on the neural correlates underlying forgiveness. Our results have provided evidence that the right and left ventromedial prefrontal cortices play important, but somewhat different, roles in the forgiveness of moral transgressions involving deception.

1) Farrow T.F., Woodruff P.W., In: Worthington E.L., Jr., (Ed.), Handbook of Forgiveness. Brunner-Routledge, New York (2005) 259.
2) Moll J., Zahn R., de Oliveira-Souza R., Krueger F., Grafman J. Nat. Rev. Neurosci. **6** (2005) 799.
3) Harada T., Itakura S., Xu F., Lee K., Nakashita S., Saito D.N., Sadato N. Neurosci. Res. **63** (2009) 24.
4) Hayashi A., Abe N., Ueno A., Shigemune Y., Mori E., Tashiro M., Fujii T., Brain Res. **1332**

(2010) 90.
5) Lissek S., Peters S., Fuchs N., Witthaus H., Nicolas V., Tegenthoff M., Juckel G., Brune M., PLoS ONE **3** (2008) e2023.
6) Stuss D.T., Gallup G.G., Jr., Alexander M.P., Brain **124** (2001) 279.
7) Young L., Saxe R., Neuropsychologia **47** (2009) 2065.

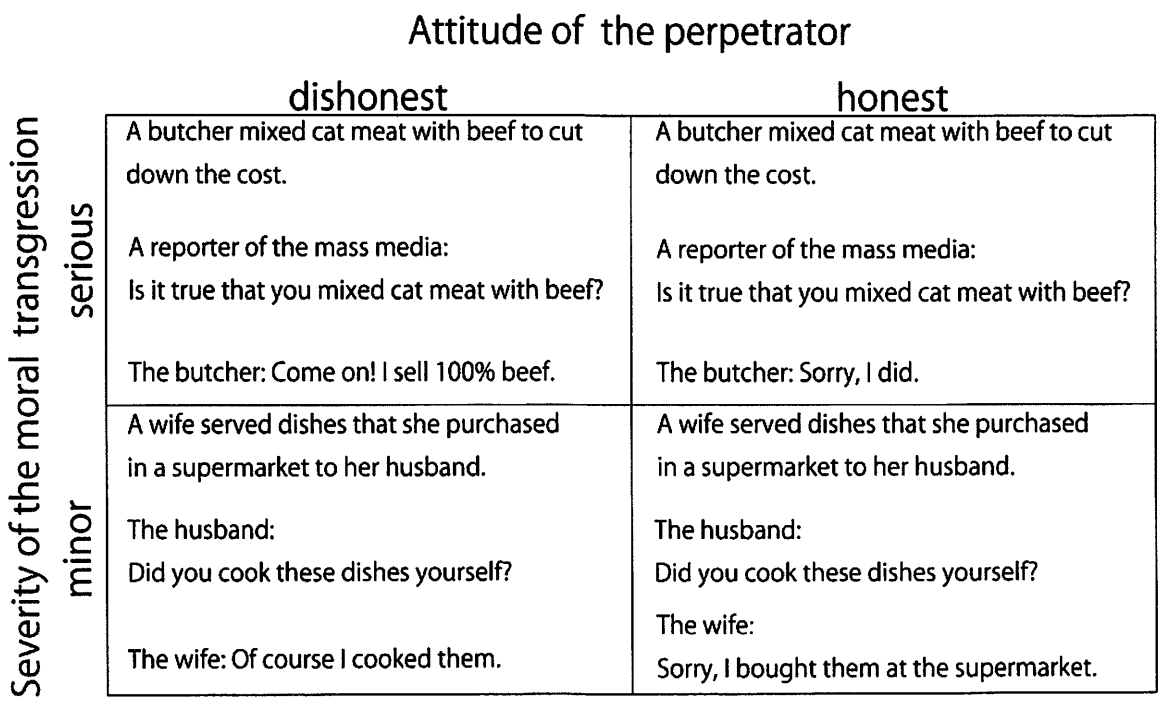

Figure 1. Schematic drawing of the four experimental conditions in the present study.

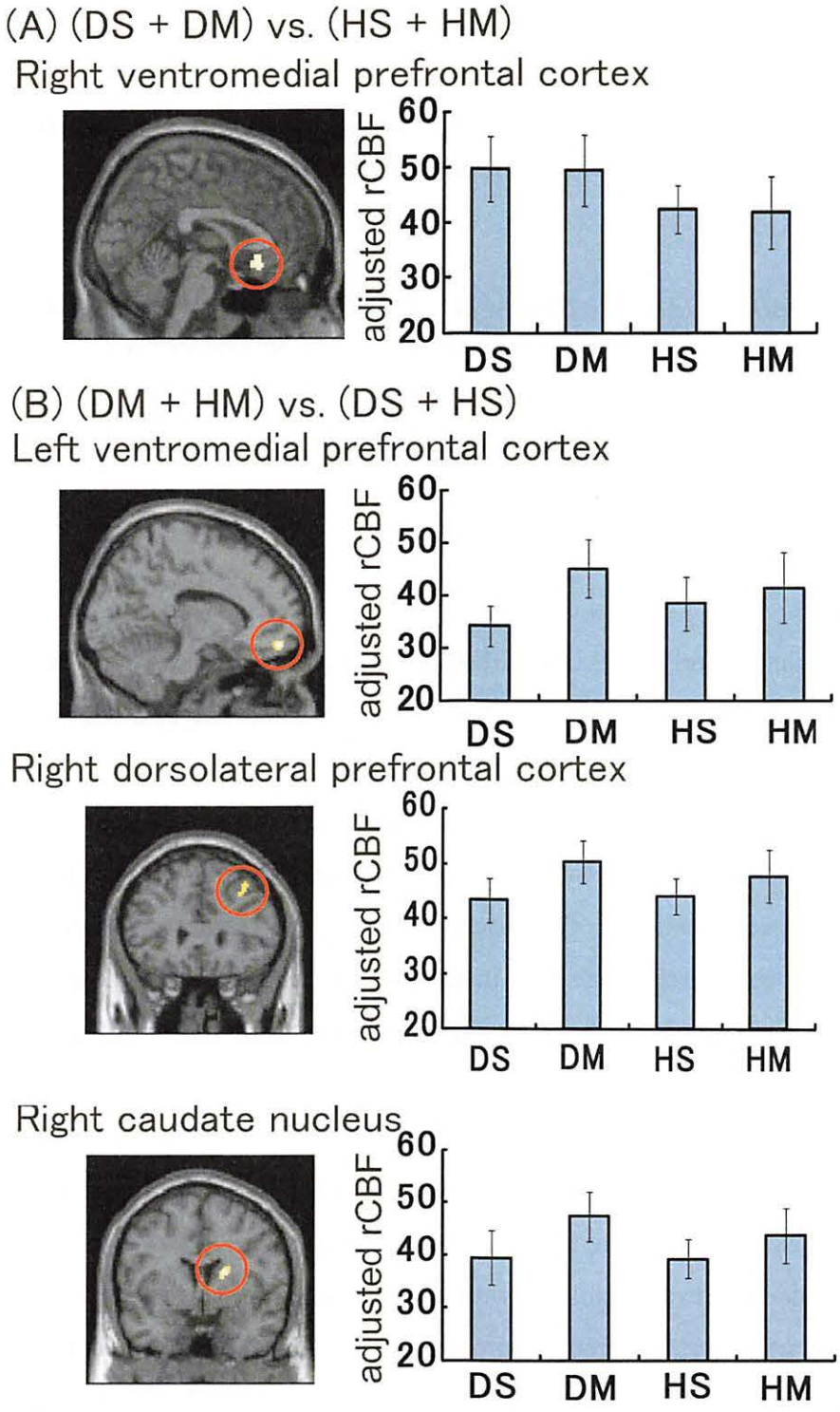

Figure 2. Patterns of rCBF in each brain region for the four conditions. Histogram bars represent the rCBF values (mean ± s.e.m.) adjusted by global normalization for the four conditions. DS, dishonest/serious; DM, dishonest/minor; HS, honest/serious; HM, honest/minor; rCBF, regional cerebral blood flow.

VIII. 13. Brain Activity Following Esophageal Acid Infusion Using Positron Emission Tomography

Kobayashi S.[1], Abe Y.[1], Tashiro M.[2], Koike T.[1], Iijima K.[1], Imatani A.[1], Ohara S.[1], Watanabe S.[3], Fukudo S.[3], and Shimosegawa T.[1]

[1]Division of Gastroenterology, Tohoku University Graduate School of Medicine
[2]Division of Cyclotron Nuclear Medicine, Cyclotron and Radioisotope Center, Tohoku University
[3]Division of Behavioral Medicine, Tohoku University Graduate School of Medicine

Introduction

Gastroesophageal reflux disease (GERD) causes reflux symptoms such as heartburn and regurgitation due to abnormal acid reflux with or without mucosal damage. Although there is a correlation between the severity of macroscopic esophagitis and acid reflux, the severity of subjective symptoms is not necessarily correlated with that of acid reflux. Therefore, the possible involvement of esophageal hypersensitivity to acid in some GERD patients has attracted attention[1)]. The susceptibility of afferent nerve terminals to luminal acid with the dilated intercellular space in the esophageal mucosa is one of the causative factors for acid hypersensitivity[2)]. However, perceived acid reflux accounts for only a minority of reflux events, and the mechanism of symptom development remains to be elucidated. Recently, brain imaging analysis using PET and fMRI demonstrated that some key brain areas, such as the anterior cingulate cortex (ACC) or insula, are involved in the processing of visceral sensation and pain. Abnormality or modulation of those brain activation have been shown in patients with irritable bowel syndrome (IBS)[3–5)], suggesting the participation of abnormal symptom processing in visceral hypersensitivity. Until now, only a few studies have investigated brain activity after esophageal acid stimulation[6-8)]. The aim of this study was to investigate induced symptoms and brain activity using PET in esophageal acid stimulation.

Materials and Methods

Subjects

Fifteen right-handed healthy adult male volunteers (mean age: 26.7 years; range:

21–37 years), who had no typical reflux symptoms such as heartburn and regurgitation, were recruited for the study. A small-diameter catheter was transnasally indwelled in the mid esophagus. A wired pH glass electrode, pre-attached at its proximal side 3 cm from the infusion catheter, was connected to a pH meter. In order to obtain correction data for γ-ray absorption in the body, subjects initially underwent a transmission scan using a $^{68}Ge/^{68}Ga$ radiation source.

Esophageal acid infusion

The procedures for esophageal infusion and PET scan are schematically shown in Fig. 1. Infusions of 50 mL HCl (pH 1 and 2) or distilled water (pH 7) were provided by a catheter using an automatic syringe pump in the supine position. In order to counterbalance the effects of the infusion order, the order was randomly selected from pH 1-7-2-7-1, pH 2-1-7-7-1, and pH 7-1-1-7-2. Then ^{15}O-labeled water was administered intravenously in synchronization with the completion of each 5-min infusion. After confirming that the brain activity could be detected, a PET emission scan of the head was performed for 60 s prior to the PET scan. Using a PET scanner in a 3D data acquisition mode, a total of 10 scans were taken before and after each of the five infusions, to measure the regional cerebral blood flow in each subject. Subjects were asked to rate the severity of heartburn symptoms on an analog scale of 0–10 after each infusion. Symptoms were statistically analyzed by Fisher's test and the Wilcoxon signed-ranks test. Differences were considered statistically significant when the P value was < 0.05.

PET data analysis

The PET data were analyzed using statistical parametric mapping (SPM) software (SPM2), and significantly different changes in regional cerebral blood flow were mapped. First, brain images taken following infusion with hydrochloric acid (pH 1 and 2) or distilled water (pH 7), as well as images taken at baseline (prior to all infusions) were subjected to subtraction analysis to investigate the brain regions that were activated by each infusion. Next, the effects of repeated infusion of acid or distilled water were assessed by subtraction analysis of images obtained following the first and second infusions with pH 1 and pH 7 solutions. All statistical methods were evaluated using linear convolution and contrasts, and the voxel values for each image were constructed using a statistical parametric map of the t-statistic statistical parametric mapping. The location of statistical peaks was

determined in Talairach and Tournoux atlas. *P* (uncorrected) < 0.001 was defined as statistically significant for increased cerebral blood flow.

Results

Enhanced incidence and severity of symptoms following acid infusion

As shown in Table1, the incidence of heartburn symptoms following each infusion showed a step-wise increase with increasing acidity of the perfusate. The incidence of heartburn tended to be higher after the second pH 1 infusion than after the first, and these scores were significantly increased following the second pH 1 infusion. On the other hand, the heartburn incidence and scores in both pH 7 infusions were much lower compared to the pH 1 infusions. Heartburn incidence and scores following pH2 infusion were higher than that of the pH 7 infusions and lower than that of the pH 1 infusions.

Activated brain areas following acid infusion Comparison of brain images following each infusion:

The brain image obtained at rest prior to all infusions was defined as the baseline image. Differences between brain images at baseline and those taken after infusion with acid or distilled water were subjected to subtraction analysis. Brain regions with increased blood flow were defined as those neurologically activated by each infusion. Brain regions activated following each infusion are are summarized in Table 2. In the insula, activation was observed at the second pH 1 and 2 and first pH 7 infusions. Activation in the cingulate cortex was observed in nearly all infusions, with no particular trend observed for the topography of the activated sub-regions. At pH 1 and 2, activation was observed in the more anterior (rostral) part of the ACC (BA 24a) and, at pH 7, in the more posterior (dorsal) part of the ACC (BA 24a'). After infusions at pH 1 and 2 but not pH 7, activation was observed in the temporal pole (BA 38). Activation was also observed in the cerebellum following infusions at pH 1 and 2, and in the parahippocampal gyrus after both pH 1 infusions. The frontal area, precentral gyrus, and thalamus were less activated after each infusion.

Comparison of brain imaging with first and second infusion at pH1 and 7:

As shown in Table 3, the second pH 1 infusion minus the first showed that cerebral blood flow was increased in the right orbitofrontal cortex (Fig. 3a), right cuneus, left cerebellum, right superior temporal gyrus, right middle frontal gyrus(Fig. 3b), right pons,

right lingual gyrus, left putamen, and right caudate nucleus. On the other hand, the result of the second pH 7 infusion minus the first showed an increase in cerebral blood flow in the right middle frontal gyrus, left cerebellum, right midbrain, left PCC, and right superior frontal gyrus.

Discussion

In the present study, we found that brain activity was substantially increased in the cingulate cortex and frontal lobe following esophageal acid infusion, with little activity observed in the thalamus and somatosensory areas. The insula was not consistently activated by acidic or non-acidic stimulations in this study. Activation of the ACC predominantly occurred in the anterior part (BA 24) at pH 1 and 2 with severer heartburn symptom, consistent with the more anterior part of the ACC is involved in affective and emotional responses[9].

The heartburn symptom scores following infusions at pH 1 and 2 were higher compared with those at pH 7. We found that the parahippocampal gyrus was activated only by pH 1 infusion. This area is an important part of the limbic system, which plays a major role in the processing of emotional reaction or memory[10]. Therefore, activation of the parahippocampal gyrus is also compatible with induction of uncomfortable heartburn by acid infusion. In addition, activation was observed in the temporal pole (BA 38) following infusions at pH 1 and 2, but not at pH 7. This area is activated by distention in the proximal stomach[11], and another report has described activation of the temporal pole by distention of the descending colon, with a feeling of anxiety[12]. In a study using visual stimulation, the temporal pole was activated by emotions of comfort and discomfort, wakefulness, and attended stimulation[13]. Therefore, the activation of the temporal pole observed in our study could have been due to alterations in the level of arousal, attention and emotion following acid infusion.

In this study, the heartburn scores were significantly higher after the second pH 1 infusion compared to the first, which suggests that esophageal sensation was sensitized by repeated acid infusion. Visceral sensitization, which can occur at the primary afferent nerve level (peripheral sensitization) and/or the spinal cord level (central sensitization), is considered as a very important phenomenon in the development of visceral sensation[14]. Recent studies using cortical evoked potentials or fMRI have reported that esophageal sensitization induced by acid stimulation results in alterations in the neural activity of the ACC and insula[15-17]. We found that, by subtraction analysis of the second pH 1 minus the

first, that the orbitofrontal cortex was strongly activated with the highest Z-score and cluster level. The orbitofrontal cortex, which is frequently observed to be activated following stimulation of the lower gastrointestinal tract, was less activated following esophageal stimulation in previous studies[18,19]. As a higher center of sensory integration, this area is thought to participate in the assessment of reward, punishment, comfort, discomfort, and memory or its verification[20]. The orbitofrontal cortex might also play a role in symptom processing with esophageal acid sensitization.

In summary, this present study showed that the insula, cingulated gyrus, temporal gyrus, and cerebellum were activated in esophageal acid perception in healthy volunteers, and that involvement of the somatosensory and prefrontal areas was minimal. In particular, emotion-related brain regions such as the anterior part of ACC, the parahippocampal gyrus and the temporal pole were activated under acidic conditions in the esophagus. It is also suggested that activation of the orbitofrontal area is involved in esophageal sensitization to repeated acid stimulation at the cerebral level. Dysfunction of these brain areas may be associated with the pathogenesis of functional heartburn or non-erosive reflux disease. Further studies are warranted to elucidate the mechanism of esophageal acid perception and sensitization

Acknowledgments

This study was partly supported by a JST grant on research and education in molecular imaging and by Grant-in-Aid for Young Scientists (B) (KAKENHI No.19790465)

References

1) Tack J., Fass R., Aliment. Pharmacol. Ther. **1** (2004) 28.
2) Knowles C.H., Aziz Q., Gut **57** (2008) 674.
3) Silverman D.H., Munakata J.A., Ennes H., et al., Gastroenterology **112** (1997) 64.
4) Mertz H., Morgan V., Tanner G., et al., Gastroenterology **118** (2000) 42.
5) Hobson A.R., Aziz Q., Gut **53** (2004) 1198.
6) Aziz Q., Andersson J.L., Valind S., et al., Gastroenterology **113** (1997) 50.
7) Kern M.K., Birn R.M., Jaradeh S., et al., Gastroenterology **115** (1998) 1353.
8) Kern M., Hofmann C., Hyde J., Shaker R., Am. J. Physiol. Gastrointest. Liver Physiol. **286** (2004)174.
9) Bush G., Luu P., Posner M.I., Trends Cogn. Sci. **4** (2000) 215.
10) Craig A.D., Nat. Rev. Neurosci. **3** (2002) 655.
11) Vandenbergh J., Dupont P., Fischler B., et al., Gastroenterology **128** (2005) 564.
12) Hamaguchi T., Kano M., Rikimaru H., et al., Neurogastroenterol Motil **16** (2004) 299.
13) Lane R.D., Chua P.M., Dolan R.J., Neuropsychologia **37** (1999) 989.
14) Anand P., Aziz Q., Willert R., et al., Neurogastroenterol Motil. **19**(Suppl 1) (2007) 29.
15) Sami S.A., Rössel P., Dimcevski G., et al., Neuroscience. **140**(1) (2006) 269.
16) Yang M., Li Z.S., Xu X.R., et al., Neurogastroenterol Motil. **18**(4) (2006) 292.

17) Lawal A., Kern M., Sanjeevi A., et al., Am. J. Physiol. Gastrointest. Liver Physiol. **294**(3) (2008) G787.
18) Hobday D.I., Aziz Q., Thacker N., et al., Brain **124** (2001) 361.
19) Kern M.K., Jaradeh S., Arndorfer R.C., et al., Am. J. Physiol. Gastrointest. Liver Physiol. **281** (2001) 1512.
20) Kringelbach M.L., Nat. Rev. Neurosci. **6** (2005) 691.

Table 1. Incidence of heartburn symptoms and heartburn scores induced by each infusion.

	Heartburn incidence	Mean heartburn scores (range)
pH 7 (first infusion)	5/15 (33.3%)	1.4 (0-7)
pH 7 (second infusion)	5/15 (33.3%)	1.0 (0-6)
pH 2	7/15 (46.7%)	1.9 (0-9)[b]
pH 1 (first infusion)	10/15 (66.7%)	3.2 (0-10)[c]
pH 1 (second infusion)	12/15 (80.0%)[a]	5.0 (0-10)[d]

a: $P = 0.0253$ vs. pH 7 (first infusion) and pH 7 (second infusion)
b: $P = 0.0269$ vs. pH 7 (second infusion)
c: $P = 0.0464$ vs. pH 7 (first infusion), $P = 0.0253$ vs. pH 7 (second infusion)
d: $P = 0.0040$ vs. pH 1 (first infusion), $P = 0.0075$ vs. pH 2, $P = 0.0041$ vs. pH 7 (first infusion), $P = 0.0071$ vs. pH 7 (second infusion)

Table 2. Summary of brain activated regions by each infusion (comparison with baseline).

Major brain regions	Subregions	BA	First pH7	Second pH7	pH2	First pH1	Second pH1
Frontal lobe	Superior frontal gyrus	10		R	L		
	Middle frontal gyrus	10		R			
	Inferior frontal gyrus	47		L			
Temporal lobe	Superior temporal gyrus	38			L	R	L
	Superior temporal gyrus	42	L				
	Middle temporal gyrus	21		L		L	
	Middle temporal gyrus	42	L		L		
	Inferior temporal gyrus	45			R		
PMA	Precentral gyrus	4	R				
	Precentral gyrus	6				R	
PSA	Postcentral gyrus	1,2,3		R			
ACC	Anterior part	24			R	L+R	
	Mid/posterior part	24'	L+R	R			
PCC				R	L		L
Insula	Anterior part		R		R		R
cerebellum					C+L		L
thalamus				R+L			R+L
PHG						L	R

PMA, primary motor area; PSA, primary somatosensory area; ACC, anterior cingulate cortex; PCC, posterior cingulate cortex; PHG, parahippocampal gyrus; BA, Brodmann area; R, right; L, left; C, center

Table 3. Results of subtraction analysis of brain images after the first and second infusions at pH 1 and 7.

Condition	Region	Side	BA	x	y	z	Z-score	Voxels in cluster
Second pH 1 – first	Orbitofrontal cortex	R		38	36	-24	4.44	167
	Cuneus	R	19	2	-82	36	3.79	51
	Cerebellum	L		-22	-40	-50	3.74	23
	Superior temporal gyrus	R	8	26	36	40	3.69	37
	Middle frontal gyrus	R	32	22	50	8	3.69	23
	Pons	R		10	-36	-12	3.47	31
	Lingual gyrus	R	19	4	-60	-2	3.37	12
	Putamen	L		-24	-8	2	3.32	16
	Caudate nucleus	R		18	-34	16	3.30	16
Second pH 7 – first	Middle frontal gyrus	R	10	36	46	0	4.03	47
	Cerebellum	L		-18	-98	-18	3.98	40
	Midbrain	R		2	-40	2	3.65	27
	Posterior cingulate cortex	L	23	-14	-16	30	3.61	11
	Superior frontal gyrus	R	8	14	22	42	3.57	33

R, right; L, left

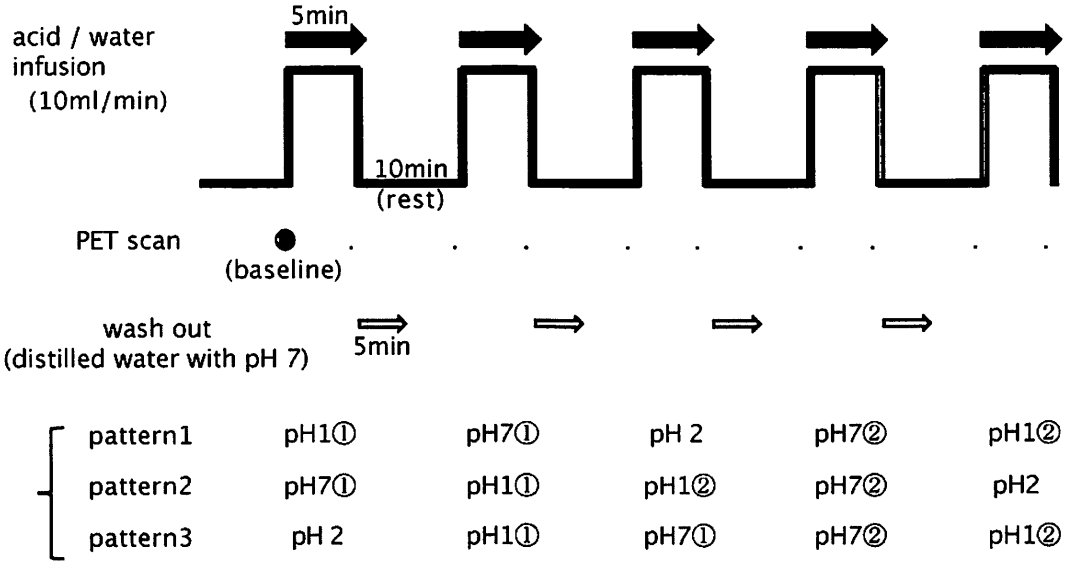

Figure 1. This schema illustrates the procedure of esophageal infusion and brain PET scanning. The infusions were performed twice for pH 1 and 7 solutions (distilled water) and once for the pH 2 solution. In order to counterbalance the effects of the infusion order, the order was randomly selected per each subject from pH 1-7-2-7-1, pH 7-1-1-7-2 and pH 2-1-7-7-1 as shown. First infusion, Second infusion, PET: Positron emission tomography.

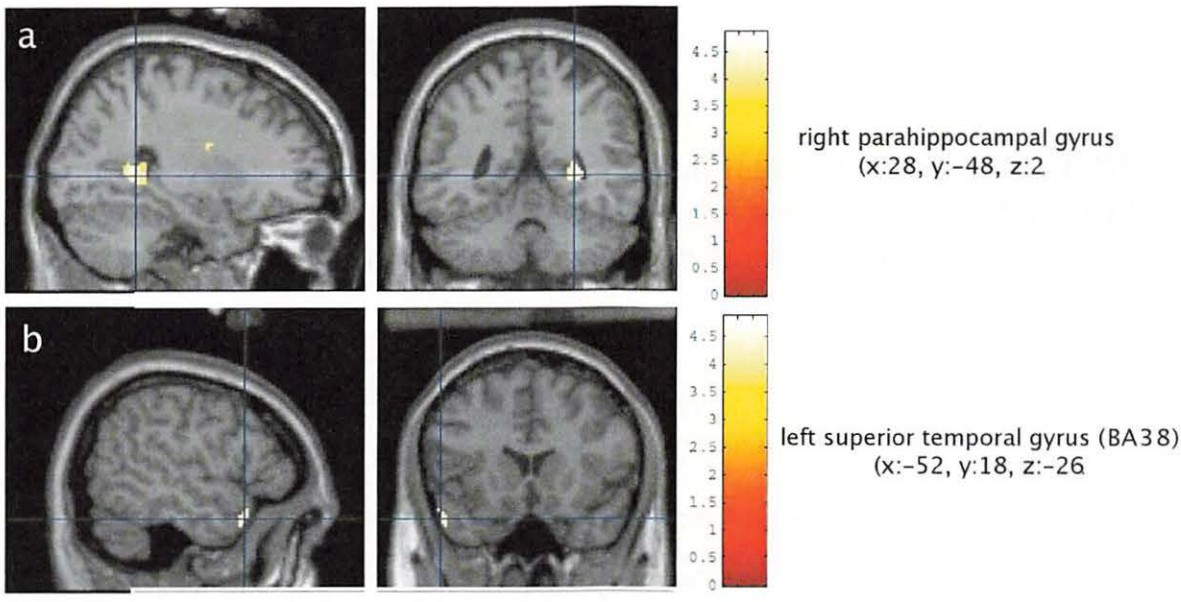

Figure 2. Representative images from the subtraction analysis of the second pH 1 infusion minus the baseline. Left, sagittal view; right, cranial view. a. Right parahippocampal gyrus (x: 28, y: –48, z: 2). b. Left superior temporal gyrus (temporal pole, BA38) (x: –52, y: 18, z: –26)

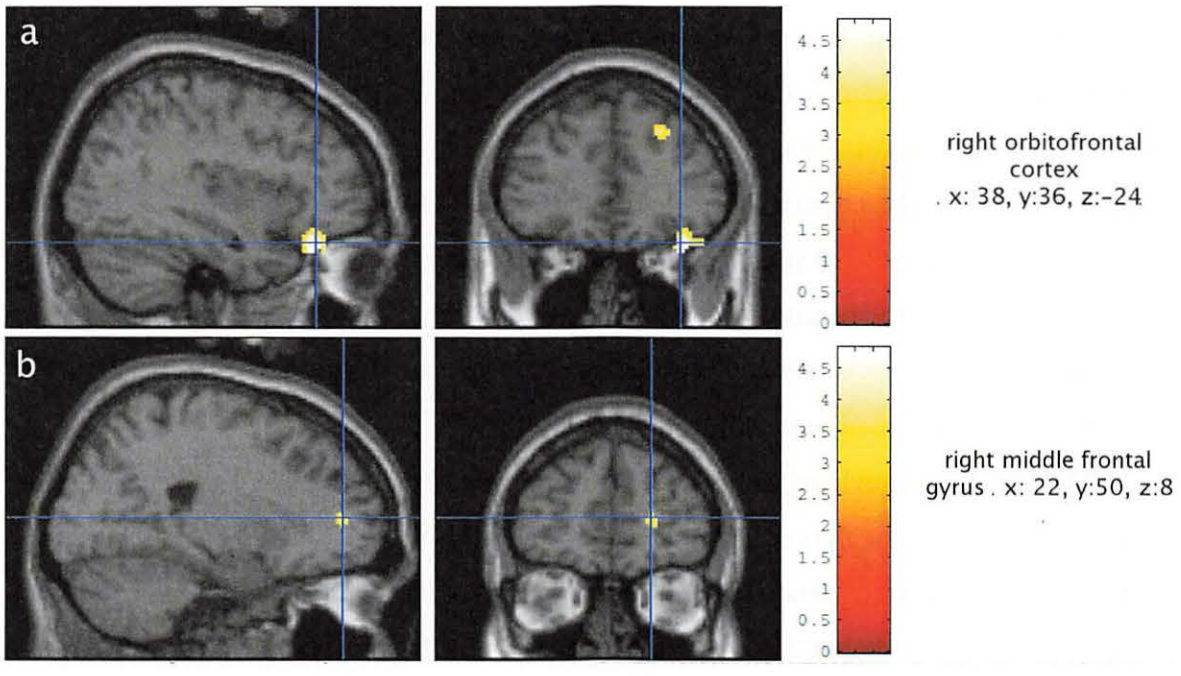

Figure 3. Representative images from the subtraction analysis of the second pH 1 infusion minus the first. Left, sagittal view; right, cranial view. a. Right orbitofrontal cortex (x: 38, y: 36, z: –24). b. Right middle frontal gyrus (x: 22, y: 50, z: 8)

VIII. 14. Scientific Evaluation on Effects of Chiropractic Treatment, a Type of Manual Therapy, Using Magnetic Resonance Imaging (MRI) and Positron Emission Tomography (PET)

Ogura T.[1], Tashiro M.[1], Masud M.[1], Watanuki S.[1], Shibuya K.[2], Itoh M.[1], Yamaguchi K.[1,3], Fukuda H.[4], and Yanai K.[1,2]

[1]Division of Cyclotron Nuclear Medicine, Cyclotron and Radioisotope Center, Tohoku University
[2]Department of Pharmacology, Tohoku University Graduate School of Medicine
[3]Advanced Image Medical Center, Sendai Welfare Hospital
[4]Institute of Development, Aging and Cancer, Tohoku University

Introduction

Chiropractic is one of the manipulative therapies initiated by Daniel David Palmer in 1895 in the United States, and its purpose has been thought to be "improving neurophysiological functions that lead to enhancing the ability of natural healing of the body by adjusting dysfunction of the joint called subluxation in the spine, pelvis, and extremity[1)]". Currently, chiropractic is legislated in the U.S. and in over 20 other countries of the world. Chiropractic spinal manipulation (CSM) is considered as one of the main treatment techniques for neuro-muscular-skeletal problems, and its main complaints of the patient are neck pain, back pain and low back pain[2)]. The autonomic nervous system (ANS) is also thought to be one of the areas influenced by CSM[3,4)].

Despite clinical evidences for benefits of the spinal manipulation and apparent wide usage of it, physiological mechanisms underlying the effects of CSM are not clearly known[5,6)]. Although many studies on chiropractic have been performed all over the world, no study has been conducted to evaluate effects of one CSM treatment utilizing MRI and PET analyses. The aim of the present study is to investigate effects of one CSM in the treated peripheral structures and in the central nervous system (CNS)[6)].

Methods

For the MRI investigation, twenty low back pain patients (mean age: 28.0 y.o.) were divided into three groups, normal group, sacral base (SB) anterior group and SB

posterior group, by the pressure testing in Activator Methods (AM), one of chiropractic techniques, and the subjects received chiropractic treatment depending on the results of the pressure testing. T2 weighted sagittal lumbo-sacral MRI images were taken on subjects before and after the treatment, and measurements on the images were compared. The measurements included angles of sacral base (SBA), L5-S1 disc (LSDA), and lumbar lordosis (LLA) (Fig. 1)[7]. The values were statistically analyzed by paired *t*-test. The present MRI study was approved by the Ethics Committee of Sendai Welfare Hospital.

For the present study, healthy male volunteers were recruited by putting up a poster in the campus of Tohoku University. Inclusion criterion was 1) men of 20 to 40 years old with the presence of cervical pain and shoulder stiffness, but without experience of receiving any types of manipulative treatment for at least one month prior to the experiment. Exclusion criteria were 1) the presence of disc problems such as disc herniation and significant disc degeneration, and 2) any other physical and mental disorders and medication that might affect brain function or perfusion. After giving informed consent, all 15 candidates were first assigned for MRI examination of the cervical region, and 3 subjects with disc problems were excluded from the study. Medical screening was also performed to confirm absence of any apparent disorders and medication that might affect brain function. In result, 12 male volunteers aged 21 to 40 (mean age ± S.D.: 28.0±6.8) were recruited into this study.

The present study was conducted in cross-over study design, in which each subject was examined twice (once in the "treatment" and the other time in the "control" conditions) in purpose of comparing the resting regional brain activity in the two conditions. In the treatment condition, subjects received a single CSM intervention, taking for around 20 minutes including a diagnostic procedure. And shortly after the CSM treatment, FDG-containing saline solution was injected to the subject through the left cubital vein (37 MBq) in a quiet room with the dim light. Subjects were asked to sit in a relaxed mood with their eyes closed for 30 min before scanning. The brain scan of the subject was initiated after 30 min of FDG injection, using a PET scanner, SET2400W (Shimadzu Inc., Kyoto, Japan). The PET scanning covered the entire brain in one scan, taking 10 minutes for emission scan, and another 5 min or so for transmission scan for tissue attenuation correction. In the other scan in the control condition, FDG was injected to the subject after a 20-min-long resting phase instead of CSM intervention. The following procedure was identical to the treatment condition. The radiation exposure due to one PET scan in this

study was estimated to be approximately 0.9 mSv[6].

In addition, the order of these two scans, that is, "control – treatment" and "treatment – control", was counter-balanced to minimize an "order effect". The meaning of this order effect is that the study subjects tend to feel psychophysiological stress more in the first scan than in the second and following scans. Therefore, the protocol was prepared to minimize this order-associated effect. In result, the first scan was performed in the treatment condition in half of the subjects, and vice versa. And, the interval between the first and second scans was set to be at least 1 week in order to eliminate residual effect of treatment. The interval ranged from 1 to 6 weeks (mean interval ± S.D.: 22.4 ± 12.5 days). CSM was performed by the same chiropractor, an advanced proficiency rated doctor of Activator Methods (AM)[6].

PET brain images were ana lyzed to identify regional changes in glucose metabolic rate using a software package, Statistical Parametric Mapping (SPM2, Functional Imaging Laboratory, London, UK). Positional errors between the 2 scans were corrected for each subject, using realignment function of SPM2. An FDG brain template distributed by Montreal Neurological Institute, McGill University, Canada, was used for anatomical standardization (spatial normalization) of the PET images by applying linear and non-linear transformations, by minimizing the inter-subject differences in gyral and functional anatomy. The normalized data were smoothed using isotropic Gaussian kernel of 12 mm (for x,y,z axes) to increase the signal-to-noise ratio by suppressing high frequency noise in the images[6].

Voxel-by-voxel analysis such as SPM is the standard tool in detecting regional changes in radioactivity levels in certain brain regions. The most popular contrast in these studies has been to contrast "resting" with "task or stimulus". For statistical analysis, all "voxel" values were normalized to an arbitrary global mean value of 50 mg/100 ml/min by ANCOVA to exclude the effects of inter-subject variability in global cerebral glucose metabolism. Paired t-test was applied to each voxel; only voxel clusters were maintained with voxels corresponding to $p<0.001$ in a single test and a cluster size of 10 voxel minimum in two ways. The statistical significance of a regional metabolic change was given in Z scores. The Z-value is the amount of difference between the target group mean value (the treatment condition, in this study) and the control mean value, divided by standard deviation of the control values $[(Mean_{target}-Mean_{control})/SD_{control}]$. Empirically in SPM analysis, a Z score higher than 3.0 (approximately corresponding to $p<0.001$) is

roughly considered as statistically significant. The location of each statistical peak was identified based on a co-planar stereotaxic atlas of the human brain. Statistically significant areas were superimposed on the standard MRI brain template images (Fig. 2)[6].

Results

In the MRI analysis, nine subjects were classified into the SB anterior group, and 11 subjects were classified into the SB posterior group in this study. No subject was divided into the normal group in the present study. Apparent angle changes were observed between pre- and post-CSM MRI images in both groups. In the SB Anterior group, SBA was decreased in 8 subjects on the post-CSM MRI images except for one subject who showed a slight increase in the angle (Table 1). Decrease in both LSDA and LLA were observed in all 9 subjects (Table 1). In SB Posterior group, increasing of SBA was seen in 10 subjects, and no change was seen on one subject on the post-CSM MRI images (Table 1). Increased LSDA and LLA were observed in all 11 subjects (Table 1).

FDG-PET analysis revealed significant changes in regional cerebral metabolism between resting and treatment conditions. Increased glucose metabolism was observed in the inferior prefrontal cortex (BA 47), perigenual anterior cingulate cortex (BA 32), and middle temporal gyrus (BA 21) whereas decreased glucose metabolism was observed in the cerebellar vermis and visual association cortex (BA 19) in the treatment condition with comparison to resting condition (Fig. 2, Table 2)[6].

Subjective and objective measures indicated significant differences. SRS-18 scores were significantly lower in the treatment condition ($p<0.01$), and VAS was also lower after CSM ($p<0.001$). Measurements of cervical muscle tone revealed significant differences after CSM (right: $p<0.002$, left: $p<0.001$). Reduced salivary amylase values were also observed in treatment condition ($p< 0.02$)[6].

Brain regions with metabolic increase in the treatment condition, and the regions with metabolic reduction in the treatment condition (Table 2 and Fig. 2). Both figures demonstrate results of voxel-by-voxel comparison of regional brain glucose metabolic images using statistical parametric mapping (SPM) (height threshold: $p<0.001$, extent threshold: 10 voxel minimum)[6].

Discussion

Results of the MRI study indicated apparent changes of measurements on the

post-CSM MRI images compared to pre-CSM MRI images; however, two subjects did not show same kinds of changes on SBA measurement. One subject showed slightly increased angle in SB Anterior group, and the other indicated no change of the angle in SB Posterior group while measurements of LSDA and LLA on these two subjects showed same kinds of changes as others. It is clearly demonstrated that this phenomenon is caused by balancing effect of CSM on the alignment of the lumbar spine and the sacrum.

The measurements of SBA and LLA after CSM in this study were lower relative to the average value (SBS: 41.0/±7.0 degree) or normal range (LLA: 50~60 degree) of those angles in an article. These differences seem to be caused by recumbent position of the subject during imaging. Yochum and Rowe stated that the value of average SBA increases from recumbent to the upright position by 8 to 12 degree[7]. Additionally, Andreasen et al. indicated that it is possible to reproduce the lumbar lordosis in the supine position by positioning the patient supine with straightened lower extremities[8]. Beattie et al. reported a mean difference between the flexed and straightened lower extremities in the supine position are 12.2 degree[9]. Therefore, the mean values of LLA after CSM in this study are within or close to the normal ranges of SBA and LLA.

In the present study, the most significant change was detected in the cerebellar vermis, which was deactivated in the treatment condition compared to the resting condition. The cerebellar vermis is considered to be playing a role in pain perception. Neuroimaging studies revealed a pattern in the cerebellar activation during pain response[10]. In addition, the cerebellar vermis is thought to be involved with the autonomic nervous system[10]. Thus, deactivation of the cerebellar vermis may be related to pain reduction and reduced sympathetic tone in this study[6]. The perigenual anterior cingulate cortex, inferior prefrontal cortex, and middle temporal gyrus were activated in the treatment condition in the present study. The cingulate cortex and inferior prefrontal cortex are known to be involved in the generation of autonomic responses[11]. Thus, the results of the present study suggest that activation of the perigenual anterior cingulate cortex and inferior prefrontal cortex may arise from sympathetic relaxation. In conclusion, the present study might demonstrate effects of one CSM in the treated peripheral structures and in CNS. Further neuroimaging studies are needed on effects of CSM[6].

References

1) Jansen J., Chiropractic Theory, Application, and Practice. Kagaku-shinbunsha: (1969) 3.
2) World health organization Kobe Centre. Traditional Medicine, Annual Report (2004) 24.
3) Budgell B.S., J. manipulative Physiolo. Ther. **23** (2000) 104.
4) Slosberg M., J. manipulative Physiolo. Ther. **11** (1988) 181.
5) Picker J.G., Spine J. Sep-Oct **2**(5) (2002) 357.
6) Ogura T., Tashiro M., Masud M., Watanuki S., Shibuya K., Yamaguchi K., Itoh M., Fukuda H., Yanai K., Regional cerebral metabolic changes in patients with neck pain following chiropractic spinal manipulation: [^{18}F]FDG PET Analysis. Alternative Therapies in Health and Medicine (in press).
7) Yochum T.R., Rowe L.J., Essentials of Skeletal Radiology. Second Ed. Williams and Wilkuins (1996) 159.
8) Andreasen M.L., Langhoff L., Jensen T.S., et al., J. Manipulative Physiol. Ther. **30** (2007) 26.
9) Beattie P.F., Brooks W.M., Rothstein J.M., et al., Spine **19** (1994) 2096.
10) Sacchetti B., Scelfo B., Strata P., Neuroscience **162** (2009) 756.
11) Schlindwein P., Buchholz H.G., Schreckenberger M., et al., Autonomic Neuroscience **143** (2008) 27.

Table 1. Comparisons of angles betweåen before and after CSM.

	Group	Before Mean (SD)	After Mean (SD)	P Value
SBA	SB A	39.2 (+/-4.9)	35.3 (+/-4.9)	p=0.001
	SB P	31.3 (+/-3.8)	35.0 (+/-3.9)	p=0.0001
LSDA	SB A	16.0 (+/-3.5)	11.5 (+/-3.7)	p=0.001
	SB P	12.7 (+/-2.8)	16.0 (+/-2.9)	p=0.001
LLA	SB A	45.7 (+/-4.9)	38.9 (+/-5.2)	p=0.001
	SB P	37.0 (+/-3.7)	41.9 (+/-5.2)	p=0.000001

Abbreviations: SBA=Sacral Base Angle, LSDA=L5-S1 Disc Angle, LLA=Lumbar Lordosis Angle, SB A=Sacral Base Anterior, SB P= Sacral Base Posterior, SD=Standard Deviation.

Table 2. Activation/Deactivation areas after CSM.

	Anatomical Region	coordinates x,y,z (mm)	Brodmann Area (BA)	Z score
Activation	IPC	54 24 -8	47	3.82
	MTG	-48 -36 0	21	3.73
Deactivation	PACC	22 24 38	32	3.48
	CV	4 -42 -18		4.62
	VAC	4 -90 24	19	3.64

Abbreviations: IPC=Inferior Prefrontal Cortex, MTG=Middle Temporal Gyrus, PACC=PACC=Perigenual Anterior Cingulate Cortex, CV=Cerebellar Vermis,VAC=Visual Association Cortex.

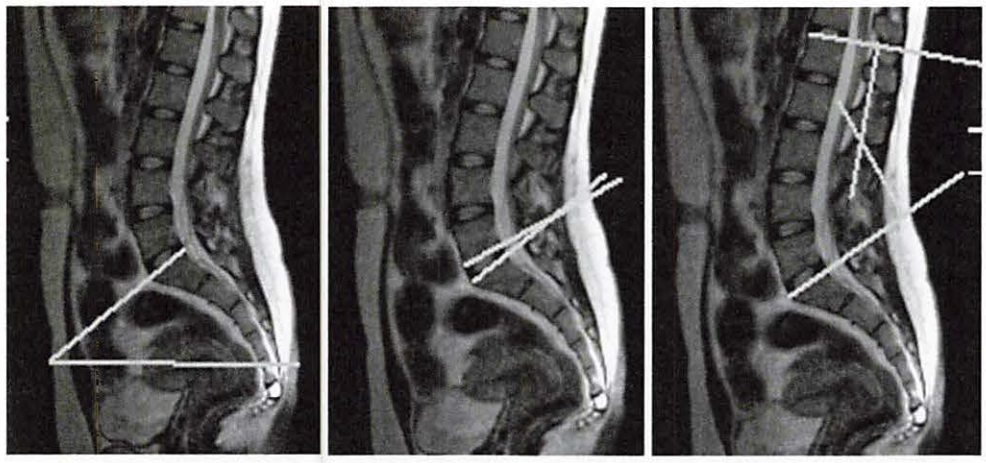

Figure 1. Angle measurements on MRI images. Sacral Base Angle (LEFT), L5-S1DiscAngle (MIDDLE), Lumbar Lordosis Angle (RIGHT)

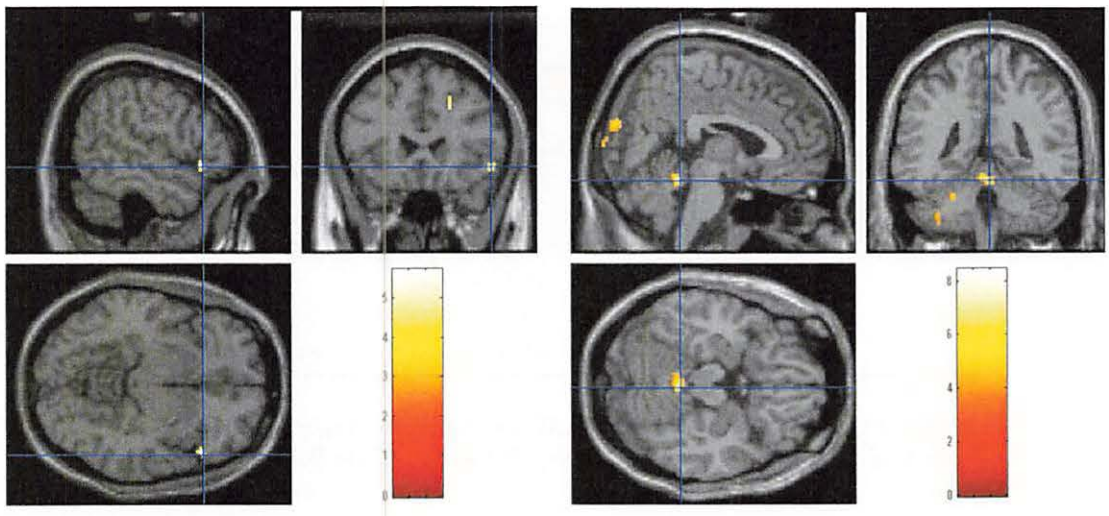

Figure 2. Results of FDG-PET Analysis Regional activation (Left) and deactivation (Right) due to chiropractic spinal manipulation. Brain regions showing a metabolic increase (Left) and a metabolic reduction (Right) in the treatment condition. Both figures demonstrate results of voxel-by-voxel comparison of regional cerebral glucose metabolic images using statistical parametric mapping (SPM) (height threshold: $p<0.001$, extent threshold: 10 voxel minimum).

VIII 15. Occipital Glucose Metabolic Decrease by Donepezil Treatment Correlated with the Improvement of Visual Hallucinations in Dementia with Lewy Bodies: the Osaki-Tajiri Project

Satoh M.[1], Ishikawa H.[1], Meguro K.[1,2], Kasuya M.[1], Ishii H.[3], and Yamaguchi S.[2]

[1]Department of Geriatric Behavioral Neurology, Tohoku University Graduate School of Medicine
[2]Osaki-Tajiri SKIP Centeer
[3]Kawasaki Kokoro Hospital

Introduction

Deficits in the neocortical cholinergic system are more pronounced in Dementia with Lewy bodies (DLB) than in Alzheimer's disease (AD)[1], and are more severe in patients with hallucinations[1,2]. Treatment with cholinesterase inhibitor (ChEI) reduces the severity of hallucinations as well as improving general cognitive function[1,3,4]. Using technetium-99m hexamethyl-propyleneamine oxine (^{99m}Tc-HMPAO) single photon emission tomography (SPECT), some authors showed the relationship between the improvement of visual hallucinations (VHs) and the increase of the occipital perfusion[1,5]. Mori et al.[5] reported serial cerebral blood flow (CBF) in DLB by ^{99m}Tc-HMPAO SPECT before and after dobepezil treatment. They showed an increased regional CBF (rCBF) in lateral surface of bilateral occipital lobes corresponded to visual association cortices[5]. O'Brien et al.[1] compared how changes in brain perfusion over 1-year period were related to changes in the severity of core features of DLB, and found a significant correlation between an increase in perfusion in midline posterior cingulate and decrease in the severity of VHs. In the O'Brien's study, the duration of donepezil intake was not controlled, so the authors suggested that the effect of donepezil of the reduction in VHs was likely to be in part.

In order to ascertain the functional alteration of occipital cortex by the treatment with ChEI, we performed the investigation of the metabolic and symptomatic changes during donepezil treatment in DLB with VHs using FDG-PET.

Methods

Participants

The study included 13 patients (age 80.0±4.0 years; 7 women) with DLB with VHs, who were living with a responsible caregiver. The diagnosis of DLB was established by consensus of 2 experienced clinicians according to consensus guidelines[6]. All participants fulfilled diagnostic criteria for probable DLB, but, because of the nature of this study, a history of VHs was a mandatory inclusion criterion[5].

After the first PET scan, all patients were treated for 12 weeks with donepezil according to Japanese dosing guidelines[5]. Donepezil was commenced at 3 mg/day. After 2 weeks, patients were reassessed for adverse effects. Patients who were tolerating then had their dose titrated up to 5 mg/day for remaining 10 weeks. The second PET scan was performed approximately 3 months after the first one.

For the neuropsychological assessment, the Mini-Mental State Examination (MMSE), and the category-B (Hallucination) of the Behavioral Pathology in Alzheimer's Disease Rating Scale (BEHAVE-AD) were administered at baseline and 12 weeks. MMSE was used for the assessment for global cognitive function. The category-B (Hallucination) of BEHAVE-AD was used for the assessment of VHs (VH score).

PET data acquisition

The PET study was performed using a model SET 2400W scanner (Shimadzu, Kyoto, Japan; axial) under resting condition with eyes opened. This scanner acquires 63 image slices at a center-to-center interval of 3.125 mm and has a spatial resolution of 3.9 mm full width at half maximum (FWHM) and a Z-axis resolution of 6.5 FWHM at center of field of view[7]. The PET room was kept lighted and quiet. A short cannula was placed in a cubital median vein for blood sampling. Transmission scan (6 minutes (min)) was performed with a $^{68}Ge/^{68}Ga$ external rotating line source, approximately 30 min after an intravenous bolus injection of 185 MBq of ^{18}F-FDG. 40 min after the injection, 2D emission scan (10 min) was performed for quantitative analysis followed by 3D emission scan (5 min). A blood sample was collected at 40 min after the injection and ^{18}F radioactivity was measured with a well-type scintillation counter. The plasma glucose concentration was also measured 40 min after the injection. The time activity curve was estimated from the plasma radioactivity according to a simplified method[8]. The same procedure was used in a post-treatment PET scan.

Image analyses

ROI method

Cerebral metabolic rates for glucose (CMRglc) parametric image were obtained from each 2D image by the autoradiographic method. Quantitative analyses were performed with conventional region of interest (ROI) settings using Dr. View/LINUX software (AJS, Japan). Circular ROIs (10 mm diameter) were placed on the cortical ribbon of medial and lateral occipital region on the CMRglc images. Two ROIs were placed on medial and lateral occipital lobe in each hemisphere on five serial slices (20 per each region). Regional CMRglc (rCMRglc) were obtained from mean values of ROIs placed on each region. The post-treatment CMRglc image was coregisterd to the pre-treatment image by SPM2 (Wellcome Department of Cognitive Neurology, London, U.K.) in each participants, and was analyzed using common ROIs to eliminate possible rater's arbitrariness. The detailed methodology has been described previously[9,10]. The changes of rCMRglc were analyzed by the paired t-test. The normalized rCMRglc values by the cerebellar CMRglc were also used on account of intersubject variability.

Outcome

The assessment of the change of VHs was performed using the score of category-B of BEHAVE-AD (VH score) at pre- and post-donepezil treatment. The changes of neuropsychological tests were analyzed by the Wilcoxon signed-ranks test. Spearman's rank correlation test was used to examine the correlation between change in VH score and that in occipital CMRglc.

Results

Clinical outcome and changes in neuropsychological tests

VHs in 6 participants were completely disappeared after donepezil administration. Figures 2 and 3 show the results of MMSE and category-B of BEHAVE-AD (VH score) at pre- and post-donepezil treatment, respectively. There were significant changes in VH score ($p=0.009$). Among 13 participants, 10 participants showed the decreasing VH score, namely improvement of VH, at the post-donepezil treatment, 2 no change, and only 1 participant (Pt. 9) increasing score (worsening of VH). The change of MMSE was insignificant ($p=0.579$).

ROI: Changes in rCMRglc

The rCMRglc in medial occipital cortex was significantly decreased (mean±S.D.: pre 7.86±1.90; post 6.72±1.09 mg/100 g/min., p=0.044) though the decrease in lateral occipital cortex was insignificant (pre 6.52±1.89; post 5.71±1.08 mg/100 g/min., p=0.15). As for the correlation between changes in VH and rCMRglc in medial and lateral occipital cortex, the scatter plot graphs show a positive correlation between VH score and rCMRglc in medal and lateral occipital cortex (medial: rs=0.783, p=0.002; lateral: rs=0.716, p=0.006). About the VH score change, no significance was detected between the patients with increased and decreased rCMRglc in medial and lateral occipital cortex by donepezil treatment (medial: p=0.125, lateral: p=0.088).

Discussion

The present PET study demonstrated that the VH in DLB patients was improved by donepezil treatment, and that the improvement was significantly correlated with the metabolic change of occipital cortices. The results of the present study are different, in the following two points, from those of two SPECT studies which investigated the correlation between the donepezil treatment for VHs and cerebral perfusion change: brain regions within the occipital lobe, and the increase or decrease of its perfusion. First, about the difference of brain regions, previous studies showed the alteration of cerebral perfusion at lateral surface of bilateral occipital lobes[5] and right posterior cingulate gyrus[1]. The latter region was included in our study, and we also observed metabolic change at left medial occipital lobe (BA 18) which belonged to a primary visual area. Second, the functional change of the present study was quite contrary to that of reported literatures: by the donepezil treatment, occipital metabolism was decreased in our study and its perfusion was increased in the literatures[1,5]. We are surprised at the opposite result of cerebral metabolism/perfusion by the donepezil treatment between the present and previous two studies[1,5], but it is possible that this difference was caused by the analytic procedure. For the image analyses, Mori[5] and O'Brien[1] used the SPECT, and the quantitative assessment was not carried out.

We found a significant positive correlation between change in VH score and metabolic change in medial and lateral occipital cortex. Perry et al.[2] reported that the extensive loss of cholinergic cells correlated with VHs in DLB. Imamura et al.[11] revealed that the hypometabolim in the right posterior temporal and parietal areas was significantly

milder in DLB with VHs than in DLB without VH. They suggested that the hypometabolism in the primary visual cortex and the relatively preserved metabolism in the temporoparietal association cortices might be associated with the occurrence of VHs in DLB patients. A relatively higher glucose metabolism for the neuronal loss in occipital lobe may underlie the development of VH in DLB. Donepezil may be effective for VH by modifying this disproportion.

References

1) O'Brien J.T., Firbank M.J., Mosimann U.P., Burn D.J., McKeith I.G., Psychiatry Research Neuroimaging **139** (2005) 79.
2) Perry E.K., Irving D., Kerwin J.M., McKeith I.G., Thompson P., Collerton D., Fairbairn A.F., Ince P.G., Morris C.M., Cheng A.V., perry R.J., Alzheimer Disease and Associated Disorders **7** (1993) 69.
3) Aarsland D., Hutchinson M., Larsen J.P., International Journal of Geriatric Psychiatry **18** (2003) 937.
4) Minett T., Thomas A., Wilkinson L.M., Daniel S.L., Sanders J., Richardson J., Littlewood E., Myint P., Newby J., Mckeith I.G., International Journal of Geriatric Psychiatry **18** (2003) 988.
5) Mori T., Ikeda M., Fukuhara R., Nestor P.J., Tanabe H., Neurology **66** (2006) 935.
6) McKeith I.G., Galasko D., Kosaka K., et al., Neurology **47** (1996) 1113.
7) Fujiwara T.,Watanuki S., Yamamoto S., Miyake M., Seo S., Itoh M., Ishii K., Orihara H., Fukuda H., Satoh T., Kitamura K., Tanaka K., Takahashi S., Ann. Nucl. Med. **11** (1997) 307.
8) Wakita K., Imahori Y., Ido T., Fujii R., Horii H., Shimizu M., Nakajima S., Mineura K., Nakamura T., Kanatsuna T., J. Nucl. Med. **41** (2000) 1484.
9) Ishii H., Ishikawa H., Meguro K., Tashiro M., Yamaguchi S., International Psychogeriatrics **21** (2009) 148.
10) Yamaguchi S., Meguro K., Itoh M., Hayasaka C., Shimada M., Yamazaki H., Yamadori A., J. Neurol. Neurosurg. Psychiatry **62** (1997) 596.
11) Imamura T., Ishii K., Hirono N., Hashimoto M., Tanimukai S., Kazuai H., Hanihara T., Sasaki M., Mori E., Neuroreport **10** (1999) 1903.

VIII. 16. Anterior Cingulate Cortex Activates after Achievement of Obligatory Purpose

Fujimoto T.[1], Tashiro M.[2], Chiba N.[3], Masud M. M.[2], Watanuki S.[2], Ishii K.[3], and Gondoh Y.[4]

[1]Center for Advancement of Higher Education, Tohoku University
[2]Division of Cyclotron Nuclear Medicine, Cyclotron and Radioisotope Center, Tohoku University
[3]Department of Medicine and Science in Sports and Exercise, Graduate School of Medicine, Tohoku University
[4]Seika Women's Junior college, Science of Early Childhood Care and Education

Introduction

After a few days of consecutive exercise, people often feel positive psychological changes not only immediately but also the next day after exercise, despite their fatigue not recovering completely. Our purpose was to study a part of the mechanism of this positive psychological change. We observed the change in regional brain activities 24 hr after four days consecutive exercise using positron emission tomography (PET) and ^{18}Fluorine-fluoro-deoxy-glucose (^{18}F-FDG).

Methods

Subjects were nine healthy male volunteers (age, 21.2±1.9 years, means ± SD). Subjects performed the intermittent exercise during four continuous days. PET scans were performed two times, before the exercise period and 24 hr after the exercise period. During the exercise period, subjects pedaled a bicycle ergometer for 90 min two times a day (total 180 min) at workloads of 55% of maximum aerobic power ($\dot{V}_{O2max}$). All subjects refrained from eating and drinking at least 6 hr before PET scan. Before PET scans, all subjects were requested to rest on a bed for 30 min. After ^{18}F-FDG (37 MBq) injection, subjects continued to rest for an additional 30 min. After the rest, a whole brain three-dimensional (3D) static emission scan was performed. The voxel-based statistical analysis of the relative parametric glucose metabolic rate images was conducted using the Statistical Parametric Mapping[1)] software version 2002 (SPM2) and Matlab 6.5.1 for Windows (Math

Works, Natick, MA, USA). For statistical analysis, all pixel values were normalized to an arbitrary global mean value of 50 mg/100 ml/min by ANCOVA, in order to exclude the effects of inter-subject variability in global cerebral glucose metabolism. A paired t-test was applied to each voxel; only voxel clusters were kept with voxels corresponding to $p<0.001$ in a single test and cluster size of 50 voxel minimum, in two ways (before the exercise period - after exercise 24 hr later, and 24 hr after exercise- before the exercise period). Subjects results were recorded on the Mood checklist–short form 2 (MCL-S.2), visual analogue scales (VAS) as a subjective index and critical flicker fusion frequency (CFF).

Results

^{18}F-FDG uptake of the left anterior cingulate cortex (ACC) was significantly higher 24 hr after exercise than before the exercise period (uncorrected, $p<0.001$, Fig. 1). The fatigue VAS was significantly elevated on the 3rd and the 4th exercise days compared with the value before the exercise period ($p<0.01$ and $p<0.05$). Fatigue VAS, 24 hr after exercise recovered to the level before the exercise period. CFF of the 4th exercise day was significantly lower than before the exercise period ($p<0.05$), and CFF at 24 hr after exercise had declined more (Fig. 2). Pleasure score declined significantly from 2nd to 4th exercise day as compared with that of before the exercise period ($p<0.05$), and it recovered 24 hr after exercise.

Discussion/Conclusion

These results demonstrated that subjects would be tired at least neurophysiologically (CFF decrease), but they would not feel much fatigue or stress psychologically 24 hours after exercise. This discrepancy on recovery between the CFF, the pleasure score, and fatigue VAS level might be related to the ACC function.

Reference

1) Friston K. J., Neuroimage 4 (1996) 97.

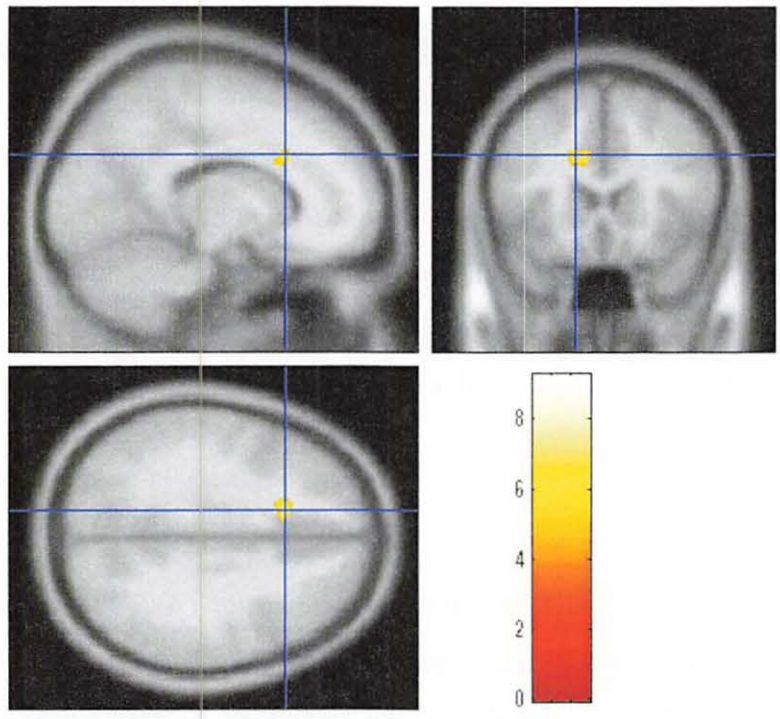

Figure 1. The *t*-statistics superimposed on the subject's average MR brain image.
Increase in normalized ^{18}F-FDG up take on left Anterior cingulate cortex (ACC) (Brodmann 32) after exercise 24 later in comparison with that of previous exercise period. Statistical threshold was set at P<0.001 (uncorrected) for height threshold and 50 voxels minimum for extent threshold. A:sagittal view, B:cornnal view, C:anxial view.

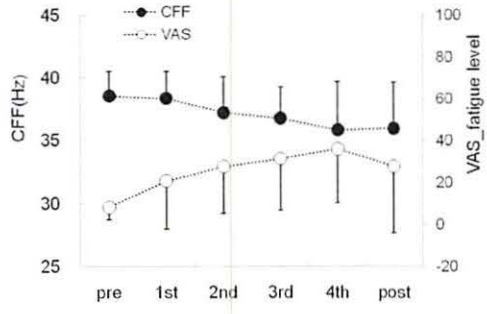

Figure 2. Change in fatigue VAS and CFF during experiment. *p<0.05 and #p<0.01 vs. previous exercise period. Values are expressed as means±SD.

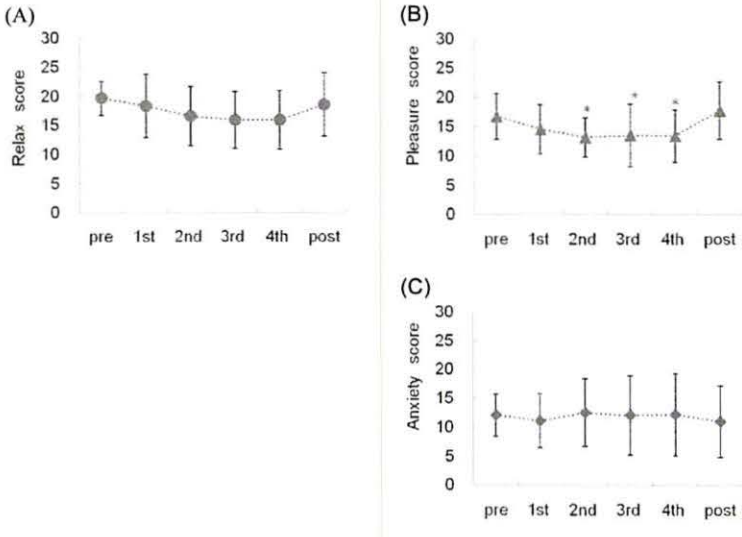

Figure 3. Change in MLC-S.2 factor scores during experiment. A; Relax score, B; Pleasure and C; Anxiety score during exercise period. Values are expressed as means ±SD. *p<0.05 vs. previous exercise period. Number of subjects are 9.

VIII. 17. Differences in Muscle Activities during Shoulder Elevation in Patients with Symptomatic and Asymptomatic Rotator Cuff Tears: Analysis Using Positron Emission Tomography

Shinozaki N.[1], Sano H.[1], Omi R.[1], Kishimoto K.[1], Watanuki S.[2], Tashiro M.[2], and Itoi E.[1]

[1]*Department of Orthopaedic Surgery, Tohoku University School of Medicine*
[2]*Cyclotron Radioisotope Center, Tohoku University*

Introduction

Shoulder pain is a common symptom of patients with rotator cuff tears, which may need to be surgically repaired if the conservative treatment does not work. On the other hand, a considerable number of people are found to have rotator cuff tears without pain in general population[1-3]. However, differences between patients with symptomatic and asymptomatic rotator cuff tears have not yet been fully clarified.

Recently, muscle activities during exercise were successfully evaluated by positron emission tomography (PET) using fluorodeoxyglucose (FDG). PET is a nuclear medicine tool for quantification of regional blood flow and tissue glucose metabolism in vivo. Once ^{18}F-FDG is taken up by the muscle cells, it remains in the cells as FDG-6-phosphate after phosphorylation; therefore, ^{18}F-FDG accumulation in the muscle can be used as a parameter of glucose intake by the muscle or the muscle activity.

Nowadays, FDG-PET is widely used for the assessment of skeletal muscle activities, especially in the area of sports medicine[4-6]. However, application of FDG-PET to shoulder muscles remains sparse[7,8]. Omi et al. established the standardized experimental protocol for shoulder scaption exercise for FDG-PET measurement[8].

We hypothesized that muscle activity patterns during arm elevation were different in patients with symptomatic and asymptomatic rotator cuff tears. The purpose of the present study was to compare the muscle activities detected by FDG-PET during shoulder scaption exercise between patients with symptomatic and asymptomatic rotator cuff tears.

Materials and Methods

The experimental protocol of the present study was approved by the Institutional Ethics Committee, and a signed consent form was obtained from each patient prior to FDG-PET examination.

Subjects

Subjects evaluated in the present study were divided into three groups (asymptomatic, symptomatic, and control). Twelve shoulders in 11 patients (five males and six females) with full-thickness rotator cuff tears were included in the present study. The average age of the patients was 69 years. In all patients, the presence of a full-thickness rotator cuff tear was confirmed by magnetic resonance imaging (MRI). To standardize patient conditions, we included rotator cuff tears involving the supraspinatus alone or involving the supraspinatus and the infraspinatus. The tear size was categorized with its longest diameter as small (<1 cm) for two patients, medium (1–3 cm) for eight patients, and large (3–5 cm) for two patients. Patients who had partial-thickness or massive rotator cuff tears (>5 cm) were excluded. Patients with any history of shoulder surgery, metabolic disease, or diabetes mellitus were also excluded.

To divide patients with rotator cuff tears into symptomatic and asymptomatic groups, patients were asked to grade the pain at rest as well as at movement on a numerical rating scale (0-10). When the highest pain score in these scores was equal to or less than 1, the rotator cuff tear was defined as asymptomatic. When the highest pain score in these scores was greater than 3, the rotator cuff tear was defined as symptomatic. In the control group, six shoulders of six healthy, age-matched volunteers were analyzed (three males and three females, average age, 73.8).

Experimental protocol

Experimental protocols for both shoulder scaption exercise and FDG-PET examination were previously established by Omi et al.[8] FDG was injected after scaption exercise of bilateral arms (200 repetitions in 10 minutes) in the scapular plane using a weight of 0.25 kg (Steel Band; Tiger Medical Instruments, Osaka, Japan), which was fixed to the wrists. After FDG injection, the subjects were asked to repeat the same exercise (Fig. 1).

PET examination

Using a PET scanner (SET-2400W; Shimadzu Inc., Kyoto, Japan) with an intrinsic spatial resolution of 3.9 mm full width at half maximum, a set of emission scans in the three-dimensional data acquisition mode was obtained from the base of the neck to the middle of the upper arm 50 min after FDG injection. The axial field of the view of this scanner was 200 mm, and images were obtained by performing two incremental scans, which took 8 min each. Using a $^{68}Ge/^{68}Ga$ external rotating line source, transmission scans (lasted 5 min each) were obtained after the emission scans (post-injection transmission) to correct tissue attenuation. All data were corrected for dead time, decay, and measured photon attenuation. They were reconstructed into a 128×128×63 matrix for a set of three-dimensional volume images using Fourier rebinning[9] and the ordered subset Expectation–Maximization[10] algorithm with the aid of a supercomputer SX-7 at the Information Synergy Center, Tohoku University.

MRI examination

MRI was performed on both shoulders of all subjects for the purpose of image fusion using the FSE-XL Sequence (Signa Horizon LX 1.5T Ver.9.1; GE Healthcare, Milwaukee, Wisconsin, USA). Measurement conditions were as follows: repetition time/echo time was 3000/85 ms, number of excitations was one, field of view was 46 cm, number of matrices was 512×512, slice thickness was 3 mm, and slice gap was 1.5 mm.

Image analyses

The PET images were fused with MR images at the same level using a specialized software Dr. View/LINUX (AJS Inc., Tokyo, Japan), which enabled us to delineate the contour of each muscle (Fig. 3). Subsequently, the volume of interest (VOI) was placed on the MR image for each shoulder muscle.

Then, SUV was calculated to quantify the activities for each VOI using the following equation:

$$SUV = \frac{\text{mean VOI count (cps/g)} \times \text{body weight (g)}}{\text{injected dose (MBq)} \times \text{calibration factor (cps/MBq)}}$$

SUV is the ratio of the amount of FDG accumulated in a certain VOI compared to the situation, where FDG is distributed equally over the whole body.

Statistical analyses

One-way factorial analysis of variance followed by the Tukey's multiple comparison test was employed for multiple comparisons of SUVs in each portion of the shoulder muscle between the three groups. $P<0.05$ was considered statistically significant.

Results

The PET/MRI fusion image in the coronal plane clearly exhibited an increased uptake of FDG in the trapezius of the symptomatic group. Interestingly, the uptake was rather decreased in the deltoid of the symptomatic group compared to the asymptomatic group (Fig. 4). In the axial plane, uptakes of FDG both in the trapezius and the levator scapulae were greater in the symptomatic group than in the asymptomatic group (Fig. 5).

SUV of the middle deltoid in the symptomatic group was significantly lower than that in the asymptomatic or control group (Table 1). The average SUVs of rotator cuff muscles are shown in Table 2. SUV of the supraspinatus in the symptomatic group was significantly lower than that in the control group. On the other hand, SUVs of other rotator cuff muscles did not show any significant differences among the three groups, although the symptomatic group represented lower muscle activities than the other two groups (Table 2).

The average SUVs of the scapular muscles are shown in Table 3. In comparison among the scapular muscles, SUV of the superior portion of trapezius was significantly higher in the symptomatic group than the other two groups (Table 3). In the levator scapulae, SUV was significantly higher in the symptomatic group than in the asymptomatic group (Table 3).

Discussion

Results of the present study clearly demonstrated that the middle deltoid activities were significantly lower in the symptomatic group than in the other groups. The supraspinatus activities were significantly lower in the symptomatic group than in the control group. The scapular muscle activities were significantly higher in the symptomatic group than in the other groups.

A consensus exists that the deltoid is the most important elevator of the arm in the scapular plane[11]. Several asymptomatic simulation studies were conducted to clarify the cause of decreasing deltoid activity. Itoi et al. reported that abduction strength was significantly increased after pain block[12]. Recently, Cordasco et al. supported that subacromial injection of local anesthetics improved the deltoid firing in patients with

symptomatic rotator cuff tears[13]. Furthermore, Scibek et al. reported that glenohumeral elevation increased significantly with decreasing scapular upward rotation after pain block[14]. On the basis of these previous studies, we assumed that the decreased deltoid activity observed in symptomatic patients might be substituted by the increased activities of the superior trapezius and levator scapulae.

In conclusion, the muscle activity pattern during shoulder scaption differed between rotator-cuff-tear patients with and without symptoms. Dysfunction of the rotator cuff muscles caused by tendon tearing seemed to be compensated by the deltoid in asymptomatic patients and by the scapular muscles in symptomatic patients.

References

1) Sher J.S., Uribe J.W., Posada A., et al., J. Bone Joint Surg. Am. **77** (1995) 10.
2) Siegbert T., Stefan R., Romain S., J. Shoulder Elbow Surg. **8** (1999) 296.
3) Yamaguchi K., Tetro A.M., Blam O., et al., J. Shoulder Elbow Surg. **10** (2001) 199.
4) Fujimoto T., Itoh M., Kumano H., et al., Lancet **348** (1996) 266.
5) Tashiro M., Fujimoto T., Itoh M., et al., J. Nucl. Med. **40** (1999) 70.
6) Shimada H., Kimura Y., Suzuki T., et al., IEEE Trans. Neural. Syst. Rehabil. Eng. **15** (2007) 442.
7) Shinozaki T., Takagishi K., Ichikawa A., et al., J. Shoulder Elbow Surg. **12** (2003) 544.
8) Omi R., Sano H., Ohnuma M., et al., J. Anat. **216** (2010) 643.
9) Defrise M., Kinahan P.E., Townsend D.W., et al., IEEE Trans. Med. Imaging **16** (1997) 145.
10) Hudson H.M., Larkin R.S., IEEE Trans. Med. Imaging **13** (1994) 601.
11) McMahon P.J., Jobe F.W., Pink M.M., et al., J. Shoulder Elbow Surg. **5** (1996) 118.
12) Itoi E., Minagawa H., Sato T., et al., J. Bone Joint Surg. Br. **79** (1997) 77.
13) Cordasco F.A., Chen N.C., Backus S.I., et al., HSSJ **18** (2009).
14) Scibek J.S., Mell A.G., Downie B.K., et al., J. Shoulder Elbow Surg. **17** (2008) 172.

Table 1. SUV in each portion of the deltoid.

Deltoid	symptomatic	asymptomatic	control	ANOVA p value
anterior	0.885± 0.151	1.425 ± 0.551	1.306 ± 0.362	0.071
middle	1.378 ± 0.494 *a, *b	2.413 ± 0.273 *a,	2.196 ± 0.540*b	0.0030
posterior	1.108 ± 0.201	1.462 ± 0.341	1.397 ± 0.155	0.0546

Values are the mean ± SD. *a : $p < 0.01$, *b : $p < 0.05$ When ANOVA resulted in significance at 95%, the Tukey HSD post-hoc test was applied.

Table 2. SUV of the cuff muscles.

	symptomatic	asymptomatic	control	ANOVA p value
Supraspinatus	1.738 ± 0.456*b	1.895 ± 0.426	2.479 ± 0.542*b	0.0402
Subscapularis				
superior	1.792 ± 0.228	2.589 ± 1.118	2.411 ± 0.502	0.167
middle	1.360 ± 0.166	2.030 ± 0.933	1.888 ± 0.442	0.163
inferior	1.262±0.148	1.528 ± 0.434	1.502 ± 0.190	0.239
Infraspinatus				
superior	1.105 ± 0.240	1.348 ± 0.398	1.426 ± 0.266	0.206
inferior	0.924 ± 0.188	1.260 ± 0.475	1.151 ± 0.231	0.218
Teres minor	1.194 ± 0.125	1.338 ± 0.298	1.352 ± 0.150	0.364

Values are the mean ± SD. *b : $p < 0.05$ When ANOVA resulted in significance at 95%, the Tukey HSD post-hoc test was applied.

Table 3. SUV in the scapular muscles.

	symptomatic	asymptomatic	control	ANOVA p value
Trapezius				
superior	1.615 ± 0.441 *a, *b	0.791 ± 0.331 *a	1.019 ± 0.129 *b	0.0016
inferior	1.011 ± 0.135	0.784 ± 0.176	0.867 ± 0.154	0.0665
Levator scapulae	1.449 ± 0.290 *b	0.988 ± 0.235 *b	1.211 ± 0.192	0.0168
Rhomboids	1.181 ± 0.132	0.979 ± 0.153	1.064 ± 0.122	0.0645
Serratus anterior	1.259 ± 0.172	1.602 ± 0.463	1.406 ± 0.171	0.177

Values are the mean ± SD. *a : $p < 0.01$, *b : $p < 0.05$ When ANOVA resulted in significance at 95%, the Tukey HSD post-hoc test was applied.

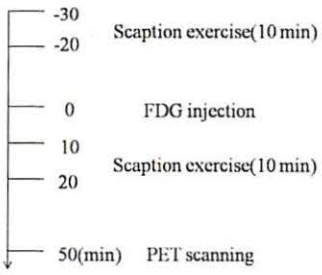

Figure 1. PET examination protocol. Scaption exercises were performed for 10 min before and after FDG injection. PET scanning was initiated 50 min after FDG injection.

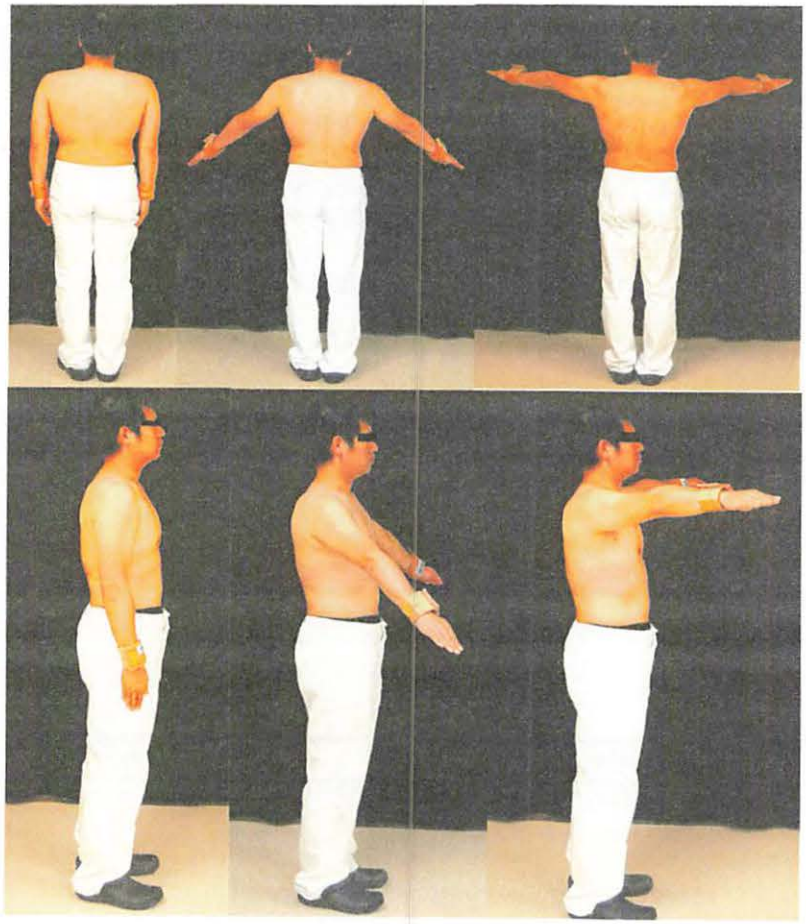

Figure 2. Photographs of scaption exercise. The scapular plane was defined as a plane that inclines 30° anteriorly from the coronal plane. The exercise consisted of 200 repetitions of elevation in the scapular plane from 0 to 90° with weights of 0.25 kg tied around the wrists. The exercise was performed at a constant speed of 90°/s

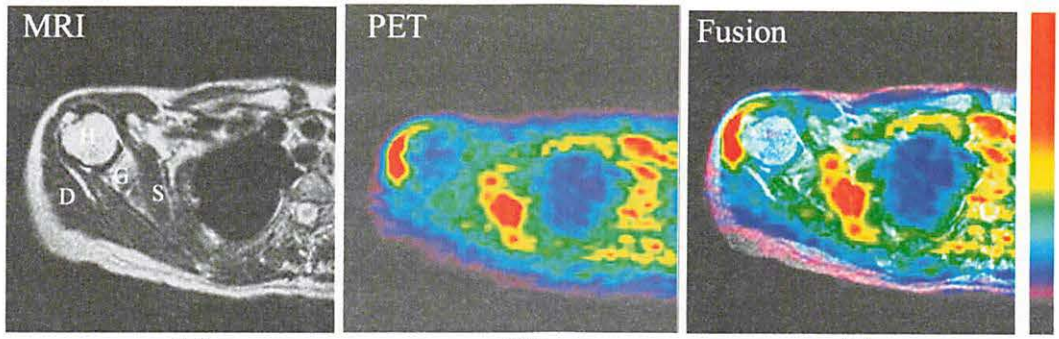

Figure 3. The MR image of axial view (a), the PET image at the same plane as the MR image (b), and the MR image fused to the PET image (c). A fusion image enabled to determine the exact location of each muscle precisely. High FDG uptakes were observed in subscapularis and deltoid muscles. The color scales indicate the pattern of FDG uptake. Red indicates maximum FDG uptake (Right shoulder at the level of humeral head, H: humeral head, G: glenoid; D: deltoid, S: subscapularis).

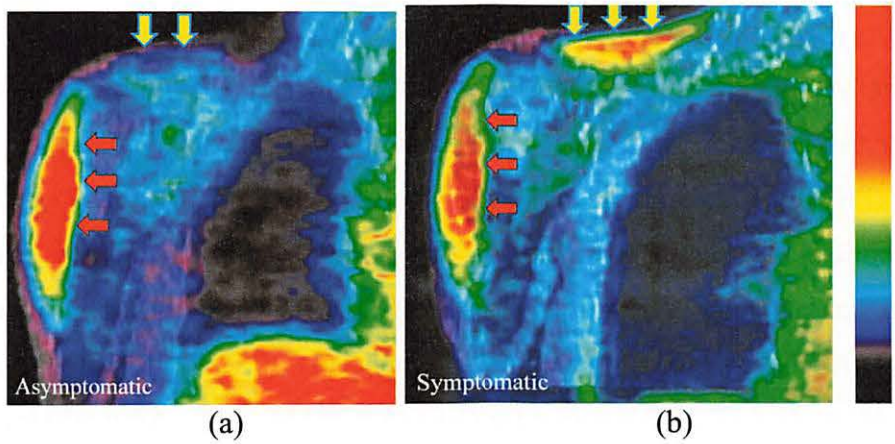

Figure 4. The typical muscle activity pattern observed in asymptomatic and symptomatic patients (coronal view of PET/MRI fusion images) The symptomatic patient (b) showed an increased activity of trapezius (yellow arrow) and a decreased activity of the deltoid (red arrow) compared to the asymptomatic patient (a).

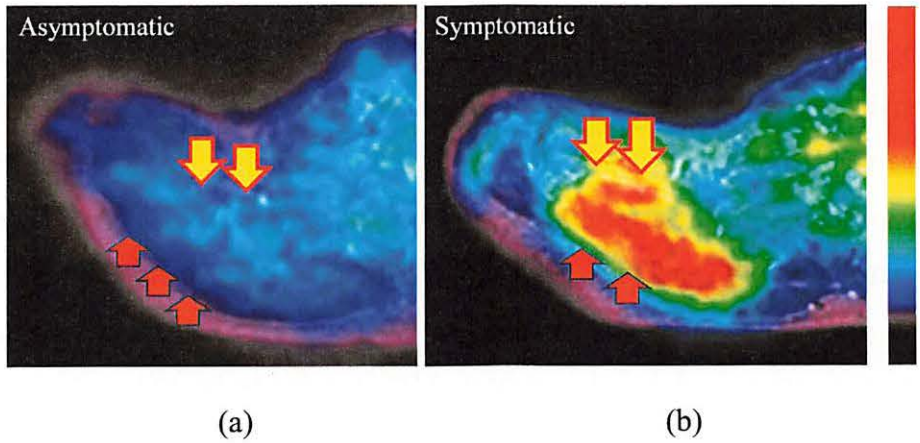

Figure 5. The typical muscle activity pattern observed in asymptomatic and symptomatic patients (axial view of PET/MRI fusion images)
The symptomatic patient (b) showed an increased activity in both the levator scapulae (yellow arrow) and trapezius (red arrow) compared to the asymptomatic patient (a).

VIII. 18. Evaluation of Skeletal Muscle Activity of Rower Limb Based on Surface and Deep Layers in Humans *in vivo*: A PET Study

Masud M.M.[1], *Fujimoto T.*[2], *Watanuki S.*[1], *Miyake M.*[1], *and Tashiro M.*[1]

[1]*Division of Cyclotron Nuclear Medicine, Cyclotron and Radioisotope Center, Tohoku University*
[2]*Center for the Advancement of Higher Education, Tohoku University*

Introduction

Nowadays, the physiological research involving skeletal muscle demonstrates a growing interest in sport medicine and rehabilitation science. Positron emission tomography (PET) is a useful imaging tool which elucidates individual skeletal muscle activity in humans *in vivo*. Reduction of radiation exposure to the healthy human volunteers is an advantage of this three dimensional positron emission tomography technique (3-D PET). 2-Deoxy-2-[^{18}F]fluoro-D-glucose ([^{18}F]FDG), an analogue of glucose, has been established as a valuable tracer for glucose metabolism[1,2]. After administration in the body, [^{18}F]FDG is trapped inside the cell after phosphorylation up to [^{18}F]FDG-6-phosphate in the presence of hexokinase enzyme. Therefore, the trapped [^{18}F]FDG-6-phosphate inside cell reflects glucose metabolism at rest and after any task. This trapping nature of [^{18}F]FDG is beneficial for imaging evaluation of skeletal muscle activity. Previous investigators assessed individual skeletal muscle activity of lower limb after exercise task (running) using [^{18}F]FDG and PET technique[3,4]. However, until now, the imaging evaluation of lower limb skeletal muscle activity associated with surface and deep layers has not been done elaborately using [^{18}F]FDG and PET technique.

In the present investigation, we tried to elucidate the skeletal muscle activity of thigh in respect of surface and deep layers using PET imaging technique.

Materials and methods

Ten healthy male volunteers (average age, 21.2±1.6 years) were enrolled in this investigation. A written informed consent was taken from each subject before the

investigation was started. The study protocol was approved by the Ethics Review Committee of Tohoku University Graduate School of Medicine. All the subjects abstained from eating or drinking at least 5 h prior to the start of the investigation. Each subject was studied twice – at rest and after exercise (ergometer bicycle pedal at 55% $\dot{V}O_{2max}$ workload).

In task condition, each subject was studied on two separate days within 3-week-long period with an interval of at least 2 days. Subjects' $\dot{V}O_{2max}$ was measured after an intermittent ergometer bicycle exercise task (Monark 818E, Monark, Varberg, Sweden). The oxygen consumption rate was determined by an automated metabolic unit machine (AE280-S, Minato, Osaka, Japan). The $\dot{V}O_{2max}$ was measured by the discontinuous method (5) and the power (watt) of the workload was determined at 55% $\dot{V}O_{2max}$. Before investigation, subjects rested for 20 min in a dimly lit and quiet room. A Teflon catheter was inserted into the antecubital veins of left hand to measure plasma radioactivity and glucose. Another Teflon catheter was inserted into the antecubital veins of opposite hand for [^{18}F]FDG injection (dose, 1.15 ± 0.11) (mean ± SD). The subjects performed ergometer bicycle pedal for 30 min following after [^{18}F]FDG injection to accomplish a total of 40 min exercise task.

After exercise and urination at around 45 min following intravenous [^{18}F]FDG injection, a set of whole-body emission scan was done with transaxial spatial resolutions of 4.4, 5.4, and 3.9 mm at full width half maximum in the tangential, radial and axial directions, respectively. Whole-body emission scan (3 min×9 frames) was performed from the knee joint to the vertex followed by transmission scan (3 min×9 frames). The post-injection transmission scan was performed with a ^{68}Ge/^{68}Ga external rotating line source (370 MBq at purchase).

In addition, all the subjects were studied at resting control condition maintaining the similar study protocol with exercise task. In resting control study, subjects sat on chairs with eyes open following after intravenous [^{18}F]FDG injection (40.7±7.0 MBq) (mean ± standard deviation, SD) for 40 min in a dimly lit and quiet room.

MRI measurement

MRI scan was performed in the thigh region (from knee joint to the hip joint) using Spin Echo Sequence (MR Vectra, GE Yokogawa, Tokyo, Japan) at 0.5 or 1.0 Tesla. The measurement conditions are mentioned as following:

Repetition time/Echo time was 330/20 ms, number of excitations was 3, the field of view

was 45 cm, number of matrix was 224×128, slice thickness was 10 mm and a gap between slices was 3 mm.

Data analysis [ROI]

PET image data was analyzed based on regions of interest analysis (ROIs) on the skeletal muscles of thigh region. ROIs were drawn on quadriceps group muscles of thigh region – vastus lateralis (VL), vastus intermedius (VI), VM (vastus medialis), based on surface and deep layers. Here, VM muscle was analyzed according to surface and deep layers by drawing an imaginary line between mid-points at transaxial direction, referring VMs (vastus medialis surface) and VMd (vastus medialis deep), respectively. The location of individual skeletal muscle was determined from their respected MRI images, as anatomical reference. Therefore, coregistration of PET data (thigh) to the MRI data (thigh) was performed using statistical parametric mapping software (SPM 5)[6]. ROIs analysis was done by using image processing software, Dr. View (Asahikasei Joho System Co. Ltd. Tokyo, Japan).

Semiquantification analysis (standardized uptake value, SUV) for individual skeletal muscle of thigh (surface and deep layers) was performed by using the following formula:

$$\text{SUV} = \frac{Mean\ ROIcts\ (cps/pxls) \times Body\ weight(g)}{Injected\ dose\ (MBq) \times Calibration\ factor\ (cps/MBq)}$$

Statistical analysis

For statistical analysis, nonparametric Wilcoxon signed rank test was performed for two conditions (resting control and exercise task), in terms of skeletal muscles of surface and deep layers. The significant difference was set at $P < 0.05$.

Results

SUV ([^{18}F]FDG uptake) was shown significantly increased ($p < 0.50$) in the skeletal muscles of both surface and deep layers (surface: VL, VMs, and deep: VI, VMd) after exercise (55% $\dot{V}O_{2max}$), when compared with the resting condition (Fig. 1). In another, SUV in thigh skeletal muscles based on surface and deep layers was shown in Fig. 2 and Fig. 3, respectively. In the resting condition and after exercise (55% $\dot{V}O_{2max}$), SUV was significantly increased ($p < 0.05$) in the deep muscles (VI and VMd) than surface muscles (VL and VMs) (Fig. 2 and Fig. 3). In another, SUV ([^{18}F]FDG uptake) of exercise to rest

ratio in the surface and deep skeletal muscles was shown in Fig. 4 and Fig. 5, respectively. It revealed that SUV of exercise to rest ratio was relatively higher in the surface muscles (VL and VMs) than deep muscles (VI and VMd) of thigh (Fig. 4 and Fig. 5).

Discussions and Conclusion

The present investigation evaluated glucose metabolic distributions in different skeletal muscles of thigh (quadriceps group) at two conditions – at rest and after exercise (ergometer bicycle pedal at an intensity of 55% $\dot{V}O_{2max}$). [^{18}F]FDG and PET imaging technique was applied for the evaluation of skeletal muscle activity, based on surface and deep layers. It was found that [^{18}F]FDG uptake (SUV) by the thigh skeletal muscles of both surface (VL, vastus lateralis and VMs, vastus medialis surface) and deep layers (VI, vastus intermedius and VMd, vastus medialis deep) was significantly higher ($p < 0.05$) after ergometer bicycle exercise (55% $\dot{V}O_{2max}$) when compared with the resting condition. In another, [^{18}F]FDG uptake (SUV) by the skeletal muscles of deep layer (VI and VMd) was higher ($p < 0.05$) than surface layer (VL and VMs) both at resting condition and after exercise. However, [^{18}F]FDG uptake (SUV) of exercise to rest ratio by the surface muscles (VL and VMs) was higher than deep muscles (VI and VMd).

Quadriceps group muscles of thigh has a dominant role in locomotion (walking, running, jogging or bicycle pedal). Therefore, it is noteworthy to assess the skeletal muscle activity of thigh (quadriceps group) based on layer arrangement (surface and deep), which would persuade the self-care of musculoskeletal system. Previous investigators already revealed the skeletal muscle activity of lower limb and pelvis after exercise task using [^{18}F]FDG and PET imaging technique[3,4]. They assessed energy metabolic changes (glucose metabolism) of lower limb skeletal muscles induced by exercise. However, to date, no studies have assessed the skeletal muscle activity of lower limb associated with surface and deep layers.

Some, physiological factors such as blood flow distribution, glucose transporter and plasma metabolite affect the glucose uptake of working skeletal muscle during exercise task[7,8]. Present study revealed that glucose uptake by the skeletal muscles of deep layer (VI and VMd) was higher than skeletal muscles of surface layer (VL and VMs) of thigh (quadriceps group) at rest and after exercise (55% $\dot{V}O_{2max}$). This variation in glucose uptake of skeletal muscle of thigh associated with surface and deep layers might be caused by the effects of blood flow distribution or nerve function.

In another, it was found that [^{18}F]FDG uptake (SUV) of exercise to rest ratio by the surface muscles (VL and VMs) was higher than deep muscles (VI and VMd), suggesting of higher glucose uptake of skeletal muscles of surface layer than skeletal muscles of deep layer of quadriceps group of thigh after exercise (55% $\dot{V}O_{2max}$). We were able to confirm that the functional levels of skeletal muscles of surface and deep layers of thigh (quadriceps group) serve as dynamic homeostatic control, and exercise may adjust uniform energy distribution.

[^{18}F]FDG and PET is a useful imaging technique in evaluation of skeletal muscle activity of lower limb associated with surface and deep layers. The results of this investigation may contribute to rehabilitation science.

Acknowledgment

This work was supported in part by a Grant-in-Aid (No. 222500605 T Fujimoto) from the Ministry of Education, Culture, Sports, Science and Technology of Japan, and as well as by a grant from the Japan Society of Technology (JST), on Research and Education in "molecular imaging."

References

1) Hamacher K., Coenen H.H., Stocklin G., J. Nucl. Med. **27** (1986) 235.
2) Phelps M.E., Huang S.C., Hoffman E.J., Selin C., Sokoloff L., Kuhl D.E., Ann. Neurol. **6** (1979) 371.
3) ujimoto T., Itoh M., Kumano H., Tashiro M., Ido T., Lancet **48** (1996) 266.
4) Tashiro M., Fujimoto T., Itoh M., Kubota K., Fujiwara T., Miyake M., Watanuki S., Horikawa E., Sasaki H., Ido T., J. Nucl. Med. **40** (1999) 70.
5) Masud M.M., Fujimoto T., Miyake M., Watanuki S., Itoh M., Tashiro M., Ann. Nucl. Med. **23**(1) (2009) 81.
6) Friston K.J., Frith C.D., Liddle P.F., J. Cereb. Blood Flow & Metabo. **11** (1991) 690.
7) Otori T., Katsumata T., Muramatsu H., Kashiwagi F., Katayama Y., Terashi A., Clin. Exp. Pharm. Physiol. **30** (2003) 266.
8) Hirshman M.F., Wallberg-Henriksson H., Wardzala L.J., Horton E.D., Horton E.S., FEBS Lett. **238** (1998) 235.

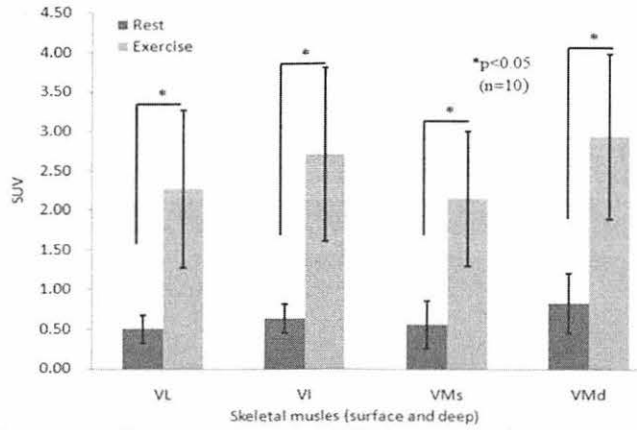

Figure 1. Glucose uptake (standardized uptake value, SUV) in the thigh skeletal muscles at rest and after exercise (55% $\dot{V}O_{2max}$). The x-axis shows the respective muscles (surface and deep) and the y-axis shows the SUV values.
VL = vastus lateralis, VI = vastus intermedius, VMs = vastus medialis surface and VMd = vastus medialis deep.

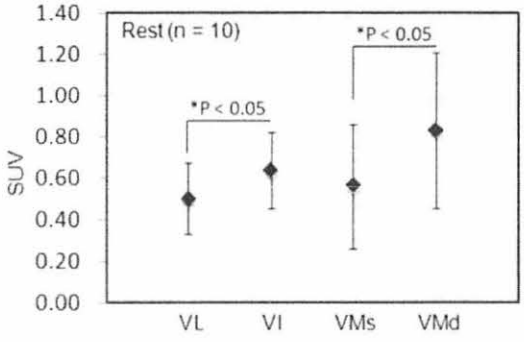

Figure 2. Glucose uptake (standardized uptake value, SUV) in the thigh skeletal muscles (surface and deep) at resting condition. The x and y-axis show the skeletal muscles and SUV values, respectively.
VL = vastus lateralis, VI = vastus intermedius, VMs = vastus medialis surface and VMd = vastus medialis deep.

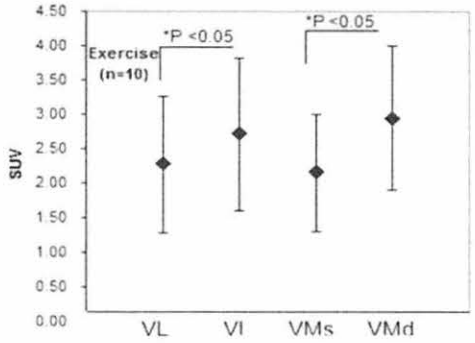

Figure 3. Glucose uptake (standardized uptake value, SUV) in the skeletal muscles of thigh (surface and deep) after exercise (55% $\dot{V}O_{2max}$). The x and y-axis show the skeletal muscles and SUV values, respectively.
VL = vastus lateralis, VI = vastus intermedius, VMs = vastus medialis surface and VMd = vastus medialis deep.

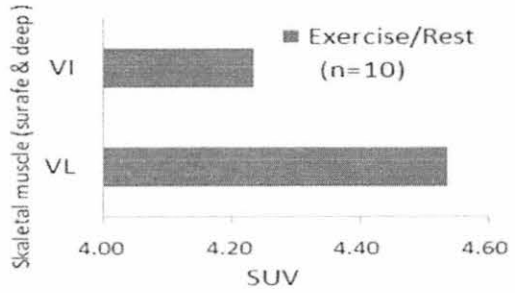

Figure 4. SUV (standardized uptake value) of exercise to rest ratio of VL (surface) and VI (deep) skeletal muscles of thigh.
VL = vastus lateralis, VI = vastus intermedius.

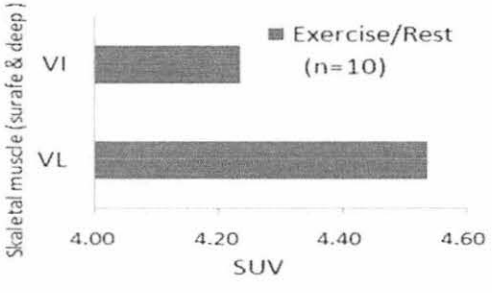

Figure 5. SUV (standardized uptake value) of exercise to rest ratio of VMs (surface) and VMd (deep) skeletal muscles of thigh.
VMs= vastus medialis surface, VMd = vastus medialis deep.

IX. RADIATION PROTECTION AND TRAINING OF SAFETY HANDLING

IX. 1. Beginners Training for Safe Handling of Radiation and Radioisotopes in Tohoku University

Yamazaki H., Baba M., Miyata T., and Yuki H.

Cyclotron and Radioisotope Center, Tohoku University

During 2009, the beginners training for safe handling of radiation and radioisotopes in Tohoku University was conducted in three courses as usual:

1) Radiation and Isotopes, 2) X-ray Machines and Electron Microscope, and 3) Synchrotron Radiation (SOR). The training was held twice a year, May and November, under the help for lectures and practice from various departments and research institutes of the university.

Lectures in English which were started in November of 2002 were continued for students and/or researchers who are not so familiar with Japanese language, by using PC projector and text of copies of view graphs (English class). The membership of the English class is almost constant as shown later.

The training for "Radiation and Radioisotopes" is for persons who use unshielded radioisotopes and accelerators, and has been conducted from 1977. The contents of lectures and practices are shown in Table 1. The order and content of the lecture was slightly modified from 2005 aiming at better understanding by trainees: the lecture on "the effect of radiation on human" was moved to the second to give stronger motivation for the training course and the following lectures. Along with the change, a new introductory lecture of "Introduction to radiation" was newly prepared as the first lecture to provide knowledge required to understand the lecture of "the effect of radiation on human". In the fiscal year of 2009, the training was performed for 483 persons (20 persons in the English class). The departments or institutes to which they belong are given in Table 2.

The training for "X-ray machines and electron microscopes" started at the end of 1983. The training is scheduled twice a year at the same time as that for "Radiation and Radioisotopes". In this course, only lectures are given with no practice. The contents of

the lectures and the distributions of trainees are shown in Table 3 and Table 4, respectively. The number of trainees was 341 (57 in the English class).

The training for the "Synchrotron Radiation" began at the end of 1995. The contents of the lectures are the same as those of the radiation and radioisotopes but no practice. In 2009, the number of trainees of the SOR course was 80 (8 in the English class).

Table 1. Contents of the lectures and practices for safe handling of radiation and radioisotopes in 2009.

Lectures (one day)	Hours
Introduction to radiation	0.5
Effects of radiation on human	1.0
Radiation physics and measurements	1.0
Chemistry of radioisotopes	1.0
Radiological protection ordinance including video	1.5
Safe handling of radioisotopes	1.5

Practices (one day)	Hours
Treatment of unsealed radioactive solution	4.0
Measurement of surface contamination and decontamination	1.0
Measurement of gamma-rays and beta-rays	2.0

Table 2. Distribution of trainees for "Radiation and Radioisotopes" in 2009.

Department	Staff	Student	Total	English class
CYRIC	2	7	9	0
Medicine	62	18	80	1
Dentistry	1	2	3	0
Pharmacy	1	81	82	2
Science	5	67	72	2
Engineering	7	85	92	7
Agriculture	1	54	55	0
Research Institutes	12	78	90	8
The others	0	0	0	0
Total	91	392	483	20

Table 3. Contents of the lectures for "X-ray machines and Electron microscopes" in 2009.
(same for both Japanese and English class)

Lectures (one day)	Hours
Safe handling of X-ray machines	1.5
Radiological protection ordinance	0.5
Video for safe handling of radiation and radioisotopes	0.5

Table 4. Distribution of trainees for "X-ray machines and Electron microscopes" in 2009.

Department	Staff	Student	Total	English class
Dentistry	0	6	6	0
Pharmacy	1	9	10	0
Science	4	45	49	3
Engineering	4	154	158	13
Arts and Letters	0	12	12	0
Research Institutes	26	92	118	41
The others	0	0	0	0
Total	35	306	341	57

Table 5. Distribution of trainees for "Synchrotron radiation" in 2009.

Department	Staff	Student	Total	English Class
Science	1	8	9	1
Engineering	2	25	27	3
Research Institutes	13	31	44	4
The others	0	0	0	0
Total	16	64	80	8

IX. 2. Radiation Protection and Management

Yuki H.[1], Miyata T.[1], Yamazaki H.[1], Baba M.[1], and Nakae H.[2]

[1]Cyclotron and Radioisotope Center, Tohoku University
[2]Japan Radiation Protection Co., Ltd.

(1) Overview

During the fiscal year of 2009, research and education in the center were conducted as active as usual.

The measurement of radioactivity concentration which was started along with the reorganization of national university in 2004 is continued periodically but the observed level was low enough generally. Devices and gas counters with automatic sample changer for radioactivity concentration measurement (samplers, α-β automatic counters) were routinely used without serious problems by several radiation facilities in Tohoku University.

(2) Unsealed radio nuclides used in CYRIC

The species and amounts of unsealed radio nuclides handled in CYRIC during the fiscal year of 2009 are summarized in Table 1. The table includes the isotopes produced by the cyclotron as well as those purchased from the Japan Radio Isotope Association or taken over from other radioisotope institutes.

(3) Radiation exposure dose of individual worker

The exposure doses of the workers in CYRIC during 2009 are given in Table 2. The doses were sufficiently lower than the legal dose limits.

(4) Radiation monitoring of the workplace

Radiation dose rates inside and outside of the controlled areas in CYRIC were monitored periodically and occasionally when needed. They were generally below the legal dose limits although there are several "hot spots" in mSv/hr range like slits or beam stopper of the 930 cyclotron and so on. Surface contamination levels of the floors inside

the controlled areas were also measured with a smear method and a survey meter method. They were under the legal regulation levels.

(5) Wastes management

The radioactive wastes were delivered to the Japan Radio Isotope Association twice in the fiscal year of 2009.

The concentration of radioisotopes in the air released from the stack after filtration was monitored with stack gas monitors. The values of concentration were well below the legal regulation levels. The radioactive water was stocked in the tanks at least for 3 days and then released to the sewerage after confirming that the concentration was lower than the legal regulation levels.

Radioactive organic scintillator waste was treated periodically by incinerator provided by Fuji-kogyo Co.Ltd.

Table 1. Unsealed radioisotopes used in each building of CYRIC during the fiscal year of 2009.

(a) Cyclotron Building (kBq)

Group 1, 2		Group 3		Group 4	
		^{11}C	210,715,000.000	^{18}F	415,954,000.000
Total	0	Total	210,715,000.000	Total	415,954,000.000

(b) Radio-isotope Building (kBq)

Group 2		Group 3		Group 4	
^{125}I	133,499.820	^{11}C	407,000.000	^{14}C	22,416.000
		^{32}P	1,337,789.583	^{18}F	222,333,000.000
		^{99m}Tc	370,000.000	^{3}H	16,544.500
Total	133,499.820	Total	2,114,789.583	Total	222,371,960.500

(c) Research Building (kBq)

Group 1, 2		Group 3		Group 4	
		^{15}O	2,220,000.000	^{18}F	185,000.000
Total	0	Total	2,220,000.000	Total	185,000.000

Table 2. Occupational radiation exposures at CYRIC during the fiscal year of 2009.

Dose range (mSv)	Number of individuals
No measurable exposure	36
0.0 - 1.0	10
1.0 - 2.0	1
2.0 - 3.0	0
3.0 -	0
Total number of persons monitored	47

X. PUBLICATIONS

X. PUBLICATIONS

[761] Increased Brain Histamine H1 Receptor Binding in Patients with Anorexia Nervosa.
Masahiko Yoshizawa, Manabu Tashiro, Shin Fukudo, Kazuhiko Yanai, Atsushi Utsumi, Michiko Kano, Masako Karahasi, Yuka Endo, Joe Morisita, Yasuhiro Sato, Masasi Adachi, Masatosi Itoh, Michiko Hongo.
Biol. Psychiatry, **65** (2009) 329-335.

[762] Decreased cortical glucose metabolism in converters from CDR 0.5 to Alzheimer's disease in a community: the Osaki-Tajiri Project.
Hiroshi Ishii, Hiroyasu Ishikawa, Kenichi Meguro, Manabu Tashiro, Satoshi Yamaguchi.
Int. Psychogeriatrics, **21** (2009) 148-156.

[763] Redistribution of whole-body energy metabolism by exercise: a positron emission tomography study.
Md. Mehedi Masud, Toshihiko Fujimoto, Masayasu Miyake, Shoichi Watanuki, Masatoshi Itoh, Manabu Tashiro.
Ann. Nucl. Med., **23** (2009) 81-88.

[764] ^{11}C-Methionine PET of Acute Myocardial Infarction.
Miyako Morooka, Kazuo Kubota, Hiromu Kadowaki, Kimiteru Ito, Osamu Okazaki, Mitsuo Kashida, Takuya Mitsumoto, Ren Iwata, Kumi Ohtomo, Michiaki Hiroe.
J. Nucl. Med., **50** (2009) 1283-1287.

[765] Impact of serotonin transporter gene polymorphism on brain activation by colorectal distention.
S. Fukudo, M. Kanazawa, T. Mizuno, T. Hamaguchi, M. Kano, S. Watanabe, Y. Sagami, T. Shoji, Y. Endo, M. Hongo, Y. Itoyama, K. Yanai, M. Tashiro, M. Aoki.
NeuroImage, **47** (2009) 946-951.

[766] Quantitative analysis of donepezil binding to acetylcholinesterase using positron emission tomography and [5-^{11}C-*methoxy*]donepezil.
Kotaro Hiraoka, Nobuyuki Okamuta, Yoshihito Funaki, Shoichi Watanuki, Manabu Tashiro, Motohisa Kato, Akiko Hayashi, Yoshiyuki Hosokai, Hiroshi Yamasaki, Toshikatsu Fujii, Etsuro Mori, Kazuhiko Yanai, Hiroshi Watabe.
NeuroImage, **46** (2009) 616-623.

[767] Dose dependancy of brain histamine H1 receptor occupancy following oral administration of cetirizine hydrochloride measured using PET with [^{11}C]doxepin.
Manabu Tashiro, Motohisa Kato, Masayasu Miyake, Shoichi Watanuki, Yoshihito Funaki, Yoichi Ishikawa, Ren Iwata, Kazuhiko Yanai.
Hum. Psychopharmacol. Clin. Exp., **24** (2009) 540-548.

[768] Reactivation of medial temporal lobe and human V5/MT+ during the retrieval of motion information: A PET study.
Aya Ueno, Nobuhito Abe, Maki Suzuki, Yayoi Shigemune, Kazumi Hirayama, Etsuro Mori, Manabu Tashiro, Masatochi Iyoh, Toshikatsu Fujii.
Brain Res., **1285** (2009) 127-134.

[769] Comparison study of amyloid PET and voxel-based morphometry analysis in mild cognitive impairment and Alzheimer's disease.
Masaaki Waragai, Nobuyuki Okamura, Katsutoshi Furukawa, Manabu Tashiro, Shozo Furumoto, Yoshihito Funaki, Motohisa Kato, Ren Iwata, Kazuhiko Yanai, Yukitsuka Kudo, Hiroyuki Arai
J. the Neurol. Sci., **285** (2009) 100-108.

[770] Evaluation of individual skeletal muscle activity by glucose uptake during pedaling exercise at different workloads using positron emission tomography.
Yuichi Gondoh, Manabu Tashiro, Masatoshi Itoh, Mohammad M. Masud, Hiroomi Sensui, Shoichi Watanuki, Kenji Ishii, Hiroaki Takekura, Ryoichi Nagatomi, Toshihiko Fujimoto.
J. Appl. Physiol., **107** (2009) 599-604.

[771] Half-life and magnetic moment of the first excited state in ^{132}I.
M. Tanigaki, S. Izumi, H. Ouchi, A. Sasaki, Y. Miyashita, N. Sato, S. Hoshino, K. Shimada, T. Wakui, T. Shinozuka, Y. Ohkubo.
Phys. Rev., *C* **80** (2009) 034304.

[772] Revised spin-parity assignment and a new interpretation of the high-spin isomer in ^{151}Er.
T. Fukuchi, T. Hori, T. Masue, K. Tajiri, A. Sato, T. Furukawa, A. Odahara, T. Shimoda, Y. Wakabayashi, Y. Gono, T. Suzuki, M. Ukai, T. Wakui, A. Yamazaki, Y. Miyashita, N. Sato, M. Takeoka, M. Ohguma, T. Shinozuka, T. Koike, K. Shirotori, Y. Miura, S. Kinoshita, Y. Ma, Y.Y. Fu, H. Tamura.
Eur. Phys. J., *A* **39** (2009) 49-51.

[773] Activation cross sections of the ^{nat}Yb(p,xn)^{169}Lu reaction for indirect production of the therapeutic radionuclide ^{169}Yb.
F. Tárkányi, A. Hermanne, S. Takács, F. Ditrói, B. Király, H. Yamazaki, M. Baba, A. Mohammadi, A. V. Ignatyuk.
Nucl. Instrum. Methods in Phys. Res., *B* **267** (2009) 2802-2807.

[774] Differential Diagnosis Between Radiation Necrosis and Glioma Progression Using Sequential Proton Magnetic Resonance Spectroscopy and Methionine Positron Emission Tomography.
Takeshi Nakajima, Toshihiro Kumabe, Masayuki Kanamori, Ryuta Saito, Manabu Tashiro, Mika Watanabe, Teiji Tominaga.
Neurol. Med. Chir., **49** (2009) 394-401.

[775] Development of GEM tracking detector for intermediate-energy nuclear experiments.
K. Fujita, Y. Sakemi, M. Dozono, K. Hatanaka, M. Nomachi, T. Sawada, T. Wakasa.
Nucl. Instrum. Methods in Phys. Res., *A* **608** (2009) 48-54.

[776] 3D imaging of human cells by using PIXE-μ-CT.
Y. Kawamura, K. Ishii, S. Matsuyama, M. Nakhostin, M. Fujiwara, M. Watanabe, S. Okura, N. Hamada, S. Tsuboi, K. Yamanaka, Y. Hashimoto, M. Fujikawa, G. Catella, Y. Hatori, K. Fujiki, H. Yamazaki, R. Ortega, G. Deves, A. Carmona.
Int. J. PIXE, **19** (2009), 29-37.

[777] Characterization of corrosion layer of carbon steel by micro-PIXE/RBS analysis.
S. Matsuyama, K. Ishii, M. Fujiwara, Y. Kikuchi, M. Nakhostin, Y. Kawamura, S. Tsuboi, K. Yamanaka, M. Watanabe, S. Ohkura, Y. Hashimoto, M. Fujikawa, G. Catella, K. Fujiki, Y. Hatori, N. Hamada, S. Tanino, H. Abe, Y. Watanabe, H. Yamazaki.
Int. J. PIXE, **19** (2009), 61-66.

[778] Time resolution improvement of Schottky CdTe PET detectors using digital signal processing.
M. Nakhostin, K. Ishii, Y. Kikuchi, S. Matsuyama, H. Yamazaki, A. Esmaili Torshabi
Nucl. Instrum. Methods in Phys. Res. A **606** (2009) 681-688.

[779] Upgrading of the 4.5 MV Dyanamitron accelerator at Tohoku University for microbeam and nanobeam applications.
S. Matsuyama, K. Ishii, M. Fujisawa, Y. Kawamura, S. Tsuboi, K. Yamanaka, M. Watanabe, Y. Hashimoto, S. Ohkura, M. Fujikawa, T. Nagaya, K. Komatsu, H. Yamazaki, Y. Kikuchi
Nucl.r Instrum. Methods in Phys. Res. B **267** (2009) 2060-2064.

[780] A method to modify coordinates of detectors in positron emission tomography system.
H. Sabet, K. Ishii, S. Matsuyama, Y. Kikuchi, K. Nakazawa, A. Esmaili Torshabi, H. Yamazaki.
Nucl. Instrum. Methods in Phys. Res. A **600** (2009) 678-682.

XI. MEMBERS OF COMMITTEE

XI. MEMBERS OF COMMITTEE (as of Jan. 1, 2010)

General

(Chairman)	Keizo	Ishii	(Graduate School of Engineering)
	Toshio	Iijima	(Executive Vice President)
	Kazushige	Maeda	(Graduate School of Science)
	Kazuaki	Iwasa	(Graduate School of Science)
	Tetsuya	Ono	(Graduate School of Medicine)
	Keiichi	Sasaki	(Graduate School of Dentistry)
	Norimichi	Nakahata	(Graduate School of Pharmaceutical Sciences)
	Akira	Hasegawa	(Graduate School of Engineering)
	Minoru	Sato	(Graduate School of Agricultural Science)
	Kazuhiko	Sogawa	(Graduate School of Life Science)
	Atuki	Terakawa	(Graduate School of Biomedical Engineering)
	Isamu	Sato	(Institute for Materials Research)
	Hiroshi	Fukuda	(Institute for Development, Aging and Cancer)
	Mihiro	Ynanagihara	(Institute of Multidisciplinary Research for Advanced Materials)
	Syoki	Takahashi	(University Hospital)
	Jirohta	Kasagi	(Laboratory of Nuclear Science)
	Ren	Iwata	(CYRIC)
	Hiromichi	Yamazaki	(CYRIC)
	Yasuhiro	Sakemi	(CYRIC)
	Etusyu	Kuraoka	(CYRIC)
	Tsutomu	Shinozuka	(CYRIC)
	Manabu	Tashiro	(CYRIC)
	Hirokazu	Tamura	(Graduate School of Science)
	Kazuhiko	Yanai	(Graduate School of Medicine)

	Tetsuya	Ono	(Radiation Safety Committee, Research Promotion Council)
	Michio	Niwano	(Radiation Safety Committee, Research Promotion Council)
(Observer)	Hideaki	Ishida	(Head of Administration Office, Graduate School of Information Science)

Cyclotron

(Chairman)	Yasuhiro	Sakemi	(CYRIC)
	Toshio	Kobayashi	(Graduate School of Science)
	Osamu	Hashimoto	(Graduate School of Science)
	Kazuaki	Iwasa	(Graduate School of Science)
	Hirokazu	Tamura	(Graduate School of Science)
	Kazushige	Maeda	(Graduate School of Science)
	Yasushi	Kino	(Graduate School of Science)
	Keizo	Ishii	(Graduate School of Engineering)
	Akira	Hasegawa	(Graduate School of Engineering)
	Atuki	Terakawa	(Graduate School of Engineering)
	Isamu	Sato	(Institute for Materials Research)
	Mihiro	Ynanagihara	(Institute of Multidisciplinary Research for Advanced Materials)
	Tsutomu	Otsuki	(Laboratory of Nuclear Science)
	Ren	Iwata	(CYRIC)
	Hiromichi	Yamazaki	(CYRIC)
	Etusyu	Kuraoka	(CYRIC)
	Tsutomu	Shinozuka	(CYRIC)
	Manabu	Tashito	(CYRIC)

Radiation Protection and Training of Safe Handling

(Chairman)	Hiromichi	Yamazaki	(CYRIC)
	Kazuaki	Iwasa	(Graduate School of Science)
	Yoshihiko	Uehara	(Graduate School of Medicine)

	Tetuya	Terasaki	(Graduate School of Pharmaceutical Sciences)
	Keizo	Ishii	(Graduate School of Engineering)
	Michio	Komai	(Graduate School of Agricultural Science)
	Tatsushi	Muta	(Graduate School of Life Science)
	Tatuo	Shikama	(Institute for Materials Research)
	Katuyoshi	Hori	(Institute for Development, Aging and Cancer)
	Kentaro	Takanami	(University Hospital)
	Ren	Iwata	(CYRIC)
	Tsutomu	Shinozuka	(CYRIC)
	Etusyu	Kuraoka	(CYRIC)

Life Science

(Chairman)	Ren	Iwata	(CYRIC)
	Kazuhiko	Yanai	(Graduate School of Medicine)
	Shogo	Yamada	(Graduate School of Medicine)
	Syoki	Takahashi	(Graduate School of Medicine)
	Teiji	Tominaga	(Graduate School of Medicine)
	Hozumi	Motohashi	(Graduate School of Medicine)
	Yukitsuka	Kudo	(Biomedical Engineering Research Organization)
	Keiichi	Sasaki	(Graduate School of Dentistry)
	Masayuki	Seki	(Graduate School Pharmaceutical Sciences)
	Keizo	Ishii	(Graduate School of Engineering)
	Kazuhiko	Nishitani	(Graduate School of Life Science)
	Hiroshi	Fukuda	(Institute for Development, Aging and Cancer)
	Nariyasu	Mano	(University Hospital)
	Yoshihiro	Takai	(College of Medical Sciences)
	Hiromichi	Yamazaki	(CYRIC)

	Manabu	Tashiro	(CYRIC)
	Yoshihito	Funaki	(CYRIC)

Prevention of Radiation Hazards

(Chairman)	Hiromichi	Yamazaki	(CYRIC)
	Naohito	Iwasa	(Graduate School of Science)
	Yasushi	Kino	(Graduate School of Science)
	Keizo	Ishii	(Graduate School of Engineering)
	Ren	Iwata	(CYRIC)
	Yasuhiro	Sakemi	(CYRIC)
	Tsutomu	Shinozuka	(CYRIC)
	Etusyu	Kuraoka	(CYRIC)
	Manabu	Tashiro	(CYRIC)
	Hideyuki	Yuki	(CYRIC)
	Katuo	Aizawa	(CYRIC)

Research Program

(Chairman)	Hiromichi	Yanazaki	(CYRIC)
	Toshio	Kobayashi	(Graduate School of Science)
	Hirokazu	Tamura	(Graduate School of Science)
	Kazushige	Maeda	(Graduate School of Science)
	Kazuhiko	Yanai	(Graduate School of Medicine)
	Shin	Fukudo	(Graduate School of Medicine)
	Akira	Takahashi	(Graduate School of Medicine)
	Akira	Hasegawa	(Graduate School of Engineering)
	Atuki	Terakawa	(Graduate School of Engineering)
	Isamu	Sato	(Institute for Materials Research)
	Hiroshi	Fukuda	(Institute for Development, Aging and Cancer)
	Syoki	Takahashi	(University Hospital)
	Jirohta	Kasagi	(Laboratory of Nuclear Science)
	Tsutomu	Otsuki	(Laboratory of Nuclear Science)

	Tsutomu	Sekine	(Center for the Advancement of Higher Education)
	Ren	Iwata	(CYRIC)
	Yasuhiro	Sakemi	(CYRIC)
	Etusyu	Kuraoka	(CYRIC)
	Tsutomu	Shinozuka	(CYRIC)
	Manabu	Tashiro	(CYRIC)
(Observer)	Masatoshi	Itoh	(CYRIC)
(Observer)	Takashi	Wakui	(CYRIC)

XII. STAFF

XII. STAFF (as of Jan. 1, 2010)

Director Keizo Ishii

Division of Accelerator

Osamu	Hashimoto[1)]
Tsutomu	Shinozuka
Takashi	Wakui
Kenji	Shimada
Shizuo	Chiba[7)]
Yasuaki	Ohmiya[7)]
Naoto	Takahashi[7)]
Shigenaga	Yokokawa[7)]
Jyunya	Suzuki[7)]

Division of Instrumentations

Sakemi	Yasuhiro
Hirokazu	Tanura[1)]
Hikonojo	Orihara[5)]
Atuki	Terakawa[3)]
Masatoshi	Itoh
Hidetomo	Yoshida

Division of Radiopharmaceutical Chemistry

Ren	Iwata
Yukitsuka	Kudo[4)]
Kazutoshi	Suzuki
Shozo	Furumoto[4)]
Yoshihito	Funaki
Yohichi	Ishikawa

Division of Cyclotron Nuclear Medicine

Kazuhiko	Yanai[2)]
Masatoshi	Itoh[6)]
Keiichiro	Yamaguchi[5)]
Kohichiro	Kawashima[5)]
Manabu	Tashiro
Sho-ichi	Watanuki
Kazuaki	Kumagai
Mehedi	Masud
Xuclong	Duan
Kazuko	Takeda

Division of Radiation Protection and Safety Control

Hiromichi	Yamazaki
Takashi	Nakamura[5)]
Masayuki	Hasegawa
Mamoru	Baba[5)]
Shigekazu	Usuda
Liu	Ruigin
Yang	Tinbo
Hideyuki	Yuki
Takamoto	Miyata
Kazuhiro	Ootomo
Hirokazu	Nakae[8)]

Division of Nuclear Fuel Science

Etusyu	Kuraoka
Sonyun	kim
Ryoki	Uejyo

Division of Advanced Radiation Application

Keitaro	Hitomi
Masayasu	Miyake

Graduate Student and Researcher

Hiroyuki	Ouchi	(Graduate School of Science)
Ayako	Sasaki	(Graduate School of Science)
Sayaka	Izumi	(Graduate School of Science)
Naoya	Sugimoto	(Graduate School of Science)
Toshiya	Takahashi	(Graduate School of Science)
Yoshitaka	Aono	(Graduate School Pharmaceutical Sciences)
Eita	Sakai	(Graduate School Pharmaceutical Sciences)
Mari	Satoh	(Graduate School Pharmaceutical Sciences)
Wong	Rebecca	(Graduate School Pharmaceutical Sciences)
Ryo	Shinbo	(Graduate School Pharmaceutical Sciences)
Akihiro	Sugawara	(Graduate School, Division of Medicine)
Takeshi	Ogura	(Graduate School, Division of Medicine)
Katuhiko	Shibuya	(Graduate School, Division of Medicine)
Kotaro	Nagatu	(Graduate School of Engineering)
Hauaki	Tokuda	(Graduate School of Engineering)
Hiroki	Nakamura	(Graduate School of Engineering)
Toru	Takayama	(Graduate School of Engineering)
Yutaro	Hashimoto	(Graduate School of Engineering)
Yasuki	Kimura	(Graduate School of Engineering)
Daisuke	Tozawa	(Graduate School of Engineering)

Office Staff

Hideaki	Ishida
Katuo	Aizawa
Nasashi	Koide
Satoshi	Arao

Yu-ko	Yamashita
Kyoko	Fujisawa
Fumiko	Mayama
Kimiko	Abe
Yumiko	Matsubara
Katuo	Ibuka
Chihiro	Saeki
Asami	Sawada
Yukie	Minbuta
Yoshio	Muroi

1) Graduate School of Science
2) Graduate School of Medicine
3) Graduate School of Engineering
4) TUBERO
5) Visiting Professor
6) Specially-approved visiting professor
7) SUMI-JU Accelerator Service Ltd.
8) Japan Radiation Protection Co., Ltd.